First principles simulations of high-entropy materials for energy storage

Yin-Ying Ting

Energie & Umwelt / Energy & Environment
Band / Volume 677
ISBN 978-3-95806-858-2

Mitglied der Helmholtz-Gemeinschaft

JÜLICH
Forschungszentrum

Schriften des Forschungszentrums Jülich
Reihe Energie & Umwelt / Energy & Environment Band / Volume 677

Forschungszentrum Jülich GmbH
Institute of Energy Technologies (IET)
Theorie und computergestützte Modellierung von Materialien
in der Energietechnik (IET-3)

First principles simulations of high-entropy materials for energy storage

Yin-Ying Ting

Schriften des Forschungszentrums Jülich
Reihe Energie & Umwelt / Energy & Environment Band / Volume 677

ISSN 1866-1793 ISBN 978-3-95806-858-2

Bibliografische Information der Deutschen Nationalbibliothek.
Die Deutsche Nationalbibliothek verzeichnet diese Publikation in der
Deutschen Nationalbibliografie; detaillierte Bibliografische Daten
sind im Internet über http://dnb.d-nb.de abrufbar.

Herausgeber und Vertrieb: Forschungszentrum Jülich GmbH
Zentralbibliothek, Verlag
52425 Jülich
Tel.: +49 2461 61-5368
Fax: +49 2461 61-6103
zb-publikation@fz-juelich.de
www.fz-juelich.de/zb

Umschlaggestaltung: Grafische Medien, Forschungszentrum Jülich GmbH

Druck: Grafische Medien, Forschungszentrum Jülich GmbH

Schriften des Forschungszentrums Jülich
Reihe Energie & Umwelt / Energy & Environment, Band / Volume 677

D 82 (Diss. RWTH Aachen University, 2025)

ISSN 1866-1793
ISBN 978-3-95806-858-2

Vollständig frei verfügbar über das Publikationsportal des Forschungszentrums Jülich (JuSER)
unter www.fz-juelich.de/zb/openaccess.

Abstract

The transition to clean energy systems relies on advanced energy storage technologies, such as lithium-ion and solid-state batteries. In this realm, high-entropy materials (HEMs) have been attracting significant attention due to their potential to increase the energy density of electrodes and improve the ionic conductivity and stability of solid electrolytes. Atomistic simulations are a powerful tool to understand the fundamental behavior of HEMs and accelerate their design process. However, the complex ionic and electronic structures of these materials introduce substantial computational challenges. This dissertation addresses these challenges by advancing computational methodologies for modeling and understanding of HEMs.

The scope of the thesis is to (1) benchmark and apply state-of-the-art electronic structure calculation methods such as the DFT+U method with Wannier functions (WF) as projectors, (2) investigate different techniques for realistic modeling of ionic configurations of HEMs and (3) to understand the performance of HEMs considered for battery applications with joint atomistic simulations and experimental investigation. Firstly, the DFT+U(WF) methodology was benchmarked for conventional electrode materials and extended to simple HEMs. This methodology was shown to improve the accuracy of electronic structure predictions compared to standard DFT+U, providing reliable estimates of oxidation states and band gaps that are comparable to computationally expensive hybrid functionals, while maintaining computational efficiency. Secondly, thermodynamic and electrochemical degradation mechanisms in Li-rich HEM cathodes were investigated together with experiments done by experimental collaborators, revealing critical pathways such as oxygen dimer formation, transition metal migration, and secondary phase formation. These findings highlight the limitations of the high-entropy effect and underscore the influence of local atomic environments in de-stabilizing electrochemically active phases. The research was further extended to garnet-based solid electrolytes, for which the impact of configurational entropy and atomic distributions on ionic conductivity and structural stability was analyzed. Increasing dopant diversity was shown to stabilize cubic phases with higher-ionic conductivity over tetragonal phases. A computationally derived high-entropy garnet with improved ionic conductivity was successfully synthesized by experimental colleagues at reduced synthesis temperatures. Studies were extended to high-entropy fluorides and Prussian white and blue analogs for diverse energy storage and electronic applications, such as sodium-ion batteries and memristors, showcasing the versatility of HEMs. Both computational and experimental results indicate that entropy-driven phase stabilization in these systems enhances their cycling performance. Additionally, we proposed a resistive switching mechanism for non-volatile memristors composed of HEMs, which was verified through atomistic simulations and experiments. Finally, advanced computational techniques were introduced to address challenges in the modeling of ionic configurations in disordered materials. In a pioneering work, quantum annealing was successfully applied to optimize ionic arrangements driven by Coulomb energy. Additionally, the persistence of short-range order (SRO) in disordered materials was revealed by calculating the Warren-Cowley SRO parameters and radial distribution function (RDF) analysis in a well-mixed four-component phosphate system, emphasizing the need to incorporate SRO into structural models of HEMs for more realistic modeling.

In summary, this dissertation addresses fundamental challenges in understanding disordered systems at an atomistic level. Computational approaches that have been proposed lead to more accurate descriptions of electronic structures and provide insights into how ionic arrangements influence material properties. The results build a solid basis for accurate computational studies of complex disordered materials for next-generation energy storage applications and could serve as the foundation for further research into accurate and computationally feasible approaches for modeling HEMs and other multi-component systems, contributing to the broader advancement of energy materials research.

Zusammenfassung

Der Übergang zu nachhaltigen Energiesystemen erfordert fortschrittliche Energiespeichertechnologien wie Lithium-Ionen- und Festkörperbatterien. In diesem Zusammenhang haben Hochentropie-Materialien (HEMs) aufgrund ihres Potenzials, die Energiedichte von Elektroden zu erhöhen sowie die Ionenleitfähigkeit und Stabilität von Festelektrolyten zu verbessern, erhebliche Aufmerksamkeit erlangt. Atomistische Simulationen sind inzwischen zu einem leistungsstarken Ansatz zur Untersuchung der grundlegenden Materialeigenschaften von HEMs und zur Optimierung ihres Designprozesses geworden. Allerdings stellt die Simulation der komplexen ionischen und elektronischen Strukturen dieser Materialien weiterhin erhebliche Herausforderungen dar. Diese Dissertation befasst sich mit diesen Herausforderungen und sie trägt zur Weiterentwicklung computergestützter Methoden zur Modellierung und zum Verständnis von HEMs bei.

Die Zielsetzung dieser Arbeit ist es, (1) modernste Methoden zur Berechnung der elektronischen Struktur, insbesondere die DFT+U-Methode mit Wannier-Funktion-Projektoren (WF), zu benchmarken und anzuwenden, (2) verschiedene Modellierungsansätze zur realistischen Beschreibung der Ionenverteilungen in HEMs zu untersuchen und (3) das elektrochemische Verhalten bestimmter HEMs für Batterieanwendungen durch die Kombination atomistischer Simulationen mit experimentellen Untersuchungen zu analysieren. Zunächst wurde die DFT+U(WF)-Methode an konventionellen Elektrodenmaterialien validiert und anschließend auf einfache HEMs erweitert. Diese Methode erwies sich als präziser als die Standard-DFT+U-Methode und lieferte zuverlässige Vorhersagen von Oxidationszuständen und Bandlücken, die mit den Ergebnissen rechenintensiver Hybridfunktionale vergleichbar sind, während sie gleichzeitig eine hohe rechnerische Effizienz beibehält. Darüber hinaus wurden in Zusammenarbeit mit experimentellen Kollaboratoren die thermodynamischen und elektrochemischen Degradationsmechanismen in Li-reichen HEM-Kathoden untersucht. Kritische Prozesse wie die Bildung von Sauerstoffdimeren, die Migration von Übergangsmetallen und die Ausbildung sekundärer Phasen wurden identifiziert. Diese Ergebnisse zeigen die Grenzen des Hochentropieeffekts auf und verdeutlichen den Einfluss der lokalen atomaren Umgebung auf die Destabilisierung elektrochemisch aktiver Phasen. Die Untersuchungen wurden auf Festelektrolyte aus der Garnetgruppe ausgeweitet, wobei der Einfluss der Konfigurationsentropie und der atomaren Verteilung auf die Ionenleitfähigkeit und strukturelle Stabilität analysiert wurde. Eine höhere Dotierungsvielfalt stabilisiert die kubische Phase mit höherer Ionenleitfähigkeit gegenüber der

tetragonalen Phase. Zusätzlich konnte eine hochentropische Verbindung der Granatgruppe mit verbesserter Ionenleitfähigkeit von experimentellen Partnern bei reduzierten Synthesetemperaturen erfolgreich hergestellt werden. Neben Batterieanwendungen wurden hochentropische Fluoride sowie Preußisch-Weiße- und Preußisch-Blaue-Analoga für verschiedene Energiespeicher- und elektronische Anwendungen wie Natrium-Ionen-Batterien und Memristoren untersucht, wodurch die Vielseitigkeit von HEMs unterstrichen wird. Computergestützte und experimentelle Studien zeigen, dass die entropiegetriebene Phasenstabilisierung in diesen Systemen die Zyklenstabilität verbessert. Zudem wurde ein Mechanismus zur Schaltung des Widerstandes von nichtflüchtigen Memristoren auf Basis von HEMs vorgeschlagen und durch atomistische Simulationen und Experimente verifiziert. Schließlich wurden fortschrittliche computergestützte Methoden eingeführt, um Herausforderungen bei der Modellierung ionischer Konfigurationen in ungeordneten Materialien zu überwinden. Quantum Annealing wurde erfolgreich zur Optimierung von Ionenanordnungen unter Berücksichtigung der Coulomb-Wechselwirkung eingesetzt. Darüber hinaus konnte die Persistenz von Nahordnungsstrukturen (SRO) in ungeordneten Materialien durch die Berechnung der Warren-Cowley-SRO-Parameter und Radialverteilungsfunktionen (RDF) in einem vierkomponentigen Phosphatsystem nachgewiesen werden. Dies unterstreicht die Notwendigkeit, SRO in Strukturmodelle von HEMs für eine realistischere Modellierung zu integrieren.

Diese Dissertation hat die grundlegenden Herausforderungen beim Verständnis ungeordneter Systeme auf atomistischer Ebene behandelt, indem präzise Beschreibungen elektronischer Strukturen entwickelt wurden und der Einfluss ionischer Anordnungen auf die Materialeigenschaften untersucht wurde. Die Ergebnisse bilden eine Grundlage für exakte computergestützte Studien von komplexen ungeordneten Materialien für zukünftige Energiespeicheranwendungen und bieten eine fundamentale Basis für weiterführende Forschung zu präzisen und recheneffizienten Modellierungsansätzen für HEMs und andere Multikomponentensysteme, wodurch ein Beitrag zur Weiterentwicklung der Energieforschung geleistet wurde.

Acknowledgments

First and foremost, I want to thank my supervisors, Prof. Michael Eikerling and Dr. Piotr Kowalski, for their guidance and support throughout my PhD journey. I deeply appreciate Michael's consistent support in monitoring my research progress and providing insightful suggestions to deepen my understanding and broaden the scope of my work. I am especially thankful to Piotr for day-to-day supervision and especially for introducing me to advanced computational approaches, guiding me in the preparation of papers and presentations, connecting me with experimental partners, and providing opportunities to visit different labs abroad. This support has been invaluable and truly shaped my academic journey. I would also like to extend my gratitude to Prof. Payam Kaghazchi for co-supervising my thesis research, introducing me to the field of computational research on batteries and relevant modeling approaches, and always being there to support my research in any aspect.

To my IET-3 family, thank you for creating such a warm, supportive, and inspiring environment. It's been a privilege to work alongside all of you. Special thanks to Ying Sun, Conor Price, and Simon Ospina for the meaningful discussions and constant encouragement. A special thanks to Fabian Tipp, who inspires me to continuously go running, helping clear my mind and recharge my personal "battery". I'm also grateful to everyone in the CMM division for their support and insightful conversations. A special thanks to Dr. Tobias Binninger for introducing me to the field of quantum computing and sharing valuable expertise on simulation of energy materials..

I acknowledge Forschungszentrum Jülich for funding my research and JARA-CSD for providing crucial computational resources on the supercomputers at Forschungszentrum Jülich and RWTH Aachen. I also thank the DAAD for supporting my project, which enabled the research stay of my undergraduate student André Koch Liston. My gratitude also goes to all the students I had the privilege to supervise, including André Koch Liston, Noah Dohrmann, and Marharyta Okhrymenko. I've learned so much from working with you, and I'm proud of what we've achieved together.

During my PhD, I had the opportunity to visit Prof. Alexander Urban's group at Columbia University. I am deeply thankful for this opportunity, the fruitful discussions we had, and the kindness shown in giving me a tour of New York City, making it a memorable experience.

To my family, words cannot express my gratitude for the love and support I got from you. I am

profoundly grateful to my family for their unwavering support, both emotionally and financially. You have always encouraged me to follow my dreams, even when it meant being far away from home. Your love and encouragement have strengthened me to overcome the challenges I encountered. Xiaochen Zheng, Ruijie Ye, and Ting Ye, I'm so grateful for the time we've spent together. You've given me so many moments of laughter and joy, which helped me truly relax and recharge.

Finally, I want to express my deepest gratitude to my partner, Wei Zhao, for everything. From moving to Jülich to support me every step of the way, both academically and personally. Whether it was proofreading my manuscripts, giving feedback on my presentations, or simply being there on tough days, I couldn't have done this without you.

Declaration

I hereby declare in lieu of an oath that I have completed the dissertation entitled

First principles simulations of high-entropy materials for energy storage

independently and without illegitimate assistance from third parties. I have used no other than the specified sources and aids. I have complied with the principles for ensuring good scientific practice at RWTH Aachen University. The publication of the thesis does not breach any existing trade secrets. I agree to the internal use of this thesis in the libraries of RWTH Aachen University as well as in Forschungszentrum Jülich GmbH.

Erklärungen zur Dissertation

Ich erkläre hiermit eidesstattlich, dass ich die Dissertation mit dem Titel

First principles simulations of high-entropy materials for energy storage

selbstständig verfasst, alle in Anspruch genommenen Hilfen in der Dissertation angegeben habe und die schriftliche und elektronische Fassung übereinstimmen. Die Grundsätze zur Sicherung guter wissenschaftlicher Praxis der RWTH Aachen habe ich eingehalten. Die Veröffentlichung verletzt keine bestehenden Betriebsgeheimnisse. Mit der internen Verwendung dieser Arbeit in den Bibliotheken der RWTH Aachen sowie im Forschungszentrum Jülich GmbH bin ich einverstanden.

Ort, Datum	Unterschrift

Contents

List of figures

List of Tables

List of abbreviations

AO	atomic orbital
ATAT	Alloy Theoretic Automated Toolkit
BESS	Battery Energy Storage Systems
BZ	Brillouin zone
CE	cluster expansion
CEI	cathode electrolyte interphase
CV	cyclic voltammetry
DFPT	density-functional perturbation theory
DFT	density functional theory
DOS	density of states
EA	electron affinity
ECI	effective cluster interaction
EIS	electrochemical impedance spectroscopy
ESO	entropy-stabilized oxide
EV	electric vehicle
GGA	generalized gradient approximation
GS	ground-state
HE	high-entropy
HEA	high-entropy alloy
HEF	high-entropy fluoride
HEG	high-entropy garnet
HEM	high-entropy material
HEO	high-entropy oxide
HF	Hartree-Fock
HOMO	highest occupied molecular orbital
IP	ionization potential
LIB	lithium-ion battery
LCO	lithium cobalt oxide
LDA	local density approximation
LFP	lithium iron phosphate
LLO	Li-rich layered oxide
LLZO	lithium lanthanum zirconium oxide
LMO	lithium manganese oxide
LTO	lithium titanium oxide
LUMO	lowest unoccupied molecular orbital
MAE	mean absolute error

MC	Monte Carlo
MD	molecular dynamics
MF	metal fluoride
MLWF	maximally localized Wannier functions
NCA	lithium nickel cobalt aluminum oxide
NMC	lithium nickel manganese cobalt oxide
OS	oxidation states
PBA	Prussian blue analogue
PW	Prussian white
QA	quantum annealing
QUBO	quadratic unconstrained binary optimization
RDF	radial distribution function
REMC	replica exchange Monte Carlo
RS	resistive switching
SEI	solid electrolyte interphase
SIB	sodium-ion battery
SQS	special quasirandom structures
SRO	short-range order
SSB	solid-state battery
TM	transition metal
VASP	Vienna Ab initio Simulation Package
WF	Wannier functions
XRD	X-ray diffraction

1 Introduction

1.1 Energy transition towards clean energy

Fossil fuels, such as coal, crude oil, and natural gas, have been the primary energy sources driving human activities and industrial growth since the start of the Industrial Revolution in the 18th century [1]. However, the rapid economic growth enabled by the executive exploitation of fossil fuels has come at a steep environmental cost, most notably in the form of air pollution and greenhouse gas emissions, particularly carbon dioxide (CO_2) [2]. Currently, the global carbon dioxide emissions originate mainly in the high energy demand and consumption of member countries of the Organization for Economic Cooperation and Development and emerging economies such as China, India, Brazil, and South Africa [3]. These emissions have increased the greenhouse effect, leading to severe consequences including rising global temperatures, melting polar ice caps, rising sea levels, and increasing the frequency and impact of extreme weather events, such as heatwaves, floods, droughts, and storms [4–6]. In addition to the environmental damage, fossil fuels are limited and non-renewable resources, with supplies expected to be largely exhausted within one to two centuries, while being distributed unevenly across the world [7]. This imbalance can result in supply disruptions, price volatility, and geopolitical tensions, all of which pose significant challenges to long-term energy security. As a result, the need for a transition away from fossil fuels has become critical, both to mitigate climate change and to ensure sustainable energy supplies for future generations. The energy transition involves shifting from reliance on finite and polluting energy sources to renewable and clean alternatives. The energy sources that could drive this transition must be sustainable, environmentally friendly, and sufficiently scalable to meet global demand. Currently utilized clean energy resources mainly include solar, wind, and geothermal power.

While renewable energy sources such as solar and wind could be easily utilized, there are challenges to be addressed and solved. A major issue is the high dependence on local climate conditions. For instance, the intermittency of suitable weather conditions can cause interruptions in energy supply, as solar panels generate electricity only during sunlight hours, and wind turbines rely on sufficient wind strength. This problem could be addressed by large-scale, reliable energy storage solutions that can accumulate energy during favorable weather conditions to be used when demand exceeds supply. As a result, energy storage technologies are critical to ensure the continuous and efficient use of renewable power resources.

Various energy storage solutions have been explored and implemented. These include thermal storage, mechanical storage (such as pumped hydroelectric storage and flywheels), hydrogen production storage through water electrolysis, and, most importantly, batteries. Among these, Battery Energy Storage Systems (BESS), particularly Li-ion batteries (LIBs), have been gaining increasing attention due to their scalability, efficiency, and adaptability for applications such as grid-level energy storage and consumer electronics [8]. BESS's capacity is expected to grow globally from 11 GWh (2017) to between 100 GWh and 167 GWh in 2030 [9]. LIBs have emerged as the dominant technology in the energy storage landscape, primarily due to their high energy density, long cycle life, and decreasing cost. LIBs have found extensive use not only in portable electronic devices but also in electric vehicles and large-scale energy storage systems supporting renewable power grids [8, 10, 11]. Other types, like sodium-ion batteries, flow batteries, sodium-sulfur, and advanced lead-acid batteries, are also used depending on needs of specific applications, such as longer discharge times or lower cost.

To meet the increasing demand for advanced rechargeable batteries, it is essential to explore new electrode materials that could offer longer cycle life, higher energy density, and more efficient charge-discharge rates, as well as materials with higher conductivity and stability for solid electrolytes in all-solid-state batteries. This dissertation contributes to related research by harnessing and testing state-of-the-art computational methodologies and, with their aid, investigating some key processes that drive the performance of battery materials. As a rich history of battery development led to today's state-of-the-art materials and technologies, in the next section we provide a brief overview of the key breakthroughs. A more detailed historical overview can be found in Refs. [12–14].

1.2 Historical outlook on the development of batteries

The history of batteries spans over two centuries, starting with Benjamin Franklin, who first coined the term 'battery' to describe a system of charged plates in 1749 [15]. The electrochemical battery can be traced back to around 1800, when Luigi Galvani and Alessandro Volta found that electrical phenomena could be generated through chemical reactions between two different metals (zinc and copper), separated by paper or cloth soaked in an electrolyte. This cell, later known as the Voltaic pile, was the first working battery [16]. It provided a continuous electric current and demonstrated the conversion of chemical energy into electrical energy, setting the stage for future developments in electrochemical storage. However, the Voltaic pile suffered from hydrogen bubbles forming on the copper metal surface, which caused a short lifetime of the battery. In 1836, John Frederic Daniell addressed this issue by adding a second electrolyte to consume the hydrogen produced by the first, in a setup known as the Daniell Cell.

In 1859, Gaston Planté invented the lead-acid battery - the first rechargeable battery. Planté's design, consisting of lead plates immersed in sulfuric acid, could be recharged by passing a reverse current, making it suitable for energy storage applications. However, the lead-acid battery's relatively high weight limits its suitability for portable or lightweight applications. Instead, it is still commonly used in automobiles and heavy-duty applications where weight is less of a concern. In 1866, Georges Leclanché introduced a battery that used a zinc rod as the anode, a manganese dioxide-carbon mixture as the cathode, and an ammonium chloride solution as the electrolyte. The use of manganese dioxide as a depolarizer improves its practicality and reliability. The Leclanché Cell was widely adopted for telegraph systems and became the foundation for modern dry-cell batteries. The design principles of the Leclanché Cell are still used in consumer primary batteries, such as carbon-zinc and alkaline cells.

At the end of the 19th century, the rechargeable nickel-cadmium (NiCd) and nickel-iron (NiFe) batteries were developed by Waldemar Junger and Thomas Edison, respectively. Like lead-acid batteries, NiCd and NiFe batteries were rechargeable. NiCd batteries have been extensively used in high-power consumer devices, as they can endure high discharge rates with no loss of capacity. However, the primary disadvantages are their higher cost and the use of cadmium. Until the late 1950s, the zinc-carbon battery remained a popular primary cell, but its relatively short lifespan hampered its use. The next major advancement came with the development of alkaline batteries by Lewis Urry, who found a way to expand the lifespan of the zinc-carbon battery. Urry's design, which comprised powdered zinc and manganese dioxide in an alkaline electrolyte, offered a longer-lasting and more powerful energy source with an energy density up to 400 Wh/L or 150 Wh/kg [17].

The development of LIBs in 1970s marked a milestone in energy storage technology. Stanley Whittingham laid the foundation for rechargeable lithium batteries by using titanium disulfide (TiS_2) at the cathode and metallic lithium at the anode [18, 19]. While Whittingham's work demonstrated lithium's potential for energy storage, the use of metallic lithium presented safety concerns, particularly with the release of toxic H_2S gas upon contact with moisture [20]. In 1980, John B. Goodenough advanced lithium battery technology by developing the lithium cobalt oxide ($LiCoO_2$) cathode, which offered better energy density and stability [21]. This development addressed many of the earlier safety concerns. Building on Goodenough's work, Akira Yoshino in 1985 developed the first practical, commercially viable LIB by replacing metallic lithium anode with carbon-based compound, which significantly improved the safety and feasibility of lithium-ion technology [22]. Sony commercialized the first LIB in 1991, revolutionizing portable electronics with this small, lightweight, and durable power source with an energy density of 200 Wh/L and 80 Wh/kg [23, 24].

Various designs for rechargeable batteries have been successfully commercialized [25–27]. Because of high power, energy density, long cycle life performance and good safety performance, LIBs are, as of today, the most advanced rechargeable batteries [28–30]. However, further improvements in performance aspects are needed for the widespread application of LIBs as high-capacity storage devices. Ongoing research focuses on improving safety, cost-efficiency, and energy density to meet the demands of the clean energy transition [31, 32]. Cathode materials have evolved from lithium cobalt oxide (LCO) to alternatives such as lithium iron phosphate (LFP) and lithium nickel manganese cobalt oxide (NMC), offering longer life cycles, enhanced safety, and lower production costs. Innovations in electrolyte and separator technologies, such as the introduction of lithium bis(trifluoromethanesulfonyl)imide (LiTFSI), have further enhanced battery performance. The development of solid-state batteries towards higher energy densities and improved safety represents the next frontier in battery technology [33].

The search for more efficient battery materials continues to address the increasing demand for high-performance and sustainable batteries. One promising direction is the exploration of high-entropy materials (HEMs) for LIBs, which offer unique advantages due to the variety of active elements and the potential to improve battery performance through enhanced cycling stability, reduced phase transitions, and greater resistance to degradation. Research on HEMs could pave the way towards the next generation of batteries, pushing the boundaries of energy storage and addressing the growing need for sustainable and scalable solutions [34–37].

1.3 Fundamentals of Li-ion batteries

A LIB consists of three internal components: two electrodes, an electrolyte, plus a separator (Figure 1.1). The positive electrode of the battery is typically made of a lithium-transition metal (TM)-based compound like lithium cobalt oxide ($LiCoO_2$), while the negative electrode is commonly composed of graphite. The electrolyte is a medium that allows the transfer of lithium ions between the electrodes during charge and discharge, and is usually lithium salt in organic solvent. Finally, the separator is a porous membrane made up of polyethylene or propylene that physically separates the electrodes to prevent short-circuiting while still allowing ions to pass through.

There are two types of LIBs based on their reaction mechanisms: intercalation-type and conversion-type. In intercalation-type batteries, lithium ions move into and out of the crystal structures of the anode and cathode without significantly altering their internal structure. This type is the most widely used and forms the basis for commercial LIBs. In this section, we focus primarily on intercalation-type batteries due to their prevalence in commercial applications.

1.3.1 Mechanism of intercalate-type in LIBs

In an intercalation-type LIB, the charging and discharging processes involve the movement of lithium ions and electrons between the electrodes. There are two electrodes in a battery, namely the cathode and anode, defined by their redox process. The anode is the electrode where the oxidation of lithium takes place, producing lithium ions (Li^+) and electrons. The

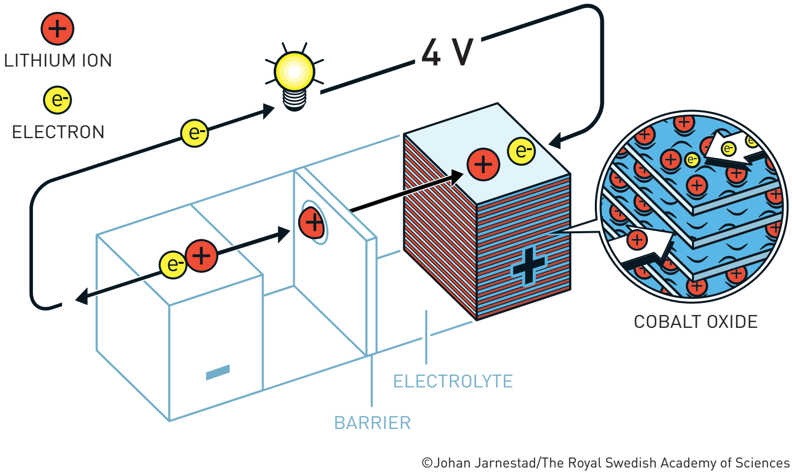

©Johan Jarnestad/The Royal Swedish Academy of Sciences

Figure 1.1: A schematic representation of a typical Li-ion battery cell during discharge, including the cathode (positive electrode), anode (negative electrode), and the electrolyte. Figure reproduced from [38].

cathode is the electrode that accepts electrons, reducing the Li^+ to Li atoms. During the discharging process (see Figure 1.1), Li^+ are extracted from the anode (negative electrode) and move through the electrolyte toward the cathode (positive electrode). Electrons travel through an external circuit to the cathode, where they combine with Li^+, forming neutral lithium atoms that intercalate into the cobalt oxide. The following reactions describe the discharge process in a typical battery composed of $LiCoO_2$ (cathode or positive electrode) and graphite C_6 (anode or negative electrode) system:

Cathode (reduction during discharging):

$$\mathrm{CoO_2 + Li^+ + e^- \longrightarrow LiCoO_2} \tag{1.1}$$

Anode (oxidation during discharging):

$$\mathrm{LiC_6 \longrightarrow Li^+ + e^- + C_6} \tag{1.2}$$

The overall reaction for the battery can be written as:

$$\mathrm{LiC_6 + CoO_2 \rightleftharpoons LiCoO_2 + C_6} \tag{1.3}$$

During the charging process, when electrical energy is applied to the battery, the direction of ion and electron flow is reversed, and so the assignment of anode/cathode is switched. However, to avoid confusion and to maintain consistency, the term anode/cathode only refers to the discharge process. The charging process stores energy within the battery, placing the system in a metastable state with increased Gibbs free energy. Electrochemical redox processes play a key role in charging and discharging cycles. During charging, electrical energy is converted into chemical energy and stored within the electrode materials. Conversely, during discharging, the stored chemical energy is converted back into electrical energy, which could be used to power external devices.

1.3.2 Mechanism of conversion-type LIBs

In the ongoing quest for higher energy density and improved performance in energy storage devices, conversion-type batteries, which potentially provide a higher specific capacity than conventional intercalation-based electrode materials, have emerged as a promising alternative to traditional intercalation-type batteries [39]. Unlike intercalation-type batteries, which rely on the reversible insertion and extraction of ions into the host material, conversion-type batteries operate based on a fundamentally different mechanism. It involves a solid-state redox reaction where the active material undergoes a complete transformation during charge and discharge processes. This transformation typically involves a change in the crystalline structure of the electrode material, including the breaking and reformation of chemical bonds that leads to the formation of entirely new phases. An example of such a reaction can be represented as follows,

$$MX + yLi^{+} + ye^{-} \rightarrow M + Li_{y}X.$$

Here, MX represents a metal oxide or sulfide, M is the reduced metal, and Li_yX is a lithium compound. As a result, conversion-type batteries can potentially offer much higher energy densities, as the full capacity of the electrode material can be utilized. Since in a conversion process multiple electrons can be transferred per formula unit during the redox reaction, conversion materials can deliver capacities three to five times larger compared to intercalation materials [40]. Among the different conversion material types, metal fluorides (MFs) show a relatively high lithiation potential due to the large enthalpy of formations [41–43]. Additionally, MFs show high volumetric and gravimetric capacities, which enable them to be attractive candidates for high energy density cathode materials [44, 45].

Unfortunately, conversion materials suffer from large volume changes upon cycling and unfavorable interactions between active material and electrolyte caused by significant chemical transformations [46]. The former can lead to cracking of individual particles, structural disintegration, swelling of the electrode, and disconnection of the active material. The latter is accompanied by a loss of active material, re-precipitation of cathode components, which can lead to blockage of the ion pathways, and migration of soluble species to the anode side which negatively affects the SEI (blockage of the anode) [47, 48]. In addition, electrolyte decomposition can also occur (gas evolution), which is a relevant factor from a safety point of view. These interrelated processes may lead to an increase in cell resistance, poor cycling performance, and poor coulombic efficiency [39, 49, 50]. While conversion-type batteries offer higher energy densities, these challenges make them less suitable for commercial applications. In Section 6.1, we will show how HEMs can potentially solve these issues and improve the electrochemical performance of a conversion-type battery.

1.3.3 Battery voltage

The voltage of a lithium-ion battery represents the thermodynamic driving force for lithium transfer between the electrodes. Under open-circuit conditions, it is determined by the difference in the chemical potential of lithium between the two electrodes, which corresponds to the difference in the electrochemical potential (Fermi level) of electrons in the external circuit. The electrochemical potential of an electrode can be expressed as:

$$\tilde{\mu} = \mu + zF\phi, \tag{1.4}$$

where μ is the chemical potential of lithium ions in the electrode, z the valency (charge) of ions involved in the electrochemical reaction, F the Faraday constant, and ϕ the electrical potential. Under open-circuit (equilibrium) conditions, the electrochemical potentials of lithium at cathode ($\tilde{\mu}_{\mathrm{C}}$) and anode ($\tilde{\mu}_{\mathrm{A}}$) are equal, $\tilde{\mu}_{\mathrm{C}} = \tilde{\mu}_{\mathrm{A}}$. Thus the chemical potential difference $\mu_{\mathrm{C}} - \mu_{\mathrm{A}}$ is exactly balanced by an opposite electrical potential difference $zF(\phi_{\mathrm{C}} - \phi_{\mathrm{A}})$, which we measure as the cell voltage. The resulting open-circuit voltage V_{oc} is therefore

$$V_{\mathrm{oc}} = \phi_{\mathrm{C}} - \phi_{\mathrm{A}} = -\frac{\mu_{\mathrm{C}} - \mu_{\mathrm{A}}}{zF}. \tag{1.5}$$

V_{oc} is related to the Gibbs free energy change (ΔG) of the electrochemical reaction occurring within the battery. In thermodynamics, the Gibbs free energy change of a reaction between different charge states can be expressed in terms of enthalpy and entropy changes

$$\Delta G = \Delta H - T\Delta S, \tag{1.6}$$

where ΔH and ΔS are the enthalpy and entropy differences, respectively, between the two given states of charge, and T is the temperature. The relationship between enthalpy change, internal energy change (ΔU_{int}), and pressure-volume work is given by

$$\Delta H = \Delta U_{\text{int}} + P\Delta V. \tag{1.7}$$

Therefore, the reaction Gibbs free energy is

$$\Delta G = \Delta U_{\text{int}} + P\Delta V - T\Delta S. \tag{1.8}$$

In practical batteries, the terms $P\Delta V$ and $T\Delta S$ correspond to changes in volume and configurational entropy caused by ion intercalation and de-intercalation. At low temperatures, since pressure-volume changes and entropy contribution are typically small, with negligible contribution to ΔG compared to ΔU_{int}, the Gibbs free energy simplifies to

$$\Delta G \approx \Delta U_{\text{int}}. \tag{1.9}$$

For a given state of charge with lithium concentration of x and x_0, the Gibbs free energy of the battery ΔG_{cell} can be expressed in terms of the free energy changes in the cathode (ΔG_C) and anode (ΔG_A):

$$\Delta G_{cell}(x) = \Delta G_C - \Delta G_A = \left[G_C(x) - G_C(x_0)\right] - \left[G_A(x) - G_A(x_0)\right]. \tag{1.10}$$

Given that the chemical potential μ is defined as:

$$\mu = \frac{\partial G}{\partial x}, \tag{1.11}$$

The average Li chemical potentials of the anode and cathode can be expressed as

$$\mu_{\text{C}}(x) = \frac{G_{\text{C}}(x) - G_{\text{C}}(x_0)}{x - x_0}, \mu_{\text{A}}(x) = \frac{G_{\text{A}}(x) - G_{\text{A}}(x_0)}{x - x_0}. \tag{1.12}$$

Substituting these back into the Equation 1.5 and using $n = z(x - x_0)$, the voltage becomes

$$V_{oc}(x) = -\frac{\mu_{\text{C}}(x) - \mu_{\text{A}}(x)}{zF} = -\frac{[G_{\text{C}}(x) - G_{\text{C}}(x_0)] - [G_{\text{A}}(x) - G_{\text{A}}(x_0)]}{z(x - x_0)F} = -\frac{\Delta G_{cell}(x)}{nF}, \tag{1.13}$$

where n is the total number of electrons transferred during the reaction. Thus, the voltage of a battery can be calculated from the difference in chemical potential between lithium ions in the cathode and anode materials, as well as the Gibbs free energy difference between the electrodes. For instance, consider a lithium TM oxide cathode paired with a lithium metal anode. During discharge, lithium ions migrate from the anode to the cathode, which corresponds to a transition from a lower lithium concentration state x_1 to a higher concentration state x_2 in the cathode. The process is represented by the following reaction:

$$\mathrm{Li}_{x_1}\mathrm{MO}_2 + (x_2 - x_1)\mathrm{Li} \rightarrow \mathrm{Li}_{x_2}\mathrm{MO}_2. \tag{1.14}$$

The voltage can thus be computed using the following equation:

$$V_{oc} = -\frac{\Delta G_{cell}}{nF} = -\frac{G_{\mathrm{Li}_{x_2}\mathrm{MO}_2} - G_{\mathrm{Li}_{x_1}\mathrm{MO}_2} - (x_2 - x_1)G_{\mathrm{Li}}}{(x_2 - x_1)F}. \tag{1.15}$$

Applying Equation 1.9, when the contributions from volume and entropy changes are negligible, the Gibbs free energy can be replaced by the internal energy, which can be computed by density functional theory (DFT).

Stability window

We have demonstrated previously that the battery voltage is fundamentally governed by the Gibbs free energy difference, or equivalently, the chemical potential difference, between the anode and cathode materials. However, the working voltage of the battery is not determined solely by the electrode materials. It is also constrained by the stability window of the electrolyte, which plays a crucial role in ensuring the long-term stability of the system. The stability window is defined by the energy gap between the highest occupied molecular orbital (HOMO) and the lowest unoccupied molecular orbital (LUMO), as illustrated in Figure 1.2. For efficient and stable operation, the chemical potential of the anode, μ_A, must remain below the LUMO of the electrolyte, while the chemical potential of the cathode, μ_C, should lie above the HOMO of the electrolyte.

During the charging process, μ_A increases while μ_C decreases. As these potentials shift, they can eventually exceed the electrolyte's stability window. In the first charging process, when the anode's chemical potential surpasses the LUMO, the electrolyte undergoes reduction, and when the cathode's potential drops below the HOMO, the electrolyte experiences oxidation. This leads to the formation of passivating layers. On the anode side, this reduction of the electrolyte results in the formation of a solid electrolyte interphase (SEI). The SEI is essential for stabilizing the anode, as it forms a passivating layer that allows lithium ions to diffuse through it while preventing further electron transfer and electrolyte decomposition. The SEI formation, while crucial, results in some capacity loss during the first cycle. This is because some charge is consumed to form this layer. At higher voltages on the cathode side, a cathode electrolyte interphase (CEI) may form due to electrolyte oxidation. The CEI functions similarly to the SEI by stabilizing the cathode and preventing continuous electrolyte decomposition. However, their formation mechanisms differ: the CEI forms due to oxidation reactions at the cathode-electrolyte interface, whereas the SEI results from reduction reactions at the anode.

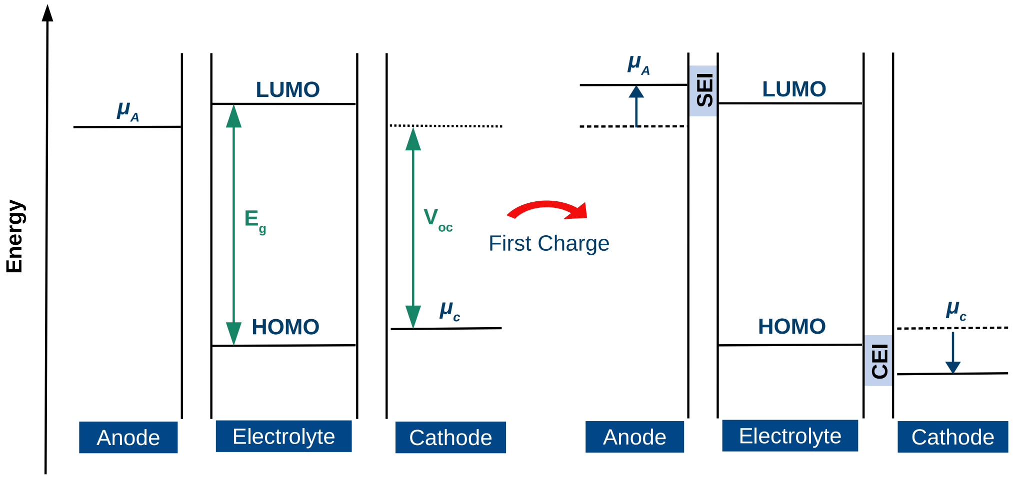

Figure 1.2: A schematic showing the relative energies of the electrolyte stability window (E_g) and the relationship between the electrochemical potentials of electrodes and the HOMO/LUMO levels of the electrolyte.

The typical stability window for LIB electrolytes lies between 2.5 V and 4.5 V. Operating outside of this range can lead to electrolyte decomposition, increased side reactions, capacity fade, and safety hazards like thermal runaway. In high-voltage cathodes, such as nickel-rich materials, the CEI becomes increasingly important for maintaining long-term cycling stability. Thus, both SEI and CEI are critical for ensuring the stability of the anode and cathode, respectively, especially as the chemical potentials shift during charging and discharging cycles. Failure to maintain these passivating layers or operating outside the electrolyte's stability window results in a risk of electrolyte degradation and loss of performance.

1.3.4 Metrics of battery performance

Understanding voltage alone is not sufficient to understand the battery's performance. Here, we introduce additional specific parameters relevant to this aspect.

Specific capacity. The specific capacity refers to the amount of charge a material can store per unit mass, typically expressed in milliamp-hours per gram (mAh/g). In LIBs, this is determined by the number of Li^+ that can be reversibly inserted into and extracted from the electrode material during charge and discharge cycles.

For instance, in the case of $LiCoO_2$, the theoretical specific capacity can be calculated as

$$\text{Specific Capacity (mAh/g)} = \frac{n \times F}{M} \times \frac{1}{3600}, \tag{1.16}$$

where n is the number of moles of electrons transferred (for $LiCoO_2$, $n = 1$), F the Faraday constant, M the molar mass of the material, and 3600 the conversion factor from Coulombs to milliamp-hours. Substituting the values for $LiCoO_2$ gives

$$\text{Specific Capacity} = \frac{1 \times 96485}{97.87} \times \frac{1}{3600} \approx 272\,\text{mAh/g}.$$

This estimate indicates that $LiCoO_2$ has a theoretical specific capacity of approximately 272 mAh/g, meaning that for each gram of $LiCoO_2$, the material can theoretically store and deliver 272 milliamp-hours of charge during operation. In reality, the specific capacity usually does not reach the theoretical value because the Li ions cannot be fully extracted.

Energy density. The energy density represents the amount of energy a material can store per unit mass, typically expressed in watt-hours per kilogram (Wh/kg). Unlike the specific capacity, which focuses solely on charge storage, the energy density accounts for the operating voltage of a battery and thus gives a more comprehensive measure of the energy storage capacity.

At nominal battery voltage, the energy density can be calculated from specific capacity and operating voltage as

$$\text{Energy Density (Wh/kg)} = \frac{\text{Specific Capacity (mAh/g)} \times \text{Operating Voltage (V)}}{1000}. \tag{1.17}$$

For $LiCoO_2$, the average operating voltage is approximately 3.7 V. Using the calculated specific capacity of 272 mAh/g, the energy density is:

$$\text{Energy Density} = \frac{272\,\text{mAh/g} \times 3.7\,\text{V}}{1000} \approx 1.00\,\text{Wh/g}.$$

This indicates that $LiCoO_2$ has a theoretical energy density of about 510 Wh/kg, making it a highly efficient material for energy storage. The combination of both high specific capacity and operating voltage makes $LiCoO_2$ an essential material in modern LIB technologies.

Coulombic Efficiency. The coulombic efficiency is a key performance metric for batteries that indicates the ratio of the total charge extracted from the battery during discharge to the total charge input during charging. In other words, it measures how effectively a battery can store and deliver charge over a cycle, and is typically expressed as a percentage

$$\text{Coulombic Efficiency (\%)} = \frac{\text{Discharge Capacity}}{\text{Charge Capacity}} \times 100.$$

The ideal coulombic efficiency is close to 100%, meaning almost all the charge input is recovered during discharge. However, due to side reactions such as the formation of the SEI or parasitic reactions within the electrolyte, the efficiency is usually slightly less than 100%.

After the initial cycle, subsequent cycles typically show improved coulombic efficiency as the SEI layer stabilizes. Maintaining high coulombic efficiency is critical, particularly for long-term cycling applications, as it affects the overall lifetime of the battery. Small inefficiencies in each cycle, when accumulated over many charge and discharge cycles, can lead to significant capacity loss and reduced battery performance. More details of terms for batteries can be found in [51].

1.3.5 Electrochemical techniques

To evaluate the performance of electrode materials in batteries, several electrochemical techniques are commonly employed. Two widely used methods are cyclic voltammetry (CV) and galvanostatic cycling. These techniques provide insights into the redox behavior, reaction kinetics, and stability of battery materials, which are critical for designing high-performance energy storage systems. Below we provide a brief description of both techniques. A more detailed introduction can be found in [52, 53].

Cyclic Voltammetry (CV). Cyclic voltammetry is a widely employed technique to investigate the redox behaviors of materials. As shown in Figure 1.3a, during CV, the potential is varied linearly vs. time between two limits (denoted as E_1 and E_2) and then reversed, scanning through both oxidation (anodic) and reduction (cathodic) processes. The transient current is recorded as a function of potential. A typical current response for LIBs is shown in Figure 1.3b, where the peaks correspond to redox reactions. During the forward scan, the potential is increased, inducing the oxidation of species in the system (the anodic peak). For instance, in the case of $LiCoO_2$, during charging, Co^{3+} is oxidized to Co^{4+}. Conversely, during the reverse scan, the reduction reaction representing discharging (the cathodic peak) occurs, where Li^+ ions are reinserted into the electrode material. The potentials at which these peaks occur, the anodic peak potential E_{pa} and cathodic peak potential E_{pc}, provide insight into the energy levels of the redox reactions occurring at the electrode. By analyzing the CV peaks, key voltages where lithium ions enter and exit the electrodes can be identified, along with the reaction kinetics. A narrower separation between E_{pa} and E_{pc} generally indicates more efficient, reversible reactions with minimal polarization, which is essential for materials designed to maintain high capacity and long cycle life.

In some materials, particularly more complex systems, multiple anodic and cathodic peaks can be observed in the CV curve. These multiple peaks suggest the presence of multiple redox couples, indicating that several distinct redox reactions occur at different voltage levels. For example, in layered lithium TM oxides, such as NMC, these peaks often reflect the sequential extraction and insertion of lithium ions from multiple redox-active TMs (e.g., Ni, Mn, Co) during cycling. Each peak corresponds to a specific electrochemical reaction that contributes to the overall capacity of the battery.

CV curves can also be transformed into voltage vs. capacity profiles. The capacity, Q, can be calculated by integrating the current, i, as a function of potential E and dividing by the scan rate v, where $v = \frac{dE}{dt}$, as follows:

$$Q = \int i dt = \int i \frac{dE}{v}. \tag{1.18}$$

The discharge and charge plateaus in the voltage-capacity graph correspond to the cathodic and anodic peak voltages, respectively, as shown in Figure 1.3c.

In short, CV is particularly useful in identifying the redox reactions of lithium-ion intercalation and deintercalation in materials, such as $LiCoO_2$, and in assessing the reversibility of these reactions by comparing the current peaks in forward and reverse scans. The area under the curve is proportional to the charge passed during these processes, helping quantify the specific capacity of the electrode material.

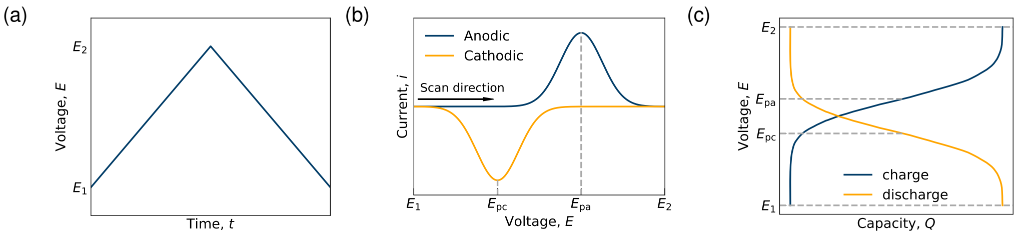

Figure 1.3: Electrochemical characterization of battery behavior. (a) Linear potential sweep during CV. (b) CV curve illustrating anodic (oxidation) and cathodic (reduction) peaks. (c) Charge-discharge voltage profiles, demonstrating lithium-ion intercalation and deintercalation.

Galvanostatic Cycling. Unlike CV, galvanostatic cycling charges and discharges the battery at constant current (Figure 1.4a) while tracking the corresponding voltage response over time. This method is one of the most practical techniques to check the capacity, reversibility, stability, and rate capability of electrode materials. In half-cell battery tests, the capacity is typically expressed in gravimetric terms (mAh g^{-1}), with the current normalized to a specific value (A g^{-1}) or a C-rate, where 1 C represents the current required to fully charge or discharge the battery in one hour. This approach thus simulates battery performance under realistic operation conditions, making it a standard method for evaluating the long-term performance and efficiency of electrode materials.

For a typical single discharge-charge cycle under constant current, the resulting voltage profile exhibits a sloped curve with recognizable plateaus, as shown in Figure 1.3c. Similar to the CV technique, these plateaus correspond to phases during which lithium ions are inserted or extracted at nearly constant voltage. A clearer visualization of these voltage plateaus can be obtained by plotting a differential capacity curve (dQ/dV vs. V), which highlights changes in capacity with respect to voltage, as seen in Figure 1.3b.

The rate capability is another critical aspect evaluated through galvanostatic cycling, which can be assessed by changing the applied current (C-rate) during cycling. As an example, Figure 1.4b demonstrates how the capacity decreases as the current rate increases from 0.1C to 5C, followed by a recovery at 0.1C, reflecting the battery's recovery after high-rate cycling. By changing the C-rate, one can test how well a material performs under faster or slower charging and discharging conditions. At low rates (e.g., 0.1C), the battery operates with minimal polarization, reflecting the theoretical capacity of the material. However, as the rate increases (e.g., 1C or 2C), the battery's performance may decline due to aggravated polarization. A material with good rate capability will retain a significant portion of its capacity, even at high rates, making it more suitable for applications requiring rapid charging or discharging.

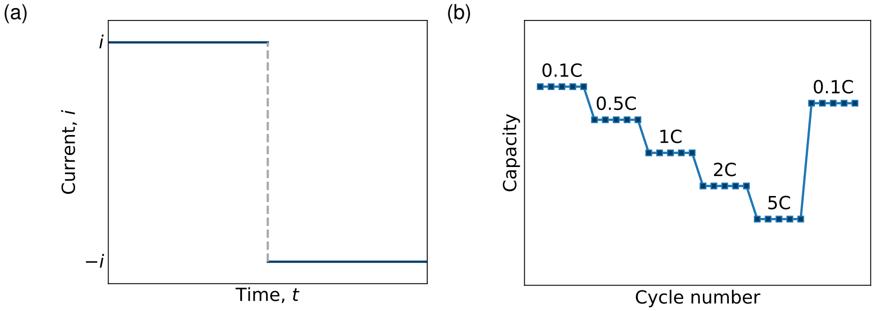

Figure 1.4: (a) Constant current profile applied during galvanostatic cycling for both charge and discharge phases. (b) The rate capability under various C-rates. The C-rate values shown here are provided as an example to demonstrate how battery capacity responds to different charging and discharging rates.

We can also evaluate the cycle life of a material by repeatedly charging and discharging the battery over multiple cycles and monitoring the capacity retention. The cycle life is generally defined as the number of cycles before the battery's reversible capacity diminishes to 80% of its initial value, providing a measure of the long-term durability of the electrode material.

1.4 Review on common materials used in LIBs

LIBs have emerged as the leading energy storage solution across a wide range of applications, from portable electronics to electric vehicles, due to their impressive energy density, long cycle life, and low self-discharge rate. The performance and safety of LIBs are heavily influenced by the materials used in their anodes, cathodes, and electrolytes, with each component playing a vital role in determining the battery's efficiency and stability. Significant research has focused on optimizing these materials to achieve higher rate capabilities, larger charge capacities, and—for cathodes—higher operating voltages, as these improvements can enhance both energy and power density. This, in turn, could enable the development of smaller, more cost-effective batteries, under the condition that raw material costs remain manageable.

Developing optimal battery materials involves balancing multiple factors, including cost, specific energy, specific power, safety, performance, and cycle life. This section provides an overview of the most widely used materials in LIB cathodes, anodes, and electrolytes, discussing their performance, advantages, limitations, and economic considerations. A summary of performance metrics for common LIB electrode materials is shown in Table 1.1, and a comparison across key metrics is illustrated in Figure 1.5.

Type	**Material**	***Specific Capacity (mAh/g)**	**Voltage (V)**	**Volume Expansion (%)**
Cathode	LCO	272 (140)[54]	3.8	2
	LFP	170 (165)[55]	3.4	7
	LMO	285 (140)[56]	4.1	7
	NMC 111	280 (160)[57]	3.7	3–4
	NMC 622	280 (180)[58]	3.7	3–4
	NMC 811	280 (200)[59]	3.7	4
	NCA	279 (199)[60]	3.7	4
Anode	C_6	372 (350)[61]	0.1–0.2	10
	LTO	175 (160)[62]	1.55	0.2 (negligible)
	Si	4200 (2000)[63]	0.2	270

*The specific capacity values are presented as theoretical values with practical values in parentheses.

Table 1.1: Summary of performance for common LIB electrode materials.

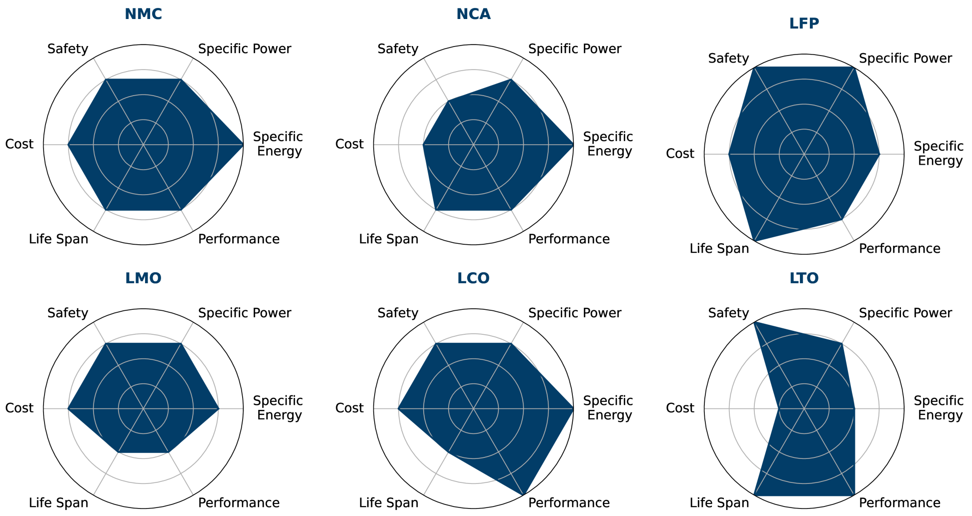

Figure 1.5: Spider plot illustrating the performance comparison of six common LIB electrode materials across six key metrics: specific capacity, voltage, cycle life, safety, cost, and rate capability.

1.4.1 Cathode materials

A key component that limits the performance of LIBs is the positive electrode (cathode), which in most batteries is mainly composed of layered lithium TM oxides, e.g., $LiCoO_2$ [64–66]. Other similar, but environmentally friendly materials, such as $LiNiO_2$, (Ni,Co,Mn)-oxides or high entropy disordered-rocksalt (HE-DRX) are investigated as alternatives to the toxic and expensive cobalt-based cathodes [67–70]. The main requirements for cathode materials are high free energy of reaction with lithium, incorporating large quantities of lithium and insoluble in electrolytes.

Lithium Cobalt Oxide (LCO). $LiCoO_2$ is one of the earliest and most commonly used cathode materials in commercial LIBs, particularly in portable electronics [30]. It operates at an average voltage of around 3.8 V and offers a specific capacity of approximately 140 mAh/g in practical applications. Theoretically, it can reach a capacity of 272 mAh/g, which makes it attractive as high-energy-density cathode. However, it shows some disadvantage in terms of high cost, environmental concerns, and thermal instability, especially at high states of charge [71]. This instability can lead to thermal runaway, a critical safety concern. Efforts to enhance the stability and reduce the cost of LCO involve doping with other elements like manganese or aluminum and applying surface coatings to improve the structural integrity during cycling.

Lithium Iron Phosphate (LFP). $LiFePO_4$ is favored for its excellent thermal stability, long cycle life, and safety profile, although it has a lower energy density than materials like NCM and LCO, with a specific capacity around 165 mAh/g and a typical voltage of 3.4 V. LFP's olivine structure is stable, preventing oxygen release during overcharging and making it a safe choice for stationary energy storage and lower-cost electric vehicles. The main drawback is its lower energy density due to the moderate operating voltage. Strategies like carbon coating and particle downsizing have been employed to enhance its conductivity and rate performance.

Lithium Manganese Oxide (LMO). $LiMn_2O_4$ has a spinel structure that provides three-dimensional pathways for lithium-ion diffusion, resulting in good rate capability. LMO has a moderate capacity of around 120 mAh/g and a higher operating voltage of approximately 4.1 V. This material is less costly and more environmentally friendly than LCO. This is mainly due to the high abundance of manganese. However, it suffers from capacity fading due to manganese dissolution into the electrolyte during cycling, especially at elevated temperatures. This issue has led to the development of strategies utilizing surface coating, doping, and nanostructuring to improve stability and reduce capacity loss.

Lithium Nickel Manganese Cobalt Oxide (NMC). NMC is a popular class of cathode materials in LIBs due to their tunable composition, allowing for a tailored balance between energy density, thermal stability, and cost. The general formula for these materials is $LiNi_xMn_yCo_zO_2$, where the ratios of Ni, Mn, and Co can be adjusted. By adjusting the ratios, manufacturers can tailor NMC to either increase energy density (higher Ni content) or improve safety and longevity (higher Mn content). One such tailored compositions is NMC 111 ($LiNi_{0.33}Co_{0.33}Mn_{0.33}O_2$). It offers a specific capacity of around 160–170 mAh/g with a moderate operating voltage of about 3.7 V. NMC 111 is known for its balanced metrics in energy density, thermal stability, and cost, making it widely used in early electric vehicle batteries and portable electronics. NMC 622 ($LiNi_{0.6}Co_{0.2}Mn_{0.2}O_2$ and NMC 811 ($LiNi_{0.8}Co_{0.1}Mn_{0.1}O_2$) increase the nickel content to boost energy density, achieving a specific capacity of 180-200 mAh/g and average operating voltages of about 3.7 V. The higher nickel ratio provides improved energy output, which is particularly beneficial for applications like electric vehicles requiring higher range. However, the high nickel content also presents challenges: it can reduce thermal stability and lead to increased reactivity with the electrolyte, risking capacity fade and thermal runaway at high states of charge.

Lithium Nickel Cobalt Aluminum Oxide (NCA). $LiNi_{0.8}Co_{0.15}Al_{0.05}O_2$ is known for its high capacity of around 200 mAh/g and an average voltage of approximately 3.7 V. NCA's high nickel content contributes to its high energy density, making it suitable for applications requiring large amounts of energy storage, such as electric vehicles. However, the low cobalt and aluminum content provides some stability, but this material still has thermal instability issues, particularly at high states of charge. NCA is widely used in high-performance applications, with ongoing research focusing on improving its thermal stability and reducing its tendency to form microcracks during cycling.

1.4.2 Anode materials

Graphite (C_6). Graphite is the most commonly used anode material in commercial LIBs, with a theoretical capacity of 372 mAh/g and an average working voltage of about 0.1-0.2 V relative to lithium. Its layered structure allows reversible lithium intercalation, providing good cycle stability. However, graphite anodes are limited by their moderate specific capacity and issues with lithium plating at high charging rates, which can lead to dendrite formation and safety risks [72]. Alternatives like silicon or tin are being researched to boost capacity, although they face challenges related to volume expansion during lithiation and delithiation.

Lithium Titanium Oxide (LTO). $Li_4Ti_5O_{12}$ is an anode material characterized by its zero-strain property during lithiation and delithiation, providing exceptional cycle life and safety [73, 74]. With a relatively low operating voltage of around 1.55 V, LTO prevents the formation of lithium dendrites, making it highly safe and stable. LTO is often used in applications that prioritize longevity and safety over energy density, such as in power tools and hybrid vehicles. Ongoing research focuses on improving LTO's conductivity and reducing its cost.

Silicon (Si). Silicon has attracted significant attention due to its exceptionally high theoretical capacity of approximately 3580 mAh/g, nearly ten times that of graphite. However, silicon anodes expand substantially during lithium intercalation, leading to particle fracture and poor cycle life. Researchers are exploring silicon-carbon composites and nanostructures to mitigate these effects and enhance stability [75].

1.4.3 Electrolyte materials

Electrolytes enable ion transport between the cathode and anode, and their ion transport properties determine LIB performance. The stability of an electrolyte affects directly battery safety and lifespan, especially in high-voltage batteries. There are three main types of electrolytes: liquid, solid and polymer electrolytes. Below we briefly discuss all three cases and more details can be found in [76].

Liquid electrolytes. The most widely used electrolyte in LIBs is a liquid solution of lithium salts (such as lithium hexafluorophosphate (LiPF6)) dissolved in organic solvents (e.g., ethylene carbonate and dimethyl carbonate). Liquid electrolytes offer high ionic conductivity, typically around 10^{-2} S/cm, but they have a limited electrochemical stability window of approximately 2.5-4.5 V. Beyond this voltage range, the electrolyte can degrade, forming by-products and leading to capacity fade. Research on additives and alternative solvents seeks to enhance electrolyte stability, prevent gas formation, and improve safety [77]. However, the flammability of organic electrolytes poses a significant safety risk, where battery failure can lead to fires [78].

Solid electrolytes. Solid electrolytes offer several advantages over traditional liquid electrolytes, including non-flammability, better thermal stability, and a wider electrochemical stability window. These features make them particularly promising for use in high-energy applications that prioritize safety, such as electric vehicles and grid storage. Additionally, solid electrolytes demonstrate increased durability under thermal and mechanical stress, which contributes to longer battery life and improved reliability [79]. One widely studied solid electrolyte is lithium garnet oxide (e.g., lithium lanthanum zirconium oxide (LLZO)), valued for its stability and compatibility with lithium metal anodes. However, LLZO exhibits relatively low ionic conductivity (typically lower than 10^{-3} S/cm) at room temperature compared to traditional liquid electrolytes, which is a limitation for high-power applications [80, 81]. This type of electrolyte is investigated in the scope of this dissertation (Chapter 5). Sulfide-based solid electrolytes, such as $Li_{10}GeP_2S_{12}$ (LGPS), have also drawn significant attention due to their high ionic conductivity (up to 10^{-2} S/cm), which is comparable to liquid electrolytes [82]. Sulfide electrolytes provide excellent interface compatibility with a range of electrode materials, improving overall battery performance and efficiency. Despite these benefits, sulfide-based electrolytes have stability issues, particularly at high voltages, and can be chemically reactive with moisture, releasing toxic hydrogen sulfide gas (H_2S).

Gel Polymer Electrolytes. Gel polymer electrolytes combine the high ionic conductivity of liquid electrolytes with improved safety features of solid-state systems, making them promising candidates for energy storage applications [83, 84]. Due to their flexibility and relatively high ionic conductivity (10^{-3} to 10^{-2} S/cm), they are particularly suitable for flexible and wearable devices. However, challenges related to their mechanical strength and long-term chemical stability, especially under high electrochemical stress, need to be addressed before their widespread commercialization.

Electrolytes in commercial LIBs typically consist of a liquid organic solvent. However, the flammability of organic electrolytes poses a significant safety risk, where battery failure can lead to fires. In recent years, solid-state batteries (SSBs) have gained considerable interest, primarily due to the safety concerns associated with conventional LIBs [31, 85]. Employing metallic lithium as an anode in SSBs offers enhanced energy density and capacity, which are critical attributes for application in electric vehicles (EVs) [33, 86]. Moreover, SSBs inherently enhance safety, as their solid electrolytes are not prone to the leakage and flammability issues associated with liquid electrolytes in conventional LIBs [87]. Additionally, SSBs demonstrate increased durability under thermal and mechanical stress, which contributes to longer battery life and improved reliability [79]. A key challenge in SSB development is finding suitable replacements for the liquid electrolytes used in conventional LIBs. Among the candidates, garnet-type solid electrolytes, such as $Li_7La_3Zr_2O_{12}$ (LLZO), have emerged as promising candidates owing to their thermodynamic stability against lithium metal and relatively high conductivity ($\sim 10^{-3}\mathrm{S/cm}$ at 25℃) compared to other solid electrolytes [88, 89]. LLZO is also stable over a wide voltage window, making it a strong contender for next-generation LIBs.

1.5 High-entropy materials for energy storage

In recent years, as the demand for efficient, long-lasting, and stable energy storage solutions has surged, there has been a tremendous effort to develop materials that can meet these requirements across a range of applications. Traditional materials used in LIBs have seen significant progress in terms of capacity, cycle life, and safety, yet they are still limited by issues such as capacity fade, thermal instability, and resource scarcity. HEMs present a promising approach to overcoming these challenges due to their unique structural and chemical properties.

The high-entropy (HE) concept was introduced theoretically in the 1980s and gained attention in the field of materials science in 2004 after Yeh and Cantor published their work [90, 91]. The "entropy" mentioned here is the configurational entropy, which is discussed in Section 1.5.2. A HE solid solution compound involves a combination of multiple different elements, typically five or more, in a specific lattice structure [36]. The high configurational entropy resulting from a large number of possible combinations of these elements has been speculated to play a crucial role in stabilizing the material's structure [92, 93]. The application of the HE concept to various ceramics shows promise for developing new materials in battery research. For example, high-entropy fluorides (HEFs) serve as high-capacity conversion cathodes for LIBs [94] (Section 6.1), while high-entropy Prussian White has been demonstrated to enhance structural stability upon electrochemical cycling when used as cathodes in sodium-ion batteries [95] (Section 6.2). Numerous theoretical and experimental analyses have shown the superior electrochemical properties of HEMs, including high capacity, cycle stability, and relatively high rate capability [35, 36, 70, 92, 96, 97]. A considerable compositional adaptability enables a wide exploration of element combinations to uncover optimized compositions with diverse elements decreasing the dependence on critical elements. Thus, HEMs can be potentially promising alternatives to traditional cathode materials.

In this section, we provide a brief introduction to HEMs, focusing on the key developments in their application to batteries, in particular their applicability as electrodes and solid electrolytes, as well as their performance and stability in energy storage devices.

1.5.1 History of HEMs

A HEM compound consists of a combination of typically five or more different elements in a single-phase [36]. The idea of mixing multiple elements in near equal-atomic ratio first became popular in alloying metals. In particular, due to the stabilization caused by high configurational entropy, high-entropy alloys (HEAs) show unique properties. Research on HEAs began in 1980s when researchers challenged traditional alloy design, which typically involves one or two main elements with smaller additions. In 2004, Yeh et al. [90] introduced HEAs, defining them as multi-element systems with five or more elements in nearly equal ratios, specifically designed to increase the mixing entropy. The high entropy is anticipated to help thermodynamically stabilize a single-phase solid solution, rather than forming a phase-separated material. Unlike conventional alloys, which often have complex, multi-phase structures, HEAs maintain a disordered single-phase structure. This structure generally results in enhanced strength, toughness, and stability at elevated temperatures. By leveraging the configurational entropy, HEAs can maintain stable single-phase structure and show advantageous structural effects compared with conventional materials.

After the initial success of HEAs, the high-entropy concept was extended to other systems, including oxides [34, 35, 37, 98–100], carbides [101], borides [102], nitrides [103, 104], fluorides [105], sulfides [106], and oxyfluorides [34]. This broadened the potential applications of HEMs, especially for environments requiring high-temperature stability, corrosion resistance, and special electrochemical properties. In 2015, Rost et al. [92] reported novel entropy-stabilized oxides (HEO), opening up new possibilities in areas such as energy storage and catalysis. These compounds demonstrate that high entropy can stabilize single-phase structures in nonmetallic and ionic compounds, leading to materials with unique structural and electrochemical properties.

As HEMs gained attention, researchers explored their use in energy storage systems, such as batteries, supercapacitors, and fuel cells. The high configurational entropy in HEMs enables these materials to maintain structural stability during repeated charge-discharge cycles, thereby offering superior cycling stability and capacity retention compared to conventional materials [34, 36, 97]. HEOs and carbides, for example, have shown promise as electrode materials in batteries because they can hold multiple oxidation states and resist capacity fading during repeated cycling [34, 101]. High-entropy electrolytes have also been studied to improve ionic conductivity and stability at high temperatures, which is essential for advanced battery technologies. Additionally, the compositionally complex structures of HEMs allow for tunable electrochemical properties, enhancing their adaptability for battery applications. Thus, the application of the high-entropy concept holds great promise in the ongoing development of materials that can withstand the rigorous demands of modern energy storage applications. By exploiting the synergies among constituent elements, HEMs pave a pathway toward achieving improved performance, adaptability, and reliability in LIB technology and beyond.

1.5.2 Concept of HEMs

The general concept of HEMs was introduced by Yeh et al. [90] and Cantor et al. [91]. Typically, HEMs consist of at least five elements in near-equal atomic ratio. Unlike conventional alloys that often form multiple phases, HEMs stabilize as a single disordered phase due to the high configurational entropy achieved during synthesis at elevated temperatures. Yeh et al. defined HEMs by considering the configurational entropy of mixing (S_{conf}), which depends on the composition of the elements. In an ideal solid solution, S_{conf} can be calculated as [107]:

$$S_{conf} = -R\sum_{i=1}^{N} x_i ln x_i, \tag{1.19}$$

where x_i is the concentration of element i, and R is the universal gas constant. This concept can be extended to more complex crystal structures with sublattices, such as oxides, where the entropy of mixing also accounts for the multiplicity of each sublattice:

$$S_{conf} = -R\sum_{s} m_s \sum_{i=1}^{N} x_{i,s} ln x_{i,s}. \tag{1.20}$$

In the above equation, m_s represents the multiplicity of sublattice s, and $x_{i,s}$ is the mole fraction of element i at sublattice s. S_{conf} increases with the number of components (N). Based on the value of the configurational entropy, materials are generally categorized into three groups: high entropy, where S_{conf} exceeds $1.5R$; medium entropy, when it ranges between 1 and $1.5R$; and low entropy, with values below $1R$ [107]. The term ‘high-entropy’ primarily reflects the elevated configurational entropy arising from the incorporation of different types of elements at specific site types.

Since HEMs were developed from early ideas of HEAs, several unique characteristics of HEAs may be relevant to our discussion [107]. These distinctive properties are often attributed to what is known as the "four core effects": high configurational entropy, sluggish diffusion, lattice distortion, and the "cocktail" effect. Each of these effects contributes to the performance, stability, and potential applications of HEMs as energy materials.

High-Entropic Effect. The high-entropic effect is primarily associated with configurational entropy (S_{conf}), which arises from the diverse elemental composition in HEMs and plays a crucial role in determining the phase stability of a material. In thermodynamic terms, the stability of a phase is governed by the Gibbs free energy, G:

$$G = H - TS_{tot}, \tag{1.21}$$

where the total entropy, S_{tot}, includes contributions from vibrational, magnetic, electronic, charge, and configurational entropies. When considering the entropy difference between two phases of the same elemental composition, it is the difference in configurational entropy that dominates, as the other entropy contributions, like vibrational entropy, are similar for both phases [108, 109]. Thus, in the following discussion, we will focus primarily on configurational entropy when addressing the mixing entropy.

The mixing free energy, enthalpy, and entropy are defined as the respective differences between the thermodynamic parameters of the mixed phase and the weighted sum of the parameters of the pure phases (end-members). For example, if H_A and H_B represent the enthalpies of compounds A and B, and H_{AB} is the enthalpy of the mixed phase for the case with equimolar composition, then the enthalpy of mixing is given by

$$H_{\text{mix}} = H_{AB} - 0.5H_A - 0.5H_B. \tag{1.22}$$

A negative H_{mix} indicates an exothermic mixing process, suggesting alternative interactions between components, whereas a positive H_{mix} corresponds to an endothermic process, implying that the mixture is less stable compared to its unmixed components.

In a system with at least five equimolar elements, the high mixing entropy (S_{mix}, equal 13 kJ/mol at 1000 K for 5 elements with equal mixing ration) often overcomes the enthalpy (H_{mix}) involved in forming intermetallic compounds, lowering the free energy (G_{mix}) and promoting the formation of a single solid-solution phase, especially at elevated temperatures. However, when the formation enthalpy of an intermetallic compound is sufficiently negative, the entropy effect may not be strong enough to prevent multi-phase formation or phase separation, and intermetallic compounds can still form at high temperatures [110]. Therefore, to predict whether a multi-element mixture will favor a single-phase solid solution or a multi-phase structure, it is essential to consider both the mixing enthalpy (H_{mix}) and mixing entropy (S_{mix}). Based on Equation 1.21, the absolute value of the entropy associated with Gibbs free energy ($-TS_{\text{tot}}$) increases with temperature. When H_{mix} is low, the entropy term can stabilize a disordered single-phase structure. As described by Equations 1.19 and 1.20, an increase in elemental diversity raises S_{mix}, potentially lowering the synthesis temperature required to achieve a disordered structure.

Nevertheless, it remains a subject of ongoing debate whether enthalpy or entropy is the dominant factor governing the structural stability of disordered compounds [111]. Additionally, questions persist as to whether ideal, fully disordered atomic arrangements are achievable in real HEMs, as structural ordering tendencies may still occur under certain conditions [112–114]. Many researches have shown the importance of interplay between disordering entropy and enthalpy as well as partial ordering in real, disordered compounds for stabilization of various materials (e.g., [114, 115]).

Diffusion Effect. The sluggish diffusion effect is a unique feature observed in HEAs. Studies have shown that atomic diffusion in HEAs is slower than in pure metals and conventional alloys [107, 116]. Unlike conventional alloys, where atomic sites are usually similar, HEAs may exhibit varying local energy at each site due to the mixture of multiple elements. During atomic diffusion, when an atom moves from a higher-energy site to a lower-energy site, it can become "trapped." Conversely, when an atom moves from a lower-energy site to a higher-energy site, it is likely to return to its original position. This leads to slower atomic diffusion because complex energy landscapes create barriers to atomic mobility. Nevertheless, the sluggish diffusion effect can be advantageous for maintaining structural stability at high temperature.

On the other hand, the sluggish diffusion effect as described above may not fully apply to HEMs used as electrodes in batteries. Ouyang and Zeng suggest that the large tolerance for lattice distortion in HEMs can affect the energy landscape for ion diffusion, creating interconnected diffusion pathways that enhance ionic conductivity [117]. This phenomenon has been demonstrated in HEOs and sulfide-based argyrodites solid electrolytes [118, 119].

Lattice Distortion Effect. Because HEMs consist of multiple elements randomly distributed within a specific lattice structure, the variation in atomic radii among these elements can lead to significant lattice distortion. This distortion is evident in both crystalline and non-crystalline forms, and can influence the material's mechanical, thermal, electrical, optical, and chemical properties [107].

Cocktail effect. The cocktail effect refers to the synergistic interactions between different elements in an HEM, resulting in enhanced or entirely new properties that individual elements alone would not exhibit. This effect can be manifested in various forms, such as improved electrochemical performance or increased corrosion resistance. In energy storage applications, the cocktail effect can enhance capacity, rate capability, and overall stability, providing performance benefits that a single TM could not achieve independently [107].

1.5.3 HEMs as electrodes

HEMs exhibit several characteristics that make them promising candidates for next-generation battery electrodes, particularly in LIBs. Their highly disordered phases can influence electrochemical behavior positively. For instance, Ouyang and Zeng proposed that the significant tolerance of lattice distortion introduced by disorder in HEMs perturbs the energy landscape for ion diffusion [117]. This results in the creation of percolating pathways, facilitating higher ionic conductivity. Additionally, the highly disordered nature of HEMs can mitigate the volume change during charge and discharge. It also suppresses the short-range ordering that can decrease electrochemical performance, therefore allow HEMs to have increased capacity and rate capability. HEMs also allow for tunable elemental composition, enabling the optimization of electrochemical properties. This flexibility makes them ideal for applications demanding materials with high specific capacity and durability [35, 36].

Numerous studies have demonstrated the potential of HEMs as electrodes. HEM electrodes exhibit different structures, including rock-salt, spinel, and perovskite. Sarkar et al. [97] investigated a rock-salt structured HEM, (CoCuMgNiZn)O, as an anode material. This material achieved a capacity of approximately 650 mAh/g after 900 cycles at a current density of 200 mA/g, showcasing excellent capacity retention. As demonstrated by experiments, such high capacity originates from the conversion mechanism. Additionally, it maintained a Coulombic efficiency of over 99.5%, demonstrating minimal capacity fading and high reversibility over extended cycles. Moreover, by testing each 4-cation oxide (medium-entropy oxide) in the same system Sarkar et al. [97] showed the importance of entropy-stabilization concept in the material performance and cell cycling. The rapid capacity degradation of cells with medium entropy oxides indicates that the high configurational entropy of the five-cation system is the main factor for the stable structure of the electrode material and its cycling stability.

Chen et al. [120] introduced a spinel-structured HEM, $(Mg_{0.2}Ti_{0.2}Zn_{0.2}Cu_{0.2}Fe_{0.2})_3O_4$, for LIBs. This material demonstrated a capacity of 504 mAh/g at a current density of 100 mA/g and retained 96.2% capacity after 800 cycles at a high current density of 2000 mA/g, highlighting its stability and rate performance. The spinel structure provided three-dimensional pathways for lithium-ion diffusion, enabling enhanced rate capabilities and superior long-term cycling stability.

Yan et al. [121] studied high-entropy perovskite oxides, such as $La_{0.2}Nd_{0.2}Sm_{0.2}Ca_{0.2}Sr_{0.2}MnO_3$, which exhibited a reversible capacity of 120 mAh/g at 1000 mA/g with remarkable cycling stability over 300 cycles. The perovskite structure, stabilized by high configurational entropy, allowed for uniform lithium-ion diffusion and reduced capacity degradation. Due to their excellent cycle stability and high rate performance, these materials demonstrated potential as anodes.

Wang et al. [34] developed a high-entropy, multi-anionic, and multi-cationic oxyfluoride system, Li(HEO)F, designed for LIB applications. This material features a rock-salt structure formed by incorporating fluorine and lithium into a high-entropy oxide (HEO) matrix. The configurational entropy generated by the multi-anionic and multi-cationic composition enhances structural stability and electrochemical performance. Li(HEO)F operates at an average potential of 3.4 V versus Li^+/Li and delivers a specific capacity of approximately 168 mAh/g at C/20 and 161 mAh/g at C/10, retaining a reversible capacity of around 120 mAh/g. It demonstrates stable Coulombic efficiency over multiple cycles and exhibits improved resistance to capacity degradation compared to conventional materials like LiNiOF. The multi-anionic approach not only stabilizes the structure during cycling but also opens pathways for next-generation energy storage systems with enhanced safety and performance.

1.5.4 HEMs as solid electrolytes

The enhancement of cubic-phase stability and ionic conductivity at lower temperatures remains a priority for advancing the performance of solid-state lithium batteries. One innovative approach involves the "high-entropy" concept, where introducing multiple elements into a material can increase configurational entropy, leading to a single disorder phase which, due to the frustrated energy landscape, could potentially boost the ionic conductivity. Thus, HEMs have been explored as Li-ion solid electrolytes, showing comparable ionic conductivities to the best-performing solid-state ion conductors while providing additional benefits in many cases [118, 119, 122, 123]. In the context of lithium garnet systems like LLZO, the high-entropy approach has yielded enhanced room temperature conductivity and ease of synthesis, both effects attributable to the induced disorder [124]. Some high-entropy garnets (HEGs) have been developed, demonstrating the flexibility of lithium garnet materials to multiple doping.

Stockham et al. [124] reported first HEGs with 9-elements $Li_{5.75}Ga_{0.2}La_{2.5}Nd_{0.5}Nb_{0.65}Ce_{0.1}Zr Ti_{0.25}O_{12}$) and 11-elements ($Li_{5.75}Ga_{0.2}La_{2.5}Nd_{0.5}Zr_{0.75}Ta_{0.3}Nb_{0.35}Ce_{0.1}Hf_{0.25}Ti_{0.25}O_{12}$). Despite the low lithium content of 5.75 per formula unit, these HEGs exhibit room-temperature ionic conductivities of 0.1 and 0.2 mS cm^{-1} for the 9- and 11-element systems, respectively. Subsequently, Stockham et al. [124] developed a HEG with dopants localized on the Zr site: $Li_{6.5}La_3ZrNb_{0.5}Ce_{0.25}Ti_{0.25}O_{12}$, which demonstrated an improved ionic conductivity of 0.5 mS cm^{-1} at 25℃ [125]. Fu and Ferguson [126] synthesized $Li_6La_3Zr_{0.5}Nb_{0.5}Ta_{0.5}Hf_{0.5}O_{12}$, where Zr, Nb, Ta, and Hf were equimolarly distributed on the Zr site in the garnet structure. This cubic HEG exhibits an ionic conductivity of 4.67×10^{-4} S cm^{-1} with an activation energy of 0.25 eV and a low electronic conductivity in the order of 10^{-8} S cm^{-1}. They also observed that the HEG had a finer grain size ($\sim$10 µm) compared to its low-entropy counterpart $Li_{6.75}La_3Zr_{1.75}Ta_{0.25}O_{12}$ (>100 µm), resulting in higher flexural strength and hardness. Chen et al. [127] elucidated the influence of multiple cations on the short-range structure of $Li_6La_3Zr_{0.5}Nb_{0.5}Ta_{0.5}Hf_{0.5}O_{12}$, resulting in extended bottleneck size, elongated Li-O bond length, and local clustering of 16a sites.

Other HEGs with equimolar distributions of dopants on the Zr site, such as $Li_7La_3Zr_{0.5}Hf_{0.5}Sc_{0.5}Nb_{0.5}O_{12}$, $Li_7La_3Zr_{0.4}Hf_{0.4}Sn_{0.4}Sc_{0.5}Ta_{0.5}O_{12}$, and $Li_{6.6}La_3Zr_{0.4}Hf_{0.4}Sn_{0.4}Sc_{0.2}Ta_{0.6}O_{12}$, were investigated by Jung et al. [122]. They showed that the cubic phase is stabilized by increasing entropy and the introduction of aliovalent elements into the garnet structure. While the $Li_{6.6}$ HEG exhibits higher ionic conductivity (0.32 mS cm^{-1} at 25℃) than the Li_7 HEG (0.17 mS cm^{-1} at 25℃), the latter demonstrates better reduction stability against lithium metal. Similarly, Feng et al. [128] synthesized $Li_{6.6}La_3Zr_{0.4}Sn_{0.4}Sc_{0.4}Ta_{0.4}Nb_{0.4}O_{12}$, which achieved a high ionic conductivity of 0.357 mS cm^{-1}. Interestingly, when the number of elements on the Zr site was increased to 8 or 10 (increasing configurational entropy), the ionic conductivity decreased. This suggests that a particular combination of cations may play more important role in ionic conduction than configurational entropy.

1.6 Atomistic simulations of HEMs

With the rapidly increasing computational power of supercomputing resources, first principles-based atomistic simulation methods can be successfully applied to facilitate the investigation of novel materials by aiding in the pre-selection of target materials with desired electronic structures, redox capabilities, and phase stability, as well as assisting in the interpretation of experimental data [129, 130]. For more than two decades, DFT has been a workhorse of the quantum-chemistry-based atomistic modeling of materials [131–133]. Although molecular-level simulations are very powerful and popular research tools, the computation of complex disordered HEMs poses a significant challenge. Capturing the details of their ionic and electronic structures requires advanced, beyond standard, modeling techniques and approaches. In this section, we will discuss specific challenges associated with simulating the ionic and electronic structures of HEMs and provide an overview of the current techniques used to tackle these difficulties.

1.6.1 Simulation methods for ionic structures

Atomistic modeling is a useful tool to decipher the role of enthalpy and entropy in disordered multi-compound materials [113, 114, 134]. In these calculations, correct input model structures are essential to correctly calculate the thermodynamic properties of investigated materials [113]. HEMs often have multiple principal elements randomly distributed across crystallographic sites. Modeling random atomic distributions with DFT is challenging because of the inherent ionic structural complexity of these materials. In particular, correct modeling of ionic interactions in local atomic environments is a challenge. Unlike traditional materials, which often contain only one or two principal elements, allowing for relatively straightforward prediction of their atomic arrangements and bonding characteristics, HEMs contain five or more principal elements in near-equiatomic ratios, leading to a highly complex system with multiple possible configurations. This level of configurational disorder requires extensive computational resources, as it is necessary to simulate sufficiently large supercells to model a random distribution of different atomic species. Moreover, to capture the true behavior of HEMs, atomic configurations must be sufficiently sampled, and local ordering must be accounted for, both of which increase the overall computational cost. The resulting ionic structure can have a profound impact on the overall stability and behavior of the material, influencing everything from phase stability to transport properties. For instance, variations in the local ionic environment can affect the material's defect chemistry, diffusion rates, and, ultimately, its functional performance, particularly in energy storage applications like cathode materials [115, 130]. Hence, accurate modeling of the ionic structure is vital for molecular simulation aiming to predict the material's real-world performance. Below we briefly discuss the common simulation approaches.

Molecular dynamics simulations. Molecular dynamics (MD) simulations provide a potential way to model dynamics of the ionic structure of HEMs over time and at finite temperatures. In particular, MD can capture the dynamic behavior of ions, including diffusion and local lattice distortions [133, 135]. Classical MD simulations [136], which rely on either analytical interaction potentials or machine learning-based force fields [137, 138], are often applied. However, the typically accessible nanosecond time scales are not always sufficient to explore the complex energy landscape in HEMs. In addition, *ab initio* (first-principles) methods are often required to increase accuracy, particularly for systems with complex bonding environments involving TM elements. However, the use of *ab initio* MD for HEMs is computationally expensive due to the large number of atoms in a sufficiently large supercell and the limitation to short timescales, usually not sufficient to capture ionic movements in the investigated materials.

Coulomb energy based models. When mixed cations have different charges, the ionic distribution may be primarily driven by Coulomb interaction. Finding an optimal ionic distribution by minimizing Coulomb energy is a challenge by itself. Monte Carlo (MC) algorithms are often applied and are also utilized in Chapter 7. In the scope of this dissertation, we harnessed emerging quantum annealing resources for finding optimum ionic configuration in some common cathode materials, which is broadly discussed in Chapter 7.

Special quasirandom structures. One widely used approach to effectively simulate ionic distributions in multicomponent materials is the special quasirandom structures (SQS) method [139]. SQS is a representative ionic arrangement model that describes a fully disordered ionic configuration, corresponding to maximal configurational entropy. It is typically constructed so that the statistical pair distribution of cations matches the fully disordered system. The SQS model enables more manageable DFT calculations by using a single representative structure instead of performing statistical sampling or computations on multiple structures, while still retaining the essential features of chemical disorder. This method is particularly suited for high-entropy systems, where computational sampling of several configurations is impractical.

The SQS models of ionic arrangements have been used to quantify the phase stability, electronic structure, and voltage curves in other studies [70, 134, 140, 141]. However, while SQS approach can effectively represent the full randomness in high-entropy systems, it does not always capture the true ionic configuration, in particular short-range order (SRO) that may occur in real materials (see e.g., [113]). As a result, further improvements (as investigated in Chapter 7) or other modeling approaches are needed to derive more realistic ionic arrangements and representative SQS-based models.

Cluster expansion. The cluster expansion (CE) method is another common approach used to model disorder in HEMs [70, 142]. In this approach, the energy of the system is represented by a sum of interactions among clusters of atoms. The resulting expression for the energy of the system allows for a fast and efficient sampling of different ionic configurations and the exploration of phase stability across a wide compositional range. The CE method is usually coupled with an MC sampling method. This type of hybrid approach can be effectively applied for the statistical sampling of ionic configurations at given temperatures. However, the construction of CE requires an extensive set of DFT calculations as references, and its accuracy depends on the computational setup. For instance, including the magnetic properties of TM elements in the calculation can significantly influence the energy calculated by DFT, and thus a different fitting of CE. That is why correct computation of electronic structure of HEMs is essential not only for CE method, but all the simulation approaches to ionic structures o HEMs.

In summary, modeling the ionic structure of HEMs is a significant challenge due to the inherent complexity and chemical disorder of these systems. The thermodynamically driven distribution of multiple elements in HEMs can lead to a highly varied local ionic environment that is difficult to model with conventional computational methods. While techniques like MD, SQS, and CE offer promising approaches to this problem, they are limited in applicability, particularly in terms of computational cost and the ability to capture local atomic arrangements. The exploration and development of more efficient and accurate methods for modeling ionic structures of HEMs is crucial for advancing the understanding and design of these novel materials, and represent one of the goals of this dissertation (see Chapter 7).

1.6.2 Simulation methods for electronic structures

Computation of the electronic structure of HEMs is particularly challenging due to the complex interactions between different elements, often involving TMs that have strongly correlated electrons. In general, DFT has serious limitations that affect the quality of the computed electrochemical parameters. One of the well-known shortcomings of DFT is the underestimation of band gaps and the tendency to over-delocalize the *d*-electrons [133, 143–145]. Materials with a wide band gap that are considered as electrodes for energy storage applications are often predicted by DFT to be metals [130]. An incorrect electronic structure can also result in an in-accurate prediction of the redox mechanisms. Certain techniques help improve the description of strongly correlated electrons. In this subsection, we focus on key aspects of simulating the electronic structure of HEMs, focusing on computation of strongly correlated $3d$ electrons.

DFT+*U* method. TMs, which are often integral to HEMs, have d electrons that exhibit strong electron-electron correlations. Standard DFT methods, particularly those using local density approximation (LDA) or generalized gradient approximation (GGA), are not capable of accurately capturing the behavior of strongly correlated electrons [146]. For this reason, a majority of studies use advanced DFT-based approaches such as hybrid functionals [147], other advanced exchange-correlation functionals such as SCAN [148] or Hubbard model-based DFT+U approach [130, 141, 149]. The latter method is especially popular due to its low computational cost. In this method, a term with Hubbard U parameter is introduced to the Hamiltonian to correct for electronic correlations in d- or f- orbitals. The application of such computational approaches to battery cathode materials is the topic of this dissertation and is widely discussed in Chapter 3.

Hubbard *U* Parameter. One of the primary challenges in using the DFT+U method for HEMs is the appropriate selection of the Hubbard U parameter. The U value determines the strength of the correction applied to d and f electrons and it can significantly influence the accuracy of the predicted electronic structure (e.g., [149, 150]). Finding the optimal U value is non-trivial, as it is usually compound-dependent and varies for different TM elements [151]. In practice, the U parameter is often adopted from prior studies or adjusted empirically to reproduce experimental results, such as band gaps, formation enthalpies, or lattice parameters [70, 150, 152–157]. While this approach can yield reasonable results, it introduces a degree of arbitrariness and limits the predictive power of the method for novel compounds, especially when redox reactions are considered [130, 158]. Materials-specific impacts further complicate the selection process, requiring careful consideration of the computational setup to ensure consistency and accuracy. To overcome these limitations and provide a more systematic and consistent way of determining U, theoretical approaches like the linear response method proposed by Cococcioni and de Gironcoli have been developed [145, 159] (see Section 2.1.4). These have been successfully applied to describe electronic structures and redox chemical reactions in different molecular and solid compounds (e.g., [130, 151]).

Projectors for the DFT+*U* method. Several studies indicate that besides computing the Hubbard U parameter, the selection of the projector functions to account correctly for the occupancy of d or f states is crucial to improve the accuracy of computational investigation of energy materials. These involve predictions of reaction enthalpies [160], phase stability [161], or spectroscopic responses [158, 162]. The widely used atomic orbitals (AOs) lead on many occasions to overestimation of orbital occupancies, due to a spurious assignment of non-negligible, fractional occupations to empty orbitals [160, 163]. Since HEMs involve multiple TM atoms, each capable of exhibiting different oxidation states and local environments, using improper projection of *d* orbitals can lead to inaccuracies in the computed electronic structure. This aspect is especially important for distinguishing between various oxidation states of the same element, which is common in cathode materials where changes in lithium concentration during charging and discharging alter the oxidation states of TM elements. For example, in HEMs, cobalt can exist as both Co^{2+} and Co^{3+}, and distinguishing between these oxidation states is critical for predicting the material's electronic properties. Advanced projection schemes, such as those based on maximally localized Wannier functions (MLWF) [164], have been successfully employed by Kowalski's group to improve the accuracy of the DFT+*U* method for different materials properties, as listed above. These studies show that the application of Wannier functions (WF)-based projectors conjunction with the DFT$+U$ method improves predictive capabilities [158, 161]. It also leads to the correct assignment of the oxidation states [158, 160]. These methods are benchmarked and used in this dissertation to compute electronic structures of some common electrode materials (see Chapter 3).

In summary, computing the electronic structures of HEMs requires careful consideration of several factors, particularly the accurate treatment of strongly correlated 3*d* electrons and the proper selection or computation of the Hubbard *U* parameter and projectors for *d* states in DFT+*U* schemes. Accurate simulation of electronic structures of HEMs is a challenging task, requiring further development and adaptation of computational techniques.

1.7 Aims of this thesis

This dissertation focuses on the benchmarking, development, and application of novel computational methodologies to investigate different classes of HEMs for energy storage technologies, particularly exploring application in lithium-ion and all-solid-state batteries. By integrating computational approaches with experimental insights provided by collaborators (such as Breitung's group), this work explores the thermodynamic, structural, electronic, and electrochemical properties of various HEMs, including oxides, garnets, fluorides, Prussian whites, and Prussian blues. The primary objective has been to leverage advanced computational techniques alongside experimental data to comprehensively understand the effects of configurational entropy, local atomic environments, and multi-element of materials with enhanced capacity, stability, and efficiency in energy storage applications. Below, we outline specific research objectives and scientific questions that will be addressed in each chapter.

Chapter 3 presents results obtained with the advanced DFT+*U*+Wannier projector methodology that has been applied to compute the electronic structure of conventional electrode materials, such as $LiCoO_2$ and $LiNiO_2$, as well as HEMs. Research discussed in this chapter has aimed to address the following scientific questions:

- Does the advanced DFT+U scheme improve the predictive power of the computational approach?
- How does its performance compare with that of the SCAN exchange-correlation functional?
- Can Wannier projectors be used as a reliable tool to estimate oxidation states of TMs in HEMs?

The study demonstrates that the parameter-free DFT+U+Wannier method enhances the accuracy of electronic structure predictions, outperforming the conventional DFT+U, which has often failed for the considered systems, in capturing structural and electronic properties of electrode materials. We emphasize that the U parameters should not be used blindly. It is evident that results obtained with U values that have been derived from first-principles improve the agreement with experimental data. The employed methodology has also provided reliable estimates of oxidation states, showcasing its applicability in analyzing electrochemically active cations in electrode materials.

Chapter 4 focuses on computational studies of two Li-rich layered oxide cathode materials, categorized as medium or high entropy. The aim of this work was to understand the structural and electrochemical degradation mechanisms during cycling. Specifically the following questions has been explored:

- What are the structural and electronic changes that lead to capacity fading in Li-rich HEMs?
- How do local atomic environments, such as Li/Ni interchange and TM migration, influence degradation?
- Does configurational entropy contribute to stabilizing these materials or increase disorder-induced instabilities?

DFT calculations have revealed critical degradation pathways, including oxygen dimer formation, TM migration, and secondary phase formation, such as spinel $LiTiO_2$. The study has helped unreveal the role of configurational entropy and the potential instability of disordered phases. These findings provide essential insights into the limitations of the high-entropy approach and the element selections in HEMs. They address the question of how the local environment affects the electrochemical performance of cathodes.

Chapter 5 focuses on designing and analyzing HEG-based solid electrolytes for all-solid-state lithium batteries. The reported research has addressed the following questions:

- How does increasing configurational entropy through multi-doping affect the structural stability and ionic conductivity of garnets?
- What role do atomic distributions (e.g., SQS vs. minimized Coulomb energy configurations) play in determining stability?

DFT studies and experimental validation demonstrate that high configurational entropy stabilizes cubic garnet phases, enabling reduced synthesis temperatures. However, ionic conductivity improvements with increased doping have been found to be less significant than expected, revealing the complex interplay between configurational entropy and ionic transport mechanisms.

Chapter 6 explores diverse energy storage systems, extending the application of HEMs to sodium-ion batteries (SIBs) and memristive devices. The following scientific questions has been investigated:

- How do HEFs perform as conversion-type cathodes for LIBs?
- Can entropy effects enhance structural stability and cycling performance in high-entropy Prussian White (HE-PW) for SIBs?
- What mechanisms underlie resistive switching in high-entropy Prussian Blue Analog (HE-PBA) memristors?

The reported findings reveal that HEFs with TMs such as Cu and Mn facilitate redox processes, while electrochemically inactive elements like Mg serve as stabilizing components for disordered phases. In HE-PW, the entropy-driven stabilization suppresses phase transitions, improving cycling stability. In HE-PBA memristors, DFT calculations uncovered ion-driven resistive switching mechanisms, providing energy-efficient solutions for memory applications. These studies underscore the potential applications of HEMs across various fields.

Chapter 7 is devoted to advanced thermodynamics-driven methodologies and emerging quantum computing techniques to address challenges in modeling and optimizing ionic configurations in battery materials. The chapter focuses on two main areas: the application of quantum annealing (QA) for Coulombic energy minimization and the investigation of SRO in disordered systems by the cluster expansion method. This chapter has been aiming to answer the following questions:

- Can QA be effectively applied to optimize ionic configurations in disordered materials?
- What is the extend of SRO in systems assumed to exhibit ideal mixing?

The study has demonstrated the successful application of QA for Coulomb energy minimization in a disordered material. By reformulating the energy model into a QUBO problem and incorporating constraints, QA has achieved results comparable to classical methods like MC sampling. Additionally, the investigation into SRO in a monazite system ($(\mathrm{La, Ce, Pr, Nd})\mathrm{PO}_4$) has revealed the presence of local atomic ordering even at elevated synthesis temperatures. These results emphasize the importance of considering SRO in computational models of ionic structures. We have proposed a method for integrating SRO into SQS to generate more realistic input structures for electronic calculations. These advancements represent a step forward in the computational modeling of disordered materials.

Chapter 8 summarizes the contributions made and insights gained with this dissertation. It provides a comprehensive conclusion of the work, reflecting on key achievements as well as challenges encountered during the research. Furthermore, I propose directions for future work to address the limitations of the current modeling approaches and methodologies, particularly in improving the accuracy and realism of modeling HEMs using DFT.

2 Computational methods

In this chapter, I discuss the main computational methodologies that have been utilized in this thesis. The computational work is mainly based on the electronic structure calculation performed with DFT methods. DFT is therefore briefly introduced in the next section. Comprehensive descriptions of different aspects of DFT can be found in various textbooks and review papers, e.g. [133, 165, 166]. Subsequent sections describe other methodologies used to construct models of ionic configurations of HEMs, which have been subsequently applied as input model structures for DFT calculations.

2.1 Computing electronic structures of HEMs

2.1.1 Density Functional Theory

Historically, describing electronic structure of materials begins with the introduction of the many-body Schrödinger equation, which governs the quantum-mechanical behavior of nuclei and electrons in a material [167]. The time-independent Schrödinger equation is written as

$$\hat{H}\,\psi = E\,\psi, \tag{2.1}$$

where $\hat{H}$ is the Hamiltonian operator, ψ the wave function describing the quantum state of the system, and E the total energy of the system. The Hamiltonian for an ensemble of nuclei and electrons includes contributions from the kinetic energy of nuclei (T_N) and electrons (T_e), the potential energy from nuclei-nuclei (V_{NN}), nuclei-electron (V_{Ne}), and electron-electron (V_{ee}) interactions

$$\hat{H} = \hat{T}_N + \hat{T}_e + \hat{V}_{NN} + \hat{V}_{Ne} + \hat{V}_{ee}, \tag{2.2}$$

where

$$
\begin{aligned}
&\hat{T}_N = -\sum_I \frac{\hbar^2}{2M_I}\nabla_I^2, \quad \hat{T}_e = -\sum_i \frac{\hbar^2}{2m_e}\nabla_i^2, \\
&\hat{V}_{NN} = \sum_{I<J} \frac{Z_I Z_J e^2}{|R_I - R_J|}, \quad \hat{V}_{Ne} = -\sum_{i,I} \frac{Z_I e^2}{|r_i - R_I|}, \\
&\hat{V}_{ee} = \sum_{i<j} \frac{e^2}{|r_i - r_j|}.
\end{aligned}
\tag{2.3}
$$

Here, M_I and Z_I are the mass and charge of the nucleus I, m_e is the electron mass, R_I and r_i are the positions of nuclei and electrons, respectively, e is the elementary charge, and $\hbar$ is the reduced Planck constant.

Directly solving the Schrödinger equation for many-body systems is computationally impossible due to the coupling between nuclei and electrons. The Born-Oppenheimer approximation decouples their motions by treating nuclei as fixed, given their much larger mass compared to electrons [168]. Under this approximation, the nuclear kinetic energy ($\hat{T}_N$) is neglected, and the nuclei-nuclei interaction (V_{NN}) becomes a constant. The resulting electronic Hamiltonian is

$$
\hat{H}_{\text{el}} = \hat{T}_e + \hat{V}_{Ne} + \hat{V}_{ee}, \tag{2.4}
$$

or equivalently

$$
\hat{H}_{\text{el}} = \hat{T}_e + \hat{V}_{\text{ext}} + \hat{V}_{\text{int}}, \tag{2.5}
$$

where $\hat{V}_{\text{ext}}$ represents the external potential acting on electrons resulting from fixed nuclei, and $\hat{V}_{\text{int}}$ accounts for the electron-electron interactions. The use of pseudopotentials simplifies the treatment of electron-core interactions [169, 170]. Pseudopotentials replace the complex, rapidly varying all-electron potential near the nuclei with a smoother potential that acts only on the valence electrons. This approach eliminates the need to explicitly describe core electrons, significantly reducing the computational effort.

Still, this equation is practically unsolvable due to the complex electron-electron interactions (except a few trivial cases, e.g., hydrogen atom). One of the early approximations used to address this issue is the Hartree-Fock (HF) approximation [171]. The HF approximation assumes that the total electronic wave function can be approximated by a single Slater determinant as a product of N one-electron wave functions. This approach applies the concept of mean-field, where each electron is treated as moving independently in an averaged field produced by all other electrons. While the HF method is computationally more efficient than solving the many-body Schrödinger equation and results in the exact computation of the electronic exchange effects, it neglects electron correlation due to a mean-field approach, which usually results in low accuracy and disagreement of the computed values with the experimental results.

An alternative to many-body wavefunction methods is DFT, which takes both exchange and correlation electronic effects into account. DFT reformulates the many-body Schrödinger equation in terms of the electron density, $n(\mathbf{r})$. The electron density is defined as

$$n(\mathbf{r}) = N \int d^3\mathbf{r}_2 \cdots \int d^3\mathbf{r}_N \Psi^*(\mathbf{r}, \mathbf{r}_2, \ldots, \mathbf{r}_N)\Psi(\mathbf{r}, \mathbf{r}_2, \ldots, \mathbf{r}_N), \tag{2.6}$$

where $\Psi(\mathbf{r}, \mathbf{r}_2, \ldots, \mathbf{r}_N)$ is the many-body wavefunction of the system. This expression is general and holds for any system, including interacting electrons, providing the foundation of DFT. By using the electron density as the basic variable, the computational cost of the quantum mechanical calculations is substantially reduced, as the complicated wavefunction with $3N$ of N e^- spatial variables is replaced by a three-dimensional charge density, reducing configurational space of the problem. The foundation of DFT lies in the two Hohenberg-Kohn theorems [172]:

1. *First Theorem*: For a given external potential $V_{\text{ext}}(\mathbf{r})$, the ground-state electron density $n_0(\mathbf{r})$ is uniquely determined. This relationship can be inverted: the electron density $n_0(\mathbf{r})$ uniquely determines $V_{\text{ext}}(\mathbf{r})$, and thus the Hamiltonian and all properties of the system. This theorem establishes that the electron density is a sufficient variable to describe the ground-state properties of quantum mechanical system.

2. *Second Theorem*: The ground-state energy of a system is a functional of the electron density $E[n]$, and the density $n(\mathbf{r})$ that minimizes this functional corresponds to the exact ground-state density $n_0(\mathbf{r})$ for a given external potential

$$E[n] = F[n] + \int n(\mathbf{r})V_{\text{ext}}(\mathbf{r})\, d\mathbf{r}, \tag{2.7}$$

where $F[n]$ is a universal functional comprising the internal kinetic energy ($T[n]$) and electron-electron interaction energy ($E_{int}[n]$). The ground-state energy is obtained by minimizing $E[n]$ with respect to $n(\mathbf{r})$

$$E[n_0] = \min_n \left\{ F[n] + \int n(\mathbf{r})V_{\text{ext}}(\mathbf{r})\, d\mathbf{r} \right\}. \tag{2.8}$$

This variational principle implies that any trial electron density $n(\mathbf{r})$ provides an energy equal to or higher than the ground-state energy

$$E[n_0] \leq E[n]. \tag{2.9}$$

The Hohenberg-Kohn theorems lay the foundation for DFT by proving that the ground-state properties of a many-electron system can be described uniquely by the electron density. However, the theorems do not provide a mathematical form of a practical way to calculate the unknown universal functional $F[n]$. To address this limitation, Kohn and Sham proposed an *ansatz* to replace the interacting many-body system with an auxiliary system of non-interacting electrons - a concept similar to the HF approach - that reproduces the same electron density [173]. This approach introduces single-electron Kohn-Sham orbitals $\psi_i(\mathbf{r})$, from which the electron density is reconstructed as:

$$n(\mathbf{r}) = \sum_{i=1}^{N} |\psi_i(\mathbf{r})|^2. \tag{2.10}$$

This *ansatz* allows the total energy functional to be split into independent-electron equations for the noninteracting system, shifting all the many-body effects to a so-called exchange-correlation functional of the electron density. The accuracy of this method is thus limited only by the approximations in the exchange-correlation functional. The resulting Kohn-Sham total energy functional is

$$E_{KS}[n] = T_s[n] + \int n(\mathbf{r}) V_{\text{ext}}(\mathbf{r})\, d\mathbf{r} + E_{\text{H}}[n] + E_{\text{xc}}[n], \tag{2.11}$$

where $T_s[n]$ is the kinetic energy of the non-interacting electrons, $E_{\text{xc}}[n]$ is the exchange-correlation energy functional that accounts for quantum mechanical many-body effects, and $E_{\text{H}}[n]$ is the Hartree energy, which accounts for the classical electrostatic interaction between electron densities. The Hartree energy is expressed as

$$E_{\text{H}}[n] = \frac{1}{2} \int \int \frac{n(\mathbf{r}) n(\mathbf{r}')}{|\mathbf{r} - \mathbf{r}'|}\, d\mathbf{r}\, d\mathbf{r}'. \tag{2.12}$$

The Kohn-Sham equation, derived by minimizing the energy functional with respect to the electron density, is

$$\left[-\frac{\hbar^2}{2m_e} \nabla^2 + V_{\text{eff}}(\mathbf{r}) \right] \psi_i(\mathbf{r}) = \epsilon_i \psi_i(\mathbf{r}), \tag{2.13}$$

where $\psi_i(\mathbf{r})$ are the single-electron wavefunctions (or orbitals), ϵ_i are the corresponding orbital energies, and $V_{\text{eff}}(\mathbf{r})$ is the effective potential defined as

$$V_{\text{eff}}(\mathbf{r}) = V_{\text{ext}}(\mathbf{r}) + V_H(\mathbf{r}) + V_{\text{xc}}(\mathbf{r}). \tag{2.14}$$

Here, $V_{\text{ext}}(\mathbf{r})$ is the external potential due to the nuclei, $V_H(\mathbf{r}) = \int \frac{n(\mathbf{r}')}{|\mathbf{r}-\mathbf{r}'|}\, d\mathbf{r}'$ is the Hartree potential describing the classical Coulomb interaction, and $V_{\text{xc}}(\mathbf{r})$ is the exchange-correlation potential, which is obtained as:

$$V_{\text{xc}}(\mathbf{r}) = \frac{\delta E_{xc}[n]}{\delta n(\mathbf{r})}. \tag{2.15}$$

To solve the Kohn-Sham equation (Eq. 2.13), the effective potential $V_{\text{eff}}(\mathbf{r})$ is calculated iteratively, as shown in Figure 2.1). First, an initial guess for the electron density $n(\mathbf{r})$ is made. Using this density, the effective potential $V_{\text{eff}}(\mathbf{r})$ is constructed, and the Kohn-Sham equations are solved to obtain the single-particle wavefunctions $\psi_i(\mathbf{r})$. The electron density is then recalculated from Eq. 2.10. In practice, only a fraction of the new density is mixed with the previous one to obtain the update. The updated electron density is used to reconstruct the effective potential, and the process is repeated until self-consistency is achieved. At self-consistency, the ground-state electron density $n(\mathbf{r})$, the total energy $E[n]$, and related properties can be determined.

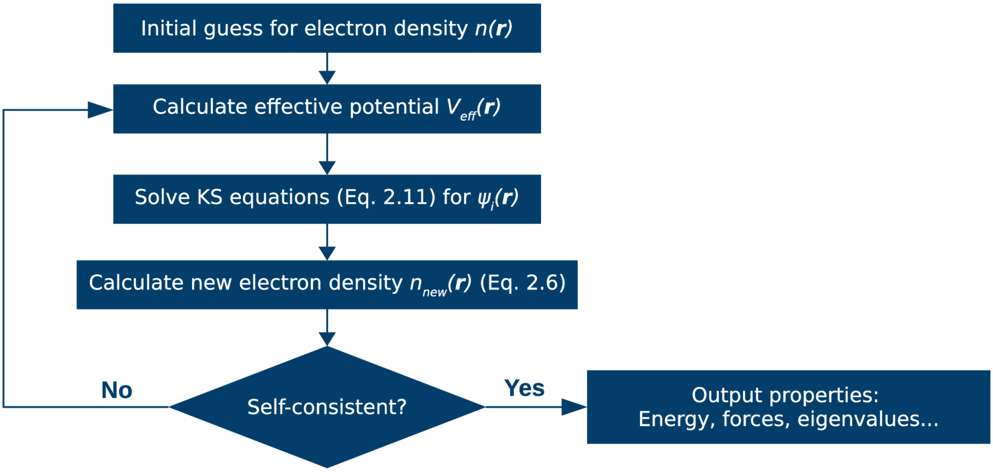

Figure 2.1: Schematic representation of the iterative loop used to solve the Kohn-Sham equations in DFT.

2.1.2 Exchange-correlational functional

The advantage of the Kohn-Sham approach is that the complex part of the full many-body interacting electron problem is contained in the exchange-correlation energy $E_{xc}[n]$, which is a functional of the electron density $n(\mathbf{r})$. However, the "exact" form of $E_{xc}[n]$ remains unknown. Fortunately, some well performed approximations for $E_{xc}[n]$ have been developed and led to accurate predictions of electronic structures for a variety of systems. In this subsection, we provide an overview of these approximations, often organized into what is referred to as *Jacob's Ladder* [174]. The detailed mathematical derivations are beyond the scope of this discussion, but an in-depth description can be found in the cited references.

The approximations to $E_{xc}[n]$ are arranged hierarchically, with increasing complexity and accuracy, as described by the *Jacob's Ladder* framework. Each rung of this ladder represents a step toward the "heaven" of the exact functional, where the accuracy improves at the cost of increased computational complexity, as shown in Figure 2.2.

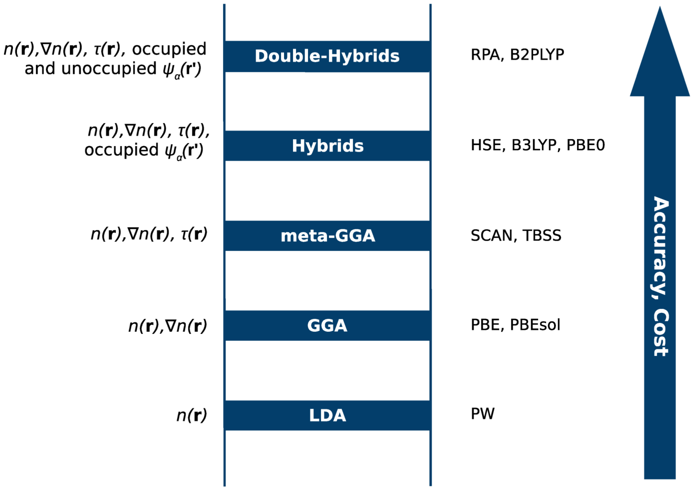

Figure 2.2: Schematic representation of *Jacob's Ladder* for exchange-correlation functionals, illustrating the hierarchy of approximations and examples of functionals at each level. Figure adapted from [174].

Local Density Approximation (LDA). The LDA represents the simplest approximation. It assumes that the exchange-correlation energy at any point depends only on the local electron density, which is approximated by a known exact solution for homogeneous electron gas. Mathematically, it is expressed as

$$E_{\text{xc}}^{\text{LDA}}[n] = \int d\mathbf{r}\, n(\mathbf{r})\epsilon_{\text{xc}}^{\text{hom}}(n(\mathbf{r})), \tag{2.16}$$

where $\epsilon_{\text{xc}}^{\text{hom}}(n(\mathbf{r}))$ is the exchange-correlation energy per electron for a homogeneous electron gas. LDA works remarkably well for systems with slowly varying electron densities, such as simple metals, but it struggles with systems exhibiting large inhomogeneities, like molecules or transition-metal (TM) oxides [175].

Generalized Gradient Approximation (GGA). The GGA improves upon LDA by including the gradient of the electron density $\nabla n(\mathbf{r})$, better accounting for spatial variations in the density

$$E_{\text{xc}}^{\text{GGA}}[n] = \int d\mathbf{r}\, n(\mathbf{r})\epsilon_{\text{xc}}^{\text{GGA}}(n(\mathbf{r}), \nabla n(\mathbf{r})). \tag{2.17}$$

Popular GGA functionals include PBE (Perdew-Burke-Ernzerhof) [176] and PBEsol (a revision of PBE for solids and approximation that were applied in this dissertation) [177]. PBE functional is widely used due to its balance of accuracy and computational efficiency, while PBEsol improves the description of structural parameters of solids by modifying the gradient corrections.

Meta-GGA. The Meta-GGA functionals represent the next rung of *Jacob's Ladder*. In addition to $n(\mathbf{r})$ and $\nabla n(\mathbf{r})$, these functionals include the kinetic energy density $\tau(\mathbf{r})$ and higher-order derivatives, which provides information about the local behavior of the electron orbitals

$$E_{\mathrm{xc}}^{\text{meta-GGA}}[n] = \int d\mathbf{r} n(\mathbf{r}) \varepsilon_{\mathrm{xc}}^{\mathrm{MGGA}}(n(\mathbf{r}), \nabla n(\mathbf{r}), \tau(\mathbf{r})). \tag{2.18}$$

Notable examples are SCAN and TPSS, which additionally include second derivatives of the electron density for meta-GGA functionals [178, 179].

Hybrid Functionals. Hybrid functionals combine density-dependent GGA functionals and exact HF exchange to improve accuracy. The exchange-correlation energy in hybrid functionals takes the form

$$E_{\mathrm{xc}}^{\mathrm{hybrid}} = \alpha E_{\mathrm{x}}^{\mathrm{HF}} + (1-\alpha) E_{\mathrm{x}}^{\mathrm{GGA}} + E_{\mathrm{c}}^{\mathrm{GGA}}, \tag{2.19}$$

where α is a mixing parameter that determines the fraction of HF exact exchange. HSE (Heyd-Scuseria-Ernzerhof) is a widely used screened hybrid functional, particularly for solid systems with bandgap, such as semiconductors and strongly correlated materials [180, 181].

Double-hybrid Functionals. Double-hybrid functionals, representing the current top rung of Jacob's ladder, combine exact HF exchange with a portion of second-order perturbative correlation energy alongside conventional DFT exchange and correlation [182].

The selection of the exchange-correlation functional depends on the specific properties of interest, the nature of the system being investigated, and the available computational resources. While higher-rung functionals, such as hybrid and meta-GGA types, offer improved accuracy, they also come with significantly increased computational costs. Therefore, a balance must be struck between accuracy and efficiency depending on the problem at hand. Among the functionals, the PBE functional remains the most commonly used due to its balance between computational feasibility and reliable performance.

2.1.3 DFT+*U*

While DFT with LDA or GGA provides excellent approximations for systems with delocalized electrons, such as metals, these approaches often fail when applied to systems with strongly localized d- or f-electrons, as introduced in Section 1.6.2. The strongly-correlated electrons lead to significant electron-electron Coulomb interaction effects that are not fully accounted for in LDA or GGA. As a result, standard DFT frequently predicts incorrect electronic structures, such as metallic states for materials that are experimentally observed to have wide band gaps [146]. For materials like TM oxides, which are commonly used in battery applications due to their electrochemical properties, this failure poses a significant challenge. Accurate descriptions of such systems often require computationally intensive methods, such as hybrid functionals, which incorporate a fraction of exact exchange energy (see Section 2.1.2). However, these methods demand significantly more computational resources, making them impractical for large-scale systems or high-throughput studies.

An alternative approach that balances computational efficiency with improved accuracy is the DFT$+U$ method, also referred to as LDA$+U$ or GGA$+U$ [146, 183–185]. The DFT$+U$ method modifies the conventional DFT energy functional by adding a Hubbard-like term to explicitly account for the on-site Coulomb interactions in localized orbitals. This approach provides a practical solution for studying strongly correlated materials, making it particularly popular in solid-state physics and chemistry. For a comprehensive review of DFT$+U$, readers are referred to Ref. [186].

The DFT$+U$ formalism adds a Hubbard correction to the conventional DFT functional to capture the on-site Coulomb interactions explicitly. The total energy functional in DFT$+U$ is written as

$$E_{\text{DFT+U}}[n(\mathbf{r})] = E_{\text{DFT}}[n(\mathbf{r})] + E_{\text{Hub}}[n_{Im\sigma}] - E_{\text{DC}}[N_{I\sigma}], \tag{2.20}$$

where $E_{\text{DFT}}[n(\mathbf{r})]$ represents the standard DFT energy as a functional of the electron density $n(\mathbf{r})$, $E_{\text{Hub}}[n_{Im\sigma}]$ is the Hubbard correction, and $E_{\text{DC}}[N_{I\sigma}]$ is the double-counting term that removes the interaction already accounted for within DFT. $n_{Im\sigma}$ represents the occupation matrix for localized orbitals of atom I with spin σ and magnetic quantum number m. $N_{I\sigma}$ corresponds to the total occupation number for the same localized orbitals $\sum_m n_{Im\sigma}$.

The DFT$+U$ method has been extended and refined through multiple formulations, one of the earliest approaches was proposed by Liechtenstein and colleagues [187]. This formulation introduces a fully rotationally invariant treatment of the on-site Coulomb interaction, which includes not only the Hubbard U correction but also the Hund J correction. Dudarev formulation simplifies the Hubbard correction by consolidating the U and J terms into a single effective parameter, $U_{\text{eff}} = U - J$ [188]. This approach focuses on the trace of the occupation matrix, significantly reducing computational complexity while retaining the core physics. The simplified functional is expressed as

$$E_{\text{Hub}} = \frac{U_{\text{eff}}}{2} \sum_{I,\sigma} \text{Tr}\left[n_{Im\sigma}(1 - n_{Im\sigma})\right], \tag{2.21}$$

where $\text{Tr}\left[n_{Im\sigma}\right]$ is the trace of the orbital occupation matrix $n_{Im\sigma}$. The term $\text{Tr}\left[n_{Im\sigma}(1 - n_{Im\sigma})\right]$ penalizes fractional occupations, thereby promoting localization of the electrons. By adding a penalty to the total energy for the fractional occupied states, the system is driven towards integer occupations, which corresponds to more localized electron states. The Dudarev approach is widely adopted for its computational efficiency and effectiveness in correcting electronic structures, which we also used in this dissertation.

The DFT+U approach can also be interpreted as a correction to the DFT total energy, aiming to restore the piecewise linear behavior of the exact total energy with respect to the number of electrons, as illustrated in Figure 2.3. In exact DFT, the total energy $E(N)$ should exhibit piecewise linearity as a function of electron number N, with discontinuities at integer values. The fundamental band gap, which is defined as the energy difference between the ionization potential (IP) and the electron affinity (EA)

$$E_g = IP - EA = [E(N-1) - E(N)] - [E(N) - E(N+1)]\,, \tag{2.22}$$

should be determined by the discontinuity in the derivative of $E(N)$. However, in standard DFT approximations (e.g., LDA, GGA), self-interaction errors smooth out these discontinuities, leading to an over-delocalization of electrons and a systematic underestimation of the band gap.

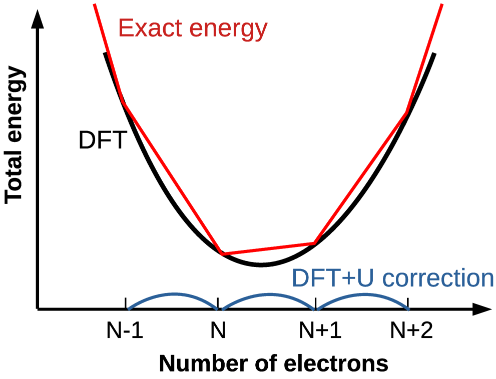

Figure 2.3: Illustration of the total energy as a function of the number of electrons for standard DFT (black curve) and the correction of $+U$ on the total energy (blue curve). The inclusion of the Hubbard U parameter brings the energy closer to the exact linear behavior (red curve), which is critical for accurately describing strongly correlated systems. Figure adapted from [145].

The Hubbard U term, as introduced in Equation 2.21, acts as a penalty function that drives the orbital occupations toward integer values, correcting the curvature in $E(N)$ and restoring a more piecewise linear behavior. This correction pushes the occupied states down by $-U/2$ and the unoccupied states up by $+U/2$, resulting an increase in band gap by approximately U. Consequently, the DFT+U method is particularly effective in improving the description of TM oxides and other strongly correlated materials, where standard DFT functionals tend to underestimate localization effects and band gaps. The DFT+U approach is especially relevant for battery materials, where TMs play a central role in redox mechanisms. By effectively correcting the electronic structure of TM-containing compounds, DFT+U enables more accurate predictions of redox potentials, electronic structures, and ionic transport properties, thereby contributing to the design and optimization of next-generation battery materials [151, 189, 190].

2.1.4 Linear response method

The Hubbard U parameter in DFT$+U$ represents the on-site Coulomb interaction, quantifying the strength of electron-electron repulsion within localized d- or f-orbitals. The selection of this parameter is not trivial and significantly influences the accuracy of electronic structure calculations. Instead of choosing the U parameter by fitting to experimental data, we use the linear response method to compute U self-consistently from first principles, offering a more rigorous and transferable determination of the Hubbard parameter. It has been successfully applied in computation of different d and f elements-bearing materials (e.g.,[145, 160, 161, 191, 192]). It also improves the prediction of structural [192, 193] and thermochemical [160, 194] parameters, and provides good description of the x-ray spectroscopic data [161].

The linear response method evaluates the curvature of the total energy as a function of localized orbital occupations. To achieve this, a small perturbation α_I is applied to the localized potential associated with atomic site I, and the induced changes in their occupation numbers n_I are measured. The linear response method distinguishes between two types of response functions: the non-interacting response and the fully interacting response. The non-interacting response, denoted as χ^0, captures the changes in orbital occupation due to the perturbation without self-consistent relaxation of the electronic density. This is given by

$$\chi^0_{IJ} = \frac{\partial^2 E^{KS}}{\partial \alpha_I^{KS} \partial \alpha_J^{KS}} = \frac{\partial n_I}{\partial \alpha_J^{KS}}, \tag{2.23}$$

where E^{KS} is the Kohn-Sham energy functional and α_J^{KS} represents the perturbation in the Kohn-Sham potential. In contrast, the fully interacting response, χ_{IJ}, accounts for the self-consistent adjustment of the electronic density to the applied perturbation, which can be expressed as

$$\chi_{IJ} = \frac{\partial^2 E}{\partial \alpha_I \partial \alpha_J} = \frac{\partial n_I}{\partial \alpha_J}, \tag{2.24}$$

where E is the total energy, α_I represents the applied perturbation at site I, and n_I is the corresponding orbital occupation. The difference between these response functions captures the many-body electronic interactions intrinsic to the system. The Hubbard U parameter is calculated as the inverse of the interacting response function subtracted by the inverse of the non-interacting response function

$$U = (\chi_0^{-1} - \chi^{-1})_{II}. \tag{2.25}$$

The practical implementation of the linear response method involves constructing a supercell to account for long-range Coulomb interactions, applying small perturbations α to localized orbitals, and monitoring changes in the orbital occupations to compute the response functions. The computed U parameter is thus system-specific, accounting for the local electronic environment and screening effects intrinsic to the material.

The electronic structure obtained from the DFT+U method often differs significantly from that predicted by standard DFT, which is typically used as the starting point for calculating the Hubbard U parameter. Ideally, a more refined approach should ensure "internal consistency" between the electronic structure used to compute U parameter and the one resulting from the application of the computed U parameter. This can be achieved through an iterative refinement process, where the U parameter is recalculated using a functional that already incorporates a DFT+U correction. In this iterative approach, the newly computed U parameter serves as a correction to the previously calculated value, and the process continues until the correction becomes negligible (i.e., the U parameter converges) [145]. Additionally, the computed Hubbard U parameter depends on factors such as supercell size, pseudopotentials, k-mesh, the exchange-correlation functional, and the projectors used for d- or f-orbitals [145, 186].

Another way to compute the self-consistent Hubbard U parameter is via density functional perturbation theory (DFPT), which is also based on linear-response theory [195]. Unlike the traditional linear-response approach that requires large supercells to eliminate periodic image interactions, DFPT allows the use of primitive cells and thereby reduces the computational cost while retaining accuracy. This method has been implemented in Quantum-ESPRESSO package as the "HP" code [196].

2.1.5 From Bloch Functions to Wannier Functions

In DFT calculations, crystalline solids are treated as infinite periodic arrays of atoms, i.e., with periodic boundary conditions and translational symmetry. The periodicity of the potential $V(\mathbf{r})$ can be expressed as

$$V(\mathbf{r}+\mathbf{T}) = V(\mathbf{r}), \tag{2.26}$$

where $\mathbf{T}$ is a lattice translation vector. For such periodic potentials, the solutions of the Schrödinger or Kohn–Sham equations must satisfy the translational symmetry requirement. For computational convenience, calculations for periodic solids are often performed in reciprocal space, which is related to real (direct) space via a Fourier transform. The reciprocal space is organized into a special unit cell called the Brillouin zone (BZ), and the wave vector $\mathbf{k}$ lies within the first BZ. The Bloch functions allow electron's wavefunctions to be efficiently expanded in terms of plane waves in reciprocal space [197]

$$\psi_{\mathbf{k}}(\mathbf{r}) = e^{i\mathbf{k}\cdot\mathbf{r}} u_{\mathbf{k}}(\mathbf{r}). \tag{2.27}$$

Here, $\mathbf{k}$ is wave vector in reciprocal space, and $u_{\mathbf{k}}(\mathbf{r})$ is a periodic function that satisfies $u_{\mathbf{k}}(\mathbf{r} + \mathbf{T}) = u_{\mathbf{k}}(\mathbf{r})$. The exponential term $e^{i\mathbf{k}\cdot\mathbf{r}}$ represents the plane-wave-like behavior of the electron, while the periodic part $u_{\mathbf{k}}(\mathbf{r})$ accounts for the modulation of the wavefunction due to the periodic potential of the crystal lattice. The periodic part $u_{\mathbf{k}}(\mathbf{r})$ can be expressed as a Fourier series [165]

$$u_{\mathbf{k}}(\mathbf{r}) = \sum_{\mathbf{G}} c_{\mathbf{k}}(\mathbf{G}) e^{i\mathbf{G}\cdot\mathbf{r}}, \tag{2.28}$$

where $\mathbf{G}$ are the reciprocal lattice vectors, and $c_{\mathbf{k}}(\mathbf{G})$ are the expansion coefficients. Substituting this into the Bloch function gives

$$\psi_{\mathbf{k}}(\mathbf{r}) = \sum_{\mathbf{G}} c_{\mathbf{k}}(\mathbf{G}) e^{i(\mathbf{k}+\mathbf{G})\cdot\mathbf{r}}. \tag{2.29}$$

This Fourier expansion provides the mathematical foundation for plane-wave methods widely used in electronic structure calculations. Plane waves are an ideal choice for periodic systems because they inherently satisfy the periodic boundary conditions of the lattice.

A plane-wave basis set consists of a series of plane waves used to expand the electronic wavefunctions. The quality of the basis set depends on the number of plane waves included in the expansion. In practical computations, the number of plane waves included in the basis set is determined by a cutoff energy (E_{cut})

$$\frac{\hbar^2 |\mathbf{k} + \mathbf{G}|^2}{2m_e} \leq E_{\text{cut}}. \tag{2.30}$$

This ensures that only plane waves with kinetic energies below E_{cut} are included. Increasing the energy cutoff includes more plane waves in the basis set, leading to higher accuracy, but at the expense of greater computational cost.

In electronic structure calculations, Bloch functions provide a natural basis for describing the electronic states of periodic systems. While highly effective for plane-wave expansions in reciprocal space, Bloch functions are inherently delocalized over the entire crystal lattice. This delocalization limits their utility in studying localized phenomena, such as strong electron correlations, bonding in localized orbitals, and site-specific properties. From Equation 2.34, we see the role of projectors in determining the number of localized electrons ($n_{Im\sigma}$) on a given atom I. A way to localize the occupations in the DFT calculations are the Wannier function (WF)-based projector. WF, introduced by Gregory Wannier in 1937 [198], provides a real-space representation of electronic states through unitary transformations of Bloch functions

$$W_{n\mathbf{R}}(\mathbf{r}) = \frac{1}{N_k} \sum_{\mathbf{k},m} e^{-i\mathbf{k}\cdot\mathbf{R}} U_{mn}^{(\mathbf{k})} \psi_{m\mathbf{k}}(\mathbf{r}). \tag{2.31}$$

Here, $U_{mn}^{(\mathbf{k})}$ is a unitary matrix that defines how Bloch states are rotated into the Wannier basis, $w_{n\mathbf{R}}(\mathbf{r})$ is the WF centered at lattice vector $\mathbf{R}$ for band n, and $\psi_{n\mathbf{k}}(\mathbf{r})$ is the Bloch function. In some methods, such as Maximally Localized Wannier Functions (MLWF), this matrix is optimized iteratively to minimize the spatial spread of the WFs [164]. Alternatively, simpler approaches like PoormanWannier (`pmw.x`) construct Wannier functions more directly. Wannier function-based projectors are widely used to define localized occupations in DFT+U [186, 199]. These projectors are obtained by projecting Bloch wavefunctions onto a localized atomic-like orbital

$$P_{ij}^{(k)} = \langle \psi_i^{(k)} | S | \phi_j \rangle, \tag{2.32}$$

where $P_{ij}^{(k)}$ is the overlap matrix, $\psi_i^{(k)}$ are the Bloch wavefunctions, ϕ_j are atomic-like Wannier orbitals, and S is the overlap operator that accounts for non-orthogonality in the basis. To construct a good Wannier representation, we need to project Bloch states onto a localized basis. The projection matrix must be orthonormal to ensure that each Wannier function represents a distinct localized state. However, direct projections of Bloch wavefunctions onto atomic-like functions are not necessarily orthonormal. Since $P_{ij}^{(k)}$ is not necessarily orthonormal, `pmw.x` applies a transformation to obtain a proper localized Wannier basis. This transformation is determined by analyzing the overlap matrix $P_{ij}^{(k)}$ to construct an appropriate unitary rotation $U_{jn}^{(k)}$. This approach provides a direct way to construct Wannier functions without the need for iterative localization. Using the selected $U_{jn}^{(k)}$, the final Wannier functions are obtained as

$$|W_n^{(k)}\rangle = \sum_m P_{mj}^{(k)} U_{jn}^{(k)} |\psi_m^{(k)}\rangle \tag{2.33}$$

For HEMs, which often involve multiple TMs with strongly localized d-orbitals, the poor man's Wannier approach is particularly useful for describing materials with strongly correlated electrons. By constructing Wannier-like orbitals for each atomic species, `pmw.x` enables a site-specific analysis of electronic localization and occupancy of electrons. This is crucial for accurately assigning the oxidation states and redox behavior of HEMs in battery applications. In this thesis, the `pmw.x` tool was employed to generate Wannier-like orbitals for DFT+U calculations on battery materials (see Chapter 3).

2.1.6 Atomic orbital-based vs. Wannier Function-based DFT+*U*

In order to compute the Hubbard energy, we need to know the orbital occupations of the *d*-orbitals (see Equation 2.20). The occupation matrix of the localized electronic states is constructed using the projectors. The general form of the occupation matrix is

$$n_{Im\sigma} = \sum_{k,v} f^{\sigma}_{kv} \langle \psi^{\sigma}_{kv} | P^{I}_{mm'} | \psi^{\sigma}_{kv} \rangle, \tag{2.34}$$

where ψ^{σ}_{kv} is the valence electronic wave function corresponding to the state (kv) with spin σ of the system, f^{σ}_{kv} is the corresponding occupation number, and $P^{I}_{mm'}$ are the generalized projection operators that project onto the localized electronic states with an atom I. Here, we compare two projectors, namely the widely used AO-based projectors and WF-based projectors.

AO-based projectors use predefined AOs, which are approximate solutions to the Schrödinger equation for a hydrogen-like "atom". The AO-based projection is straightforward, as it directly maps the Bloch states to the pre-defined localized atomic states. Nevertheless, the pre-defined atomic basis can lead to overlapping projections, causing ambiguity in occupation numbers, especially when electronic states spread over multiple atoms, AOs do not always provide an accurate projection. On the other hand, WF-based projectors define projection operators using WF, as explained in the previous section. Unlike AOs, WFs are constructed explicitly from Bloch states for each system, which provide a more accurate representation of localized states. The orthonormality of the WF-based projectors ensures an independent, well-defined basis localized states for applying the Hubbard correction. Table 2.1 shows the comparison between AO-based and WF-based DFT+*U*.

Projector	**AO-based**	**WF-based**
Definition	pre-defined AOs	constructs WFs from Bloch states
Localization	fixed and rigid	adaptable to materials
Computational Cost	lower	slightly higher than AO-based
Occupation number	fractional	close to 0 or 1

Table 2.1: Comparison between AO-based and WF-based DFT+*U*.

2.2 Atomic configurations in HEMs

The disordered nature of these materials poses a significant challenge because constructing a model of an ionic structure that represents a disorder is not a trivial task. Moreover, even for structures with the same composition, i.e., the same chemical formula, different atomic arrangements can result in varying calculated energies and electronic structures. Therefore, careful selection and construction of the input structure for DFT are essential to accurately compute disordered materials.

In this section, we introduce several methodologies for constructing atomic configurations as DFT inputs. A more detailed discussion of the results obtained using these different methods can be found in Chapter 5, where we present a garnet compound as an example. Here, we introduce three main methodologies. The first involves minimizing the Coulombic energy to select an optimal structure. The second is the special quasirandom structure (SQS) approach, and the third is the cluster expansion (CE) method.

2.2.1 Minimization of Coulomb energy

The minimization of Coulombic energy is widely used to identify energetically favorable configurations for disordered systems (see, e.g., [200–203]). This approach is motivated by the observation that Coulombic interactions often exhibit a linear correlation with DFT-calculated energies for ionic systems [201]. The electrostatic Coulomb energy is expressed as

$$E_{\mathrm{coul}} = \frac{e^2}{4\pi\epsilon_0} \sum_{\alpha<\beta} \frac{Z_\alpha Z_\beta}{|r_\alpha - r_\beta|}, \tag{2.35}$$

where the summation goes over any pair of ions present in the lattice, Z_α are the respective valencies, and $|r_\alpha - r_\beta|$ represents the distance between ions α and β. The constants e and ϵ_0 are the elementary charge and the electric constant, respectively. By systematically minimizing these interactions, one can obtain structural models that have low(est)-energy configurations without the need for exhaustive quantum mechanical calculations. Several strategies exist for generating structural models optimized through Coulombic energy minimization, including exhaustive sampling using combinatorial methods and Monte Carlo (MC) techniques. Below, we first introduce the exhaustive sampling method, as implemented in the `SUPERCELL` program [204], which is employed in some of the research presented in this thesis (e.g., Chapter 3). We then briefly introduce the MC methods.

Exhaustive sampling. The Coulombic energy of a periodic supercell, which accounts for the long-range interactions between charges, is computed using the Ewald summation technique [205]. The Ewald method decomposes the electrostatic interactions of a periodic system into short-range (real-space) and long-range (reciprocal-space) components, ensuring rapid convergence and high accuracy. The configurations of the supercell are generated by combinatorial sampling of all possible atomic distributions over the disordered sites, constrained by the total composition and charge neutrality. For a system with K crystallographic sites and N different types of atoms (including vacancies) occupying this site, the number of permutations P is given by

$$P\left(k_1, k_2, \ldots, k_N\right) = \frac{\left(k_1 + k_2 + \cdots + k_N\right)!}{k_1! k_2! \ldots k_N!} = \frac{\left(\sum_{i=1}^{N} k_i\right)!}{\prod_{i=1}^{N} k_i!}, \tag{2.36}$$

where $k_1, k_2, \ldots, k_N$ represent the number of sites occupied by each species i, satisfying $K = \sum_{i=1}^{N} k_i$. The `SUPERCELL` program assigns charges (given by users) to each atomic species and computes the Coulombic energy for all unique configurations. A charge neutrality constraint is enforced, ensuring that the total charge in the supercell is zero

$$\sum_i q_i N_i = 0, \tag{2.37}$$

where q_i is the charge of species i and N_i is the number of atoms of that species in the supercell. By ranking configurations based on their Coulombic energies, the most representative low-energy structures can be selected for further analysis, such as DFT calculations. This approach is particularly effective for small systems, where the number of possible configurations remains manageable. However, from Equation 2.36, it is evident that for systems with large supercells or multiple types of atoms, P grows exponentially, making exhaustive searches computationally impractical. For such cases, alternative approaches, such as MC, provide a more scalable solution.

Monte Carlo sampling. Besides exhaustive sampling, MC for the minimization of Coulombic energy has been shown to be efficient in identifying candidate configurations that approximate the configurational ground-state energies referring to DFT [201, 206, 207]. The MC algorithm begins with an initial random atomic distribution, ensuring that the system satisfies predefined constraints such as total composition and charge neutrality. At each MC step, a swap of two atomic sites is proposed, and the acceptance of this swap is determined by the Metropolis criterion

$$P = \min\left(1, \exp\left(-\frac{\Delta E}{k_B T}\right)\right), \tag{2.38}$$

where ΔE is the Coulombic energy difference (Ewald energy difference) between the initial and proposed configurations, k_B is the Boltzmann constant, and T is the simulation temperature. If the energy of the new configuration is lower ($\Delta E < 0$), the swap is always accepted. Otherwise, it is accepted with the probability, introducing a thermal fluctuation to escape local minima. The MC process is iterated until the system reaches equilibrium or a minimum. A more detailed description can be found in Section 2.2.2 and Figure 2.4. The resulting configurations represent (global) energy minima of the Coulombic energy model and are often used as input structures for further DFT calculations.

The replica exchange Monte Carlo (REMC) method extends the standard MC approach by incorporating multiple parallel simulations (replicas) at different temperatures [208]. Each replica evolves independently according to the standard MC algorithm. At predefined intervals, an exchange of configurations between replicas is proposed. The acceptance of such exchanges follows a modified Metropolis criterion

$$P_{\text{exchange}} = \min\left(1, \exp\left(\Delta E \cdot \left(\frac{1}{k_B T_1} - \frac{1}{k_B T_2}\right)\right)\right), \tag{2.39}$$

where $\Delta E = E_2 - E_1$ is the energy difference between the configurations of two replicas at temperatures T_1 and T_2. By allowing replicas to exchange configurations, REMC facilitates the sampling of high-energy regions at elevated temperatures, enabling the system to overcome energy barriers and explore a broader configurational space. This so-called parallel tempering strategy enhances the efficiency of the MC algorithm, particularly for systems with rugged energy landscapes, such as HEMs, where local minima can trap the sampling process. At lower temperatures, the replicas perform local optimizations, while the higher-temperature replicas aid in escaping from local minima by introducing greater configurational diversity. This combination ensures a comprehensive exploration of the energy landscape, leading to a more accurate identification of the global minima.

2.2.2 Special quasirandom structures

SQS are a crucial technique for modeling disordered materials at the atomic scale. This method has been widely applied to high-entropy alloys (HEAs) [209], where it has been successfully used to predict formation enthalpies [210, 211] and to model the electronic structure of random alloys [212, 213]. Additionally, the SQS approach has been extended to other HE systems, including high-entropy oxides (HEOs) [70, 134, 214]. In this thesis, SQS is extensively utilized to capture the disordered nature of HEMs in DFT calculations, and we employed the ATAT package to generate the SQS [215]. A more detailed description of the method can be found in the original work of Zunger et al. [216]. The concept of SQS is to find a disordered structure with a finite number of atoms per unit cell, whose correlation functions are close to the fully random atomic arrangement [212, 216]. These correlation functions describe the statistical distribution of atomic species over various clusters, such as pairs, triplets, or higher-order clusters. The correlation associated with a cluster α is mathematically defined as

$$\rho_\alpha(\sigma) \equiv \langle \Gamma_{\alpha'}(\sigma) \rangle_\alpha, \tag{2.40}$$

where the term $\Gamma_{\alpha'}(\sigma)$ is the product of site occupation variables σ_i over all sites i within a cluster α', which is equivalent by symmetry to cluster α. The average $\langle \dots \rangle_\alpha$ is taken over all equivalent clusters $\Gamma_{\alpha'}$. The cluster function $\Gamma_\alpha(\sigma)$ is given by

$$\Gamma_\alpha(\sigma) = \prod_{i \in \alpha} \gamma_{\alpha_i}(\sigma_i), \tag{2.41}$$

where the occupation variable σ_i specifies which atomic species occupies site i, with $\gamma_{\alpha_i}(\sigma_i)$ assigning a numeric value to each species. For a fully random state, the target correlations ρ_α^{rnd} are derived from the average site compositions as

$$\rho_\alpha = \prod_{i \in \alpha} \langle \gamma_i \rangle, \tag{2.42}$$

where $\langle \gamma_i \rangle$ represents the average occupation state for species at site i. In the simplest case of a binary alloy, γ_i typically takes values of $+1$ or -1 to distinguish between two atomic species. For a multi-component system, γ_i is assigned unique values for each atomic species. ρ_α^{rnd} accounts for the weighted contributions of all species based on their average site fractions.

In Practice, the generation of an optimal SQS involves minimizing an objective function Q, which quantifies the differences between the calculated correlations $\rho_\alpha(\sigma)$ of a candidate SQSs and the target correlations ρ_α^{rnd} of the fully disordered state. The objective function Q is expressed as

$$Q = -\omega L + \sum_{\alpha \in A} |\Delta \rho_\alpha(\sigma)|, \tag{2.43}$$

where $\Delta \rho_\alpha(\sigma) = \rho_\alpha(\sigma) - \rho_\alpha^{\text{rnd}}$ measures the deviation of the calculated correlations from the target random correlations. The parameter L represents the largest distance such that the correlations for all clusters α with lengths smaller than L match perfectly, and ω is a weighting factor that prioritizes the matching of short-distance correlations. The set A specifies the clusters considered in the optimization process. The minimization of the objective function Q is performed using a simulated annealing loop, specifically the Metropolis algorithm, as shown in Figure 2.4. Initially, the atomic sites within the supercell are randomly populated based on the desired composition (X_0). New configurations are generated by swapping atomic sites, and their acceptance is determined probabilistically based on the objective function. If the new objective function Q_{i+1} is smaller than the original Q_i, the new configuration X_{i+1} is accepted. If not, a uniform random number $u \in [0, 1]$ is generated, and the new configuration X_{i+1} is accepted if $e^{-Q/T} > u$, where T is a user-specified fictitious temperature. This iterative process continues until the objective function Q reaches its minimum. This process ensures that the algorithm avoids being trapped in local minima, ultimately converging to the global minimum of Q.

SQS provides a powerful framework for bridging the gap between disordered materials and periodic supercell calculations. By carefully matching atomic correlations, SQS enables accu-

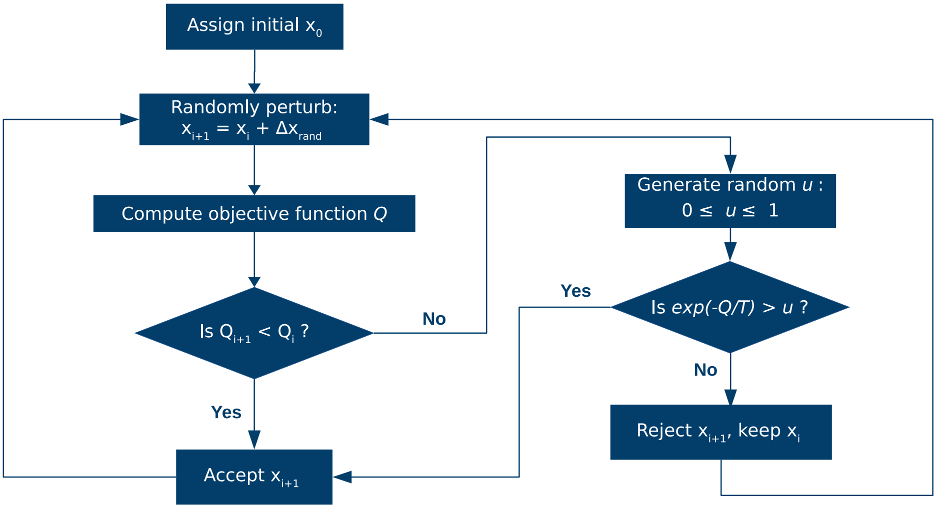

Figure 2.4: Illustration of the Metropolis algorithm for generating SQS.

rate and computationally efficient modeling of complex disordered systems, which is useful for HEMs.

2.2.3 Cluster expansion

DFT-based approaches allow for reasonably accurate computation of electronic structures of materials. However, calculating thermodynamic properties using DFT, e.g. phonon calculations, could be computationally demanding, especially for disordered systems like HEMs. Additionally, evaluating configurational properties such as short-range order or phase diagrams often involves sampling a large configuration space. An alternative approach is the CE method, which efficiently maps the configuration space of a system to thermodynamic properties. CE, combined with MC simulations, has been extensively applied to compute properties such as chemical short-range order [217, 218], phase diagrams [219, 220], and ground states [221, 222] for multicomponent systems. Here we provide a short introduction to CE, and a more detailed description can be found in references [139, 223–225].

The concept of CE is closely related to the formalism discussed in Section 2.2.2, where correlation functions $\rho_\alpha(\sigma)$ describe the statistical distribution of atomic species over clusters, including pairs, triplets, or higher-order clusters. In the CE method, these correlation functions are utilized to construct an expression for the property of interest, typically the energy of the system. The energy $q(\sigma)$ is expressed as

$$q(\sigma) = \sum_{\alpha} m_\alpha J_\alpha \rho_\alpha(\sigma), \tag{2.44}$$

where σ represents a configuration, which is a vector of site occupation variables σ_i indicating the atomic species at site i. The parameter m_α accounts for the multiplicity of cluster α, taking into consideration symmetry-equivalent clusters (α' in Equation 2.40) within the lattice. The effective cluster interaction (ECI) coefficients J_α parameterize the interaction strength for each cluster type, and $\rho_\alpha(\sigma)$ are the correlation functions previously defined in Equations 2.40. The CE essentially maps the configuration space of atomic arrangements to the energy landscape using these terms. The coefficients J_α are determined by fitting the CE model to the energies of a training set of configurations obtained from DFT calculations. This fitting process minimizes the difference between the DFT-computed energies and the CE predictions. In CE, the ability to accurately describe these correlations allows the method to model disordered materials efficiently while maintaining accuracy in predicting thermodynamic properties.

Once the ECIs (J_α) are determined, the energies of configurations can be computed at negligible computational cost. The CE model can then be coupled with various statistical mechanical techniques, such as MC simulations [226], low-temperature expansion [227], high-temperature expansion [228], and the cluster variation method [228], to study thermodynamic properties. In this thesis, we employ semi-grand canonical MC simulations [229] to explore possible configurations of HEMs at evaluated temperatures and calculate, for example, the short-range order parameters.

For simplicity, we consider the case of binary alloys. In a semi-grand canonical ensemble, the thermodynamic state is defined by a fixed total number of atoms N and the concentration is allowed to adapt to an externally imposed difference in the chemical potential of the two types of atoms. The chemical potential difference will be simply referred to as the “chemical potential” in what follows, which is $\mu = \mu_B - \mu_A$. The thermodynamic potential (expressed per atom) for the system at temperature T can be expressed as

$$\phi(\beta, \mu) = -\frac{1}{\beta N} \ln \left(\sum_i \exp(-\beta N (E_i - \mu x_i)) \right), \tag{2.45}$$

where E_i is the internal energy (per atom) approximated by CE model ($E_i \approx q(\sigma_i)$ from Equation 2.44), x_i is the concentration of state i, and $\beta = 1/(k_B T)$ is the reciprocal of the temperature T and k_B is Boltzmann’s constant. At low temperatures, the system is dominated by low-energy configurations, leading to minimal disorder. At high temperatures, the entropy term dominates, resulting in increased disorder in atomic arrangements.

The MC simulations proceed through iterative steps, similarly to the way described in Section 2.2.2. The energy change $\Delta\Phi$ associated with each proposed swap is computed using the CE model to evaluate $q(\sigma)$ and incorporating the chemical potential contribution. The acceptance of a new configuration is governed by the Metropolis algorithm (see Figure 2.4), which ensures that configurations are sampled according to the Boltzmann distribution

$$P = \min\left(1, \exp\left(-\frac{\Delta\Phi}{k_B T}\right)\right). \tag{2.46}$$

This acceptance criterion allows the system to explore the configuration space while avoiding local minima, ultimately converging to equilibrium. At equilibrium, the semi-grand-canonical MC simulations provide information about the atomic arrangements at specific temperatures and chemical potentials. These simulations reveal key properties such as chemical short-range order, compositional distributions, and configurational entropy. In this thesis, these simulations are applied to predict the realistic atomic arrangements in HEMs at elevated temperatures, bypassing the need for exhaustive first-principles calculations of all possible configurations.

2.3 Software and computational details

In the thesis, the majority of the DFT work is performed using the plane-wave Quantum-ESPRESSO package [230]. For the systems containing TMs, spin-polarized calculations were performed. The standard computational setup is described here unless otherwise specified in the respective chapters. Ultrasoft pseudopotentials [231] were applied, along with a plane-wave energy cutoff of 50 Ry. Specifically, the PBEsol exchange-correlation functional [176, 177] was used, as it improves the prediction of structural parameters for solids compared to PBE [177, 192, 232]. Structural optimization was performed with convergence criteria of 10^{-5} Ry for the total energy and 10^{-4} Ry/a_0 for forces (where a_0 is the Bohr radius).

The Hubbard U parameters for the TMs were computed applying the linear-response method [145]. For the construction of the WF-based representation of the $3d$ orbitals, for counting the occupancy of d states, we applied the Poormanwannier.x tool of the Quantum-ESPRESSO package. Hereafter, the results computed with this approach we call DFT+U(WF).

The disordered structural models of HEMs used in the calculations were mainly constructed by SQS, with some from Coulombic energy-based and CE. The model SQS was generated with the *mcsqs* code implemented in Alloy Theoretic Automated Toolkit (ATAT) package [215].

3 Computation of oxides: beyond standard DFT+*U*

In this chapter, the performance of the DFT+*U* method is tested, with the Hubbard *U* parameter derived from the linear response method and Wannier functions (WF) used as projectors to estimate the occupancies of the *d* states in transition metals (TMs). The presented analysis covers a range of materials, from simple oxides (NiO and CoO) and conventional cathode materials ($LiCoO_2$ and $LiNiO_2$) to the high-entropy oxide $Li_{1.2}(Co_{0.18}Ni_{0.18}Mn_{0.44})O_2$. The aim of this chapter is to improve the electronic calculations of DFT+*U*-based approaches for TM-containing materials. In addition, results are compared with computationally demanding methods, such as hybrid [180] and SCAN functionals [178], particularly regarding the accurate prediction of structural parameters, electronic configurations, and oxidation states. Comparison of computational predictions to experimental data is made, such as redox reaction energies and battery material voltages.

This chapter is adapted from works previously published in the research articles Y.-Y. Ting and P. M. Kowalski. *Refined DFT+U method for computation of layered oxide cathode materials*. Electrochimica Acta, 443, 141912, 2023. doi: 10.1016/j.electacta.2023.141912 and P. M. Kowalski, T. Bornhake, O. Cheong, N. Dohrmann, A. L. Koch Liston, S. K. Potts, A. Shad, R. Tesch, and Y.-Y. Ting. *Fundamentals of energy storage from first principles simulations: Challenges and opportunities*. Frontiers in Energy Research, 10, 2023. doi: 10.3389/fenrg.2022.1096190. The computational work presented here was performed by myself under the guidance of Dr. Piotr Kowalski.

3.1 Introduction

As explained in Section 1.6.2, DFT has problems when handling TMs with strongly correlated electrons. The two most commonly applied approaches to correct over-delocalized *d*-states are: (1) hybrid functionals [180] and (2) the Hubbard model-based DFT+*U* approach [145, 146, 161, 183, 184, 233]. Although often applied, the former methods relying on computation of exact exchange within the Hartree-Fock scheme are computationally intensive, which prevents large-scale, systematic screening of the materials' properties. On the other hand, computationally feasible DFT+*U* method can dramatically fail when applied to the computation of TM-oxides materials [148, 161].

To avoid the empirical selection of the *U* parameter, I have used the linear-response method to derive *U* values from first principles (see Chapter 2 for the theoretical background), which is referred to as the "parameter-free DFT+*U*" approach. Additionally, WF-based projectors were applied to improve the estimate of the *d* orbital occupations, ensuring they are very close to the expected value of either 0 or 1. This eliminates the artificial, fractional occupation of 3*d* electrons and truly localizes them.

3.2 Computational details

The LCO and LNO phases were modeled as a layered α-NaFeO$_2$-type structure with the *R-3mH* space group, using $2 \times 2 \times 1$ supercells containing 48 atoms. The structures are shown in Fig. 3.1. The Monkhorst-Pack [234] *k*-points mesh of $4 \times 4 \times 2$ was applied to sample the Brillouin zone. The initial lattice constants and atomic coordinates were taken from the experimental measurements [235].

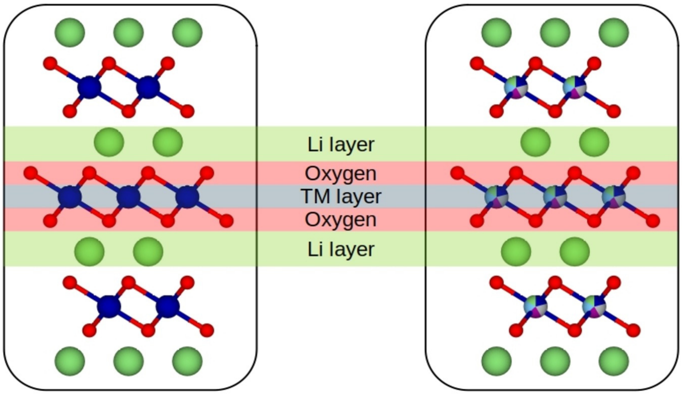

Figure 3.1: Schematic diagram of layered α-NaFeO$_2$ type structure of LCO and LNO (left) and a disordered LNMC (right) compounds, cut along the c-axis. In high-entropy layered oxide (right), the layered structure is preserved but TM layers are filled randomly by Ni, Co, Mn and Li cations, showing a disordered state with no specific atomic site arrangement.

For the structural models used in calculations of Li$_x$NiO$_2$, the most favorable arrangement of Li atoms and vacancies was selected, which gives the most negative (most stable) Coulomb energies among all possible configurations. The Coulomb energies were calculated using the package `SUPERCELL` [204].

The computed NMC-type Li-excess high-entropy oxide (HEO) $Li_{1.2}(Co_{0.18}Ni_{0.18}Mn_{0.44})O_2$ (LNMC) has a layered, high-entropy cation-disordered structure with the space group of *c/2m*, as shown in Figure 3.1. The disordered structural model used in the calculations was created with the aid of special quasirandom structures (SQS) (see Chapter 2 for more detail). For a good statistical representation of the disorder, the $2 \times 6 \times 2$ supercell containing 192 atoms was applied. The computations were made with the $2 \times 2 \times 2$ Monkhorst-Pack *k*-points grid [234].

As a reference, all the structural models were also computed with the HSE hybrid functional [180], with the standard exact exchange mixing parameter α=0.25. Ferromagnetic spin arrangements were considered for all compounds.

3.3 Electronic structure of simple oxides: NiO and CoO

I first tested the parameter-free DFT+*U* methodology on the simpler oxide systems NiO and CoO, which both containing TM-cation in +2 oxidation state. By doing so, the approach can be validated before extending the study to more complex high-entropy systems. The Hubbard *U* parameters derived for TMs and the resulting band gaps in these two compounds are provided in Table 3.1. Both, CoO and NiO are wide band gap charge transfer Mott insulators [239].

Compound	Value of Hubbard *U* (eV)	DFT+*U*	DFT+*U*(WF)	exp.
CoO	7.6	2.9	4.7	2.7-5.4[a]
NiO	6.7	3.2	3.5	3.6-4.3[b]

[a][236, 237], [b][237, 238]

Table 3.1: The Hubbard *U* parameter and the band gap values of CoO and NiO compounds computed using different methods and compared with experimental values. The same *U* parameter was applied for both compounds using the two considered *d* orbital projector types.

For such materials, the band gap should be equivalent to half of the Hubbard *U* parameter (expected shift of the unoccupied *d* states). The Hubbard *U* parameters computed here for these compounds are large and indicate wide band gaps (Table 3.1). The band gaps computed with the DFT+*U* method are consistent with the measurements. This is, however, somewhat misleading, as it results from incorrect occupations of *d* states. As the atomic orbitals (AOs) are applied as projectors, these result in significant, fractional occupations of empty orbitals (Table 3.2) and overestimated total occupancy of the *d* states. This shortcoming is corrected with the WF as projectors. The resulting occupation matrix and number of *d* electrons are also reported in Table 3.2. These reflect the expected values, which has also significant impact on the computed band gaps. The band gaps computed with the DFT+*U*(WF) method are larger than the ones predicted with the standard DFT+*U* approach. In this case, the hybrid functionals such as HSE also predict correct band gaps of the considered oxide materials [189]. This is opposite to the case of lithiated TM oxides, which show significant level of *d* elements delocalization and overestimation of the band gaps of these materials by the hybrid functionals approaches [189].

element	spin	d_1	d_2	d_3	d_4	d_5	*d* electrons
Co	↑	0.991	0.991	0.999	1.000	1.000	7.4
	↓	0.151	0.151	0.578	0.578	0.992	
Co (WF)	↑	0.992	0.992	0.997	0.998	0.998	7.0
	↓	0.005	0.005	0.005	0.996	0.996	
Ni	↑	0.998	0.998	1.001	1.001	1.001	8.4
	↓	0.203	0.203	0.999	0.999	0.999	
Ni (WF)	↑	0.992	0.992	0.999	0.999	0.999	8.0
	↓	0.009	0.009	0.999	0.999	0.999	

Table 3.2: The occupancies of 3*d* orbitals of CoO and NiO obtained with the AO- and WF-based projectors. The resulting number of *d* electrons is reported in the last column.

3.4 Electronic structure of electrode materials

With the results from simple oxides confirming the robustness of this approach, I now shift focus to more complex electrode materials, namely the HEOs used in LIB cathodes. I have tested the performance of the established method for computing LCO, LNO and $Li_{1.2}(Co_{0.18}Ni_{0.18}Mn_{0.44})O_2$ (LNMC) layered oxides electrode materials. I have been interested in the performance of this approach vs. more computationally demanding hybrid functional [180] and SCAN methods [178], for the correct prediction of the structural parameters, electronic configuration, and oxidation states.

Hubbard *U* parameter. The Hubbard *U* parameters computed for all the considered structures and TM cations are provided in Table 3.3. The obtained values are compared with the parameters applied in the previous studies of the considered compounds. For LCO and LNO compounds, I obtained values of 6.8 eV and 5.7 eV for Co and Ni, respectively. For the two elements in LNMC compound, I obtained slightly larger values, which reflect the impact of the local atomic arrangement on the strength of the Coulomb on-site repulsion, as also noticed in other studies (e.g. [192]). The Hubbard *U* parameter of 5.5 eV computed for Mn in LNMC is also consistent with the range of values applied in previous studies on TM-oxides ([94] and references hereafter).

The lattice parameters. The computed lattice parameters of LCO, LNO and LNMC compounds are provided in Table 3.4. I have reproduced the measured lattice parameters with rather unprecedented accuracy, with error smaller than $\sim 1\%$. However, because of the thermal expansion, the values measured at ambient temperature should be slightly larger than the predictions corresponding to the temperature of 0 K. The linear thermal expansion coefficient of the considered materials is $\sim 1.5 \times 10^{-5}$ K, which translates to $\sim 0.5\%$ and 1.4% change

TMO	element	U(eV)	Ref.
LCO	Co^{3+}	6.8	This work
		4.6	This work (rescaled)
		3.3	[156]
		3.4	[150]
		4.9	[159]
		4.9	[190]
LNO	Ni^{3+}	5.7	This work
		4.1	This work (rescaled)
		6.4	[156]
		6.0	[150]
		6.7	[189]
		5.3	[190]
LNMC	Co^{3+}	6.6	This work
	Ni^{3+}	6.0	This work
	Mn^{4+}	5.5	This work

Table 3.3: The Hubbard U parameter values for LCO, LNO, and LNMC compounds calculated in this work and compared with values reported in the literature. Rescaled values are included where applicable.

in the lattice parameters and volume, respectively [240, 241]. Chakraborty et al. [148] applied the DFT, DFT+U (both with the PBE exchange-correlation functional [176, 242]) and SCAN methods [178] to the computation of LCO and LNO compounds. The computed values are reported in Table 3.4 for comparison. They concluded the superiority of the SCAN functional for the computation of these materials over the DFT and DFT+U methods. I thus tested the performance of the approach studied here vs. their methodology.

In the case of LCO, I have accurately predicted the a lattice constant and only slightly underestimated the c value. I obtained a much better agreement with the measured data than the reference studies [148]. The c lattice parameter measures the distance between the layers and the van der Waals interactions, not captured by the standard DFT calculations, could be responsible for this discrepancy. However, Chakraborty et al. [148] has shown that the "D3" dispersion correction scheme results in worsening the prediction, a trend which I also observed in the calculations. Therefore, I did not consider these corrections here.

In the case of LNO, I also obtained very good match to the measured values. Similarly to the case of LCO, with the applied methodology I obtained much better agreement with the measured values of a lattice parameter than the SCAN results [148].

For LCO and LNO compounds, I also performed simulations with the rescaled Hubbard U parameter values (see later for the underlying reasoning). These may even improve the match to the experiment, having in mind the difference between the computed and measured values caused by the thermal expansion of the materials. The computed lattice parameters of LNMC also matched the measured values reasonably well. The deviation from the experimental val-

Material	a,b (Å)	c (Å)	γ (°)	Vol	Ref.	Functional
LCO	2.818	13.962	120	96.945	This work	PBEsol+U
	2.818	13.935	120	96.590	This work	PBEsol+U_{res}
	2.854	14.054	120	103.255	[148]	PBE
	2.837	14.152	120	98.695	[148]	PBE+U
	2.807	13.959	120	95.305	[148]	SCAN
	2.816	14.054	120	96.52	[243]	exp
LNO	2.882	14.136	120	101.68	This work	PBEsol+U
	2.875	14.089	120	100.84	This work	PBEsol+U_{res}
	2.887	14.202	120	103.255	[148]	PBE
	2.841	14.289	120	101.715	[148]	PBE+U
	2.823	14.094	120	99.20	[148]	SCAN
	2.8756(2)	14.2014(7)	120	101.70	[244]	exp
LNMC	4.902,8.518	4.920	108.892	203.387	This work	PBEsol+U
	4.9372(5),8.5470(7)	5.0258(5)	109.260(4)	200.21(3)	[245]	exp

Table 3.4: The lattice parameters of LCO, LNO and LNMC compounds computed here, in the studies of [148] and measured. U_{res} means the calculations with the rescaled derived Hubbard U parameter (Table 3.3).

ues of a and b lattice constants was less than $\sim 1\%$. The largest discrepancy of 2% was observed for the c lattice parameter value. It may originate from the complexity of the structure and the SQS approximation.

The electronic structure. The density of states (DOS) computed for all the compounds are illustrated in Figs. 3.2, 3.3 and 3.4. Here I provide results computed with the DFT+U, DFT+U(WF) and HSE ($\alpha = 0.25$) methods. The LCO and LNO compounds have measured band gaps of 2.7 eV [246] and 0.4 eV [247], respectively. The computed band gaps are reported in Table 3.5. As LCO has a wide band gap, I focus on the discussion of this case. The DFT+U approach predicted for this compound a correct band gap of 2.8 eV. However, the DFT+U(WF) method resulted in a much larger band gap of 4.4 eV. Such a large number could result from a large U parameter value derived with the linear response method. Another related aspect is the overestimation of the band gap by the HSE hybrid functional. This is corrected by decreasing the amount of exact exchange, as a result of partially delocalized character of d states of TM elements [189, 248]. Reducing of amount of exact exchange by a scaling factor of ~ 0.68 (i.e. selecting $\alpha = 0.17$) brings the computed band gap to an agreement with the measured value. As the DFT+U approach considers a fully localized limit [186, 249], an overestimation of the correlation effects and the band gap is expected by this method [248]. I thus performed calculations with the rescaled Hubbard U parameter by the same factor of 0.68 (marked as rescaled in Table 3.3). These also bring the predicted band gap to better agreement with the experiment. For LNO, the DFT+U method incorrectly predicts this compound to be a metal.

Another aspect of computation of the electronic state is the correct number of d electrons. As in the DFT+U approach AOs are usually used as projectors of occupancy for d states, the number

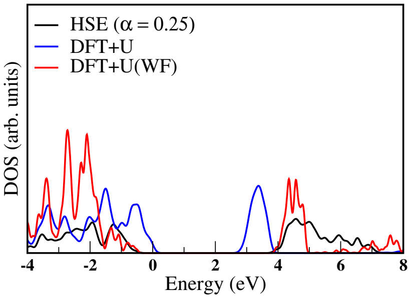

Figure 3.2: DOS of LCO computed with the HSE, DFT+U and DFT+U(WF) methods.

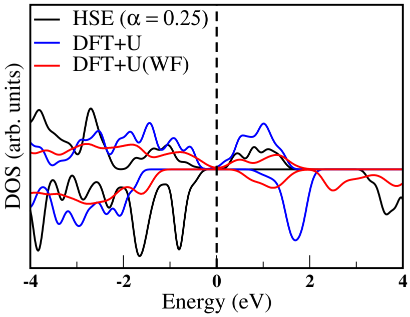

Figure 3.3: DOS of LNO computed with the HSE, DFT+U and DFT+U(WF) methods.

of d electrons computed in such a way is usually overestimated, often leading to the incorrect prediction of formation enthalpies and phase stabilities [160, 161]. The d-orbital occupations and the number of d electrons computed here with this method are reported in Tables 3.6 and 3.7. The number of d electrons is highly overestimated by at least $\sim 20\%$. For Mn in LNMC, the predicted number of d electrons is twice the expected one. I corrected this shortcoming with the application of WF as projectors. The procedure results in the expected occupations of d states (Table 3.7) and modification of the resulting DOS and band gaps. The computed band gap of LCO is 4.4 eV (3.5 eV with the rescaled U parameter, Table 3.5). With this correction, the band gap of LNO was opened by 0.2 eV.

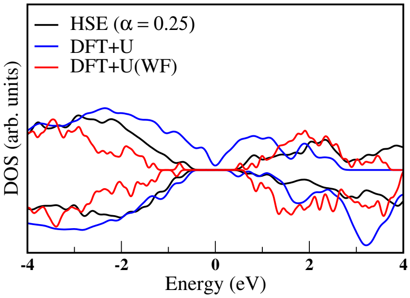

Figure 3.4: DOS of LNMC computed with the HSE, DFT+U and DFT+U(WF) methods.

System	band gaps (eV)	functional/Expt.	Ref.
LCO	2.7	Exp.	[246]
	2.8	PBEsol+U	This work
	2.4	PBEsol+U_{res}	This work
	4.4	PBEsol+U(WF)	This work
	3.4	PBEsol+U_{res}(WF)	This work
	4.1	HSE($\alpha = 0.25$)	This work
	2.2	PBE+U	[148]
	1.7	SCAN	[148]
	2.8	HSE($\alpha = 0.17$)	[189]
LNO	0.4	Exp.	[247]
	HM*	PBEsol+U	This work
	0.2	PBEsol+U(WF)	This work
	0.6	HSE($\alpha = 0.25$)	This work
	HM*	PBE+U	[148]
	HM*	SCAN	[148]
	0.9	HSE($\alpha = 0.18$)	[189]

*HM=half metal

Table 3.5: The band gaps of LCO and LNO compounds computed with different DFT functionals and methods, and measured. U_{res} means the calculations with the rescaled derived Hubbard U parameter (Table 3.3).

The occupations of the *d* states in the considered compounds obtained with the AOs and WF-based projectors are reported in Tables 3.6 and 3.8, respectively. The AOs result in significant fractional occupations of the empty states. Some empty states have significant occupations (e.g., for Mn ~ 0.6), which would indicate the occupation of these states. This often makes a correct assignment of the oxidation states impossible. Murphy et al. [161] have shown that this shortcoming leads to arise of spurious Hubbard energy term, which causes incorrect predictions of the most stable structures of mixed *d* and *f* cation-oxides by the DFT+U method.

Material	element	spin	d_1	d_2	d_3	d_4	d_5	mag. moment
LCO	Co	↑	0.481	0.481	0.955	0.955	0.955	0.00
		↓	0.481	0.481	0.955	0.955	0.955	
LNO	Ni	↑	0.863	0.988	0.997	0.998	0.999	1.16
		↓	0.317	0.384	0.992	0.997	0.997	
LNMC	Ni	↑	0.637	0.990	0.993	0.995	0.998	0.65
		↓	0.456	0.557	0.978	0.983	0.991	
	Co	↑	0.476	0.485	0.975	0.978	0.981	0.02
		↓	0.472	0.486	0.963	0.972	0.980	
	Mn	↑	0.610	0.628	0.989	0.997	0.998	2.57
		↓	0.223	0.238	0.278	0.449	0.457	

Table 3.6: The occupancies of 3*d* orbitals obtained with the AO-based projectors. The resulting magnetic moments are reported in the last column.

Material	AO	WF	ideal
LCO	7.7	6.0	6.0
LNO	8.5	7.0	7.0
LNMC:			
Co	7.7	6.0	6.0
Ni	8.5	7.0	7.0
Mn	5.7	3.0	3.0

Table 3.7: Total number of *d* electrons computed with the AO- and WF-based projectors for cations in LCO, LNO and LNMC compounds. The ideal, expected values are reported in the last column.

After applying the WF-based projection to the DFT+*U* scheme, the *d* orbitals are clearly either fully occupied or fully unoccupied, which is indicated with occupation numbers close to 1 or 0 (Table 3.8), respectively. The resulting occupancies allow for a clear assignment of the oxidation states. For instance, for Mn, the resulting electronic configuration shows 3 spin-up electrons, indicating Mn^{4+}. Furthermore, the oxidation states of the two other TMs in LNMC compound can be clearly confirmed to be $+3$.

Material	element	spin	d_1	d_2	d_3	d_4	d_5	mag. moment
LCO	Co	↑	0.002	0.002	0.993	0.993	0.993	0.00
		↓	0.002	0.002	0.993	0.993	0.993	
LNO	Ni	↑	0.020	0.985	0.989	0.991	0.997	0.97
		↓	0.005	0.032	0.989	0.994	0.995	
LNMC	Ni	↑	0.015	0.996	0.996	0.998	0.998	1.00
		↓	0.004	0.009	0.996	0.996	0.997	
	Co	↑	0.003	0.012	0.993	0.996	0.997	0.01
		↓	0.001	0.009	0.992	0.995	0.995	
	Mn	↑	0.006	0.007	0.993	0.997	0.997	2.98
		↓	0.001	0.002	0.004	0.004	0.006	

Table 3.8: The occupancies of 3*d* orbitals computed with the WF-based projectors. The resulting magnetic moments are reported in the last column.

Comparison of DOS computed with the DFT+*U*, DFT+*U*(WF) and HSE ($\alpha = 0.25$) methods (Figs. 3.2-3.4) leads to an interesting conclusion. In the case of LCO, the DFT+*U*(WF) method give DOS that is qualitatively consistent with the HSE result. The same is more clearly pronounced for LNO and LNMC compounds, for which the DFT+*U* method predicts a metallic state. The DFT+*U*(WF) and HSE approaches result in small band gaps and more consistent overall DOS distributions. This is an important result, given that the HSE method is significantly more computationally demanding than the DFT+*U*(WF) approach.

3.5 Voltage profiles of electrode materials

Voltage profile is one of the fundamental properties used to evaluate a particular material for its application as an electrode. This reveals, for example, the thermodynamic stability of different charged states, the ease of lithium intercalation or extraction, and the working potentials for a battery system. If accurately described by first-principles methods, a valuable, molecular-level insight into the properties that determine the cycle stability, energy density, and charge capacity of these materials in electrochemical systems could be obtained [148]. As explained in Chapter 1, the voltage profile is directly related to the internal energy, U_{int}, which can be computed from DFT. In this section, I extend the method previously employed to analyze the voltage profiles of $LiNiO_2$ (LNO) and $LiCoO_2$ (LCO) and compare the results to experimental data.

3.5.1 LNO

Over the past few decades, LNO has been considered as an alternative cathode material for rechargeable LIBs. This is because of its high availability and associated low cost, as well as safety and energy-density when compared to the commercial cobalt counterpart [67, 68]. There exist several first-principle studies on LNO (e.g., [153, 250–252]). However, DFT fails to correctly predict the electronic structure of these systems: the band gap is severely underestimated and oxidation states of cations are incorrectly described. The DFT+U method improves the materials description in the outlined aspects [160, 189]. However, even this correction can fail for the TM elements with multiple d-electrons, such as iron or nickel [160]. The description of d-electrons in nickel can be further improved by representing the orbitals with strongly correlated electrons with Wannier-type functions [160, 161, 199, 253]. Here, I have applied the rescaled Hubbard U parameter computed from the previous section for Ni in the layered rhombohedral ($R\bar{3}m$) structure and have carried out further voltage profile analysis.

In order to track the effect of delithiation, a series of Li_xNiO_2 compounds was computed with different Li concentration, namely with x=1.00, 0.75, 0.50, 0.25 and 0.00. The geometries were relaxed and the Hubbard U parameter was computed and rescaled for all the considered structures. Beyond the expected oxidation of Ni^{3+} into Ni^{4+} (three atoms at a time with increasing Li content), no disproportionation of Ni^{3+} into Ni^{2+} and Ni^{4+} species was observed during delithiation process, after wannierization scheme was applied. This suggests that the instability of Ni^{4+} reported in literature is due to other chemical forces during the synthesis of the material rather than to an inherent instability of the final structure itself [254]. The DFT+U(WF) method results in overall more stable structures, lower in energy by at least 10 kJ/mol, and the correct occupations of d orbitals, as in the case of NiO and CoO.

The intercalation voltage was estimated using the standard approach adapted from Equation

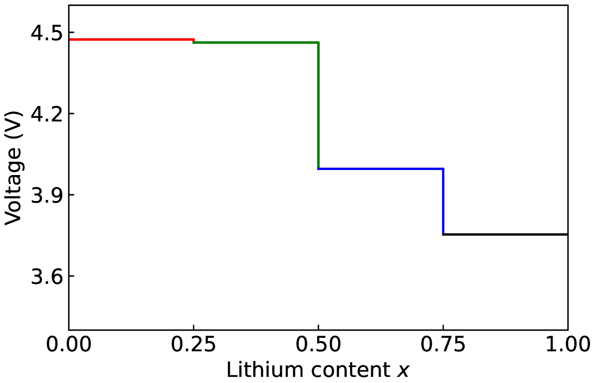

Figure 3.5: Computed specific voltage of Li_xNiO_2 as a function of Li content x.

1.15

$$V = -\frac{[E(\mathrm{Li}_{x+\Delta x}\mathrm{NiO}_2)] - [E(\mathrm{Li}_x\mathrm{NiO}_2) + \Delta x \cdot E(\mathrm{Li}_{\mathrm{bcc}})]}{\Delta x}, \tag{3.1}$$

with $\Delta x = 0.25$ as a step change of Li content, $E(\mathrm{Li}_x\mathrm{NiO}_2)$ the total energy per formula unit at Li content x, and $E(\mathrm{Li}_{\mathrm{bcc}})$ the total energy per formula unit of Li in the bulk material. As shown in Figure 3.5, the average calculated value of 4.17 eV is in good agreement with the measured value [255].

In order to test the performance of the applied method for predicting the formation enthalpy of LNO, I also computed the Li_2O and NiO compounds, and the molecular O_2. Assuming the following LNO formation reaction

$$0.5\,\mathrm{Li_2O} + \mathrm{NiO} + 0.25\,\mathrm{O_2} \longrightarrow \mathrm{LiNiO_2}, \tag{3.2}$$

the formation energy of LNO from oxide is estimated to be 65.12 kJ/mol. When the entropy of gas phase (oxygen) is considered ($S = 205$ J/mol·K at 293 K), the resulting free energy of formation is 50.31 kJ/mol, which is in good agreement with the measured value of 53.35 kJ/mol [235].

During the delithiation process, as a result of oxidation of Ni atoms, removal of Li causes a linear increase of the Hubbard parameter U (Figure 3.6). This dependence of the Hubbard U parameter on the oxidation state is consistent with previous studies [160, 194, 256]. The change in the oxidation state of Ni from +3 to +4 results in change in the DOS and the band gap (Figure 5.5), and in shortening of the Ni-Ni, Ni-O and O-O bond lengths, and increase of Ni-Li distances, as shown in Table 3.9. The cell parameters of the optimized supercell show excellent agreement with the crystallographic data.

It is worth noting that, while the applied Wannierization scheme contributes to the correct description of the oxidation states of Ni cations, it also replicates the small experimental band

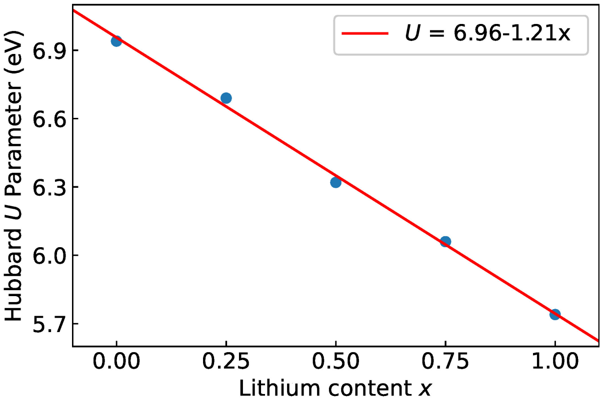

Figure 3.6: The Hubbard *U* parameter obtained with the linear response approach as a function of Li content for LNO. The linear fit to the data is presented in upper right corner.

gap of 0.4 eV in $LiNiO_2$ [190, 247], as indicated in Figure 3.7. On the other hand, in most of the computational studies, perfect-layered LNO has been reported as half-metal even with the computationally intensive hybrid functionals [148, 190, 247]. In the studies, the accurate computation of occupation of *d* orbitals was prioritized, as the changes in the oxidation state of Ni are crucial to correctly describe the delithiation process.

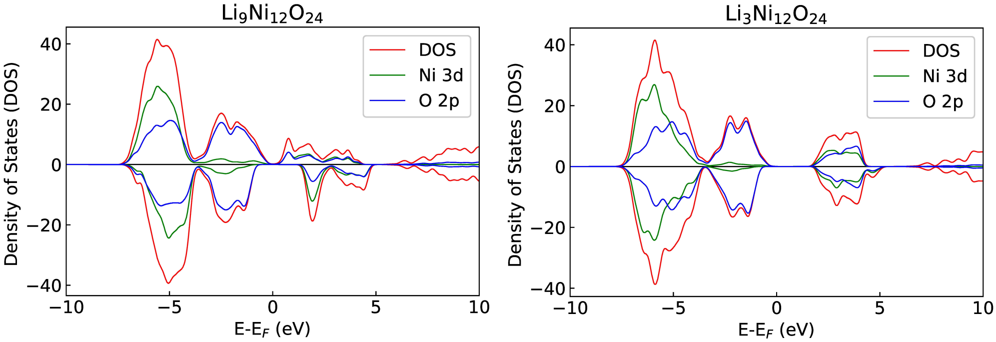

Figure 3.7: The partial and total DOS of Li_xNiO_2 with x = 0.75 (left) and 0.25 (right). The overlap between Ni *d*-bands and O *p*-bands is more pronounced upon delithiation, as expected.

3.5.2 LCO

Similar computations were performed for $LiCoO_2$ in the layered rhombohedral ($R\bar{3}m$) structure. I took the rescaled Hubbard *U* parameter value from the previous section, taking the optimal mixing parameter α for the exact Hartree-Fock exchange as a reference [189]. Applying the same computational approach as for LNO, I also computed the formation energy of LCO from oxides, following the reaction

Bond Type	Li content (x)	Distance (Å)
Ni-Ni	x = 1.00	2.8726
	0.75	2.8841
	0.50	2.8333
	0.25	2.8104
	0.00	2.7992
Ni-O	x = 1.00	1.9496
	0.75	1.9504
	0.50	1.9292
	0.25	1.8710
	0.00	1.8758
Ni-Li	x = 1.00	2.8917
	0.75	2.8920
	0.50	2.9181
	0.25	2.9677
	0.00	–
O-O	x = 1.00	2.9203
	0.75	2.8999
	0.50	2.8529
	0.25	2.8122
	0.00	2.7992
Cell Parameter	computed	exp.
a (Å)	2.873	2.880
c (Å)	14.214	14.180
V (Å^3)	101.58	101.86

Table 3.9: Different bond lengths computed for LNO compound (Li_xNiO_2) at different delithiation level. The experimental data are those of [257].

$$0.5\,\mathrm{Li_2O} + \mathrm{CoO} + 0.25\,\mathrm{O_2} \longrightarrow \mathrm{LiCoO_2} \tag{3.3}$$

the value of 128.50 kJ/mol was obtained. Though less accurate than the one obtained for LNO, the computed LCO formation enthalpy from oxides shows reasonable agreement with the experimental value of 140.18kJ/mol [235, 258].

3.6 Summary

In this chapter, I demonstrated the predictive power of parameter-free DFT+U methods, particularly methods combined with advanced projection techniques like WF, for studying the electronic structure and stability of ceramics used as battery electrodes. After carefully testing the methodology on simple oxide systems, I applied it to conventional cathode materials LCO and LNO, as well as more complex HEMs. This approach provided valuable insights into their structural parameters, electronic configurations, and redox behaviors. I found that the applied computational approach results in good predictions of the lattice parameters of all three materials, with accuracy exceeding those obtained in previous studies with the DFT+*U* or SCAN functional methods. This improvement is attributed to the use of the PBEsol exchange-correlation functional and the computation of the Hubbard *U* parameter value from first principles. The computed *U* values are close to the ones used in the previous studies, although I notice small variations in the values computed for the same cation in the different computed structures. This highlights the dependence of *U* on various factors, including the computational setup, the specific system under investigation, and the pseudopotentials employed [145]. The findings underscore the risks of adopting *U* parameter values from the literature without proper validation, emphasizing the advantage of a first-principles approach for ensuring consistency and accuracy.

One key challenge I addressed is the incorrect estimation of *d* state occupations when using AOs as projectors. This commonly used approach tends to overestimate the occupation of *d* orbitals, resulting in significant and spurious occupations of the empty states, making the assignment of the correct oxidation state to the cations difficult. These shortcomings are corrected with the application of WF as projectors. When applied to the computation of the electronic state of common battery materials, it predicts the band gap and DOS that are consistent with the results of more computationally intensive hybrid functionals. The results illustrate the capability of the DFT+*U*(WF) scheme to obtain an accurate description of the electronic configurations and oxidation states of electrochemically active cations in battery materials.

4 Computational insights into degradation pathways in high-entropy Li-rich cathodes

In this chapter, two Li-rich layered oxide (LLO) cathode materials that have multiple cations in their TM sites are studied, categorized as medium or high entropy compounds: $Li(Li_{0.2}Co_{0.18}Ni_{0.18}Mn_{0.44})O_2$ and $Li(Li_{0.2}Co_{0.18}Ni_{0.18}Mn_{0.18}Ti_{0.26})O_2$. The synthesized materials, however, experienced a large capacity degradation during the first charge/discharge cycle. I performed DFT calculations to understand the reason behind the capacity fading and discovered a few effects that led to significant structural changes during cycling in both systems. Specifically, a high concentration of Li/Ni interchange, TM ion migration to Li sites, and the formation of secondary phases have been observed. For the Ti-containing phase, which shows a larger capacity fade than the other system, the formation of a spinel phase has been identified. The computed enthalpies of secondary phase formation reactions are largely negative. However, the estimated (maximum) configurational entropy changes for these reactions are not sufficient to compensate for this effect. This study provides crucial insights into degradation mechanisms in Li-rich high-entropy systems, offering practical insights into how these challenges can be addressed when designing HEM battery electrodes.

This chapter is based on the research article: Y.-Y. Ting, B. Breitung, S. Schweidler, J. Wang, M. Eikerling, P. M. Kowalski, O. Guillon, and P. Kaghazchi. *Delithiation-induced secondary phase formation in Li-rich cathode materials*. J. Mater. Chem. A, 12, 33268–33276, 2024. doi: 10.1039/D4TA06030J. The computational work presented here was performed by myself under the guidance of Dr. Payam Kaghazchi. The experimental work was conducted by Dr. Junbo Wang and Dr. Simon Schneider from the Institute of Nanotechnology, Karlsruhe Institute of Technology.

4.1 Introduction

Building upon the advanced computational techniques and material testing discussed in Chapter 3, I now shift the focus to a deeper understanding of the practical challenges faced by high-entropy cathode materials. HEOs can be potentially promising alternatives to traditional cathode materials, as discussed in Chapter 1. Additionally, LLOs have been identified as another interesting cathode material [259, 260]. They can potentially provide a high capacity (over 250 mAh/g), making them attractive candidates for high-performance battery applications [261–263]. Unlike traditional cathodes in lithium batteries, which predominantly utilize the redox activity of TMs for electrochemical reactions, LLOs can offer a collective redox potential of both TMs and oxygen [264–266]. This synergistic approach enables them to achieve an exceptionally high capacity, surpassing what conventional cathode materials can provide. However, the structural instability of these materials exhibits non-negligible voltage decay over electrochemical cycling, presenting an obstacle to the practical application of LLOs.[267–270].

In this work, the potential synergy effects between the HE and LLO concepts have been investigated using a combination of computational and experimental techniques. Two LLO compounds were studied, namely $Li(Li_{0.2}Co_{0.18}Ni_{0.18}Mn_{0.44})O_2$ and $Li(Li_{0.2}Co_{0.18}Ni_{0.18}Mn_{0.18}Ti_{0.26})O_2$. These compounds were specifically chosen to represent different levels of configurational entropy, attributed to their varying concentrations of excess Li and TMs. The structures comprise consecutive layers of ...-Li-O-TM-O-Li-... along the c-axis (see Figure 3.1), with an excess of Li ions that are mixed with TMs in the TM sites: $(Li/Co/Ni/Mn)_{TM}$ and $(Li/Co/Ni/Mn/Ti)_{TM}$. The selection of Ti was based on previous research demonstrating its ability to stabilize the disordered state [134, 141, 271].

Applying the Equation 1.19, I have estimated the ideal configurational entropy for the synthesized compounds $Li(Li_{0.2}Co_{0.18}Ni_{0.18}Mn_{0.44})O_2$ and $Li(Li_{0.2}Co_{0.18}Ni_{0.18}Mn_{0.18}Ti_{0.26})O_2$ as 1.3 R and 1.6 R, respectively. Following the classification criteria established by Murty et al. [107], the first compound is identified as a medium-entropy LLO (hereafter called MELLO), while the second one meets the criteria for high-entropy LLO (hereafter called HELLO).

4.2 Methods

4.2.1 Computational details

The DFT setup is described in Section 2.3. In addition to PBEsol, a comparison with the PBE exchange-correlation functional [176] will be discussed. For the calculation of magnetic moments, the Hubbard-U correction was applied, with U values of 6.0, 3.4, and 3.9 eV for Ni, Co, and Mn respectively, following the reference [150]. I also calculated the electronic structure of the delithiated MELLO system employing the HSE06 hybrid functional [180]. I used a 2 $\times$ 2

× 2 k-point mesh, except for the hybrid functional calculation, for which a k-point mesh of 1 × 1 × 1 supplemented by a q-point mesh of 1 × 1 × 1 was used. The plane-wave cutoff energy and k-point mesh were selected to ensure proper convergence. To ensure the computed structures are converged to the magnetic ground state, I applied a systematic approach. Initially, I imposed a constraint on the total magnetic moment, calculated based on the most likely oxidation states (OS) of each TM. I then computed all possible total magnetization values corresponding to these OS. Once the system converged, I relaxed the constraint and recomputed the configuration to verify if it transitioned to a different magnetic state. Finally, I selected the configuration with the lowest total energy, confirming it as the magnetic ground state. The OS of each element was determined by counting the occupation in *d* orbitals. DFT+U(WF) (see Chapter 3) was applied to ensure the correct assignment of OS.

I modeled the MELLO system using 2 × 6 × 2 supercells comprising 192 atoms/cell with a space group of $C2/\mathrm{m}$ and 4 × 4 × 1 supercells containing 192 atoms/cell with a space group of $R\text{-}3\mathrm{m}$. This was to determine the most stable structure for this compound. Although the $C2/\mathrm{m}$ and $R\text{-}3\mathrm{m}$ structures do not have exactly the same TM configuration due to the different number of TM sites in these structures, I ensured that the short-range correlations (pair correlations) between TM atoms are very similar, allowing for a fair comparison of their relative stabilities. For the HELLO system, a 4 × 4 × 1 supercell was used, having 192 atoms/cell and a space group of $R\text{-}3\mathrm{m}$. To obtain the atomistic structure of LLO systems with Li/Ni interchanges and the low Li concentration of x=0.25, I performed total Coulomb energy calculations utilizing the 'SUPERCELL' code [204]. I selected the top three configurations with the lowest Coulomb energy and calculated them with DFT. The results confirm that the configuration with the lowest Coulomb energy is the most stable. Subsequently, I applied the DFT+U method with the PBEsol functional and HSE06 hybrid functional calculations to these configurations.

4.2.2 Materials synthesis

The medium-entropy oxide $Li(Li_{0.2}Co_{0.18}Ni_{0.18}Mn_{0.44})O_2$ and the high-entropy oxide $Li(Li_{0.2}Co_{0.18}Ni_{0.18}Mn_{0.18}Ti_{0.26})O_2$ were synthesized employing a modified Pechini method. $Co(CH_3COO)_2 \cdot 4H_2O$, $Ni(CH_3COO)_2 \cdot 4H_2O$, $Mn(CH_3COO)_2 \cdot 4H_2O$, titanium butoxide ($C_{16}H_{36}O_4Ti$), and excess (50%) $LiNO_3$ (all Sigma-Aldrich) were utilized as initial materials. Stoichiometric quantities of these materials were dissolved and dispersed in ethanol with citric acid and ethylene glycol (molar ratio = 1:4) under stirring to form a precursor. Following 4 hours of reaction with stirring and overnight drying, the mixtures were heated to 400 ℃ for 2 h, during which they swelled up and burned spontaneously, forming foamy masses as the temperature increased. The resulting black powder was pressed into pellets and calcined at 950 ℃ for 12 h in air. The final products were obtained by natural cooling to ambient temperature and kept inside an Ar-filled glovebox ($O_2 < 0.1$ ppm, $H_2O < 0.1$ ppm). The work was performed by experimental partners.

4.2.3 Electrode preparation

The experimental setup was performed by Dr. Junbo Wang and Dr. Simon Schneider from the Institute of Nanotechnology, Karlsruhe Institute of Technology. Cathodes were prepared by mixing oxide, Super C65 black carbon, and Solef 5130 polyvinylidene fluoride in a ratio of 7:2:1, uniformly dispersed in N-methyl-2-pyrrolidone. The slurry was then cast onto an Al current collector by doctor blading (200 µm slit size) and dried under vacuum at 120 ℃ for 12 h. The mass of the loaded active material on the dried foil was 2 to 3 mg cm^{-2}. Electrode discs of diameter 13 mm were punched from the cathode sheet and used as cathode electrodes for CR2032 coin cell assembly. The cells were assembled in an Ar-filled glovebox, using glass microfiber filter paper (GF/C, Whatman, Freiburg, Germany) as the separator, 1 M LiPF6 in a 3:7 weight mixture of ethylene carbonate:ethyl methyl carbonate (LP57, BASF SE, Ludwigshafen, Germany) as the electrolyte, and Li metal foil (Gelon LIB Co., Ltd.) as the counter electrode.

4.2.4 Cycling

Galvanostatic cycling tests were conducted by the experimental partners using a multichannel battery test system (CT2001A, Wuhan LAND Electronic Co., Ltd.). The voltage range was set to 2.0-4.8 V vs. Li+/Li, and the specific capacity was calculated based on the mass of the active material (1C = 250 mA/g).

4.2.5 X-Ray Diffraction

XRD patterns of powder samples were collected using a Bruker D8 Advance diffractometer with Cu-Kα ($\lambda = 1.5406$ Å) radiation source.

4.3 Results and discussion

Single-phase structures were observed in both synthesized MELLO and HELLO at elevated temperatures through XRD analysis conducted by the experimental partner from Karlsruhe Institute of Technology, as shown in Figure 4.1. The reflected peaks from the MELLO sample (Figure 4.1) can be indexed to either the rhombohedral structure with the *R*-3m space group or the monoclinic structure with the *C*2/m space group. A minor peak appearing in the range of 20° to 23° was identified as the characteristic peak of *C*2/m symmetry. To ascertain the most stable crystal structure for the simulation and analysis, I evaluated the total energy of both possible structures employing DFT-PBE, -PBEsol, -PBE+*U*, and -PBEsol+*U* methods (Figure 4.2). The total energy differences are normalized to the chemical formula of MELLO, $Li(Li_{0.2}Co_{0.18}Ni_{0.18}Mn_{0.44})O_2$, which consists of four atoms. All the functionals indicated that the

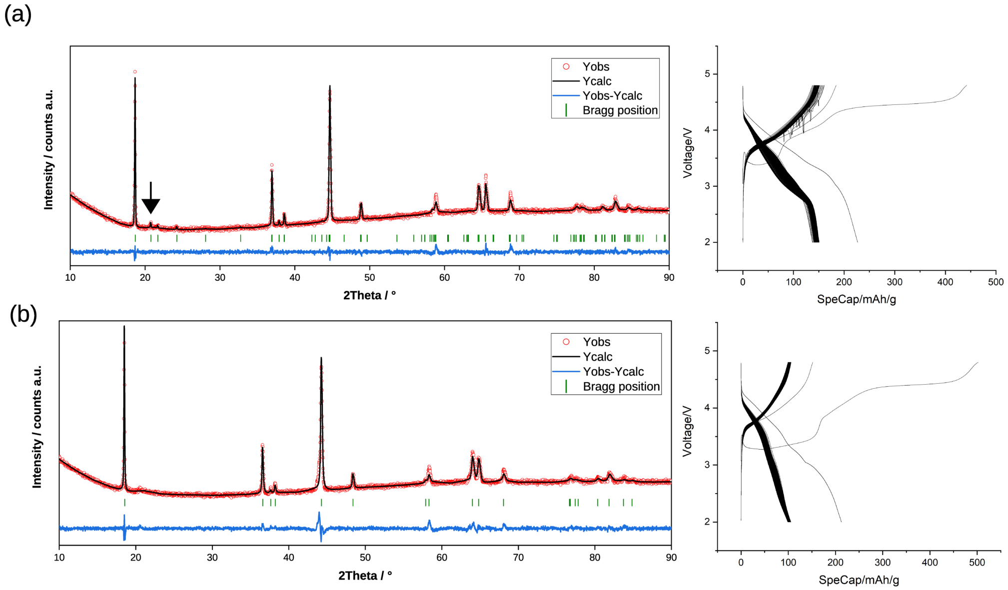

Figure 4.1: XRD patterns and voltage-capacity curves for (a) MELLO and (b) HELLO. The black arrow in (a) MELLO highlights the characteristic peaks of *C*2/m symmetry. The XRD pattern of (b) HELLO closely matches the *R*-3m space group.

monoclinic structure has a lower energy of around 2.1 meV/atom compared to the rhombohedral one. The small total energy difference between the two considered structures suggests a possibility for phase co-existence or transformation at room temperature. Hereafter, I focused on the most stable structure, according to DFT, namely the *C*2/m structure. The XRD pattern for the HELLO system (Fig. 4.1) indicates a rhombohedral structure with the *R*-3m space group.

Based on the Gibbs free energy equation ($\Delta G = \Delta H - T\Delta S$), the absolute value of the entropy term ($-T\Delta S$) increases with temperature. If the enthalpy of mixing (ΔH^{mix}) is low, the entropy term can then play a role in stabilizing the (disordered) single-phase structure. However, the enthalpy of formation for likely secondary phases might be so large that the ΔH^{mix} and $-T\Delta S$ terms become negligible.

The electrochemical test performed by the experimental partner (Figure 4.1) shows a large capacity fading after the first cycle, being larger in the case of HELLO compared to MELLO. This result most likely shows that these two compounds do not represent entropy-stabilized oxide (ESO) materials. To understand the reason behind large capacity fading in these two systems after the first cycle, I applied DFT calculations to study structural changes, defect formation, redox mechanism, and second phase formation.

Table 4.1 presents the computed lattice parameters (*a*, *b*, and *c*) for MELLO and HELLO. It

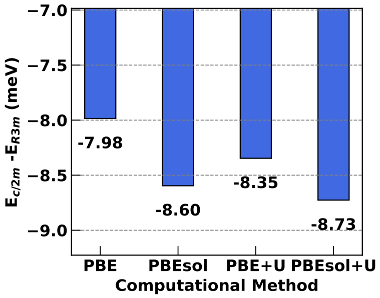

Figure 4.2: Computed energy difference between the rhombohedral (R-3m) and monoclinic (C2/m) structures for the MELLO system using DFT-PBE, -PBEsol, -PBE+U, and -PBEsol+U.

		a (Å)	b (Å)	c (Å)	α (°)	β (°)	γ (°)	vol. (Å^3)
MELLO	exp.	4.937	8.547	5.026	90.000	109.260	90.000	200.210
	PBEsol	4.962	8.608	5.011	90.096	108.882	90.005	202.117
	PBE	5.015	8.680	5.065	90.130	109.144	89.919	208.265
HELLO	exp.	2.875	2.875	14.326	90.000	90.000	120.000	102.560
	PBEsol	2.853	2.858	14.295	89.916	89.956	119.893	101.036
	PBE	2.886	2.866	14.861	90.739	89.021	120.071	106.371

Table 4.1: Experimental (exp.), DFT-PBEsol computed (PBEsol) and DFT-PBE computed (PBE) lattice parameters for LLOs.

is found that the PBEsol functional can reproduce the experimental a, b, and c values within 0.77%. The Ni/Li exchange (Ni_{Li}+Li_{Ni}), a common anti-site defect in the Ni-containing layered oxide materials, has been well documented in the previous experimental works [272, 273]. In the present study, the calculations show that HELLO has a higher tendency to form Ni_{Li}+Li_{Ni} as shown in Figure 4.3. The observed increase in energy gain for higher Ni/Li ratio in the presence of Ti cation can be attributed to its larger ionic radius (0.605 Å) relative to the other TMs such as Mn^{3+} (0.53 Å), Ni^{3+} (0.56 Å), and Co^{4+} (0.545 Å). This observation correlates with a larger O–TM–O intralayer separation in HELLO (2.18 Å) relative to MELLO (2.13 Å) for a Ni/Li concentration of 22%, as depicted in Figure 4.3, which provides more space for Li^+ ions (0.76 Å) within the lattice structure of HELLO. For further study, I selected the same Ni_{Li}+Li_{Ni} concentration of c=22.22% for MELLO and HELLO, to focus on the influence of elemental composition on other parameters such as oxidation and migration of ions.

The stability of MELLO and HELLO during electrochemical cycling was studied by analyzing their delithiated states, i.e. $Li_{0.25}(Co_{0.18}Ni_{0.18}Mn_{0.44})O_2$ and $Li_{0.25}(Co_{0.18}Ni_{0.18}Mn_{0.18}Ti_{0.26})O_2$, respectively. The low lithium concentration of 0.25 was chosen to study the extreme delithiation scenario. Following the geometry and unit cell optimization (using DFT-PBEsol) of the delithiated MELLO and HELLO, the formation of oxygen dimers was found, as shown in Figure 4.4. The presence of charged oxygen dimers ($O_2{}^{x-}$) has been reported in several previous studies on LLO systems [264, 274]. Given that the optimized structures might be confined to a local

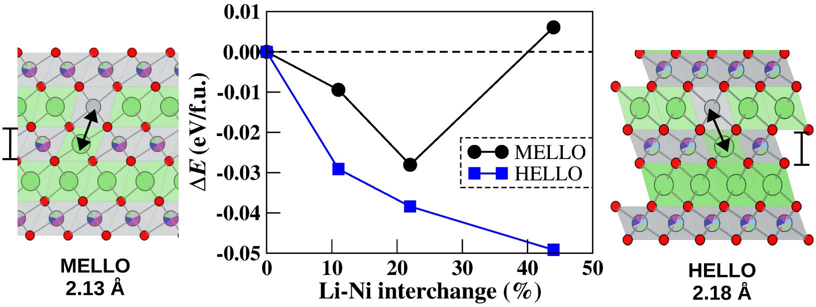

Figure 4.3: Visualization of O–TM–O intralayer separation in MELLO (2.13 Å) and HELLO (2.18 Å) for a Ni/Li concentration of 22%. Li/Ni interchanges are represented by black arrows as an example. The middle figure shows the Ni/Li interchange energy (with respect to the initial energies without interchange) for MELLO (left) and HELLO (right). The Ni/Li interchange concentration (expressed as a percentage) is calculated with respect to Ni concentration.

minimum, I further modeled additional oxygen dimers by manually adjusting the positions of isolated oxygen atoms in a sequential manner, followed by structural optimization to determine whether these manually induced dimers were energetically favorable or not. Detailed analysis, as illustrated in Figure 4.4, reveals that HELLO can have up to 10.4%, while MELLO up to 6.3% oxygen dimers. This leads to a larger delithiation-induced change in the OS of oxygen in HELLO compared to MELLO (see Table 4.2).

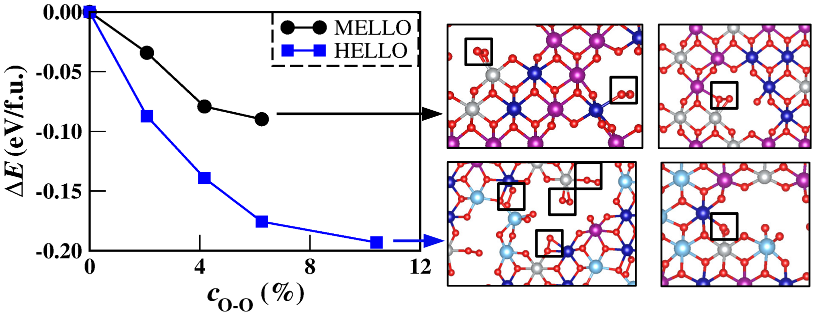

Figure 4.4: Left: Graph depicting the energy gain from O_2 dimerization as a function of O_2 concentration, expressed as a percentage of the total oxygen concentration within each compound for MELLO and HELLO systems. Right: Visual snapshots illustrating the O_2 dimers formed in MELLO (top two images) and HELLO (bottom two images).

I observed a partial migration of Ti to Li-layers and Mn to tetrahedral sites (between TM- and Li-layers) in the delithiated systems, which could potentially react with the oxygen dimers forming secondary phases. The migration of cations from TM sites to lithium sites during the delithiation process has been reported both experimentally and theoretically in several multicomponent LLO systems [275–279]. In the HELLO system, the extraction of Li from Li-layers, followed by extraction from TM-layers, provides free space for TM migration. As presented in Figure 4.5, HELLO systems exhibit significant Ti ion migration after delithiation. One reason could be the low energy penalty for Ti to distort/migrate due to its empty *d*-orbital [141] and relatively large ionic size. In the extreme delithiated state of x=0.25, 2% Mn migration from octahedral to tetrahedral sites was found.

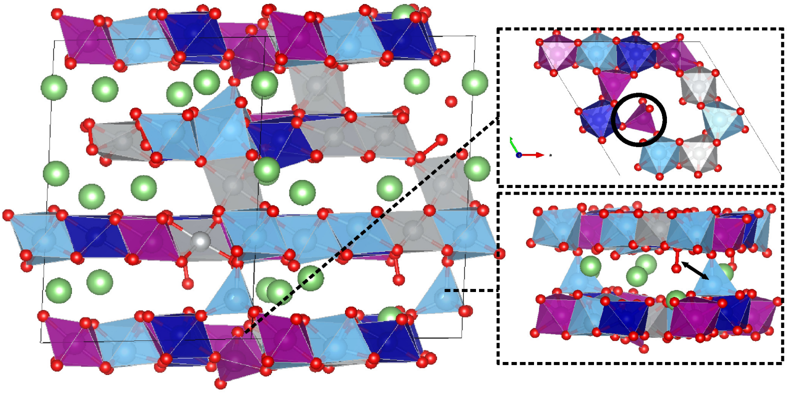

Figure 4.5: Schematic representation of cation migration during the delithiation process in the HELLO system. The upper-right figure shows the migration of Mn^{7+} to the tetrahedral site at low Li content, denoted by the black circle. The lower-right figure demonstrates the migration of Ti from the TM-layer to the Li layer, adjacent to an oxygen dimer. The migrated Ti atom proceeds to react with the oxygen dimer, culminating in the formation of a secondary phase as marked by the black arrow. The Li, O, Ti, Co, Ni, and Mn elements are represented by green, red, light blue, dark blue, gray, and purple spheres/polyhedra, respectively.

The concomitant occurrence of TM migration and oxygen dimer formation suggests a correlation where each phenomenon influences the other. I suggest that oxygen dimers reduce the activation barrier for TM migration by disrupting the TMO_6 octahedral structure, which facilitates TM mobility. Meanwhile, the migration of TM ions appears to have a significant impact on the oxygen redox process and subsequent dimerization. Gent et al. [275] suggests that TM migration triggers a substantial reorganization of electronic states, leading to an elevation of the energy levels of oxygen's projected density of states (pDOS). This reorganization enhances the reactivity involved in oxygen redox activities and fosters the dimerization of oxygen. Hence, TM migration and oxygen dimerization emerge as interlinked processes, each facilitating the other, and together influencing the electrochemical properties and stability of the material.

The OS was determined by examining the atomic magnetic moment and by analyzing the 3*d* occupation matrices for each atom. It is found that during the initial stage of delithiation when predominantly extraction of Li ions from the Li layers occurs, the charge neutrality is preserved by the oxidation of Ni^{3+} to Ni^{4+} and Co^{3+} to Co^{4+}. Further delithiation involves the extraction of Li ions from TM sites and TM migration, as well as the oxidation of Mn from +4 to +5. The depletion of Li in the TM layer, combined with vacancies created by TM migration, leads to unstable electrons on isolated oxygen atoms facilitating the formation of oxygen dimers. OS of +5 and +7 were found for Mn, with +5 in a distorted octahedral site and +7 in the tetrahedral site (see Figure 4.5). This finding is in line with other studies, which showed that MnO_4 tetrahedra can only be realized when the Li+ content is sufficiently low [280, 281]. These migrations underscore the critical impact on the stability and capacity retention of MELLO and HELLO, particularly in the latter case where more MnO_4 tetrahedra form.

	MELLO		HELLO	
	x=1.2	x=0.25	x=1.2	x=0.25
Ni	+3.00	+4.00	+3.00	+4.00
Co	+3.00	+4.00	+3.00	+4.00
Mn	+4.00	+4.93	+4.00	+4.97
Ti	-	-	+4.00	+4.00
O	-2.00	-1.91	-2.00	-1.83

Table 4.2: Calculated average OS using DFT-PBEsol for each element before and after delithiation (x=1.2 and x=0.25) in MELLO and HELLO systems.

Mn typically exhibits electrochemical activities with oxidation/reduction states of $Mn^{2+} \longleftrightarrow Mn^{3+} \longleftrightarrow Mn^{4+}$, providing a maximum of two electron transfers. The calculation shows the oxidation of Mn from +4 to +5/+7 occurring for x=1.2 $\rightarrow$ 0.25, which may be considered unrealistic. To address this, I reintroduced Li ions into the structures, adjusting the Li concentration from x=0.25 to x=0.83. I maintained i) migrated Ti and interchanged Ni (with Li) in the Li-layers, and ii) the formed O_2 dimers. The concentration of x=0.83 was chosen to achieve a more reasonable OS for Mn, which gives a capacity of $\sim$ 115 mAh/g for both systems. Interestingly, this value lies between the observed second cycle capacities of 150 mAh/g and 100 mAh/g for MELLO and HELLO, respectively (see Figure 4.1), underscoring the critical role of Mn in determining the reversible capacity of these compounds. The reintroduction of Li atoms did not affect the thermodynamic favorability of oxygen dimerization after DFT geometry relaxation. The previous experimental and theoretical works by other groups suggest both i) a reversible redox of oxygen in the form of single ion and/or charged dimer [282] as well as ii) an irreversible release of oxygen [260, 283].

Increasing the Li concentration from 0.25 to 0.83 leads to the reduction of highly oxidized Mn cations (with charges larger than 4+ oxidation). This shows the importance of oxygen redox, in particular in the form of O_2 dimer, in determining the capacity. The limited formation of oxidized oxygen in the form of dimer and single anion leads to the higher Mn OS for x=0.25. This is because of the specific composition of the studied compounds in this work. The computed charge states of ions for x=0.83 indicate oxidation of Ni, Co, and O compared to the pristine case of x=1.2 ((Table 4.3)). This shows that these elements are active during the charge/discharge process. Mn is slightly reduced in both HELLO and MELLO systems with x=0.83 compared to that with x=1.2 which can be attributed to the participation of oxygen in the redox mechanism.

The irreversible high first-cycle capacity (Fig. 4.1) in both systems can be due to the tendency of TMs to migrate from TM to Li sites and/or irreversibly O_2 formation. The migration of Ti cations to Li sites and increased O_2 dimer formation in HELLO contributes further to its capacity fading, making this fading more pronounced compared to MELLO. Migration of Ni, Mn, and Ti facilitated by O_2 formation might be the indication of layered-to-spinel phase transition, which has been proposed for Li-rich systems [284, 285]. This might explain why voltage and capacity decrease after the first cycle, which is in line with voltage fade primarily ascribed to the layered-to-spinel phase transition in the lattice structure of Li-rich electrodes [285, 286].

OS	MELLO		HELLO	
	before	after	before	after
Li	+1.00	+1.00	+1.00	+1.00
Ni	+3.78	+4.00	+3.72	+4.00
Co	+3.91	+3.40	+3.77	+3.50
Mn	+3.64	+4.00	+3.72	+4.00
Ti	-	-	+4.00	+4.00
O	-1.91	-1.94	-1.94	-1.95

Table 4.3: The OS for each element of the primary phase (with a Li concentration of 0.83) before and after the formation of thermodynamically favorable secondary phases, which are calculated in Table 4.4.

Afterwards, I investigated the formation of a few possible secondary oxide phases that might form besides the primary initial active phase during delithiation (charging) in both MELLO and HELLO systems. This was achieved by calculating the reaction enthalpies at 0 K for a series of probable reactions under the assumption that changes in zero-point energy and volume are negligible. A lithium concentration of x=0.83 was chosen to avoid the formation of unusual Mn OS higher than +4. The thermodynamically favored formation of 6.3% and 10.4% O_2 dimers, respectively, in MELLO and HELLO (see Fig. 4.4) was kept as well. The O_2 dimers or unstable oxidized oxygen ions from which the dimers form can react with the unstable TMs, in particular those that migrated from TM sites to Li sites. This can lead to the formation of the secondary phase comprising O and migrating TM atoms. The configuration of the primary phase after the reaction is constructed using SQS, in which the atomic distribution is selected based on pair correlations calculated from the configuration before the reaction, but with the migrated TM and oxygen atoms removed. This method captures the structural changes due to migration while still representing the system after secondary phase formation. These reactions and the corresponding changes of the primary phase in OS before and after the secondary phase formation are detailed in Tables 4.4 and 4.3. Reactions that are thermodynamically favorable, as indicated by negative enthalpy values, are predicted to occur spontaneously.

The calculations indicate that the formation of MnO_2 in MELLO and TiO_2 in HELLO is thermodynamically favored. As shown in Table 4.3, the OS of Ni and Mn increase in the primary phase following secondary phase formation, whereas those of Co and O decrease. This alteration in OS can result in a reduced activity of TM ions, especially for Ni and Mn, which generally provide a more reversible redox reaction than O. Consequently, secondary phase formation may limit the capacity of the materials. Notably, the decrease in TM activity is more significant in the HELLO system.

Reaction	ΔH (meV p.f.u.)
MELLO	
$Li_{0.83}Co_{0.18}Mn_{0.44}Ni_{0.18}O_2 \longrightarrow$	
$0.91Li_{0.91}Co_{0.20}Mn_{0.38}Ni_{0.20}O_2$ + 0.09 MnO_2	-171.0
$Li_{0.83}Co_{0.18}Mn_{0.44}Ni_{0.18}O_2 \longrightarrow$	
$0.875Li_{0.95}Co_{0.21}Mn_{0.36}Ni_{0.21}O_2$ + 0.125 MnO_2	140.0
$Li_{0.83}Co_{0.18}Mn_{0.44}Ni_{0.18}O_2 \longrightarrow$	
$0.91Li_{0.74}Co_{0.20}Mn_{0.38}Ni_{0.20}O_2$ + 0.09 $LiMnO_2$	199.6
HELLO	
$Li_{0.83}Co_{0.18}Mn_{0.18}Ni_{0.18}Ti_{0.26}O_2 \longrightarrow$	
$0.87Li_{0.95}Co_{0.21}Mn_{0.21}Ni_{0.21}Ti_{0.15}O_2$ + 0.13 TiO_2	-69.6
$Li_{0.83}Co_{0.18}Mn_{0.18}Ni_{0.18}Ti_{0.26}O_2 \longrightarrow$	
$0.92Li_{0.82}Co_{0.20}Mn_{0.20}Ni_{0.20}Ti_{0.20}O_2$ + 0.08 $LiTiO_2$	251.3
$Li_{0.83}Co_{0.18}Mn_{0.18}Ni_{0.18}Ti_{0.26}O_2 \longrightarrow$	
$0.87Li_{0.91}Co_{0.21}Mn_{0.21}Ni_{0.21}Ti_{0.15}O_2$ + 0.09 TiO_2 + 0.04 $LiTiO_2$	35.8

Table 4.4: Calculated reaction enthalpies ΔH (meV per formula unit p.f.u.) at 0K for likely reactions leading to the formation of secondary phases in MELLO and HELLO systems.

The enthalpy changes in the secondary phase formation reactions are more significant than the entropy changes. I assume that the vibrational and electronic entropy contributions are negligible due to the structural similarity of the primary phase before and after the secondary phase reaction. The configurational entropy changes for secondary phase formation reactions at room temperature, $T\Delta S_{conf}$, for the thermodynamically favorable reactions listed in Table 4.4, are -1.1 meV and -0.07 meV p.f.u. for MELLO and HELLO, respectively. Notably, the negative reaction entropy values indicate that the entropic contribution even slightly favors the formation of the secondary phase.

The formation of secondary phases is closely linked to TM vacancies, which result from the extraction of lithium and the migration of TMs, as well as the process of oxygen dimerization. Consequently, secondary phases can only form during the cycling process when Li is removed from the TM sites. A greater amount of secondary phase formation is expected in HELLO compared to MELLO due to its higher oxidation of O in the form of O_2 dimers. The last reaction in Table 4.4, namely the formation of $LiTiO_2$ together with TiO_2, with a small positive enthalpy of 35.8 meV per formula unit, may still be kinetically driven at room temperature for the HELLO system. This is because the energy associated with molecular motion at this temperature is approximately 26 meV, and computational uncertainties must also be considered. Therefore, a larger amount of inactive secondary phases is expected to form in HELLO compared to the MELLO system.

To further investigate the effect of Ni/Li anti-site defects, I performed calculations with a higher Ni/Li interchange concentration of $c = 44.44\%$ for HELLO at lithium concentrations of 0.25 and 0.83. I still observed TM migration and dimer formation under these conditions. The structure with Ni/Li interchange $c = 44.44\%$ was found to be more unstable than the structure with

$c = 22.22\%$ at the same lithium concentration, suggesting that increasing the Ni/Li interchange concentration makes the highly delithiated state more unstable. Furthermore, when the Ni/Li interchange concentration is $c = 44.44\%$, the secondary phase reaction becomes even more favorable, with an enthalpy of -75.8 meV p.f.u., indicating increased instability in HELLO. These results further support the mechanism proposed in this study.

Figure 4.6 shows the overview of the degradation mechanism. During cycling, the formation of irreversible oxygen dimers, spinel phases, and/or secondary phases may occur. These phenomena, particularly during the first cycle, lead to a significant capacity decrease in both MELLO and HELLO. The higher concentration of migrated TM cations, O_2 formation, and secondary phase formation, as well as the layered-to-spinel phase transition in the form of $LiTiO_2$, might explain the larger capacity fading in the HELLO system.

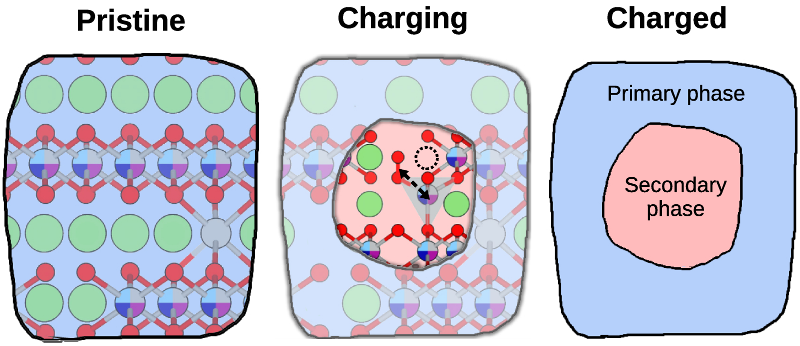

Figure 4.6: The proposed sequential stages of degradation during charging (delithiation). In the pristine stage, Li/Ni interchange was found. During the charging process, the lithium ions are extracted from the Li layers and the TM layers, leading to the oxygen dimerization and TM migration. Subsequently, oxygen dimers react with the migrated TM ions, leading to the formation of the secondary TMO_2 phase. Oxygen atoms are denoted by red circles, while lithium atoms are represented by green circles. The multi-colored circles represent a mixture of various cationic species present in the system.

4.4 Summary

In this chapter, I characterized two multi-doped LLO systems to explore their structural and electrochemical properties using DFT. I observed a preferential Ni/Li interchange in both LLOs, with a higher tendency for the process to occur in the presence of larger ionic radius cations, namely Ti. Furthermore, I found simultaneous oxygen dimer formation and TM migration during delithiation. The formation of dimers is attributed to the removal of Li at TM layers as well as to the TM vacancies created by the TM migration, which results in isolated unstable oxygen anions. This phenomenon is particularly observed under conditions of extreme delithiation. Partial oxygen dimerization and TM migration contribute to the observed irreversible capacity loss, correlating with the concentration of formed oxygen dimers.

I further investigated the tendency for secondary phase formation. The findings indicate a thermodynamically favorable mechanism for this process. The secondary phase formation can be viewed as a reaction product between unfavorably oxidized oxygen anions and TM cations that are not stable at TM sites during cycling. The calculations show that the formation of secondary phases, such as MnO_2 and TiO_2, decreases the overall activity of TM cations in the primary phase. Due to this and the likely lower electronic and ionic conductivity of secondary phases, their formation can reduce the capacity of these materials. In particular, I found a formation of a spinel $LiTiO_2$ phase in the system with the largest capacity fading.

I examined the implications of the high-entropy effect on material stability. The analysis indicates that entropy does not play a role in stabilizing these materials during the cycling process. Notably, HELLO, despite its higher theoretical configurational entropy, exhibits even poorer stability. This observation suggests that a simple increase in the configurational entropy by integrating a large number of various elements does not necessarily improve cyclability. Furthermore, the investigation suggests that the increased disorder inherent in high-entropy systems may intensify certain undesirable phenomena during cycling, such as oxygen dimerization and TM migration. These effects can lead to phase transitions, structural decomposition, and secondary phase formation. This indicates that while the high-entropy approach contributes to the stabilization of disordered phases, it can also potentially worsen certain destabilizing processes during electrochemical cycling. Thus, when evaluating the benefits of "high-entropy" materials, it is crucial to balance the gains in entropy-driven stability against the potential for increased disorder-related instabilities such as oxygen dimerization and TM migration.

5 Atomic configurations and thermodynamics in high-entropy electrolytes

This chapter explores multi-component, high-entropy garnet electrolytes for all-solid-state Li batteries. Specifically, I focus on the design of garnet-based HEMs with enhanced structural stability and ionic conductivity. Through a series of computational studies, I used DFT to study the increasing number of doping elements in garnet $Li_7La_3Zr_2O_{12}$, which raises its configurational entropy, then selected dopant sets that maximize thermodynamic stability. The impact of various atomic configurations on the structural stability of the garnet is studied by the SQS method and by Coulomb-energy minimization. The experimental partners synthesized the predicted compositions and measured the ionic conductivity between different compounds with varying dopant levels. The combined results provide valuable insights into the impact of atomic distribution on enthalpy, and the role of entropy in structural stabilization of multi-doped LLZO.

The research presented in this chapter is based on two articles: Y.-Y. Ting, R. Ye, E. Dashjav, Q. Ma, S. Taminato, D. Mori, N. Imanishi, M. Finsterbusch, M. H. Eikerling, O. Guillon, P. Kaghazchi, and P. M. Kowalski. *Thermodynamic and structural characterization of high-entropy garnet electrolytes for all-solid-state battery*. Front. Energy Res., 12, 2024. doi: 10.3389/fenrg.2024.1393914 and R. Ye, Y.-Y. Ting, E. Dashjav, Q. Ma, S. Taminato, D. Mori, N. Imanishi, P. M. Kowalski, M. H. Eikerling, P. Kaghazchi, M. Finsterbusch, and O. Guillon. *Preparation and electrochemical properties of* $Li_6La_3Zr_{0.7}Ti_{0.3}Ta_{0.5}Sb_{0.5}O_{12}$ *high-entropy Li-garnet solid electrolyte*. Front. Energy Res., 12, 2024. doi: 10.3389/fenrg.2024.1379576. The conceptualization and computational calculations were performed by myself, with guidance from Dr. Kowalski and Dr. Kaghazchi. The experimental work was conducted by Dr. Ye from IMD-2 (formerly IEK-1), Forschungszentrum Jülich.

5.1 Introduction

In Chapter 4, I demonstrated that while the high-entropy effect contributes to the stabilization of disordered phases in HEMs, the cycling instabilities arising from disorder remain a critical factor to address. The careful selection of dopants plays a pivotal role in mitigating these instabilities. Building on this foundation, this chapter shifts focus to the development of solid electrolytes for solid-state batteries (SSBs), which were introduced in Chapter 1. One of the challenges to utilize SSB is to find a suitable material as solid electrolyte that provides stability and high ionic conductivity. To address this, I aim to design a potential solid electrolyte, with a careful dopant selection that minimizes the disorder-related instabilities.

Among potential solid electrolytes, lithium lanthanum zirconium oxide $Li_7La_3Zr_2O_{12}$ (LLZO) is one of the candidates [289]. LLZO exists in two phases: a tetragonal phase with an $I4_1/acd$ space group and a cubic phase with an $Ia\bar{3}d$ space group [80, 81]. These are illustrated in Figure 5.1. The ionic conductivity of the tetragonal phase is an order of magnitude lower than that of the cubic phase. This is due to the ordered distribution of Li ions across the *8a* (Li1), *16f* (Li2), and *32g* (Li3) sites in the tetragonal phase, which increases the energetic cost of ionic diffusion [290]. In contrast, the cubic phase features a disordered sublattice of Li ions and Li vacancies at *24d* tetrahedral sites (Li1 site) and *48g/96h* octahedral sites (Li2 site), facilitating lower diffusion costs. Despite this, the tetragonal phase is more stable at room temperature due to the electrostatic repulsion between adjacent lithium positions at *96h* sites in the cubic phase, making it energetically less favorable as lithium concentration increases [291]. This structural instability in the cubic phase can be addressed by doping with supervalent cations to increase the amount of Li vacancies as well as configurational entropy, thereby reducing Gibbs free energy and diminishing Li-Li repulsion. Alternatively, the cubic phase LLZO could be stabilized and synthesized at higher temperatures above 650 °C.

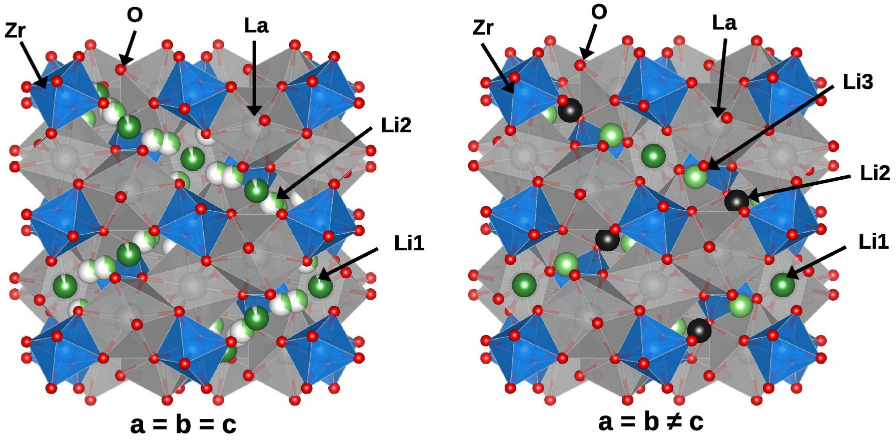

Figure 5.1: Illustration of LLZO crystal structures: cubic phase (left) and tetragonal phase (right).

Atomistic modelling is a useful tool to decipher the role of enthalpy and entropy in disordered multi-compound materials [113, 114]. For these calculations, correct input structures are essential to correctly calculate the thermodynmic properties. However, the description of lithium vacancy distribution in computational studies on LLZO has been notably inconsistent. For example, [292] reported a distribution of 13 Li atoms at the Li1 site and 43 at the Li2 site. Conversely, [293] filled the 24*d* site completely, distributing the remaining Li ions randomly within the center of the 48*g* site. This inconsistency is mirrored in experimental studies, where the exact occupancy of Li at these sites remains a subject of debate, often because of the limitations of techniques like X-ray diffraction (XRD) and nuclear magnetic resonance. For instance, [294] determined the occupancies at Li1 and Li2 sites to be 0.94 and 0.35, respectively, while [295] found them to be 0.56 and 0.44 using neutron diffraction.

To address these challenges and design a multi-doped LLZO with high cubic-phase stability, I first compare various configurations (e.g., constructed using the Minimization of Coulombic Energy approach and special quasirandom structures, or SQS) to identify the most accurate and representative structural models for DFT analysis. This enhances the reliability of computational predictions regarding LLZO's thermodynamic properties. Using the selected model, I predicted the structural stability of various doped-LLZO compositions. These were then synthesized by the experimental partners, and their electrochemical performance was evaluated experimentally.

5.2 Methods

5.2.1 Computational approach

The computational setup is detailed in Section 2.3. For thermodynamic calculations, the PBE exchange-correlation functional was applied [176], while structural parameters were calculated using the PBEsol exchange-correlation functional [177]. The supercell unit was set as $Li_{56}La_{24}Zr_{16}O_{96}$ for pure LLZO. Calculations were performed with a 4 × 4 × 4 Monkhorst-Pack k-point mesh [234] to ensure convergence.

The investigated systems were based on cubic-LLZO (*c*-LLZO) with space group *Ia-3d* and tetragonal-LLZO (*t*-LLZO) with space group $I4_1/acd$. In pure LLZO, both structures feature 8-fold coordinated La sites and 6-fold coordinated Zr sites. The Li sites differ between these two crystal structures. In *c*-LLZO, Li occupies tetrahedral 24*d* (Li1 site) and octahedral 96*h* (Li2 site), as depicted in Figure 5.2a. In *t*-LLZO, there are three Li sites: tetrahedral 8*a* (Li1), and two groups of octahedral sites, 16*f* (Li2) and 32*g* (Li3), shown in Figure 5.2b. In the initial DFT structure of *c*-LLZO, Li distribution is considered at positions 24*d* and 48*g*, with post-relaxation displacement to 96*h* (Figure 5.2c).

In the calculations, various dopants were selected to investigate their entropic effects, with

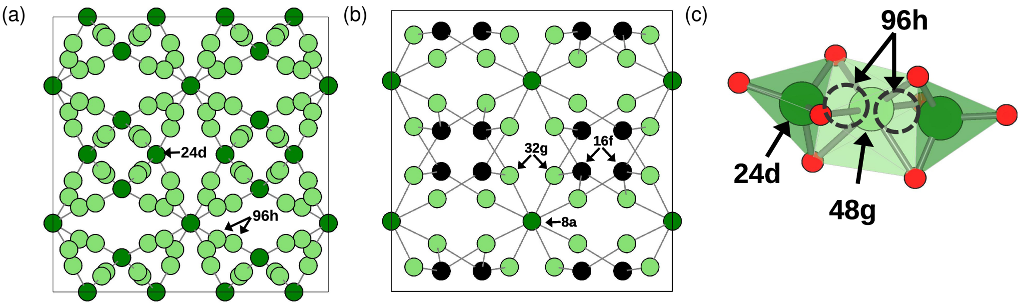

Figure 5.2: Li sublattice in LLZO phases. (a) Li distribution in *c*-LLZO. (b) Li distribution in *t*-LLZO. (c) Li site at 96*h* is displaced from 48*g* in *c*-LLZO in the DFT initial structure.

compositions detailed in Table 5.1. Starting from LLZO, the composition of HEG1 was determined by partially replacing Zr^{4+} with A^{5+} element, reducing the Li number from 7 to 6 to induce more Li-vacancies and consequently higher configurational entropy. The number of Li atoms was kept constant in subsequent compositions. This enabled us to focus on the investigation of entropic contribution from the dopant concentration. In HEG2, alongside A^{5+}, partial Zr^{4+} was substituted with B^{5+} and C^{4+}. HEG3 involved further replacement of partial La^{3+} with D^{3+}, gradually increasing configurational entropy.

Name	Chemical formula	OS of cations
LLZO	$Li_7La_3Zr_2O_{12}$	Li^+, La^{3+}, Zr^{4+}
HEG1	$Li_6La_3ZrAO_{12}$	A^{5+}
HEG2	$Li_6La_3Zr_{0.5}A_{0.5}B_{0.5}C_{0.5}O_{12}$	B^{5+}, C^{4+}
HEG3	$Li_6La_{1.5}D_{1.5}Zr_{0.5}A_{0.5}B_{0.5}C_{0.5}O_{12}$	D^{3+}

Table 5.1: The chemical composition of investigated LLZO compounds and the oxidation state (OS) of the dopants.

Element distribution in multi-doped LLZO was categorized into Li-vacancy and metal-ion sublattices. Two methodologies were utilized: the SQS and a Coulomb-energy-based approach. When species share the same oxidation number, I preferentially selected structures with higher symmetry for the Coulomb-energy-based approach. This strategic choice is underpinned by insights suggesting that structural symmetry plays a role in enhancing stability. Specifically, symmetry in a structure can lead to a reduction in the system's degrees of freedom and overall energy, making the structure inherently more stable [296]. I calculated the 50 structures with the lowest Coulomb energies using DFT and chose the one with the minimum computed energy for the analysis.

With two sublattices of element distribution and two methodologies, I explored element distribution in four distinct ways: i) both sublattices using SQS; ii) both using the CE-based method; iii) one sublattice via SQS and the other through CE-based method; iv) the inverse of arrangement iii. These configurations are referred to as $\mathrm{Li}_{\mathrm{SQS}}/M_{\mathrm{SQS}}$, $\mathrm{Li}_{\mathrm{CE}}/M_{\mathrm{CE}}$, $\mathrm{Li}_{\mathrm{SQS}}/M_{\mathrm{CE}}$, and $\mathrm{Li}_{\mathrm{CE}}/M_{\mathrm{SQS}}$, respectively, where 'Li' refers to the Li-vacancy sublattice and '*M*' to the metal-ion sublattice.

In calculating configurational entropy, Li-site vacancies are treated as distinct species. Notably, in *c*-LLZO's cubic phase, despite Li occupying 96*h* positions, the placement of two Li atoms in adjacent sites is energetically unfavorable, so the 96*h* can be treated as 48*g*. This reduces the site count from 96*h* to 48*g* (Figure 5.2c). Thus, for configurational entropy calculations in the cubic phase, the total number of Li sites is considered to be 72, with 24 at Li1 and 48 at Li2 sites. The Li concentration in tetragonal and cubic phases is calculated based on the distribution of Li atoms over available sites.

5.2.2 Experimental approach

The high-entropy garnets (HEGs) were synthesized by conventional solid-state reaction by Dr. Ye from IMD-2, Forschungszentrum Jülich. The starting materials Li_2CO_3, $La(OH)_3$, ZrO_2, TiO_2, Ta_2O_5, Sb_2O_5, and Nd_2O_3 were mixed in stoichiometric amounts with 5 wt% Li_2CO_3 in excess by ball-milling in hexane. After dried, the powder was placed on a gold sheet inside an alumina crucible for calcination at 850 ℃ for 12 h in air. After cooling down, the calcined powder was ball-milled again in hexane. The fine powder was pressed to form pellets at 13.7 MPa by using uniaxial hydraulic press, and the pellets were subsequently pressed at 150 MPa in an isostatic press. The obtained pellets were sandwiched between two gold sheets and sintered in an alumina crucible, and sintered in air at 1050 ℃ for 12 h. The sintered pellets were collected and stored in the Argon-filled glovebox.

The samples were characterized for their phase purities by XRD on a Bruker D4 Endeavor device (Bruker, Germany) using Cu Kα radiation equipped with a 1D detector LynxEye. The qualitative phase analyses were done using Panalytical's HighScore software, and LeBail profile fitting for lattice parameters of the investigated samples were carried out using the software `Jana2006` based on the structure model in the cubic space group of *Ia-3d* (ICSD 158372).

The Li-ion conductivities of HEGs were measured by electrochemical impedance spectroscopy (EIS). Prior to the EIS measurements, the HEGs pellets were polished on 400, 800, 1500 and 4000 grid sandpapers, and sandwiched by two lithium metal foils with a diameter of 6 mm. Such Li|HEG|Li symmetric assembly was then sealed in a pouch bag with two Ni bars as current collectors for the EIS measurements. EIS was measured in the frequency range from 10 MHz to 1 Hz with an electrical field perturbation of 50 mV using an impedance analyzer by Novocontrol Technologies, or in the frequency range from 1 MHz to 0.1 Hz with an electrical field perturbation of 10 mV using a frequency response analyzer by Solartron Analytical. A fitting of the impedance spectrum was conducted in the software ZView (Scribner) to obtain bulk conductivity.

5.3 The effect of atomic distribution on thermodynamic properties prediction

5.3.1 Dopant selection

Table 5.2 lists the studied dopants, their ionic radii [297] and reported doping positions from prior studies. Dopant selection was based on the similarity of their ionic radii to either Zr^{4+} or La^{3+} and their doping positions. The formation enthalpies from oxides ($\Delta H_{f,ox}$) of the considered compounds were calculated using total DFT energies of reactants and products. I then selected those with the lowest $\Delta H_{f,ox}$ for further evaluation. Atomistic structures of products in the cubic phase were generated using SQS. For HEG1, HEG2, and HEG3, $\Delta H_{f,ox}$ was determined by the energy difference between reactants and products, as described in the following reaction:

$$3\,\mathrm{Li_2O} + \frac{3\text{-x}}{4}\,\mathrm{La_2O_3} + \frac{x}{2}\,D_2\mathrm{O_3} + (2\text{-y-z-w})\,\mathrm{ZrO_2} + \frac{y}{2}\,A_2\mathrm{O_5} + \frac{z}{2}\,B_2\mathrm{O_5} + w\,C\mathrm{O_2} \\ \longrightarrow \mathrm{Li_6La}_{3-x}D_x\mathrm{Zr}_{2-y-z-w}A_yB_zC_w\mathrm{O_{12}}.$$

The results in Figure 5.3 show that Sb has the lowest formation enthalpy among the elements considered for element A in $Li_6La_3ZrAO_{12}$, leading to the identification of HEG1 as $Li_6La_3ZrSbO_{12}$. For HEG2, Ta/Ti combination was slightly more favorable by 5 kJ/mol compared to the Nb/Ti combination. Hence, HEG2 was considered as $Li_6La_3Zr_{0.5}Sb_{0.5}Ta_{0.5}Ti_{0.5}O_{12}$. Nd was chosen as the dopant D in HEG3 based on its thermodynamic stability. Notably, Sb-doped LLZO (HEG1) demonstrated the lowest $\Delta H_{f,ox}$ relative to HEG2 and HEG3. A subtle change in $\Delta H_{f,ox}$ was observed when transitioning from three-element-doped HEG2 to four-element-doped HEG3. This trend suggests that careful dopant selection leads to minor changes in $\Delta H_{f,ox}$, but enhancing the configurational entropy (ΔS_{conf}) with the addition of more dopant types.

Dopant	La site	Zr site	Ionic Radii (Å)	Reference(s)
La^{3+}	x		1.16	
Zr^{4+}		x	0.72	
Nb^{5+}		x	0.64	[124, 126, 298]
Sb^{5+}		x	0.6	[299]
Ta^{5+}		x	0.64	[126, 300]
Ge^{4+}		x	0.53	[301]
Ti^{4+}		x	0.605	[124, 302]
Te^{4+}		x	0.97	[303]
Sm^{3+}	x		1.079	[304]
Nd^{3+}	x		1.109	[124, 305]

Table 5.2: List of considered dopants and their ionic radii, with references from a comprehensive database [297].

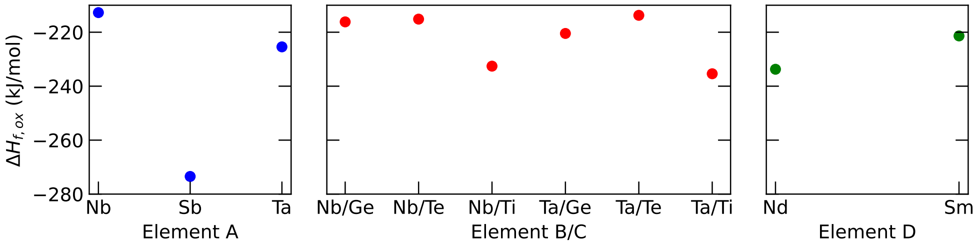

Figure 5.3: Computed formation enthalpies from oxides ($\Delta H_{f,ox}$) for selected dopants. The dopants with the lowest $\Delta H_{f,ox}$ were chosen, namely Sb, Ta, Ti, and Nd for *A*, *B*, *C*, and *D* dopants, respectively. For reference, the experimental $\Delta H_{f,ox}$ value for *t*-LLZO is -168.0 kJ mol^{-1} [306].

Following the computational predictions, the experimental partners proceeded with the synthesis of the compounds. HEG1, with composition $Li_6La_3ZrSbO_{12}$, was successfully synthesized in a cubic phase. However, challenges emerged during the electrochemical performance assessment of HEG2. A potential issue identified was the high titanium content in HEG2, which might cause a reduction of Ti^{4+} to Ti^{3+}, leading to a transformation of the garnet from an electrical insulator to a conductor. To address this problem, the composition of HEG2 was modified, reducing the Ti content by 50% and switching from $Li_6La_3Zr_{0.5}Sb_{0.5}Ta_{0.5}Ti_{0.5}O_{12}$ to $Li_6La_3Zr_{0.75}Sb_{0.5}Ta_{0.5}Ti_{0.25}O_{12}$, adjusting the Zr content correspondingly. For HEG3, the mole fraction was maintained in the Zr-sublattice and Nd doping was introduced to the La-sublattice. This resulted in the $Li_6La_{1.5}Nd_{1.5}Zr_{0.75}Sb_{0.5}Ta_{0.5}Ti_{0.25}O_{12}$ model compound.

5.3.2 Effect of Li distribution on structural relaxation

The distribution of elements in the cubic phase was modelled in four distinct ways, as described in Section 5.2.1: $\mathrm{Li_{SQS}}/M_{\mathrm{SQS}}$, $\mathrm{Li_{CE}}/M_{\mathrm{CE}}$, $\mathrm{Li_{SQS}}/M_{\mathrm{CE}}$, and $\mathrm{Li_{CE}}/M_{\mathrm{SQS}}$. The computed enthalpies illustrated in Figure 5.4 provide insights into the relative stability and phase preference across these different distribution methods. Contrary to my initial expectations, the $\mathrm{Li_{CE}}/M_{\mathrm{CE}}$ atomic distribution resulted in the highest computed energies (enthalpies) for all three compounds, indicating the lowest stability with such arrangement. On the opposite, the $\mathrm{Li_{SQS}}/M_{\mathrm{SQS}}$ method resulted in the lowest energy, suggesting the fully disordered structure as the most stable one for each of the considered compounds. I note that this is in contrast to a common expectation of disordered compounds having higher formation enthalpies than ordered compounds with identical stoichiometry [114]. After structural relaxation, I assessed lattice parameters and the position of Li to determine if the structures were in cubic or tetragonal phases. I emphasize the importance of examining the Li position since the lattice parameters for relaxed structures can vary even in the cubic phase. I note that Li-vacancy distribution could influence phase stability, particularly when the number of dopant elements is low. For example, the HEG1 structure that was determined from electrostatic calculations ($\mathrm{Li_{CE}}/M_{\mathrm{CE}}$) transitioned from cubic to tetragonal phase during the relaxation, while HEG2 and HEG3 maintained their cubic phase.

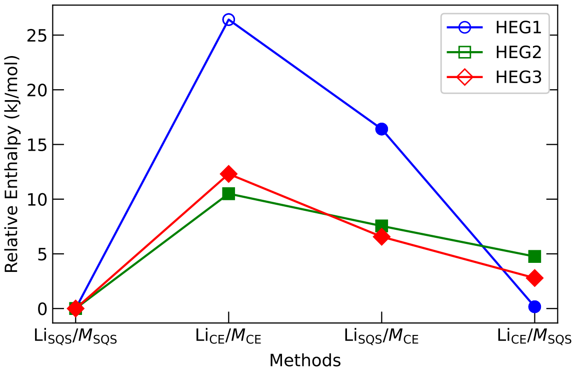

Figure 5.4: Computed energy (enthalpy) comparison of HEG1, HEG2, and HEG3 using different atomic distribution methods. Energies are normalized by subtracting the lowest computed value for each compound. Filled and hollow markers denote cubic and tetragonal phases, respectively. Marker shapes represent the compounds: circles for HEG1, squares for HEG2, and diamonds for HEG3.

Analysis of Li distribution before and after structural relaxation shows that the site occupancies and displacement degrees depend on the distribution methods, as shown in Table 5.3. The CE-based method tended to fill the Li1 site and distribute remaining Li atoms to the Li2 site, contrasting with the SQS method where occupancies of Li1 and Li2 sites were identical. After relaxation, some Li atoms migrated from tetrahedrally coordinated Li1 to octahedrally coordinated Li2 sites. The displacement, particularly at Li1 sites, appear to be influenced by the occupancy after relaxation. For each compound, the higher the occupancy at the Li1 site, the greater the displacement degree observed, as reported in Table 5.3. This relationship was not found for Li2 sites. These findings suggest that the occupation of the Li1 site may influence structural displacement, affecting other properties such as ionic conductivity, activation energy, and diffusion paths. This appears to contrast with previous reports, which indicate that variations in Li+ ion arrangements do not significantly impact DFT results [307]. The results of this study underscore the importance of Li distribution in not only influencing phase stability but also other intrinsic material properties. The choice of atom distribution method, therefore, is not trivial and demands careful consideration.

I further investigate the influence of Li- and *M*-sublattice atomic distribution on the thermodynamic stability of the phases. I uncover a nuanced relationship between changes in the atomic distributions of Li- and *M*-sublattices and their thermodynamic stability impacts. Figure 5.5 illustrates the enthalpy variation from different sublattice distribution methods for HEG1, HEG2, and HEG3 compounds. Specifically, I find that variation of energy is more sensitive to the *M*-sublattice's atomic distribution than the Li-sublattice's arrangement. This phenomenon is

Compound	Method	Li1 (init./relax)	Li1 displacement	Li2 (init./relax)	Li2 displacement
HEG1	$\mathrm{Li}_{\mathrm{SQS}}/M_{\mathrm{SQS}}$	0.67/0.54	0.133	0.67/0.73	0.133
	$\mathrm{Li}_{\mathrm{CE}}/M_{\mathrm{CE}}$*				
	$\mathrm{Li}_{\mathrm{SQS}}/M_{\mathrm{CE}}$	0.67/0.71	0.197	0.67/0.65	0.167
	$\mathrm{Li}_{\mathrm{CE}}/M_{\mathrm{SQS}}$	1.00/0.75	0.255	0.50/0.63	0.159
HEG2	$\mathrm{Li}_{\mathrm{SQS}}/M_{\mathrm{SQS}}$	0.67/0.58	0.199	0.67/0.71	0.107
	$\mathrm{Li}_{\mathrm{CE}}/M_{\mathrm{CE}}$	1.00/0.88	0.284	0.50/0.56	0.200
	$\mathrm{Li}_{\mathrm{SQS}}/M_{\mathrm{CE}}$	0.67/0.71	0.205	0.67/0.65	0.127
	$\mathrm{Li}_{\mathrm{CE}}/M_{\mathrm{SQS}}$	1.00/0.83	0.223	0.50/0.38	0.141
HEG3	$\mathrm{Li}_{\mathrm{SQS}}/M_{\mathrm{SQS}}$	0.67/0.54	0.214	0.67/0.73	0.141
	$\mathrm{Li}_{\mathrm{CE}}/M_{\mathrm{CE}}$	1.00/0.75	0.294	0.50/0.63	0.196
	$\mathrm{Li}_{\mathrm{SQS}}/M_{\mathrm{CE}}$	0.67/0.58	0.228	0.67/0.71	0.151
	$\mathrm{Li}_{\mathrm{CE}}/M_{\mathrm{SQS}}$	1.00/0.71	0.234	0.50/0.65	0.129

*relaxed structure with tetragonal phase. The occupancy (displacement) of Li1, Li2 and Li3 sites are 1.00(0.034), 0.643(0.266) and 0.94(0.146), respectively.

Table 5.3: Li site occupancy and displacement comparison for HEG compounds obtained with different distribution methods. Initial and relaxed occupancies for Li1 and Li2 sites in the cubic phase are listed, along with displacement post-relaxation. The displacement is calculated from the deviation of each Li-O bond from average Li-O bond distance. For HEG1 with $\mathrm{Li}_{\mathrm{CE}}/M_{\mathrm{CE}}$, which transitioned to a tetragonal phase, the occupancy of each Li site is specified.

evident in the energy difference, where shifts in the *M*-sublattice distribution yielded larger variances (Figure 5.5). For instance, the energy difference is more pronounced in HEG1 when the *M*-sublattice atoms change from an SQS to a CE distribution, compared to the same change in the Li-sublattice. The result suggests that the structural stability and electronic characteristics of the compounds are markedly more sensitive to the configuration of the *M*-sublattice atoms than of the Li-sublattice. This sensitivity could be attributed to the higher oxidation state of *M* ions (e.g. Zr^{4+}, Ta^{5+}) compared to Li^{+}, making the electrostatic effects more impactful on enthalpy. These findings underscore the importance of the atomic configuration of dopant in modulating the compound's energy profile and emphasize the importance of targeted distribution method selection to optimize material properties.

To investigate the influence of Coulomb interactions on the structural stability of high entropy garnets, the Ewald summation was performed for both initial and relaxed states of HEG1, HEG2, and HEG3. Figure 5.6 shows the obtained significant variations in Coulomb energy. These variations were more pronounced in structures with increased number of doping elements, particularly for those configured with $\mathrm{Li}_{\mathrm{SQS}}/M_{\mathrm{SQS}}$. The complexity introduced by increasing number of dopants contributed to this trend, highlighted by the increased displacement within the tetrahedral Li1 site (details in Table 5.3), with displacement degrees of 0.133, 0.199, and 0.214 for the respective structures. An example that underscores this observation is the comparison between the relaxed structures of HEG1 and HEG3. Despite identical Li occupancies, the larger displacement degree in HEG3 — a consequence of the greater number of doping elements — especially at the Li1 site, leads to extended interatomic distances. This, in turn, results in a more substantial impact on electrostatic energy. Hence, it is evident that

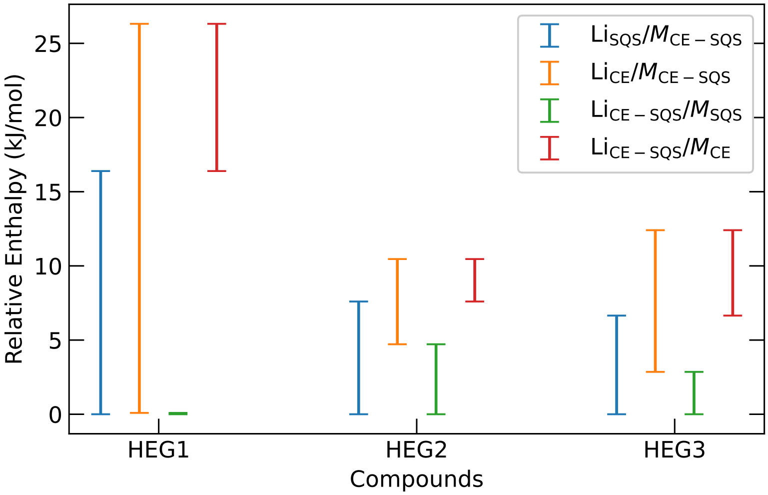

Figure 5.5: Enthalpy variations for HEG1, HEG2, and HEG3 highlight the effects of differing M- and Li- atomic distributions on thermodynamics. Each notation, such as Li_{SQS}/M_{CE-SQS}, indicates enthalpy difference $E_{Li_{SQS}/M_{CE}}$ (upper bar) $-$ $E_{Li_{SQS}/M_{SQS}}$ (lower bar). The relative enthalpy for each distribution is calculated as $E - E_{Li_{SQS}/M_{SQS}}$, setting the baseline enthalpy of Li_{SQS}/M_{SQS} as the reference point.

increased displacement of Li atoms significantly influences the electrostatic energy.

A direct correlation between Coulomb and total DFT energies for the unrelaxed structures of high entropy garnet compounds is found, which is in line with the findings presented in [201]. However, this correlation diminishes after structural geometry relaxation. For the relaxed structures across the three high entropy garnet compounds, the SQS structure exhibited the lowest computed enthalpies, whereas the CE-based model resulted in the highest computed enthalpies. In contrast, results from Ewald summation revealed an opposing trend, showing that both before and after structural relaxation, the CE-based model consistently yielded the lowest Coulombic energies. The inconsistency between DFT and Ewald summation results is likely attributable to changes in interatomic distances and electronic structures that occur during the relaxation process. These changes facilitate charge redistribution and electron delocalization, which in turn diminish the applicability of the localized point-charge model for the Coulomb energy in the relaxed state. Thus, the findings suggest that while CE-based atomic distributions effectively identify atomic configurations with the lowest energy dominated by Coulomb interactions, their predictive accuracy for determining the lowest-energy configurations decreases in materials with higher covalency and structural complexity, such as HEG LLZO. In these materials, the CE-based methods are less reliable for determining the most stable, low-energy configurations.

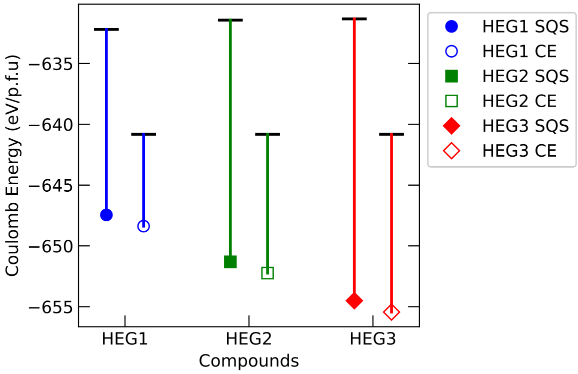

Figure 5.6: Comparison of Coulomb energy difference before and after structural relaxation for HEG1, HEG2, and HEG3 compounds, of which the structure configuration is distributed by $\mathrm{Li}_{\mathrm{SQS}}/M_{\mathrm{SQS}}$ (SQS, filled markers) and $\mathrm{Li}_{\mathrm{CE}}/M_{\mathrm{CE}}$ (CE, hollow markers) methods. The energy of each compound's unrelaxed structure is denoted by a horizontal bar, while the relaxed structure energy is depicted using colored markers: blue circle for HEG1, green square for HEG2, and red diamond for HEG3. A vertical line connects each unrelaxed energy bar to its corresponding relaxed energy marker, visually representing the energy shift upon relaxation.

5.3.3 Thermodynamic characterization of HEGs

In order to gain a deeper understanding of the thermodynamic properties of HEG compounds HEG1, HEG2, and HEG3, I performed calculations of their configurational entropy and compared these findings with their enthalpy values. Figure 5.7 shows the enthalpy differences between the tetragonal and cubic phases of these compounds. For pure LLZO, the enthalpy of the tetragonal phase is lower by $\sim$ 6.5 kJ/mol compared to the cubic phase. This observation is in line with the computational findings reported by Bernstein et al. [291]. Intriguingly, upon doping LLZO with additional elements, a change in phase stability is found; the cubic phase becomes progressively more stable than the tetragonal phase as the number of doping elements increases, as shown from HEG1 to HEG3. While previous studies have primarily emphasized the role of lithium vacancies in stabilizing the cubic phase of LLZO [308, 309], the findings shown here contribute a novel perspective by focusing on the number of doping elements. I have established, for the first time through DFT calculations, that increasing the variety of doping elements, rather than altering lithium concentrations, significantly enhances the cubic phase's stability. This finding underscores the impact of doping on the thermodynamic stability of these garnet compounds, indicating a preference for the cubic phase structure with increased number of doping elements.

Afterward, I compare the configurational entropies of the garnet compounds, as detailed in Table 5.4. For the fully ordered LLZO in its tetragonal phase, the configurational entropy ($S^{\mathrm{tet}}_{\mathrm{conf}}$) is zero. In contrast, the disordered cubic phase exhibits a configurational entropy of $\sim$ 30 J/mol/K per formula unit. This significant difference in configurational entropy allows us to estimate the

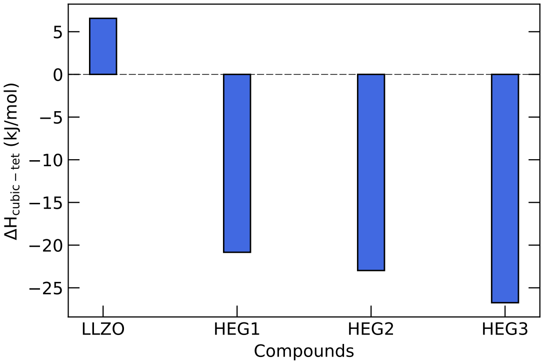

Figure 5.7: Enthalpy differences (in kJ/mol of formula unit) between cubic and tetragonal phases for HEG compounds. Each difference is derived by subtracting the computed enthalpy of the tetragonal phase from that of the cubic phase. The computed enthalpy are based on the SQS-distributed atomic configurations, which have been demonstrated to exhibit the lowest energies for these compounds (see Figure 5.4). An exception is made for *t*-LLZO, where a fully ordered configuration is used.

phase transition temperature from the tetragonal to cubic phase. This is done by assuming that $\Delta G = 0$, so $T = \Delta H / \Delta S$ [310]. Assuming that the total entropy change (ΔS) is solely due to the configurational entropy (ΔS_{conf}) and neglecting the other entropy contributions (e.g. vibrational and electronic), the calculated temperature required to overcome the enthalpy difference ($\Delta H_{\text{cubic}-\text{tet}}$) of 6.5 kJ/mol is ~ 500 ℃. However, I note that the experimentally reported phase transition temperature is around 650 ℃ [311, 312]. This discrepancy between the calculated and experimental values may be attributed to the exchange-correlation effects in DFT. Li et al. [310] demonstrated that applying the standard DFT method results in underestimation of disordering temperatures for a series of pyrochlore compounds. Additionally, the theoretical value of ΔS_{conf} represents the maximum possible value of configurational entropy; in reality, this value is expected to be lower due to the partial ordering preferences within the structure [112–114].

Name	formula unit	$S_{\text{conf}}^{\text{tet}}$ (J/K·mol)	$S_{\text{conf}}^{\text{cubic}}$ (J/K·mol)
LLZO	$Li_7La_3Zr_2O_{12}$	0.000	8.808
HEG1	$Li_6La_3ZrSbO_{12}$	35.396	48.572
HEG2	$Li_6La_3Zr_{0.75}Sb_{0.5}Ta_{0.5}Ti_{0.25}O_{12}$	45.834	59.011
HEG3	$Li_6La_{1.5}Nd_{1.5}Zr_{0.75}Sb_{0.5}Ta_{0.5}Ti_{0.25}O_{12}$	63.124	76.300

Table 5.4: The configurational entropy per formula unit calculated from Equation 1.20 for different compounds in tetragonal ($S_{\text{conf}}^{\text{tet}}$) and cubic ($S_{\text{conf}}^{\text{cubic}}$) phase.

The analysis further reveals that introducing Li vacancies and increasing the number of dopants leads to an increase in the configurational entropy. For the compounds HEG1, HEG2, and HEG3, regardless of the variety and concentration of dopants, a consistent difference in configurational entropy—approximately 13 J/mol/K per formula unit—is observed between the cubic and tetragonal phases. This difference is mainly due to the greater number of possible Li sites in the cubic phase compared to the tetragonal phase, as reflected in Equation 1.20. However, it is important to note that this entropy difference is relatively minor when compared to the enthalpy difference between the two phases. These observations suggest that while configurational entropy does play a role in stabilizing the cubic phase, enthalpy is the main driving force in the formation of this phase. I note, however, that entropy and enthalpy of a partially or fully disordered materials are correlated (e.g., [114]). This finding emphasizes the significant role of enthalpy in the stabilization of the HEG compounds, particularly under varying conditions of dopant concentrations and structural configurations.

It has been suggested that the ideal Li content to form a conductive garnet with cubic structure is 5 < Li < 6.6 per formula unit [291]. This can be seen for example, in $Li_{7-3x-y}M_xLa_3Zr_{2-y}B_yO_{12}$ (M = Al, Ga, B = Ta) [308, 313, 314]. At Li contents larger than 6.6, the cubic structure undergoes a reduction of symmetry to a tetragonal polymorph and the ionic conductivity decreases. My result is aligned with this observation. For Li content of 7, the stable structure appears to be tetragonal and as Li content reduces to 6, cubic phase is favorable. Jung et al. [122] discusses that the cubic phase stabilization in the garnet with multiple dopants is presumably caused by an entropy effect rather than the enthalpy effect for a constant lithium content of 7.0 in $Li_7La_3M_2O_{12}$ (M = Zr, Hf, Sn, Sc, Ta). From the cases studied here, a different conclusion is proposed. The main stability driver is enthalpy, and configurational entropy provides extra stabilization of cubic phase.

5.4 Electrochemical performance from experiments

All the experiments were conducted by Dr. Ye from Forschungszentrum Jülich. The HEG compounds HEG1, HEG2, and HEG3 were synthesized utilizing conventional solid-state reaction methodologies. The XRD patterns of HEG1, HEG2 and HEG3 are shown in Figure 5.8. Additionally, Thermogravimetric Analysis/Differential Thermal Analysis (TGA/DTA) was performed to examine the thermal stability of HEG2, confirming the thermal stability of the garnet material (see Figure 5.9). The experiment shows that the synthesis of the HEG2 with Ti, Sb, and Ta occupying Zr site is successfully performed for the first time. After sintering at 1050℃, a pure cubic garnet phase is obtained. Despite the microstructure not reaching full density, the introduction of Ti into the garnet structure is found to promote the sintering, as HEGs with Ti exhibit significantly higher sinterability than any mono-doped LLZO with Sb or Ta. The experimentally measured lattice parameters were in close agreement with theoretical predictions, as reported in Table 5.5, underscoring the effectiveness of the PBEsol functional for accurate prediction of structural parameters. This alignment between experimental and computational results not only validates the synthesis process but also reinforces the reliability of the computational methods employed in this study.

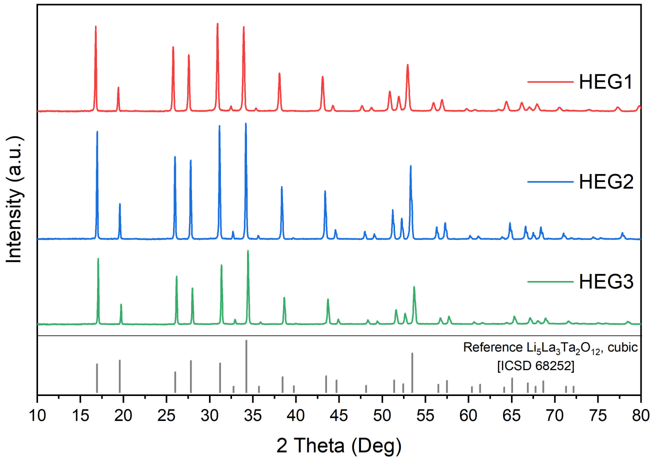

Figure 5.8: XRD patterns of HEG1, HEG2, and HEG3.

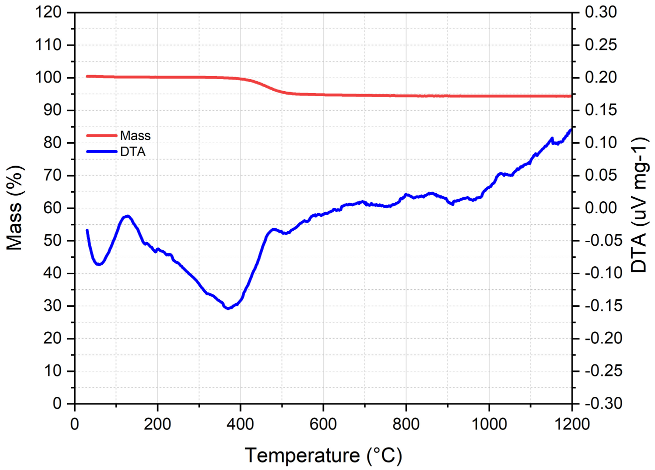

Figure 5.9: The TGA/DTA analysis of HEG2 over the temperature range of 30 ℃ to 1200 ℃. The significant mass loss observed at 400 ℃ is attributed to proton extraction from the garnet structure [315]. As the sample has been stored in ambient atmosphere for months prior to the thermal analysis, the garnet reacts with the humidity in air through a Li+/H+ exchange in the garnet structure. The decomposition of garnet usually takes place above 1000℃, as confirmed by the DTA curve. These findings confirm the thermal stability of the garnet material.

Compound	Expt./Theo.	a (Å)	V (Å^3)
HEG1	Expt.	12.9413(2)	2167.37(6)
	Theo.	12.9423	2167.66
HEG2	Expt.	12.8724(3)	2132.94(4)
	Theo.	12.8774	2135.37
HEG3	Expt.	12.7859(3)	2090.24(4)
	Theo.	12.7572	2076.16

Table 5.5: The lattice parameters measured from XRD pattern for HEG1, HEG2 and HEG3 (Expt.) compared with the computed lattice parameters (Theo.). The reported theoretical lattice parameters are from the SQS structures of each compounds.

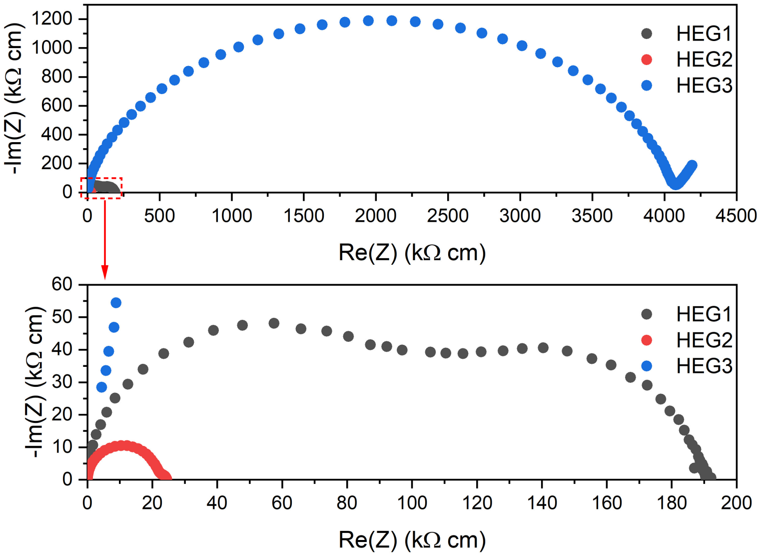

Figure 5.10: EIS spectra of HEG1, HEG2, and HEG3, normalized for thickness and area.

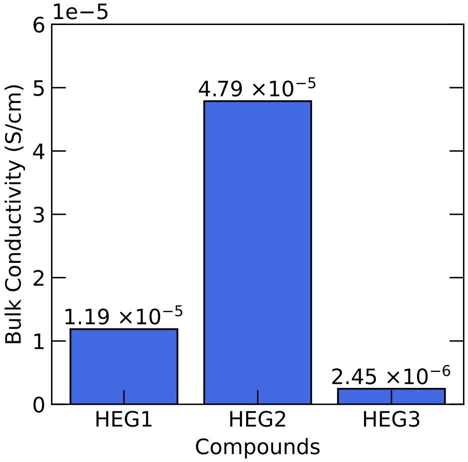

Figure 5.11: The measured bulk Li-ion conductivity of synthesized HEG1, HEG2 and HEG3.

Subsequent to synthesis, the experimental partners conducted a comprehensive analysis of the electrochemical properties of these compounds, focusing on bulk Li-ion conductivity. The EIS spectra of HEG1, HEG2, and HEG3 are presented in Figure 5.10. Figure 5.11 reveals that HEG2 exhibited superior ionic conductivity compared to others. HEG2 exhibits a bulk and total ionic conductivity of 0.099 and 0.088 mS cm^{-1} at 25℃, respectively, with a reduced sintering time of 6 hours. Impressively, the critical current density reaches 0.275 mA cm^{-2} at 25℃, which is promising for the case without any interfacial modification. Besides, the stable cycling of its symmetric cell with Li metal electrodes proves that the Ti dopant in HEG2 is chemically stable against the Li metal anode.

In contrast, HEG3, despite exhibiting the most significant displacement indicative of higher local disorder (see Table 5.3), displayed the lowest conductivity. This outcome challenges the previously suggested hypothesis by Zeng et al. [118] regarding the enhancement of ionic conductivity via local disorder and site percolation in HEMs. One of the explanations could be the unoptimized synthesis route employed for HEG3, resulting in a porosity of 50%, compared to the 20% porosity observed in HEG2. Refining the synthesis process could potentially reduce the porosity and enhance the ionic conductivity of HEG3. Overall, the minimal influence of entropy and the amount of doping elements on ionic conductivity suggests that these parameters may not be the primary drivers of conductivity in HEG compounds. Detailed experimental data encompassing the influence of cation doping on the microstructure and additional electrochemical characterizations are presented in [288].

5.5 Summary

This chapter demonstrates that the cubic phase of HEG compounds HEG1, HEG2, and HEG3 is more favorable than the tetragonal phase, primarily due to enthalpic advantages, with the configurational entropy contributing as a secondary factor to the stability enhancement. Through detailed DFT calculations, I have shown for the first time that increasing the diversity of selected doping elements significantly improves the cubic phase's stability, highlighting the profound impact of dopant variety on the thermodynamic stability of these materials. Additionally, the thorough analysis indicates that metal distribution has a more profound effect on thermodynamic stability compared to lithium distribution, highlighting the importance of atomic arrangement in these compounds. I also found that disordered structures are energetically favored in HEG1, HEG2, and HEG3, over relatively ordered phases predicted by minimal Coulombic energy considerations. This preference for disordered configurations, revealed through extensive DFT calculations across various atomic configurations, suggests a complex interplay between thermodynamic stability and atomic distribution and request further investigation.

Experimentally, three high-entropy cubic-phase garnet compounds were successfully synthesized with reduced synthesis temperatures, attributed to the increased configurational entropy. HEG2 shows a high ionic conductivity (0.099 mS/cm) However, despite obtaining cubic-phase multicomponent garnets, improvements in bulk ionic conductivity with increased doping were not as significant as expected. This outcome indicates that the interplay between ionic diffusion mechanisms and the composition of HEGs is complex and requires further investigation.

This chapter not only advances the understanding of the thermodynamic aspects of HEG compounds but also highlights the intricate relationship between atomic distribution, phase stability, and ionic transport properties in these materials. The insights gained from this study pave the way for future research aimed at optimizing the performance of high-entropy ceramics in energy storage and other advanced technological applications.

6 Application of HEMs beyond intercalated LIBs

This chapter presents collaborative research conducted with experimental partners at the Karlsruhe Institute of Technology, focusing on diverse energy storage systems. Specifically, I address three key areas via DFT: electronic structures in conversion-type high-entropy fluoride electrodes for LIBs (Section 6.1), the thermodynamic properties of high-entropy Prussian white in sodium-ion batteries (Section 6.2), and computational insights into the resistive switching mechanisms in memristive devices (Section 6.3). By integrating computational methods such as DFT with experimental observations, this chapter aims to provide deeper insights into the behavior of HEMs. The use of DFT allows us to decode unexplained phenomena observed in experiments, offering a pathway to advance the field of HEMs. This chapter highlights the potential of combining theoretical and experimental approaches to address complex challenges in energy storage and extends the applicability of HEMs across various domains. My contributions to this chapter include conducting all computational studies, ranging from electronic structure and thermodynamic analysis to elucidating atomic-scale mechanisms. The computational work was carried out by me under the guidance of Dr. Kowalski and Dr. Kaghazchi. This chapter is based on the following publications:

- Y. Cui, P. A. Sukkurji, K. Wang, R. Azmi, A. M. Nunn, H. Hahn, B. Breitung, Y.-Y. Ting, P. M. Kowalski, P. Kaghazchi, Q. Wang, S. Schweidler, and M. Botros. *High entropy fluorides as conversion cathodes with tailorable electrochemical performance*. J. Energy Chem., 72, 342–351, 2022. doi: 10.1016/j.jechem.2022.05.032
- Y. He, S. L. Dreyer, Y.-Y. Ting, Y. Ma, Y. Hu, D. Goonetilleke, Y. Tang, T. Diemant, B. Zhou, P. M. Kowalski, M. Fichtner, H. Hahn, J. Aghassi-Hagmann, T. Brezesinski, B. Breitung, and Y. Ma. *Entropy-Mediated Stable Structural Evolution of Prussian White Cathodes for Long-Life Na-Ion Batteries*. Angew. Chem. Int. Ed., 63, e202315371, 2024. doi: 10.1002/ange.202315371
- Y. He, Y.-Y. Ting, H. Hu, T. Diemant, Y. Dai, J. Lin, S. Schweidler, G. C. Marques, H. Hahn, Y. Ma, T. Brezesinski, P. M. Kowalski, B. Breitung, and J. Aghassi-Hagmann. *Printed High-Entropy Prussian Blue Analogs for Advanced Non-Volatile Memristive Devices.* Adv. Mater., 37, 2410060, 2025. doi: 10.1002/adma.202410060

6.1 HEMs as conversion cathodes

In this section, I explored high-entropy fluorides (HEFs) as conversion-type cathode materials in LIBs. I provided the computational support to understand variation in the electronic structure of HEFs with an increasing number of dopant elements, where DFT was employed to investigate the electronic structure difference with an increasing variety of dopants in HEFs. The experiments were conducted by Dr. Cui from the Institute of Nanotechnology, Karlsruhe Institute of Technology.

6.1.1 Introduction

In Chapter 1, I discussed the potential and challenges of conversion-type batteries. In order to circumvent the issues and to realize the application of MFs in rechargeable batteries, cation or anion doping is an important strategy to improve the electrochemical properties of MFs and promising progress has been achieved [44, 317–320]. For example, Wang et al. proposed the incorporation of Cu into the FeF_2 crystal lattice by preparing a ternary fluoride of $Cu_{0.5}Fe_{0.5}F_2$. This material exhibits a hysteresis of less than 150 mV with a low cycling rate, achieving high capacity [40]. Following the concept of "ternary fluorides", Gordon et al. successfully synthesized solid solution fluorides including $Ni_yFe_{1-y}F_2$, $Co_yFe_{1-y}F_2$, and $Mn_yFe_{1-y}F_2$, demonstrating that the metal composition determines the formation and growth of the cathode SEI, affecting the cathode stability [321]. Later, Villa et al. found that with the substitution of Cu into NiF_2, both the volumetric expansion during the first lithiation and the fluorine loss during delithiation are reduced, and thus the cycling performance was improved [322]. These reports show the synergistic effect of metals in the ternary fluorides, which is beneficial for the electrochemical performance of MFs based cathode materials.

In general, the synergistic effect of metals can be found more pronounced in HEMs. Many high-entropy oxides have been shown as promising candidates in cathode materials for LIBs. An HEO with very promising and unexpected properties has been explored as a conversion-type electrode material in LIBs. Sarkar et al. [97] showed that entropy is one of the important factors for the cycling stability of the HEO anode ($(Co_{0.2}Cu_{0.2}Mg_{0.2}Ni_{0.2}Zn_{0.2})O$), probably due to the reduction of some cations, while other cations remain in the rock-salt structure and facilitate the reintegration into the parent structure after conversion. Lökçü et al. [323] indicated that the electrochemical performance of HEOs would be greatly improved by increasing the lithium concentration in the structure of $(MgCoNiZn)_{1-x}Li_xO$ (x = 0.05, 0.15, 0.25, and 0.35) thereby generating more oxygen vacancies. These reports demonstrate the role of chemical disorder, i.e., mixed cations and created vacancies, for the cycling stability and tailorability. Moreover, the highly disordered nature of HEMs can mitigate the volumetric changes during the charging/discharging process by increasing isotropicity, hence improving capacity retention [324].

In the present work, a series of HEFs based materials namely are reported: $(Cu_{1/5}Ni_{1/5}Fe_{1/5}Zn_{1/5}Co_{1/5})F_2$ (HEF5), $(Cu_{1/6}Ni_{1/6}Fe_{1/6}Zn_{1/6}Co_{1/6}Mn_{1/6})F_2$ (HEF6), and $(Cu_{1/7}Ni_{1/7}Fe_{1/7}Zn_{1/7}Co_{1/7}Mn_{1/7}Mg_{1/7})F_2$ (HEF7) as electrode materials for battery applications, in an attempt to exploit their high theoretical specific capacities. HEFs were utilized as cathode materials for LIBs and their underlying storage mechanisms were investigated.

6.1.2 Computational details

The calculation setup is described in Section 2.3. The U values derived from linear-response methods were 6.2, 3.32, 2.5, 5.3, 5 eV for Ni, Co, Mn, Fe, Cu respectively. All three systems, namely HEF5, HEF6 and HEF7, were computed with rutile-type structure with $P4_2/mnm$ space group. To match the ideal correlation with respect to the composition in SQSs, a $2 \times 2 \times 5$ supercell containing 120 atoms/cell was considered for HEF5 system and a $2 \times 3 \times 7$ supercell containing 252 atoms/cell was considered for HEF6 and HEF7 system. A k-point sampling net of size $1 \times 1 \times 1$ was used for structural relaxation of the three systems and a k-point mesh of $2 \times 2 \times 2$ and $2 \times 2 \times 1$ were applied in density of states (DOS) calculation in HEF5, HEF6, and HEF7 systems, respectively.

6.1.3 Results and discussion

Among the investigated systems, HEF7, the most complex system containing seven different metal elements, exhibited high capacity at the beginning of cycling process, according to experimental results obtained by our experimental partner. More importantly, HEF7 maintained a moderate cycling performance with a capacity of more than 125 mAh/g after 100 cycles at a high specific current of 0.5 A/g. In order to investigate the better performance of HEF7 in more detail, the total electron DOS was calculated using DFT. The DOS calculated by DFT for the HEF systems showed a band gap of around 2.2 eV for all three systems (Figure 6.1d), with no significant deviation. A gap state between 0 and 0.8 eV is observed for the systems, which is related to the d band of Cu (see the projected DOS in Figure 6.1 (a-c)). This shows a strong tendency of Cu to be reduced from +2 to +1. Although the major contribution of valence band maximum is from the Fe-d states in the HFE5 system, it is dominated by Mn-d states in the HFE6 and HEF7 systems. This clearly shows that Mn has the highest tendency, compared to the other elements, to be oxidized to +3 and perhaps +4. This is in line with the previous studies showing a large charge state of +4 for Mn in the fully discharged $LiNi_xCo_yMn1\text{-}x\text{-}yO_2$ (NCM) cathodes [202, 325]. As expected, no significant change in the DOS is observed after adding Mg to the HEF6 compound. This is because Mg has only strongly localized p states that are located far away from the Fermi level. According to previous reports, increasing the number of metal species improves the lithium transport properties [70], so it is speculated that the increase in the disorder in the high entropy fluoride may improve the lithium conductivity of this system. Thus, the electrochemical properties of this system were improved with the increase in the number of metals.

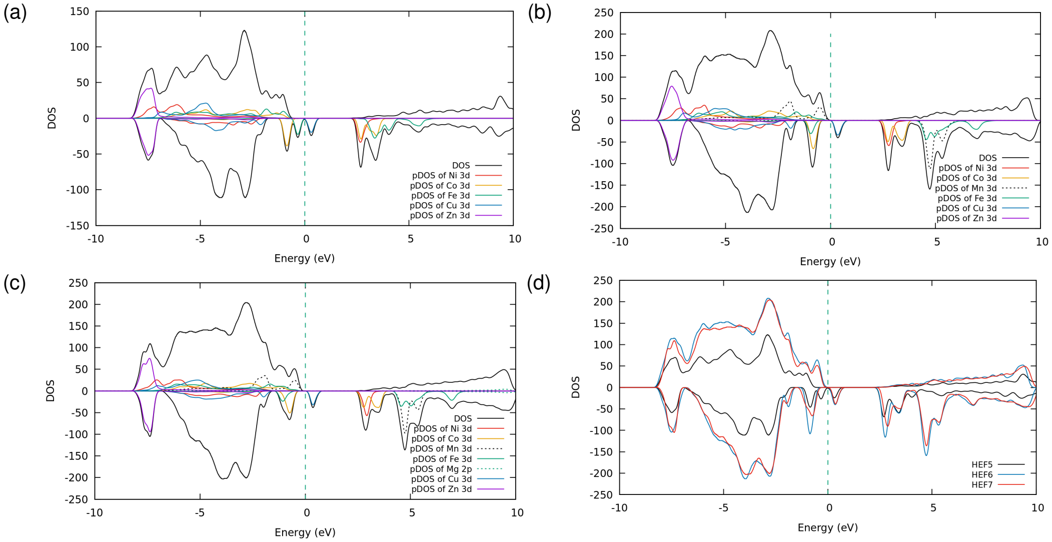

Figure 6.1: Projected DOS of (a) HEF5, (b) HEF6, (c) HEF7, and (d) total DOS of HEF system.

In summary, the computational investigation of HEFs provided valuable insights into their electronic structure and electrochemical behavior. Among the studied systems, HEF7, which contains seven distinct metal elements, exhibited the most promising performance. The DOS calculations revealed that the inclusion of multiple transition metals (TMs), particularly Cu and Mn, significantly influenced the redox processes, with Mn exhibiting a strong tendency for oxidation. The presence of Mg, though electrochemically inactive, likely contributed to the structural stability. Overall, the findings suggest that the disorder inherent to HEMs plays a crucial role in enhancing lithium transport, thereby improving the electrochemical performance of HEFs. These results highlight the potential of tailoring the elemental composition in HEFs to design conversion-type cathodes with optimized performance for next-generation lithium-ion batteries.

6.2 HEMs in Na-Ion Batteries

In this section, a high-entropy Prussian White (HE-PW) is studied as a cathode material for sodium-ion batteries (SIBs). These materials have the potential to enhance cycling stability by stabilizing the crystal structure, which can be achieved through room-temperature synthesis. My contribution to this work focused on the computational aspects, including the investigation of thermodynamic properties, such as structural stability and the roles of enthalpy and entropy in these systems.

6.2.1 Introduction

Low-cost, Mn-based Prussian White analogues ($Na_xMn[Fe(CN)_6]$, referred to as PWs, have been demonstrated as robust host materials to enable facile Na^+ insertion/extraction in SIBs. A large number of studies have found that PWs with a low defect density, a low H_2O content, and a high Na content are promising to achieve good electrochemical performance but suffer from multiple phase transitions non-cubic structures with low-symmetry [326–328]. Apart from the rhombohedral and cubic structures [329, 330], monoclinic PWs can incorporate more sodium into the structure, making them interesting for further investigations [331]. However, they are subjected to internal structural changes and severe Jahn-Teller distortions, due to the Mn-N_6 octahedra experiencing large lattice strain during the uptake and removal of Na^+ ions [331–334]. It has also been reported that such monoclinic PW materials suffer from rapid capacity decay and poor reversibility caused by pronounced lattice parameter changes during the phase transitions between monoclinic $Na_2Mn[Fe(CN)_6]$, cubic $NaMn[Fe(CN)_6]$, and tetragonal $Mn[Fe(CN)_6]$ [331]. Previous efforts to mitigate structural changes and improve the stability of PWs mainly focused on partial atom replacements [335–337], removal of interstitial water/vacancies [338, 339], introducing complexing agents [340–342], forming conductive networks [343, 344], or designing (cation) defect structures [331]. However, the high-entropy approach has not yet been applied to low-symmetry, monoclinic PW battery materials.

This work demonstrates that both the structure and cycling stability of PWs can be improved by utilizing the high-entropy approach. The experimentalists synthesized a series of Mn-based Prussian White analogs with varying degrees of configurational entropy. These materials, including low-entropy (LE-PW), medium-entropy (ME-PW), and high-entropy (HE-PW) samples, were designed by incorporating up to six different metal species at the Mn site, with the aim of enhancing the cycling stability and overall electrochemical performance. Various complementary characterization techniques, including X-ray diffraction (XRD), X-ray absorption spectroscopy, and operando gas analysis, were employed by the experimental collaborators to assess the materials' structural evolution and gas-evolving degradation reactions during cycling.

6.2.2 Computational details

First-principles DFT calculations were performed using the Vienna Ab initio Simulation Package (VASP) [345]. The spin-polarized generalized gradient approximation (GGA) with the PBE exchange-correlation functional was chosen for the electronic structure calculations [176]. The projector-augmented wave pseudopotentials [346] and a plane-wave cutoff energy of 500 eV were used with an electronic and force convergence criteria of 10^{-4} eV and 10^{-3} eV/Å, respectively. The k-point mesh for each system was carefully tested and validated to ensure reliable and accurate results, as the three systems were calculated with different supercell sizes. The simplified rotationally invariant approach to the DFT+U was used to correct for the self-interaction error in strongly-correlated 3*d* electrons [146]. The values of the Hubbard U parameters for Co, Cu, Fe, Mn and Ni were taken from reference and were 3.4, 4.0, 4.0, 3.9 and 6.0 eV, respectively [150]. The disordered structures were generated using the special quasirandom structure (SQS) method [216], which is implemented in the open-source ATAT [215, 347]. The composition was adjusted slightly to reduce the number of atoms needed to match the specific crystal structure while maintaining the configurational entropy similar to that of the synthesized material, as shown in Table 6.1.

	HE-PW	**ME-PW**	**LE-PW**
Material	$Na_xMn_{0.4}(TMs)_{0.12}$ $Fe(CN)_6$	$Na_xMn_{0.6}(TMs)_{0.08}$ $Fe(CN)_6$	$Na_xMn_{0.8}(TMs)_{0.04}$ $Fe(CN)_6$
Configurational entropy	1.640 *R*	1.320 *R*	0.820 *R*
Adjusted PW	$Na_xMn_{0.375}(TMs)_{0.125}$ $Fe(CN)_6$	$Na_xMn_{0.583}(TMs)_{0.083}$ $Fe(CN)_6$	$Na_xMn_{0.792}(TMs)_{0.042}$ $Fe(CN)_6$
Computed unit in DFT	$Na_2Mn_3(TMs)_1$ $Fe_8(CN)_{48}$	$Na_2Mn_7(TMs)_1$ $Fe_{12}(CN)_{72}$	$Na_2Mn_{19}(TMs)_1$ $Fe_{24}(CN)_{144}$
Configurational entropy	1.667 *R*	1.350 *R*	0.847 *R*

Table 6.1: The configurational entropy of HE-PW, ME-PW and LE-PW calculated from Equation 1.20. The adjusted composition used in the DFT calculations gives a similar configurational entropy to that calculated using Eqn. 3.1. The TM species are the mixed TMs, namely Fe, Ni, Cu, Co and Cd.

The structural parameters are reported in Table 6.3. For HE-PW, the cubic symmetry persists during sodiation/desodiation. The *a* lattice parameter decreases from 10.039 Å to 10.007 Å during partial desodiation (x = 1.5 to 1.0) and marginally increases to 10.014 Å for the fully desodiated state (x = 0). Both ME-PW and LE-PW undergo structural changes, precluding direct comparison. The reported formation enthalpies are derived from the energy difference between reactants and products according to:

$$\begin{aligned} &\mathrm{xMnCl_2} + \frac{\text{(1-x)}}{5}(\mathrm{FeCl_2} + \mathrm{NiCl_2} + \mathrm{CuCl_2} + \mathrm{Cd(NO_3)_2} + \mathrm{CoCl_2}) + \mathrm{Na_4Fe(CN)_6} \\ &\longrightarrow \mathrm{NaMn}_x\mathrm{(TM)}_{(1-\mathrm{x})/5}[\mathrm{Fe(CN)_6}] + \frac{2\,(\mathrm{x_4}^{+})}{5}\mathrm{NaCl} + \frac{2\,\text{(1-x)}}{5}\mathrm{NaNO_3} + \mathrm{Na}. \end{aligned}$$

The TMs are the mixed transition metals, namely Fe, Ni, Cu, Co, and Cd. The calculated formation Gibbs free energies (ΔG_f) were estimated as a difference between the formation enthalpy (ΔH_f) and the entropy term ($T\Delta S_{conf}$), assuming the configurational entropy of the compound as being the sole contributor to the entropy of formation.

6.2.3 Results and discussion

The experimental results, conducted by Dr. He from the Institute of Nanotechnology, Karlsruhe Institute of Technology, showed that HE-PW exhibited significantly improved structural stability and suppressed phase transitions during sodium insertion/extraction (see Figure 6.2). Unlike LE- and ME-PW, which underwent severe monoclinic-to-cubic and tetragonal phase transitions, HE-PW maintained a high degree of structural symmetry throughout the cycling process, contributing to enhanced cycling performance. This suppression of phase transitions was linked to the increased configurational entropy of HE-PW, which mitigated the lattice distortions that typically lead to performance degradation in conventional single-metal Prussian White cathodes.

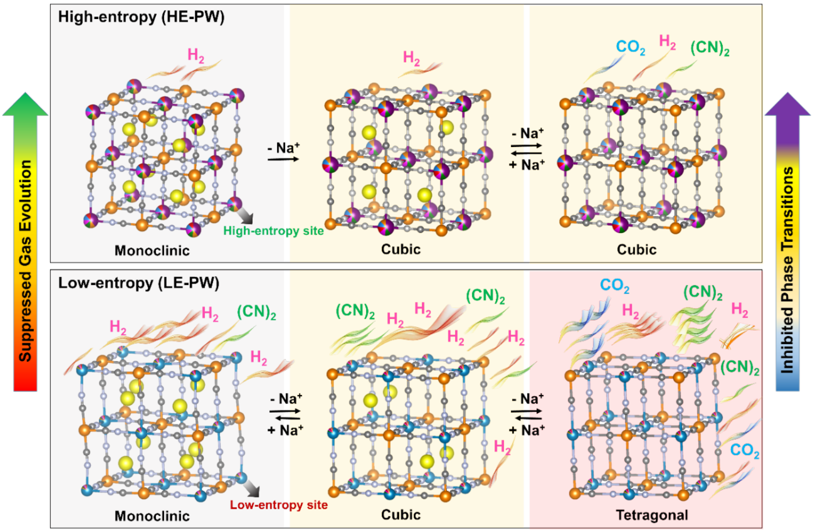

Figure 6.2: Schematic illustration of the structural evolutions and corresponding gas evolution of HE-PW and LE-PW.

To complement these experimental findings, first-principles DFT calculations were performed for the HE-, ME-, and LE-PW materials. These calculations were performed to derive the Gibbs free energy of the considered phases and understand the impact of configurational entropy on stability. The results are given in Table 6.2. For the fully de-sodiated state, the cubic (*Fm-3m* space group) and tetragonal (*I-4m2* space group) structures were considered and compared. The results indicate that upon full extraction of Na^+ ions from the lattice ($Na_xTM[Fe(CN)_6]$ with $x = 0$), HE-PW exists in the high-symmetry cubic phase, whereas both ME-PW and LE-PW adopt a tetragonal structure that is thermodynamically more stable (see Figure 6.3a). This finding is in good agreement with the XRD results and validates the experimentally observed phase transitions upon charging.

In the sodiated state ($x = 1$), the cubic phase is most stable for all three materials. To compare the stability, their Gibbs free energies of formation (ΔG_f) were calculated. Although the formation enthalpy (ΔH_f) of LE-PW is lower by approximately 1.4 and 0.6 kJ mol^{-1} (more negative) than that of HE-PW and ME-PW, respectively, the difference can be readily overcome by the entropy term ($-T\Delta S_{\mathrm{conf}}$) at room temperature (see Figure 6.3b), indicating some stabilization due to configurational entropy for HE-PW. As a result, the overall Gibbs free energies of for-

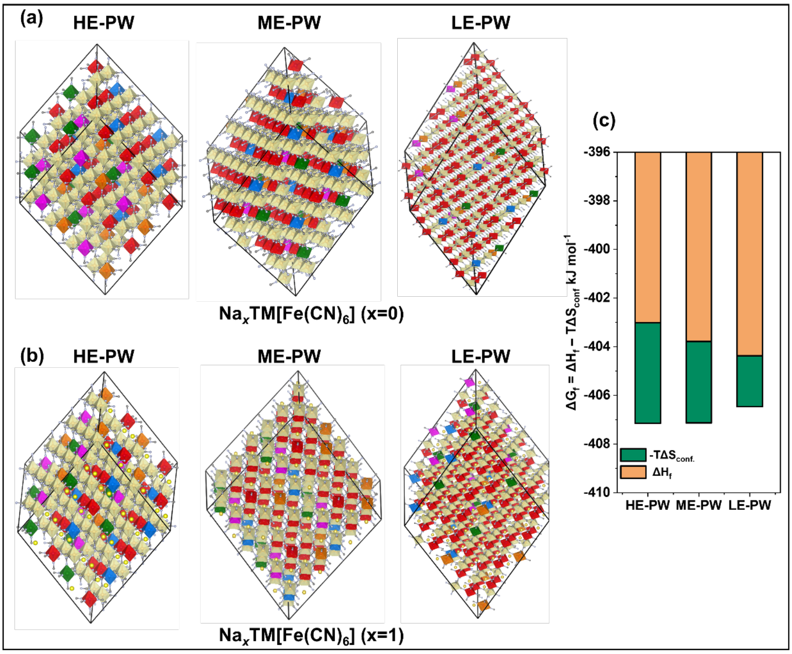

Figure 6.3: DFT calculations of crystal structures for (a) HE-PW (cubic), ME-PW (tetragonal) and LE-PW (tetragonal) in the fully charged state ($x = 0$ in $Na_xTM[Fe(CN)_6]$). (b) Corresponding structures for $x = 1$ (cubic). (c) The Gibbs free energy of formation of the three systems at 298 K.

mation at room temperature for HE-, ME-, and LE-PW (sodiated state) are similar (within 1 kJ mol^{-1}), with the structural stability sequence of LE-PW $<$ ME-PW $<$ HE-PW.

In the highly sodiated state ($x = 1.5$), which approximates the as-synthesized composition, the structural stability of the cubic and monoclinic phases was examined for HE-PW. The latter phase exhibited a consistent pattern of structural stabilization in response to electrochemical cycling. The DFT result demonstrates that, for $x = 1.5$, the cubic structure displays a greater stability than its monoclinic counterpart, as evidenced by a lower energy state (by about -13.35 kJ mol^{-1}). A potential explanation for the synthesis of monoclinic HE-PW is kinetics. Thermodynamic principles dictate that a system tends to move toward its most stable state, i.e., the state with the lowest energy. However, kinetics can prevent the system from reaching this state. If the energy barrier between the monoclinic and cubic phase is high, the system may remain trapped in the monoclinic phase, even though the cubic one is energetically more favorable. This phenomenon is often denoted as kinetic stabilization or kinetic trapping. In other words, although the cubic phase is more stable in terms of energy, as determined by DFT, the transition could be energetically prohibitive. The system may not have enough thermal energy to overcome the energy barrier and therefore is trapped in a metastable, monoclinic phase. However, during cycling, the input of external energy facilitates the phase transition, allowing the

	Energy	**HE-PW**	**ME-PW**	**LE-PW**
x=0	$\Delta H = H_{\text{cubic}} - H_{\text{tet}}$	-171.165	9.070	33.191
	ΔH_f	-403.018	-403.790	-404.369
x=1	$-T\Delta S_{\text{conf}}$ at 25℃	-4.130	-3.345	-2.099
	$\Delta G_f = \Delta H_f - T\Delta S_{\text{conf}}$	-407.148	-407.135	-406.467
x=1.5	$\Delta H = H_{\text{cubic}} - H_{\text{mono}}$	-13.351	–	–

Table 6.2: The computed thermodynamic parameters for the HE-, ME- and LE-PW materials (for different degrees of sodiation, i.e., x in Na$_x$TM[Fe(CN)$_6$]). For $x = 0$, the enthalpy difference between the cubic and tetragonal phases is presented. For $x = 1$, the formation enthalpy, the configurational entropy contribution to the Gibbs free energy at 298 K, and the Gibbs free energy of formation are reported (given in units of kJ mol^{-1}). For $x = 1.5$, the enthalpy difference between the cubic and monoclinic phase in HE-PW is given.

system to attain and maintain the more stable cubic phase. DFT-calculated structural parameters for the HE-, ME-, and LE-PW materials are given in Table 6.3. The computational results indicate that compositional disorder enables a more robust structure for accommodating the electrochemical reactions, and the preference for the high-symmetry structure of HE-PW was confirmed. This agrees well with the experimental data described above and highlights the importance of configurational entropy for increasing the stability of the materials. Last but not least, the mean voltages computed on the most stable structures (see Table 6.4) were found to match well with the electrochemical measurements.

	Sodium content	**Structure**	**a (Å)**	**c (Å)**	**V (Å^3)**
HE-PW	$x = 1.5$	Cubic	10.039	-	1011.705
	$x = 1.0$	Cubic	10.007	-	1002.158
	$x = 0$	Cubic	10.014	-	1004.239
ME-PW	$x = 1.0$	Cubic	10.170	-	1051.763
	$x = 0$	Tetragonal	7.026	9.983	492.848 (985.696)
LE-PW	$x = 1.0$	Cubic	10.366	-	1113.779
	$x = 0$	Tetragonal	7.193	10.289	532.335 (1064.670)

Table 6.3: DFT-calculated structural parameters for HE-PW, ME-PW, and LE-PW. The cubic structure is defined by $a = b = c$ and $\alpha = \beta = \gamma = 90°$, while the tetragonal structure is characterized by $a = b \neq c$ with $\alpha = \beta = \gamma = 90°$. The volume of the tetragonal structure (in parentheses) is scaled to the stoichiometry of the cubic phase for direct comparison.

	HE-PW	**ME-PW**	**LE-PW**
$x = 1$	Cubic	Cubic	Cubic
$x = 0$	Cubic	Tetragonal	Tetragonal
Mean voltage / V	3.249	3.332	3.123

Table 6.4: The most stable structures of HE-, ME-, and LE-PW at $x = 1$ and $x = 0$ in Na$_x$TM[Fe(CN)$_6$] and corresponding (calculated) mean voltage.

In summary, the application of the HE concept to Prussian White (PW) materials was evaluated by studying a series of Mn-based, monoclinic PW cathodes composed of up to six TMs on the

Mn site. The six-metal high-entropy PW, having a ΔS_{conf} of 1.64 R, exhibits superior sodium-storage properties over medium-entropy ($\Delta S_{\text{conf}} = 1.32\ R$), low-entropy ($\Delta S_{\text{conf}} = 0.82\ R$), and conventional Mn-PW ($\Delta S_{\text{conf}} = 0\ R$) materials. The mechanism of this improved performance was investigated, and it was found that the introduction of compositional disorder can suppress unfavorable phase transitions and also reduce side reactions that lead to gas evolution during cycling. A series of complementary experiments and simulation studies demonstrate that increasing entropy positively influences structural evolution and electrochemical behaviour and, for the first time, confirm the preference for a high-symmetry structure upon battery operation. The unveiling of the mechanism behind the improved cycling performance and stability resulting from the introduction of high configurational entropy may provide a reference for future battery materials design.

6.3 HEMs for non-volatile memristive devices

In this section, I turn the attention to similar materials, High-Entropy Prussian Blue Analogs (HE-PBAs), as insertion-type materials in memristive devices.The conduction mechanisms of these devices were comprehensively analyzed using a combination of experimental methods (conducted by Dr. He from the Institute of Nanotechnology, Karlsruhe Institute of Technology) and computational methods (performed by myself). Devices incorporating an active layer of HE-PBA demonstrated notable features, including non-volatility, self-compliance, and forming-free behavior. These results highlight the perspective of HEMs in the development of non-volatile, printed memristors with a unique operational mechanism. My role in this study involved providing computational insight into the resistive switching (RS) mechanism.

6.3.1 Introduction

The current Big Data era with artificial intelligence and Internet of Things that demand processing exponentially increasing mass data has sparked tremendous interest in exploring non-volatile memory technologies [348–350]. Such non-volatile memory is represented by devices known as memristors, which facilitate RS between high resistive states and low resistive states [351]. This capability enables efficient information processing for applications such as computation, data storage, and vision sensors [352, 353]. Another benefit of non-volatile memristors is that a sudden loss of electrical power will not lead to a loss of information, as it is the case for many state-of-the-art computing memories, thereby improving data safety [349]. While presently conventional computing systems are constrained by the “von Neumann bottleneck”, where memory and processing units remain separate in digital hardware, memristors aspire to break through such limitations [354]. Due to its appealing characteristics, such as fast switching speed, high scalability, and ease fabrication [355], memristors offer many possibilities for the rapid development of computing architectures, particularly in neuromorphic and in-memory computing systems [356, 357]. To date, a diverse range of materials demonstrating versatile applicability for memristors, including metal oxides [358–360], chalcogenides [361], 2D-materials [362, 363], molecular materials [364], hybrid perovskites [365, 366], organic materials [367], silicon [368, 369], nitrides [370, 371], and carbon materials [372], has garnered considerable attention. Nevertheless, limited studies have explored ion-insertion materials as potential RS candidates [373], and there is a lack of investigations into high-entropy insertion materials.

Prussian blue analogues (PBAs) exhibit a rigid 3D open framework with large interstitial sites conducive to high mobility of Na^+. Characterized by the formula $Na_xM[Fe(CN)_6]_y\square_{1-y} \cdot nH_2O$ (where $0 < x \leq 2$, $0 < y \leq 1$, M represents TM ions, $\square$ signifies $[Fe(CN)_6]$ vacancies and n is the interstitial water content in the crystal framework) [327, 374], these compounds offer the flexibility to tailor the M position, and therefore also the composition and properties using the high-entropy approach. HE-PBA have been demonstrated as robust (virtually zero-strain) host materials for application in SIBs [95, 375, 376], and exhibit great potential in electrochemical energy storage [36, 333]. These attributes led directly to the design of novel ion-insertion memristors, characterized by excellent reproducibility and controllability owing to stable ion diffusion that can be precisely and reversibly controlled by the applied bias voltage. Given these advantageous characteristics, high Na^+ diffusion coefficient ($\sim 10^{-9}$ cm^2 s^{-1}) [377, 378], stable structure and high ionic conductivity [379], HE-PBAs confer high flexibility in designing memristive devices with superior performance. However, the application of HE-PBAs as insertion materials in memristors has not been extensively explored yet, and the conducting mechanism of HE-PBA-based memristors is still relatively unknown.

In this section, a promising non-volatile bipolar memristor based on HE-PBAs modulated by Na^+ ions is presented. The device consists of a microplotted HE-PBA active layer with a laser-ablated indium tin oxide (ITO) bottom electrode and an inkjet-printed Ag top electrode. The Ag/HE-PBA/ITO device exhibits low power consumption, self-compliance, and a forming-free property. The underlying RS mechanism of the memristor was thoroughly investigated through complementary characterization techniques and DFT calculations. The resistive changes were effectively controlled by fast Na^+ ion migration under an electric field, resulting in a Na^+-deficient layer exhibiting high conductivity with metallic conduction behavior. Furthermore, this work focuses on fabricating memristors using printed technologies, including inkjet printing and microplotting. These printed methods allow for precise, low-cost, and on-demand fabrication of a large number of electronic devices [380, 381]. By contrast, other advanced manufacturing methods, like atomic layer deposition [382], spin coating [383], sputtering [384], pulsed laser deposition, or photolithographic techniques [368, 385], are inherently complex and costly. Therefore, the exploration of printed memristors merits further in-depth study. As a result, the printed $\mathrm{Ag/HE{-}PBA/ITO}$ device demonstrates several advantages for memristor applications, including low operation voltage, robust retention stability, and a high R_{OFF}/R_{ON} ratio.

These characteristics position it as a promising candidate for non-volatile memory applications with low power consumption.

6.3.2 Computational details

The computational setup is detailed in Section 2.3. The Brillouin zone was sampled with a Monkhorst-Pack [234] $2 \times 2 \times 2$ k-point grid. The values of the Hubbard *U* parameters for Co, C-coordinated Fe (Fe1), N-coordinated Fe (Fe2), Mn, Ni and Cu, as applied in previous studies, are 3.4 [150], 7.0 [386], 3.0 [386], 3.9 [150], 4.0 [387], and 3.0 eV [388], respectively. A $2 \times 2 \times 1$ supercell model of a face-centered cubic structure (*Fm-3m* space group), containing 224 atoms per cell (excluding sodium), was constructed to represent the structure of HE-PBA, with Co/Fe2/Mn/Ni/Cu distributed with SQS method on the 4*b* site. To match the specific crystal structure while maintaining configurational entropy close to that of the synthesized material, I slightly adjusted the modelled atomic composition, as detailed in Table 6.5. Following the distribution of TMs, the sodium atoms were distributed based on a Coulombic energy minimization scheme. I selected the first 20 structures with the lowest Coulombic energy for the structural relaxation. The relaxed structure with the lowest DFT total energy was then chosen for the derivation of the DOS.

	Synthesized HE-PBA	*Computed HE-PBA*
Composition	$NaxMn_{0.3}Fe_{0.3}(NiCuCo)_{0.133}[Fe(CN)_6]$	$NaxMn_{0.3125}Fe_{0.3125}(NiCuCo)_{0.125}[Fe(CN)_6]$
$S_{\mathrm{conf.}}$	1.53R	1.51R

Table 6.5: Composition and configurational entropy ($S_{\mathrm{conf.}}$) of the synthesized and computed HE-PBAs.

6.3.3 Results and discussion

The experimental investigation focused on the fabrication and characterization of HE-PBA-based memristors, designed with an Ag/HE-PBA/ITO structure. The Ag/HE-PBA/ITOAg/HE-PBA/ITO device, fabricated through advanced printed technologies, incorporated the high-entropy compound $Na_{1.38}Mn_{0.3}Fe_{0.3}Co_{0.133}Ni_{0.133}Cu_{0.133}[Fe(CN)_6]_{0.84}\square_{0.16} \cdot 0.92H_2O$ as the active layer.

Material characterization confirmed the structural and elemental homogeneity of the HE-PBA active layer. XRD verified the retention of the cubic framework while scanning electron microscopy and STEM-EDS mapping showed uniform distribution of the TM elements. Atomic force microscopy measurements indicated a smooth film morphology with a root mean square roughness of approximately 70 nm, ensuring consistent device performance. Electrochemical impedance spectroscopy (EIS) and cyclic voltammetry (CV) measurements supported the conclusion that Na^+ ion migration underpins the RS mechanism.

Electrical characterization highlighted the robust bipolar RS behavior of the memristor, with forming-free operation and low voltage thresholds ($V_{\mathrm{SET}} = -0.26\,\mathrm{V}$, $V_{\mathrm{RESET}} = 0.36\,\mathrm{V}$), as shown in Figure 6.4. Over 800 switching cycles, the device maintained a high $R_{\mathrm{OFF}}/R_{\mathrm{ON}}$ ratio of 10^4 with minimal power consumption ($P_{\mathrm{SET}} = 26\,\mu\mathrm{W}$, $P_{\mathrm{RESET}} = 8\,\mu\mathrm{W}$). Pulsed measurements further confirmed stable switching with retention exceeding 4×10^4 s. These experimental findings emphasize the advantages of HE-PBAs for energy-efficient, high-performance memory devices, including enhanced ionic conductivity, structural stability, and long-term reliability.

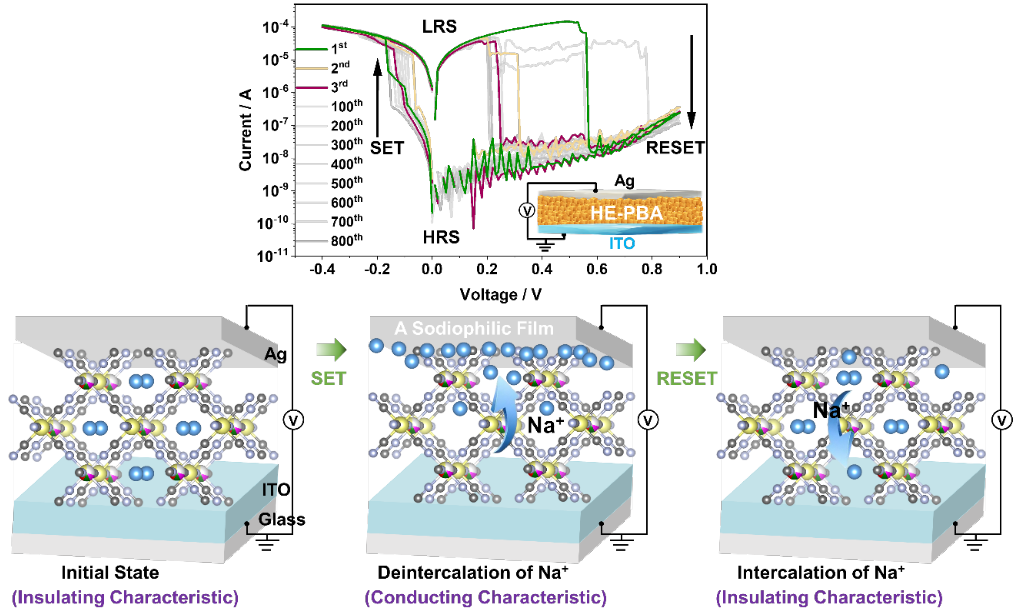

Figure 6.4: Summary of experimental results for HE-PBA-based memristors. The upper panel shows selected I–V curves (semi-logarithmic scale) from the 1st to the 800th cycle, illustrating consistent bipolar switching behavior. The inset provides a schematic representation of the device structure. The lower panel presents a proposed mechanism for RS, highlighting Na^+ ion migration and its role in modulating the device's conductivity.

Ag-based electrodes have been intensely investigated for rechargeable lithium or sodium metal batteries due to their high conductivity, excellent mechanical flexibility, and intrinsic lithiophilic or sodiophilic nature [389–391]. These properties are therefore considered fundamentally important for triggering the RS mechanism, as shown in Figure 6.4. The possible interactions between Na^+ and Ag differ from those between Na^+ and ITO, and most likely support the stability of the respective state. This could explain the excellent retention of over 4×10^4 s. During sweeping to negative potentials (with ITO grounded), the Na^+ ions diffuse toward the Ag electrode and accumulate there. It has been reported that the sodium diffusion, which results in a Na^+ deficiency in HE-PBA, and an applied potential leading to an electric field over the device, can lead to a change in conductivity. Importantly, this behavior contrasts with filamentary conduction mechanisms observed in many memristive devices [352]. When sweeping back to positive potentials, the Na$^+$ ions are released and reinserted into the HE-PBA layer, restoring its insulating state.

Building upon the experimental insights, the computational analysis delves into the atomic-level understanding of the RS mechanism in HE-PBAs. Using DFT calculations, the study focused on elucidating the role of Na$^+$ ion migration and its impact on the electronic structure of the system. I performed DFT calculations of HE-PBA with different Na concentrations. First, the relevant Na concentration at which the transition between conducting and insulating state occurs needed to be determined. By using DFT calculations to determine the reaction enthalpy (ΔH) associated with the changes of HE-PBA during the SET and RESET processes, the Na content (x) at the given potentials was found to be between 1.375 and 1.0. This was computed based on the chemical reaction

$$\begin{aligned}&\mathrm{Na_{x_1}Mn_{0.3}Fe_{0.3}Co_{0.133}Ni_{0.133}Cu_{0.133}[Fe(CN)_6] + Ag \longrightarrow}\\&\mathrm{Na_{x_2}Mn_{0.3}Fe_{0.3}Co_{0.133}Ni_{0.133}Cu_{0.133}[Fe(CN)_6] + (x_1 - x_2)Na}\,,\end{aligned} \tag{6.1}$$

where x_1 represents the initial number of sodium ions within the lattice, while x_2 denotes the number of sodium ions remaining in the lattice after the reaction. The difference ($x_1 - x_2$) corresponds to the number of ions released from the lattice, forming sodium metal. The results shown in Table 6.6 reveal that the reaction enthalpies (ΔH_1) for the complete Na removal process are significant across all examined concentrations, yielding a mean voltage $\bar{V}_1$ (2.3 V) much higher than the experimental average RS voltage of V_{SET} (-0.26 V) and V_{RESET} (0.36 V). Nonetheless, the considered reaction represents an extreme scenario where Na is fully removed from HE-PBA and forms sodium metal. The smaller experimental V_{SET} compared to the mean voltage derived from the DFT calculations suggests that Na atoms are not entirely extracted from the HE-PBA during the experiment. Instead, the atoms begin diffusing toward the Ag electrode under the influence of the applied electric field, adsorbing at the Ag|HE−PBA interface. The reaction enthalpy (ΔH_2) for such a process is calculated considering the following reaction

$$\begin{aligned}&\mathrm{Na_{x_1}Mn_{0.3}Fe_{0.3}Co_{0.133}Ni_{0.133}Cu_{0.133}[Fe(CN)_6] + Ag \longrightarrow}\\&\mathrm{Na_{x_2}Mn_{0.3}Fe_{0.3}Co_{0.133}Ni_{0.133}Cu_{0.133}[Fe(CN)_6] + (x_1 - x_2)Na|Ag}\,,\end{aligned} \tag{6.2}$$

where an Ag metal surface was used and a reaction between Na and Ag was allowed (denoted as Na|Ag). Employing a suitable methodology [391], I calculated the Na adsorption onto the (100), (110), and (111) crystal planes of silver metal, taking the average binding energies into account. As illustrated in Table 6.6, after accounting for the binding, the reaction enthalpy significantly decreases, and the average voltage $\bar{V}_2$ (0.66 V) now aligns more closely with the experimental V_{SET} and V_{RESET} values. The slight discrepancy between the theoretical predictions and experimental results may be attributed to the limitations of the simplified model. Although the model attempts to represent Na adsorption on the Ag electrode, it inherently simplifies the structure and interactions. Specifically, the model does not fully account for the complex and potentially infinite nature of the Ag crystal planes, nor does it comprehensively represent the complex Na-Ag interactions. These simplifications could be one of the main factors contributing to the observed differences [391]. Nevertheless, the DFT results demonstrate that the Na atoms are not fully extracted from HE-PBA to form Na metal. Rather, they likely bind at the interface with the Ag electrode, causing a bulk change in HE-PBA. This in turn gives rise to a low energy consumption and non-volatile character of the device. Furthermore, the formation of a complex Na-Ag network at the interface has been demonstrated previously by molecular dynamic simulation [391]. In comparison to the findings by Nguyen et al. [392], who demonstrated lithium migration from Li_xCoO_2 films into the silicon electrode in the RS device, this study provides an alternative mechanism, where Na atoms do not fully extract but rather diffuse and adsorb onto the Ag electrode.

x_1	x_2	ΔH_1 (kJ/mol)	$\bar{V}_1$ (V)	ΔH_2 (kJ/mol)	$\bar{V}_2$ (V)
1.3750	1.3125	13.1692	2.1838	3.2869	0.5451
1.3125	1.2500	14.1243	2.3422	4.2426	0.7035
1.2500	1.0000	57.4728	2.3827	17.9467	0.7440

Table 6.6: The calculated reaction enthalpy from DFT. ΔH_1 and ΔH_2 represent the reaction enthalpy calculated from Equations 6.1 and 6.2. The mean voltage is calculated by $\bar{V} = \frac{\Delta H}{(x_1 - x_2)F}$, where F is the Faraday constant.

Further DFT calculations were conducted to investigate the transition between the insulating and conducting state in the key HE-PBA concentration range between 1.375 and 1.0. This particular region was chosen based on prior observations that Li_xCoO_2 undergoes a transition from ceramic to metallic state with a minor compositional adjustment from $x = 1$ to 0.94 [393]. In analogy, I hypothesized that HE-PBA would exhibit a similar behavior. Therefore, I focused on concentrations proximate to the synthesized compound's concentration, starting at $x(\mathrm{Na}) = 1.375$ and extending toward lower concentrations down to 1.0. Considering that variations in Na content directly affect the electronic conductivity of the Ag/HE−PBA/ITO device, I examined the electronic structure of HE-PBA by calculating the total and projected density of states (pDOS). The results are shown in Figure 6.5. At $x(\mathrm{Na}) = 1.3125$, minor states associated with Co and C-coordinated Fe (Fe1) begin to overlap with the Fermi energy level, as detailed in the zoomed-in view of Figure 6.5b. This overlap increases the DOS at the Fermi level, enhancing the number of available charge carriers. As electrons can be easily excited to these states at room temperature, the excited electrons behave as free electrons that can move within the material, thus increasing the electrical conductivity. The general electronic system and the DOS that are assigned to each element in Figure 6.5b are a result of the interactions of the different elements incorporated in the HEM. These so-called cocktail effects seem to have a significant influence on the electronic band structure, enabling the superposition of the Fe1 and Co states to render the material conductive. This effect is more pronounced at $x(\mathrm{Na}) =$

1.25, where the DOS increases more at and around the Fermi level, indicating a transition to a metallic-like state. As a result, an enhancement in electrical conductivity is anticipated. With further decrease in Na content, the DOS at the Fermi energy level increases rapidly, indicating a stronger metallic character. This slight change in sodium concentration appears to be sufficient to alter the electrical properties of the films [392]. The same phenomenon has been observed, for example, in Li_xCoO_2, where studies show a nonmetal-metal transition with decreasing lithium content [393–395].

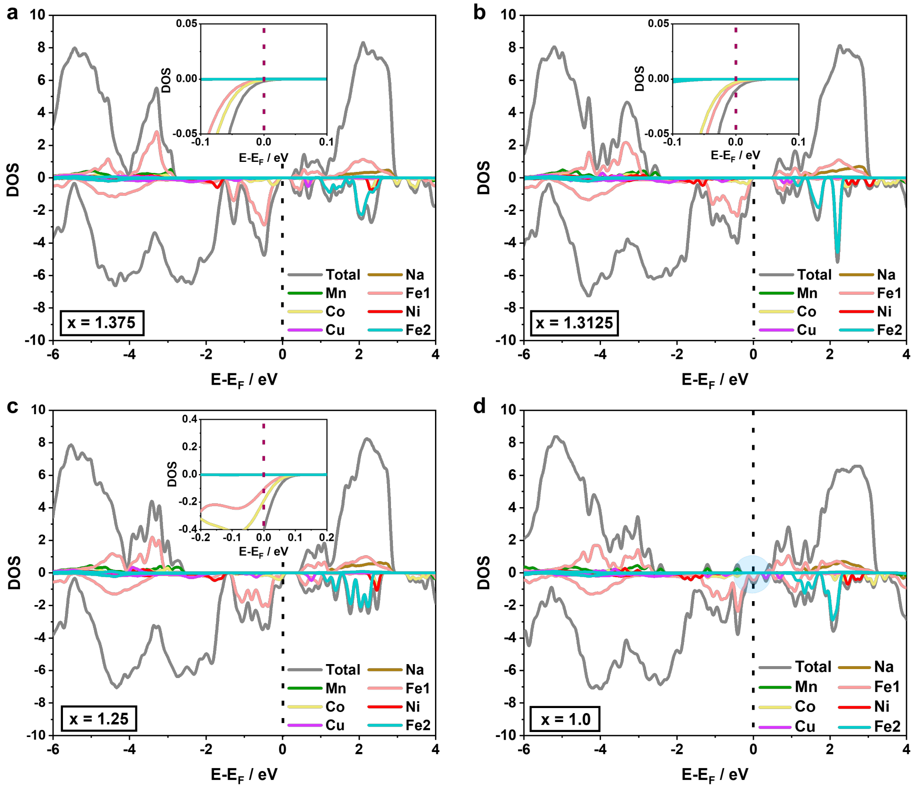

Figure 6.5: Total and projected DOS of $Na_xM[Fe(CN)_6]$ with (a) $x = 1.375$, (b) $x = 1.3125$, (c) $x = 1.25$, and (d) $x = 1.0$, with the Fermi energy shifted to 0. Panels (a), (b), and (c) include zoomed-in views of the DOS near the Fermi energy. Fe1 and Fe2 denote the C- and N-coordinated Fe, respectively.

In summary, a Na^+-modulated, non-volatile Ag/HE-PBA/ITO device is introduced, which has advantages such as low power consumption, self-compliance, and forming-free behavior in memory applications. The comprehensive experiments and simulation studies elucidate that the insulating-metallic transition arises from the extraction/insertion of Na^+ ions, rather than the formation/rupture of Ag conductive filaments proposed from other studies. Leveraging the low-energy process of Na^+ ion deintercalation/intercalation coupled with the Ag electrode, the Ag/HE – PBA/ITO device displays robust retention stability and a high R_{OFF}/R_{ON} ratio as a non-volatile memristor.

6.4 Summary

This chapter reports the results of three distinct studies that demonstrate the synergistic application of computational and experimental approaches to understanding and advancing HEMs for energy storage applications. Together, these investigations reveal the potential of high-entropy concepts in improving material performance while highlighting the critical role of computational methods in unraveling complex atomic-scale phenomena.

The first study examined the electronic structure and electrochemical behavior of HEFs for conversion-type LIBs. The calculated DOS revealed that the inclusion of multiple TMs, such as Cu and Mn, plays an important role in facilitating redox processes, while electrochemically inactive elements like Mg contribute to structural stability. The role of inherent disorder in enhancing lithium transport was particularly emphasized, highlighting the potential of HEFs as promising candidates for conversion-type cathodes [94].

The second study focused on HE-PW materials in SIBs. By systematically analyzing monoclinic PW cathodes with varying configurational entropy levels, the research demonstrated that compositional disorder not only suppresses unfavorable phase transitions but also reduces side reactions, thereby improving cycling performance and stability. The DFT results further validated the structural stability of HE-PW, providing a theoretical framework to explain the experimentally observed enhancements in cycling performance. This study provided clear evidence of entropy-driven enhancements in structural evolution and electrochemical behavior, paving the way for designing advanced battery materials with high configurational entropy [95].

The third study explored a novel Na^+-modulated HE-PBA memristor. DFT calculations revealed that the observed RS behavior arises from the insertion and extraction of Na^+ ions, in contrast to the formation of conductive filaments commonly observed in other memristive devices. The computational findings provided critical insights into the energy-efficient mechanisms underlying the observed insulating-metallic transition, demonstrating the potential of HEMs in overcoming challenges such as high power consumption in memory devices [316].

Collectively, these studies illustrate the value of advanced computational techniques in elucidating the atomic-scale properties of HEMs, enabling accurate predictions of structural and electrochemical behaviors. The strong alignment between computational findings and experimental results underscores the importance of integrating theory and experiment to tackle challenges in energy storage. Furthermore, the highlighted case studies exemplify how configurational entropy can enhance structural stability, suppress detrimental processes, and improve overall material performance. By addressing both opportunities and challenges, this work contributes to the broader understanding and application of HEMs in energy storage and electronic devices, marking a significant step toward meeting future energy demands.

7 Toward advanced techniques for computation of battery materials

In this chapter, advanced computational techniques that could be applied to address challenges in the modeling and optimization of ionic configurations in battery materials are presented. Specifically, two approaches have been explored: quantum annealing (QA) for Coulombic energy minimization and coupled clusters modeling for accounting for short-range order (SRO).

Section 7.1 demonstrates the application of QA, an emerging quantum computing-based technique, to solve the optimization problem of ionic configurations in disordered materials. By introducing a grand-canonical optimisation method to QA, an attempt was made to overcome the limitations imposed by long-range Coulomb interactions in ionic systems. The method was tested with the semi-lithiated $Li_{0.5}CoO_2$ system. With QA, the ground-state configuration with energy comparable to classical Monte Carlo (MC) approaches was successfully identified. My contributions to this work include developing a fully automated code for constructing matrices in the form of a quadratic unconstrained binary optimization (QUBO) problem, as required for the utilized QA devices, and performing DFT calculations to analyze the impact of electronic screening. This work was done under the guidance of Dr. Binninger, who performed all the tasks related to technical problem on QA and developed relevant algorithms. This section is based on the publication: T. Binninger, Y.-Y. Ting, P. M. Kowalski, and M. H. Eikerling. *Optimization of ionic configurations in battery materials by quantum annealing*. Phys. Rev. B, 110, L180202, 2024. doi: 10.1103/PhysRevB.110.L180202.

In Section 7.2, the role of SRO in disordered materials is investigated, focusing on lanthanide-phosphates ($(\mathrm{La, Ce, Pr, Nd})PO_4$) as test systems that are considered to be ideally mixed. Through a combination of cluster expansion (CE) and MC simulations, I systematically analyzed pair correlation functions to quantify the extent of SRO in the materials at elevated temperatures. The results indicate the persistence of SRO even in systems that tend to ideally mix. The results emphasize the importance of accounting for SRO in future research on HEMs. This study was conducted by myself with the guidance of Dr. Kowalski.

7.1 Optimization of ionic configurations by quantum annealing

7.1.1 Introduction

Modeling ionic arrangements in multielement compounds presents a significant computational challenge due to the exponential scaling of the configuration space. For a simulation cell with M sites, a fraction θ of which are occupied, the total number of configurations is approximately:

$$\binom{M}{\theta M} \approx \left[\theta^{-\theta}(1-\theta)^{-(1-\theta)}\right]^{M}. \tag{7.1}$$

Efficient sampling methods, such as CE, SQS or MC algorithms (see Chapter 2), are commonly used. QA offers a promising alternative for solving optimization problems in materials science. This approach maps the optimization problem onto an Ising-type Hamiltonian [396–398], which is minimized using adiabatic quantum evolution. With the emergence of commercially available hardware, such as the QA devices by D-Wave Systems Inc., such methods should be tested and deployed in materials science research.

In this study, lithium cobalt oxide (LCO) has been chosen as a test case. During charging/discharging of LCO, Li ions are extracted/intercalated according to the reaction 1.1, resulting in the formation/filling of vacancies across the Li-ion sublattice. The semi-lithiated state with $Li_{0.5}CoO_2$ stoichiometry has been targeted for modelling. The model cell, shown in Figure 7.1, comprises 36 Li sites, half of which are occupied and half are vacant. The problem consists of finding the ground-state configuration among the $\approx 10^{10}$ possible distributions of 18 Li ions over 36 available sites. This task is sufficiently complex for assessing the QA performance while being amenable for benchmarking against a classical method, such as replica exchange Monte Carlo (REMC) (see Chapter 2 for detail).

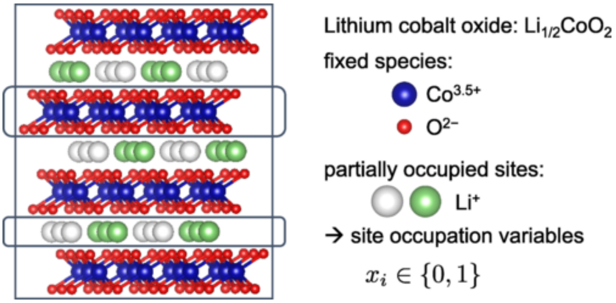

Figure 7.1: Layered crystal structure of LCO. The ground-state configuration of the Coulomb energy model is shown, with white and green spheres representing vacant and occupied Li sites, respectively.

7.1.2 Computational details

The DFT calculations were conducted with the setup described in Section 2.3. The applied Hubbard U parameter value of 4.6 eV for Co was derived from the linear-response method, and the k-point mesh was $3 \times 4 \times 2$.

7.1.3 Coulomb energy model and QUBO representation

The electrostatic Coulomb energy in Equation 2.35 serves as a cost function for optimization. Here, the summation goes over any pair of ions present in the lattice, Z_α are the respective valencies, and other constants have their usual meaning. Standard valencies of $Z_{\mathrm{Li}} = +1$ and $Z_{\mathrm{O}} = -2$ have been chosen for lithium cations and oxygen anions, respectively, and $Z_{\mathrm{Co}} = +3.5$, which is the (average) valency of cobalt cations in semi-lithiated LCO to provide overall charge neutrality. Assigning binary variables $x_i \in \{0, 1\}$ to represent lithium site occupation ($x_i = 1$ for occupied or $x_i = 0$ for vacant), the Coulomb energy can be reformulated as a QUBO problem, as required for present D-Wave QA devices:

$$E_{\mathrm{coul}} = \text{const.} + \sum_{i \in \mathcal{S}_{\mathrm{Li}}} Q_{i,i} x_i + \sum_{i<j \in \mathcal{S}_{\mathrm{Li}}} Q_{i,j} x_i x_j . \tag{7.2}$$

Here, const. $= \frac{e^2}{4\pi\epsilon_0} \sum_{i<j \in \mathrm{fix}} \frac{Z_i Z_j}{|r_i - r_j|}$ is the Coulomb interaction energy among all fixed ions, i.e., cobalt cations and oxygen anions. The coefficients $Q_{i,i} = \frac{e^2}{4\pi\epsilon_0} \sum_{j \in \mathrm{fix}} \frac{Z_j}{|r_i - r_j|}$ and $Q_{i,j} = \frac{e^2}{4\pi\epsilon_0} \frac{1}{|r_i - r_j|}$ correspond to the Coulomb interaction between a given Li site i and fixed species, and between a given pair of Li sites, respectively.

Due to periodic boundary conditions, each variable x_i represents a given Li site of the model cell plus all of its periodic images. To ensure that long-range Coulomb interactions are properly accounted for, I employed Ewald summation routines available in the `pymatgen` library for Python to compute the QUBO coefficients $Q_{i,i}$ and $Q_{i,j}$ under periodic boundary conditions. The constant term was obtained as the Ewald energy of the simulation cell with only fixed species present. To determine $Q_{i,i}$, simulation cells with only one occupied Li site i and all fixed ion species were constructed. The respective Ewald energies were corrected by subtracting the constant term to avoid overcounting the interaction energy among fixed species. The coefficients $Q_{i,j}$ were obtained from the Ewald energies of simulation cells with only Li ions on sites i and j present (without any fixed ions). To avoid double counting, the respective energies were corrected for the self-energies of sites i and j, i.e., the interaction energy of Li ions on a single given site and all of its periodic images (which is already accounted for in the respective diagonal terms $Q_{i,i}$). I note that simulation cells comprising only a subset of ion species are not charge-balanced. The Ewald method automatically adds a neutralizing homogeneous background charge to prevent divergence of the electrostatic energy. However, due to charge neutrality of the overall system, background charge contributions mutually cancel and do not affect the total Coulomb energy of Equation 7.2. The obtained QUBO coefficients for LCO were derived by me and are: const. $= -4212.68\,\text{eV}$, $Q_{i,i} = -9.40\,\text{eV}$, and $-1.04\,\text{eV} \leq Q_{i,j} \leq 2.02\,\text{eV}$ for $i < j$ ($Q_{i,j} = 0$ for $i > j$).

7.1.4 Challenges in stoichiometry enforcement

Initially, minimization of the bare Coulomb energy cost function resulted in $x_i = 1$ for all 36 Li sites, i.e., complete occupation of the Li sublattice. Unlike in classical sampling algorithms, the search space cannot be restricted to the target stoichiometry in QA. To achieve the target stoichiometry of $N_{\text{Li}}^{\text{target}} = 18$, a penalty term has been introduced

$$\lambda \left(\sum_i x_i - N_{\text{Li}}^{\text{target}} \right)^2 , \tag{7.3}$$

where $\sum_i x_i = N_{\text{Li}}$ is the total number of Li ions for a given configuration, and λ is a parameter controlling the strength of the constraint. With increasing λ, the average Li number $\overline{N}_{\text{Li}}$ of the output configurations from 1000 independent annealing runs decreased toward the desired value of 18. However, this improvement came at the cost of an increased fraction of broken qubit chains, rendering many solutions unreliable. While this issue could be mitigated by simultaneously increasing the chain strength parameter, the results still were not optimized. The respective minimum value of the Coulomb energy of $-4427.08\,\text{eV}$ is significantly larger than the minimum energy of $-4432.64\,\text{eV}$ obtained with classical REMC sampling. The poor performance of the QA method arises from the large value of $\lambda = 5$ required for the stoichiometry constraint, which adds a value of $2\lambda = 10$ to the off-diagonal elements of the coefficient matrix, a factor of 5–10 larger in magnitude than the off-diagonal contributions resulting from the Coulomb energy. As a result, the stoichiometry constraint dominates the cost function, effectively masking the Coulomb energy terms and hindering optimization efficiency.

To overcome this, a grand-canonical optimization method is introduced. Figure 7.2(a) shows the average energy of sampled configurations as a function of the average Li number (blue curve with markers). A negative slope is apparent, explaining (i) why minimization of the bare energy resulted in complete lithiation and (ii) why a large quadratic penalty λ is required to enforce a minimum of the cost function close to the target stoichiometry of 18. Within the Coulomb energy model, the local slope at the target stoichiometry can be interpreted as the chemical potential,

$$\mu = \frac{\partial \overline{E}_{\text{coul}}}{\partial \overline{N}_{\text{Li}}}, \tag{7.4}$$

and rotate the energy curve by performing a Legendre transformation from Coulomb energy to the grand-canonical cost function $E_{\text{coul}} - \mu N_{\text{Li}}$. Using the fitted value of $\mu = -13.38\,\text{eV}$

(dashed line in Figure 7.2(a)), the cost function becomes flat around the target stoichiometry with a slightly negative curvature (green curve in Figure 7.2(a)). Then, the quadratic penalty term of Equation 7.3 with a small value of $\lambda = 0.2$ is sufficient to bend the cost function upward and produce a minimum at the target Li number (red curve in Figure 7.2(a)). As a linear transformation, it only shifts the diagonal elements of the QUBO matrix by a constant $-\mu$, thus avoiding the aforementioned problem of masking off-diagonal elements. The resulting grand-canonical cost function is expressed as:

$$E_{\mathrm{gc}} = E_{\mathrm{coul}} - \mu N_{\mathrm{Li}} + \lambda \left(\sum_i x_i - N_{\mathrm{Li}}^{\mathrm{target}} \right)^2 , \tag{7.5}$$

where E_{coul} is given by Equation 7.2. Here, the objective still consists of identifying the energetic *ground state* at a given target stoichiometry.

Applying this method with a fine-tuned chemical potential of $\mu = -13.2\,\mathrm{eV}$ and a mild value of $\lambda = 0.2$, significantly better performance of the QA procedure was obtained. The minimum of returned Coulomb energies at the target stoichiometry was $E_{\mathrm{coul}}^{\mathrm{min}} = -4432.64\,\mathrm{eV}$, which is identical to the minimum energy obtained from the benchmark REMC sampling. The proposed grand-canonical method thus makes the fully connected Coulomb energy model feasible for optimization by QA, which is the main result of the present work. The respective ground-state configuration is shown in Figure 7.1. The row-like Li ordering is in agreement with previous computational and experimental findings for semi-lithiated LCO [399–401].

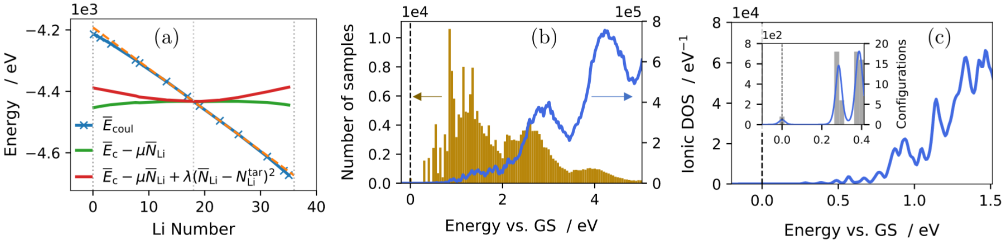

Figure 7.2: (a) Average energy vs. Li number for LCO as obtained from the bare Coulomb energy model of Equation 7.2 (blue curve with markers), after applying a Legendre transformation with $\mu = -13.38\,\mathrm{eV}$ (green curve), and including the quadratic penalty term of Equation 7.3 with $\lambda = 0.2$ (red curve). (b) Histogram of Coulomb energies obtained from QA with the grand-canonical method ($\mu = -13.2\,\mathrm{eV}$ and $\lambda = 0.2$). Only samples with $N_{\mathrm{Li}} = 18$ were counted. The energy is given relative to the ground-state (GS) energy ($E_{\mathrm{coul}}^{\mathrm{min}} = -4432.64\,\mathrm{eV}$); i.e., what is shown is the difference $E_{\mathrm{coul}} - E_{\mathrm{coul}}^{\mathrm{min}}$. The ionic configurational density of states (DOS) of the Coulomb energy model, determined by REMC sampling, is shown for comparison (blue curve). (c) Ionic DOS, obtained from REMC sampling, in the energy range around the GS (blue: DOS curve with thermal broadening, left-hand axis; gray bars in inset: DOS histogram, right-hand axis).

7.1.5 Results and discussion

A deeper analysis of the D-Wave sampling statistics is presented. Figure 7.2(b) shows a histogram of the Coulomb energies returned from 400,000 annealing runs (only using results with $N_{\mathrm{Li}} = 18$ and without any chain breaks). A broad distribution of energies is obtained, with most of the samples being a few eV above the GS, whereas the true minimum energy solution was returned in only 0.083% of annealing runs. At first glance, this appears to be a rather low optimization efficiency. However, the configurational DOS of the underlying model must be analyzed for a fair assessment of the statistics [402]. The ionic DOS of the Coulomb energy model, $N_{\mathrm{DOS}}(E)$, was obtained from extended REMC sampling runs. It is shown as a blue curve in Figure 7.2(b), with close-ups around the GS energy in Figure 7.2(c). The essential structure of the QA sampling histogram (golden bars in Figure 7.2(b)) reflects the shape of the underlying DOS. Assuming that each configuration is sampled with a certain "intrinsic" probability, $p(E)$, that only depends on the respective energy, the overall sampling rate, $N(E)$, is proportional to $p(E)$ times the number of states with energy E, i.e., the configurational DOS:

$$N(E) \propto p(E) \cdot N_{\mathrm{DOS}}(E). \tag{7.6}$$

To extract $p(E)$, the QA sampling histogram was normalized with the configurational DOS. The result is shown in Figure 7.3(a). A monotonically decreasing probability as a function of energy is obtained, clearly indicating that the lower energy configurations are sampled with higher probability, with the ground-state configuration having the highest sampling probability. The obtained $p(E)$ curve is well reproduced by a Boltzmann-type exponential, $\exp(-E/kT)$, with a fitted value of $kT = 0.31$ eV (orange curve).

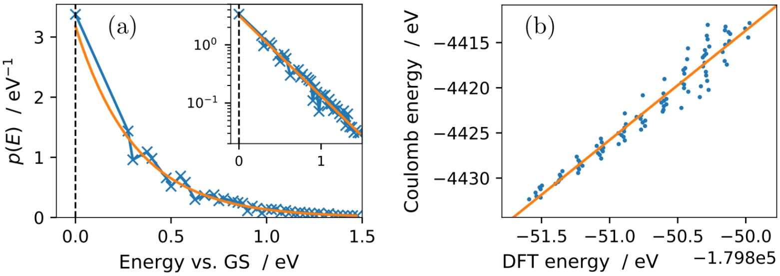

Figure 7.3: (a) Intrinsic sampling probability per energy, $p(E)$, obtained by dividing the overall sampling rate by the configurational DOS. Orange fitted curve: Boltzmann-type exponential $\exp(-E/kT)$. Inset: Same data shown on a logarithmic scale. (b) Comparison of the Coulomb energy vs. DFT energy for 100 different ionic configurations of semi-lithiated LCO.

At first glance, the fitted value of $kT = 0.31$ eV indicates "hot" sampling of the configurational space. However, the effective temperature scales with the energy scale of the problem. The Coulomb energy of Equation 7.2 represents a hard energy model, because it neglects dielectric screening. Including the latter in the form of a dielectric constant, ε_r, scales down all energies, and thus the effective sampling temperature. To estimate ε_r, I have computed the DFT energies of 100 randomly selected ionic configurations. Figure 7.3(b) reveals a linear correlation between the Coulomb and corresponding DFT energies, which demonstrates the physical meaningfulness of the ionic Coulomb energy model for LCO. Since DFT energies implicitly include the effect of electronic screening, the slope of the plot in Figure 7.3(b) is interpreted as an effective dielectric constant, $\varepsilon_r = 12$, which reduces the effective sampling temperature to $kT/\varepsilon_r = 0.026$ eV, i.e., room temperature.

In summary, this section presents an efficient grand-canonical optimization method, which renders QA feasible for sampling the ionic ground state based on a fully interacting Coulomb energy model. The method has been demonstrated on a D-Wave Advantage$^{\text{TM}}$ quantum annealer to successfully identify the lowest energy arrangement of lithium ions in LCO. Boltzmann-type output statistics were observed with the highest sampling probability for the ground-state configuration. QA and the grand-canonical optimisation approach are expected to become the methods of choice in the future for materials-structure optimisation problems.

7.2 Modeling short-range order

7.2.1 Introduction

The studies in Chapters 4 and 5 illustrate how the interplay between element selection, local environment, and subsequent mechanisms influences electrochemical performance. In chapter 4, the result indicates that the local environment affects TM stability and, consequently, oxygen stability, which in turn drives secondary phase formation in certain HEMs. In Chapter 5, the result indicates that the ionic configuration strongly impacts thermodynamic predictions—particularly the distribution of metal cations. Accurate modeling of HEMs thus requires realistic input structures. In this section, I investigated the formation of SRO in a mixed-cation test case via a more computationally demanding CE. I generated a large, disordered structure using MC methods at high temperatures, as HEM are usually synthesized at evaluated temperatures, and analyzed pair correlations between cations.

To study the SRO, I selected a simple model that converges well with the DFT test system: lanthanide phosphate $(\mathrm{La}, \mathrm{Ce}, \mathrm{Pr}, \mathrm{Nd})\mathrm{PO}_4$ with an equal-atomic ratio of mixing. Phosphate-type material was specifically chosen because it is a practical material for batteries, known for its structural stability, abundance, and low cost [403]. The considered monazite structure of lanthanide phosphates can accommodate varying compositions of light lanthanide elements, ranging from La to Tb [404, 405]. The monazite-type structure exhibits high mixing capability, making it an excellent candidate for investigating the effects of SRO [406–408].

7.2.2 Computational details

The pair correlation functions describe the probability of finding specific atomic pairs within a defined distance range. For a given structure, the Cartesian positions of atoms were extracted, and a pairwise distance matrix D_{ij} was computed. Neighbors within a specific range ($D_{\text{min}} \leq D_{ij} \leq D_{\text{max}}$) were identified for each atom. For the system studies in this section, the D_{min} and D_{max} are 4.0 Åand 5.0 Å, respectively. Observed counts of neighbors for each center atom i were normalized to calculate the probability distribution P_{ij}:

$$P_{ij} = \frac{n_{ij}}{N_i}, \tag{7.7}$$

where n_{ij} is the observed count of species j as neighbors to species i, and $N_i = \sum_j n_{ij}$ is the total number of neighbors around i.

The deviation of observed pair distributions from an ideal random distribution is quantified using the mean absolute error (MAE). The ideal random distribution assumes equal probabilities ($P^{\text{ideal}} = 0.25$ for the studied system) for each species. The MAE for a central atom i is given by:

$$\text{MAE}_i = \frac{1}{n} \sum_j \left| P_{ij} - P^{\text{ideal}} \right|, \tag{7.8}$$

where n is the number of neighbor species j.

The Warren-Cowley SRO parameter quantifies the degree of ordering or clustering between species i (center atom) and j (neighbor atom). It is expressed as

$$\alpha_{ij} = 1 - \frac{P_{ij}}{c_j}, \tag{7.9}$$

where c_j is the bulk concentration of species j. $\alpha_{ij} = 0$ corresponds to a random distribution, $\alpha_{ij} < 0$ indicates clustering preference (higher probability of i-j pairs than random), and $\alpha_{ij} > 0$ suggests a segregation tendency (lower probability of i-j pairs than random). To capture the ordering in the entire system, the overall SRO parameter was computed as a weighted average of α_{ij} values, with the probabilities P_{ij} serving as weights:

$$\text{Overall SRO} = \frac{\sum_{i,j} P_{ij}\alpha_{ij}}{\sum_{i,j} P_{ij}}. \tag{7.10}$$

The radial distribution function (RDF) provides insights into the spatial arrangement of atomic pairs in the system by describing the probability of finding a pair of atoms separated by a specific distance r. For this study, RDFs were computed using `vasppy` library with input structures obtained from MC simulations. The RDF is defined as:

$$g(r) = \frac{n(r)}{4\pi r^2 \Delta r \rho}, \tag{7.11}$$

where $n(r)$ is the number of atom pairs separated by a distance r, Δr is the bin width, and ρ is the average atomic density. The calculations of pair correlation and Warren-Cowley SRO are implemented using `pymatgen` library. Cartesian coordinates were extracted from the structures sampled by MC at 1000K and 2000K, and pairwise distance matrices were computed to identify neighbors. The RDF calculations were carried out for all unique atomic pairs (La-La, La-Ce, etc.) with a bin width of $\Delta r = 0.1$, and the resulting data were smoothed using a Gaussian broadening technique with $\sigma = 0.1$.

DFT calculations were performed on 291 structures automatically generated using the ATAT package to construct the CE. These structures were selected by ATAT to optimally fit the effective cluster interaction (ECI) coefficients in the CE. For simplicity, DFT calculations were conducted without considering the Hubbard U parameters. To ensure the uniform accuracy of K-points throughout the search process, I set KPPRA (K-point per reciprocal atom) to 500, allowing the package to generate a suitable K-point grid automatically. The rest of the computational setup followed the methodology outlined in Section 2.3.

7.2.3 Results and discussion

The observed distributions, MAE values, and Warren-Cowley SRO parameters for 1000 K and 2000 K are summarized in Table 7.1. The results demonstrate that SRO persists in $(\mathrm{La, Ce, Pr, Nd})\mathrm{PO}_4$ even at elevated temperatures, despite the expectation of ideal mixing in the system. At 1000 K, deviations from the ideal random distribution are observed, with clear clustering and segregation tendencies indicated by the SRO parameters. The overall SRO value at 1000 K is -0.005. The deviations decrease at 2000 K, reflecting the increased randomness at increased temperature, with an overall SRO of -0.002. However, the nonzero SRO values at both temperatures suggest that local atomic arrangement tendencies are substantial and are expected to be more pronounced when lowering the temperature toward ambient conditions. As shown in Figure 7.4, the SRO parameters approach zero at 2000 K compared to 1000 K. This trend reflects the expected increase in configurational entropy with temperature, which drives the system toward a more randomized atomic distribution. Nonetheless, even at 2000 K, the SRO parameters remain slightly negative or positive for specific pairs, underscoring persistent local preferences that deviate from ideal mixing.

The RDF analysis provides additional insights into the pair correlation functions. The RDFs analyzed for 1000 K and 2000 K, shown in Figure 7.5, illustrate the changes in the atomic pair correlations with temperature. For instance, at 1000 K, the La-La pair exhibits a prominent peak at 4.2 Å, indicating a higher likelihood of La-La pairs at short distances. In contrast, at 2000 K, the Ce-Ce pair becomes more dominant, suggesting that temperature-induced randomness affects atomic distributions differently for various species. These observations confirm that temperature could impact local atomic arrangements and the overall ionic distribution.

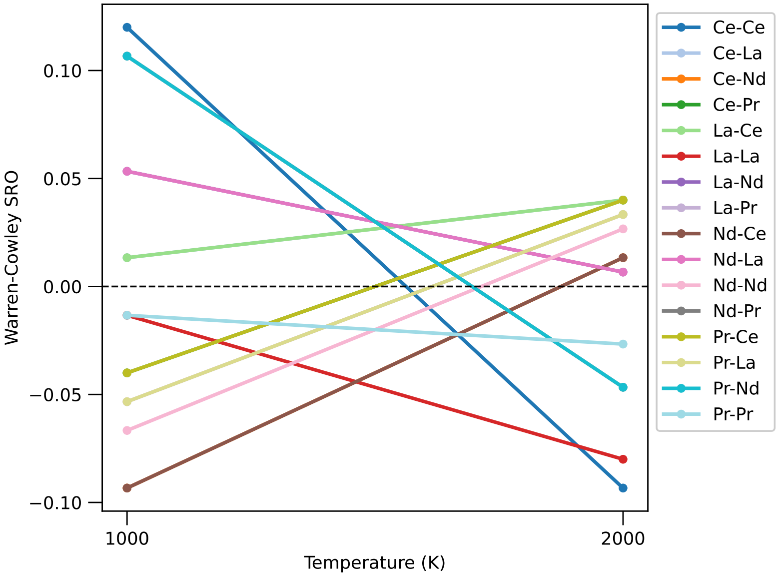

Figure 7.4: Change in Warren-Cowley SRO parameters for (La, Ce, Pr, Nd)PO_4 across temperatures. The overall SRO values are -0.005 at 1000 K and -0.002 at 2000 K.

In summary, the existence of SRO in monazite (La, Ce, Pr, Nd)PO_4 system emphasizes the importance of carefully considering local atomic ordering when constructing realistic input structures of HEMs for DFT simulations. Despite the monazite structure shows good solubility, SRO persists even at elevated temperatures. These findings underscore that accounting for SRO is crucial for accurately capturing the thermodynamic behavior and intrinsic properties of HEMs. Furthermore, this study shows that SRO can be systematically analyzed using CE combined with MC simulations. The resulting pair correlation functions from CE+MC simulations can be integrated into the construction of partially ordered special quasirandom structures (SQS). By

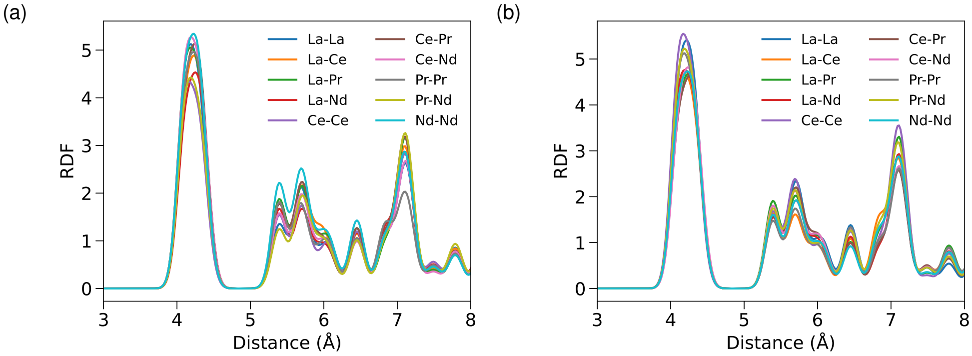

Figure 7.5: Radial distribution function (RDF) for (La, Ce, Pr, Nd)PO_4 at (a) 1000 K and (b) 2000 K.

distributing atoms based on the pair correlations derived from SRO analysis, one can obtain more realistic structural inputs that better represent the configurations of HEMs as synthesized at elevated temperatures. Such enhanced SQS models can improve the accuracy of computational predictions of thermodynamic properties, leading to a more accurate description of the electronic structure. I foresee that by incorporating SRO into SQS, future studies can better capture the interplay between local atomic environments and the electrochemical performance of HEMs, ultimately accelerating the design and optimization of these materials for energy storage applications.

7.3 Summary

In this chapter, I demonstrate two innovative approaches to modeling ionic configurations beyond conventional methods. First, I present a successful case of minimizing the Coulomb energy model using QA, an emerging quantum computing-based computational technique. The Coulomb energy problem is reformulated into a QUBO problem, incorporating constraints for target stoichiometry and applying a Legendre transformation to the Coulomb energy cost function. This approach significantly reduces the effective coupling strengths of the fully connected QUBO problem, which is essential for QA effectiveness. It is further shown that the obtained overall sampling rate can be interpreted as a product of "intrinsic" probability and configurational DOS. After normalization, a Boltzmann-type probability curve with the highest sampling probability for the ground-state configuration is observed. It is expected that similar computational techniques will be applied on a regular basis for the derivation of structural models of HEMs in the decades to come.

Second, I showcase the role of SRO in mixed-cation systems, using a phosphate-type material, namely $(\mathrm{La}, \mathrm{Ce}, \mathrm{Pr}, \mathrm{Nd})\mathrm{PO}_4$, with an equal-atomic mixing ratio as a test case. Despite the high mixing tendency in lanthanide phosphate, which is often considered to have ideal mixing, the persistence of SRO is demonstrated. To obtain a more realistic structure representing the real system, I performed CE and MC simulations at temperatures of 1000 K and 2000 K. The results show that as temperature increases, the overall SRO parameter approaches 0, corresponding to a more random distribution. However, SRO persists even at the considered high temperatures, indicating its non-negligible impact, especially under conditions closer to ambient temperature. This finding highlights the need to account for local atomic arrangements when aiming at accurately predict the thermodynamic behavior and inherent properties of HEMs. I further suggest integrating pair correlations derived from the combination of CE and MC methods into SQS-like model structures to create a more realistic ionic configuration that accounts for SRO. This more realistic input structural model should enable more accurate electronic structure calculations.

The tested novel approaches to modeling ionic structures in mixed-element materials represent a step toward more realistic modeling of disordered battery materials and enhancing the accuracy of insights into their electrochemical performance. I hope that these demonstrated cases pave the way for more precise modeling and understanding of complex material systems, ultimately contributing to the development of improved energy storage solutions.

Temperature (K)	Center Atom	Neighbor	Observed Distribution	MAE	SRO (α_{ij})
1000	La	La	0.253	0.0083	-0.013
		Ce	0.247		0.013
		Pr	0.263		-0.053
		Nd	0.237		0.053
	Ce	La	0.247	0.0167	0.013
		Ce	0.220		0.120
		Pr	0.260		-0.040
		Nd	0.273		-0.093
	Pr	La	0.263	0.0133	-0.053
		Ce	0.260		-0.040
		Pr	0.253		-0.013
		Nd	0.223		0.107
	Nd	La	0.237	0.0200	0.053
		Ce	0.273		-0.093
		Pr	0.223		0.107
		Nd	0.267		-0.067
2000	La	La	0.270	0.0100	-0.080
		Ce	0.240		0.040
		Pr	0.242		0.033
		Nd	0.248		0.007
	Ce	La	0.240	0.0117	0.040
		Ce	0.273		-0.093
		Pr	0.240		0.040
		Nd	0.247		0.013
	Pr	La	0.242	0.0092	0.033
		Ce	0.240		0.040
		Pr	0.257		-0.027
		Nd	0.262		-0.047
	Nd	La	0.248	0.0058	0.007
		Ce	0.247		0.013
		Pr	0.262		-0.047
		Nd	0.243		0.027

Table 7.1: Observed distributions, MAE, and Warren-Cowley SRO parameters for (La, Ce, Pr, Nd)PO_4 at 1000 K and 2000 K.

8 Summary and outlook

8.1 Summary

In this thesis, I employed advanced DFT-based calculations to investigate the fundamental properties of high-entropy materials (HEMs) in energy storage applications, with the main focus on intercalation-type Li-ion batteries (LIBs). HEMs are promising materials that could enhance battery performance, such as increasing specific capacity. Atomistic calculations could serve as a valuable tool to accelerate the design process of these materials. However, achieving an accurate atomistic-level understanding of these materials is challenging. Transition metals (TMs), which are critical for redox electrochemical reactions in batteries, represent a challenge to DFT-based methods due to the presence of strongly correlated *d* electrons. Moreover, the disordered nature of HEMs cannot be easily captured by simple computational models.

Here, I explicitly addressed the challenge of strongly correlated and highly localized electrons in TMs with the aim of developing a more robust description of the electronic structure of battery materials. This is essential for the accurate prediction of properties such as oxidation states and bandgaps, which are key parameters to describe the performance of battery materials. I focused on enhancing the DFT$+U$ approach for describing these strongly correlated electrons. To avoid the arbitrary selection of the Hubbard U parameter values, I employed the linear-response method to derive U from first principles. Additionally, instead of using standard atomic projections in DFT$+U$ scheme, I utilized more realistic Wannier function (WF)-based projectors. This advanced approach — DFT+U(WF) — was benchmarked on a set of simple oxides, conventional cathode materials, and ultimately HEMs. The results demonstrated that DFT$+U$(WF) yields a more accurate description of electronic structures compared to traditional methods, including DFT+U, thus providing more reliable electronic structure that align closely with experimental data. I also compared this methodology with computationally expensive approaches like SCAN and HSE hybrid functionals, finding that DFT+U(WF) achieves comparable accuracy with significantly lower computational cost.

Building on this advanced computational methodology, I investigated the performance and thermodynamic behavior of HE cathodes. Aiding experimental research with DFT-based calculations, I unraveled mechanisms contributing to severe capacity degradation in certain HE cathodes. Specifically, Ni/Li site interchange, oxygen dimer formation, and TM migration during cycling were found to promote secondary phase formation. These secondary phases reduce electrochemical activity and conductivity while accelerating capacity fading. I found that while configurational entropy contributes to stabilizing disordered phases in HEMs, it is insufficient to counterbalance the enthalpy-driven formation of secondary phases. Thus, when harnessing the “high-entropy” effect, one must also consider potential destabilizing processes arising from the increased disorder.

Motivated by these findings, I turned the attention to solid electrolytes—materials that typically avoid strongly correlated *d* electrons, allowing us to isolate the effects of atomic arrangements on thermodynamic stability. In concerted work with experimental partners, I designed garnet-type solid electrolytes with varying dopant compositions, each selected to minimize the computed Gibbs energy, and explored how different ionic distributions influence stability. The results revealed that increasing dopant diversity stabilizes higher-conductivity cubic phases over lower-conductivity tetragonal phases at room temperature. I found that the main stabilizing factor is the enthalpy of mixing, while configurational entropy plays a secondary yet non-negligible role. Moreover, I observed that metal distribution heavily affects thermodynamic stability, and disordered phases are favored over ordered ones. Experimentally, the partners synthesized these compounds and achieved higher ionic conductivity at reduced synthesis temperatures for one specific composition.

Going beyond the application of HEMs in LIBs, I explored the broader potential of HEMs through collaborative studies combining theory and experiment conducted by the experimental partners. This dissertation demonstrates the potential of high-entropy fluorides (HEFs) as conversion-type LIB cathodes by leveraging the high-entropy effect and incorporating electrochemically inactive elements for improved phase stability. Likewise, high-entropy Prussian whites (HE-PWs) exhibit enhanced cycling performance in sodium-ion batteries due to entropy-driven suppression of phase transitions and side reactions. Additionally, a non-volatile memristor based on a high-entropy Prussian blue analogue (HE-PBA) has been investigated, which utilizes sodium-ion modulation to achieve resistive switching behavior and provides robust retention stability. These studies highlight the versatility of HEMs in various energy storage and electronic applications.

Finally, this dissertation demonstrates the potential of advancing and emerging computational methods for modeling energy materials. In pioneering studies, the applicability of quantum annealing (QA) has been demonstrated for efficient sampling of ionic distributions in structural models of battery materials. Additionally, I also highlighted the importance of considering short-range ordering (SRO) for constructing realistic models of HEMs for DFT calculations. The results revealed that SRO persists even in seemingly ideal mixed cases and at elevated temperatures and it should be considered in the realistic modeling of HEMs. This observation has important implications for future research, as this dissertation research clearly demonstrates that local atomic arrangements in HEMs significantly influence various material properties, including degradation mechanisms and thermodynamic behavior. I therefore suggest to combine various state-of-the-art methods to obtain a more "realistic" structural model for accurate computation of electronic structures in disordered energy materials.

In summary, this thesis provides critical insights into the principles governing HEMs for energy storage applications and serves as guidance for further, more realistic simulation-based research on these materials. By proposing more accurate descriptions of electronic structures and providing insights into how ionic arrangements influence material properties, I addressed fundamental challenges in understanding disordered systems at an atomistic level. The methodologies developed here not only improve predictive accuracy but also pave the way for designing next-generation battery materials with enhanced stability and performance. By combining advanced computational techniques with experimental validation, this dissertation helps simulation-driven research on HEMs and speed up the process of designing next-generation battery materials with enhanced stability and performance.

8.2 Outlook

This thesis has addressed several challenges in computational modeling HEMs for energy storage applications, but it also raises important questions and highlights potential challenges in future research.

Firstly, while the DFT+U(WF) approach has shown good agreement with the results computed with hybrid functionals and experimental data in the systems studied here, further testing is required to assess its general applicability. In particular, systems with significant hybridization between d-orbitals and other orbitals — where d-electrons are more delocalized — may present challenges. The degree of hybridization could influence whether DFT+U(WF) is suitable for a given system. Additionally, in Chapter 4, I rescaled the U values derived from the linear-response method to better match experimental bandgaps, similar to how the mixing parameter in hybrid functionals like HSE06 is adjusted. Since U represents on-site Coulombic interactions, this rescaling might reflect the degree of d-electron localization. Investigating this relationship further could provide valuable insights into the limitations and applicability of DFT+U(WF). Another limitation lies in the current implementation of Wannier function-based projectors (pmw.x), which does not support force calculations for structural relaxation, which severely limits further testing and applications of this approach. Future work should focus on extending this implementation to include force calculations, enabling structural optimizations and expanding the scope of this methodology.

In addition to methodological improvements, the findings highlight the critical role of local atomic environments in determining materials properties. In Chapter 4, I observed that local environments significantly influence structural stability during cycling processes. In Chapter 5, I demonstrated that the distribution of metal cations strongly affects computed thermodynamic properties. Furthermore, in Chapter 7, I showed that SRO persists even in systems considered as "well-mixed." These findings underscore the necessity of incorporating SRO into structural models used for simulations of complex disordered materials like HEMs. To address this, I propose a more accurate modeling approach that integrates SRO into special quasi-random structures (SQS) used as inputs for DFT calculations. Specifically, pair correlations derived from the cluster expansion (CE) and Monte Carlo (MC) simulations can be incorporated into SQS construction. This approach offers a significant advantage by mimicking the "actual" representative configuration of a HEM, reflecting realistic ionic ordering rather than fully randomized ionic structures. By combining CE-derived pair correlations with SQS models, this method could offer a potential solution for self-consistent computation of ionic and electronic structures. Ultimately, I expect that the advancements considered in this dissertation will enhance the predictive power of computational electrochemistry and accelerate the development and optimization of HEMs for energy storage applications.

Bibliography

[1] N. Abas, A. Kalair, and N. Khan. *Review of fossil fuels and future energy technologies*. Futures, 69, 31–49, 2015. doi: 10.1016/j.futures.2015.03.003.

[2] D. J. Soeder. *Fossil Fuels and Climate Change*. In *Fracking and the Environment: A scientific assessment of the environmental risks from hydraulic fracturing and fossil fuels*, pages 155–185. Springer International Publishing, 2021. doi: 10.1007/978-3-030-59121-2_9.

[3] B. Lin and O. E. Omoju. *Focusing on the right targets: Economic factors driving non-hydro renewable energy transition*. Renewable Energy, 113, 52–63, 2017.

[4] T. P. Barnett, J. C. Adam, and D. P. Lettenmaier. *Potential impacts of a warming climate on water availability in snow-dominated regions*. Nature, 438, 303–309, 2005. doi: 10.1038/nature04141.

[5] C. Mora, B. Dousset, I. R. Caldwell, F. E. Powell, R. C. Geronimo, C. R. Bielecki, C. W. W. Counsell, B. S. Dietrich, E. T. Johnston, L. V. Louis, M. P. Lucas, M. M. McKenzie, A. G. Shea, H. Tseng, T. W. Giambelluca, L. R. Leon, E. Hawkins, and C. Trauernicht. *Global risk of deadly heat*. Nature Clim Change, 7, 501–506, 2017. doi: 10.1038/nclimate3322.

[6] I. P. on Climate Change (IPCC). *Global Warming of 1.5℃: IPCC Special Report on Impacts of Global Warming of 1.5℃ above Pre-industrial Levels in Context of Strengthening Response to Climate Change, Sustainable Development, and Efforts to Eradicate Poverty*. Cambridge University Press, 2022. doi: 10.1017/9781009157940.

[7] N. Lefèvre. *Measuring the energy security implications of fossil fuel resource concentration*. Energy Policy, 38, 1635–1644, 2010. doi: 10.1016/j.enpol.2009.02.003.

[8] H. C. Hesse, M. Schimpe, D. Kucevic, and A. Jossen. *Lithium-Ion Battery Storage for the Grid—A Review of Stationary Battery Storage System Design Tailored for Applications in Modern Power Grids*. Energies, 10, 2107, 2017. doi: 10.3390/en10122107.

[9] IRENA. *Electricity storage and renewables: Costs and markets to 2030*. International Renewable Energy Agency, Abu Dhabi, 2017.

[10] Y. Chen, Y. Kang, Y. Zhao, L. Wang, J. Liu, Y. Li, Z. Liang, X. He, X. Li, N. Tavajohi, and B. Li. *A review of lithium-ion battery safety concerns: The issues, strategies, and testing standards*. Journal of Energy Chemistry, 59, 83–99, 2021. doi: 10.1016/j.jechem.2020.10.017.

[11] Y.-S. Duh, K. H. Lin, and C.-S. Kao. *Experimental investigation and visualization on thermal runaway of hard prismatic lithium-ion batteries used in smart phones*. J Therm Anal Calorim, 132, 1677–1692, 2018. doi: 10.1007/s10973-018-7077-2.

[12] H. J. Bergveld, W. S. Kruijt, P. H. Notten, H. J. Bergveld, W. S. Kruijt, and P. H. Notten. *Basic information on batteries*. Battery Management Systems: Design by Modelling, pages 31–53, 2002.

[13] B. Scrosati. *History of lithium batteries*. J Solid State Electrochem, 15, 1623–1630, 2011. doi: 10.1007/s10008-011-1386-8.

[14] M. V. Reddy, A. Mauger, C. M. Julien, A. Paolella, and K. Zaghib. *Brief History of Early Lithium-Battery Development*. Materials, 13, 1884, 2020. doi: 10.3390/ma13081884.

[15] A. Allerhand. *Who invented the earliest capacitor bank (“battery” of leyden jars)? it’s*

complicated [scanning our past]. Proceedings of the IEEE, 106, 496–503, 2018. doi: 10.1109/JPROC.2018.2795846.

[16] A. Volta. *XVII. On the electricity excited by the mere contact of conducting substances of different kinds. In a letter from Mr. Alexander Volta, F. R. S. Professor of Natural Philosophy in the University of Pavia, to the Rt. Hon. Sir Joseph Banks, Bart. K.B. P. R. S*. Philosophical Transactions of the Royal Society of London, 90, 403–431, 1997. doi: 10.1098/rstl.1800.0018.

[17] M. B. Lim, T. N. Lambert, and B. R. Chalamala. *Rechargeable alkaline zinc–manganese oxide batteries for grid storage: Mechanisms, challenges and developments*. Materials Science and Engineering: R: Reports, 143, 100593, 2021. doi: 10.1016/j.mser.2020.100593.

[18] M. S. Whittingham. *The Role of Ternary Phases in Cathode Reactions*. J. Electrochem. Soc., 123, 315, 1976. doi: 10.1149/1.2132817.

[19] M. S. Whittingham. *Electrical Energy Storage and Intercalation Chemistry*. Science, 192, 1126–1127, 1976. doi: 10.1126/science.192.4244.1126.

[20] M. Li, J. Lu, Z. Chen, and K. Amine. *30 Years of Lithium-Ion Batteries*. Advanced Materials, 30, 1800561, 2018. doi: 10.1002/adma.201800561.

[21] K. Mizushima, P. C. Jones, P. J. Wiseman, and J. B. Goodenough. *LixCoO2 (0<x<-1): A new cathode material for batteries of high energy density*. Materials Research Bulletin, 15, 783–789, 1980. doi: https://doi.org/10.1016/0025-5408(80)90012-4.

[22] A. Yoshino, K. Sanechika, and T. Nakajima. *Secondary battery*, 1987.

[23] T. Yamahira, H. Kato, and M. Anzai. *Nonaqueous electrolyte secondary battery*, 1991.

[24] Y. Nishi. *Lithium ion secondary batteries; past 10 years and the future*. Journal of Power Sources, 100, 101–106, 2001. doi: 10.1016/S0378-7753(01)00887-4.

[25] Y. Liang, C.-Z. Zhao, H. Yuan, Y. Chen, W. Zhang, J.-Q. Huang, D. Yu, Y. Liu, M.-M. Titirici, Y.-L. Chueh, H. Yu, and Q. Zhang. *A review of rechargeable batteries for portable electronic devices*. InfoMat, 1, 6–32, 2019. doi: https://doi.org/10.1002/inf2.12000.

[26] C. Zhang, Y.-L. Wei, P.-F. Cao, and M.-C. Lin. *Energy storage system: Current studies on batteries and power condition system*. Renewable and Sustainable Energy Reviews, 82, 3091–3106, 2018. doi: https://doi.org/10.1016/j.rser.2017.10.030.

[27] A. R. Dehghani-Sanij, E. Tharumalingam, M. B. Dusseault, and R. Fraser. *Study of energy storage systems and environmental challenges of batteries*. Renewable and Sustainable Energy Reviews, 104, 192–208, 2019. doi: 10.1016/j.rser.2019.01.023.

[28] D. Deng. *Li-ion batteries: basics, progress, and challenges*. Energy Sci Eng, 3, 385–418, 2015. doi: 10.1002/ese3.95.

[29] T. Kim, W. Song, D.-Y. Son, L. K. Ono, and Y. Qi. *Lithium-ion batteries: outlook on present, future, and hybridized technologies*. J. Mater. Chem. A, 7, 2942–2964, 2019. doi: 10.1039/C8TA10513H.

[30] G. E. Blomgren. *The Development and Future of Lithium Ion Batteries*. Journal of The Electrochemical Society, 164, A5019, 2016. doi: 10.1149/2.0251701jes.

[31] J.-M. Tarascon and M. Armand. *Issues and challenges facing rechargeable lithium batteries*. Nature, 414, 359–367, 2001. doi: 10.1038/35104644.

[32] S. Pacala and R. Socolow. *Stabilization Wedges: Solving the Climate Problem for the Next 50 Years with Current Technologies*. Science, 305, 968–972, 2004. doi: 10.1126/science.1100103.

[33] C. Li, Z.-y. Wang, Z.-j. He, Y.-j. Li, J. Mao, K.-h. Dai, C. Yan, and J.-c. Zheng. *An advance review of solid-state battery: Challenges, progress and prospects*. Sustainable Materials and Technologies, 29, e00297, 2021. doi: 10.1016/j.susmat.2021.e00297.

[34] Q. Wang, A. Sarkar, D. Wang, L. Velasco, R. Azmi, S. S. Bhattacharya, T. Bergfeldt, A. Düvel, P. Heitjans, T. Brezesinski, H. Hahn, and B. Breitung. *Multi-anionic and -cationic compounds: new high entropy materials for advanced Li-ion batteries*. Energy Environ. Sci., 12, 2433–2442, 2019. doi: 10.1039/C9EE00368A.

[35] A. Sarkar, Q. Wang, A. Schiele, M. R. Chellali, S. S. Bhattacharya, D. Wang, T. Brezesinski, H. Hahn, L. Velasco, and B. Breitung. *High-Entropy Oxides: Fundamental Aspects and Electrochemical Properties*. Advanced Materials, 31, 1806236, 2019. doi: 10.1002/adma.201806236.

[36] Y. Ma, Y. Ma, Q. Wang, S. Schweidler, M. Botros, T. Fu, H. Hahn, T. Brezesinski, and B. Breitung. *High-entropy energy materials: challenges and new opportunities*. Energy Environ. Sci., 14, 2883–2905, 2021. doi: 10.1039/D1EE00505G.

[37] H. Xiang, Y. Xing, F.-z. Dai, H. Wang, L. Su, L. Miao, G. Zhang, Y. Wang, X. Qi, L. Yao, H. Wang, B. Zhao, J. Li, and Y. Zhou. *High-entropy ceramics: Present status, challenges, and a look forward*. J Adv Ceram, 10, 385–441, 2021. doi: 10.1007/s40145-021-0477-y.

[38] *The Nobel Prize in Chemistry 2019*. `https://www.nobelprize.org/prizes/chemistry/2019/press-release/`.

[39] F. Wu and G. Yushin. *Conversion cathodes for rechargeable lithium and lithium-ion batteries*. Energy Environ. Sci., 10, 435–459, 2017. doi: 10.1039/C6EE02326F.

[40] F. Wang, R. Robert, N. A. Chernova, N. Pereira, F. Omenya, F. Badway, X. Hua, M. Ruotolo, R. Zhang, L. Wu, V. Volkov, D. Su, B. Key, M. S. Whittingham, C. P. Grey, G. G. Amatucci, Y. Zhu, and J. Graetz. *Conversion Reaction Mechanisms in Lithium Ion Batteries: Study of the Binary Metal Fluoride Electrodes*. J. Am. Chem. Soc., 133, 18828–18836, 2011. doi: 10.1021/ja206268a.

[41] J. Hu, Y. Zhang, D. Cao, and C. Li. *Dehydrating bronze iron fluoride as a high capacity conversion cathode for lithium batteries*. J. Mater. Chem. A, 4, 16166–16174, 2016. doi: 10.1039/C6TA05929E.

[42] L. Wang, Z. Wu, J. Zou, P. Gao, X. Niu, H. Li, and L. Chen. *Li-free Cathode Materials for High Energy Density Lithium Batteries*. Joule, 3, 2086–2102, 2019. doi: 10.1016/j.joule.2019.07.011.

[43] K. Chen, M. Lei, Z. Yao, Y. Zheng, J. Hu, C. Lai, and C. Li. *Construction of solid-liquid fluorine transport channel to enable highly reversible conversion cathodes*. Science Advances, 7, eabj1491, 2021. doi: 10.1126/sciadv.abj1491.

[44] F. Wang, S.-W. Kim, D.-H. Seo, K. Kang, L. Wang, D. Su, J. J. Vajo, J. Wang, and J. Graetz. *Ternary metal fluorides as high-energy cathodes with low cycling hysteresis*. Nat Commun, 6, 6668, 2015. doi: 10.1038/ncomms7668.

[45] F. Wu, J. Maier, and Y. Yu. *Guidelines and trends for next-generation rechargeable lithium and lithium-ion batteries*. Chem. Soc. Rev., 49, 1569–1614, 2020. doi: 10.1039/C7CS00863E.

[46] C. Li, K. Chen, X. Zhou, and J. Maier. *Electrochemically driven conversion reaction in fluoride electrodes for energy storage devices*. npj Comput Mater, 4, 1–15, 2018. doi: 10.1038/s41524-018-0079-6.

[47] F. Wu, O. Borodin, and G. Yushin. *In situ surface protection for enhancing stability and performance of conversion-type cathodes*. MRS Energy & Sustainability, 4, 9, 2017. doi: 10.1557/mre.2017.11.

[48] J. P. Pender, G. Jha, D. H. Youn, J. M. Ziegler, I. Andoni, E. J. Choi, A. Heller, B. S. Dunn, P. S. Weiss, R. M. Penner, and C. B. Mullins. *Electrode Degradation in Lithium-Ion Batteries*. ACS Nano, 14, 1243–1295, 2020. doi: 10.1021/acsnano.9b04365.

[49] S.-H. Yu, X. Feng, N. Zhang, J. Seok, and H. D. Abruña. *Understanding Conversion-Type Electrodes for Lithium Rechargeable Batteries*. Acc. Chem. Res., 51, 273–281, 2018.

doi: 10.1021/acs.accounts.7b00487.

[50] K. Wei, Y. Zhao, K. Chen, K. Sun, T. Wu, Z. Dong, Y. Cui, C. Zeng, and C. Li. *Low-Overpotential LiF Splitting in Lithiated Fluoride Conversion Cathode Catalyzed by Spinel Oxide*. Advanced Functional Materials, 31, 2009133, 2021. doi: 10.1002/adfm.202009133.

[51] S. Petrovic. *Battery Technology Crash Course: A Concise Introduction*. Springer International Publishing, 2021. doi: 10.1007/978-3-030-57269-3.

[52] E. Talaie, P. Bonnick, X. Sun, Q. Pang, X. Liang, and L. F. Nazar. *Methods and Protocols for Electrochemical Energy Storage Materials Research*. Chem. Mater., 29, 90–105, 2017. doi: 10.1021/acs.chemmater.6b02726.

[53] X. Yang and A. L. Rogach. *Electrochemical Techniques in Battery Research: A Tutorial for Nonelectrochemists*. Advanced Energy Materials, 9, 1900747, 2019. doi: 10.1002/aenm.201900747.

[54] J. Cho, Y.-W. Kim, B. Kim, J.-G. Lee, and B. Park. *A Breakthrough in the Safety of Lithium Secondary Batteries by Coating the Cathode Material with AlPO4 Nanoparticles*. Angewandte Chemie International Edition, 42, 1618–1621, 2003. doi: 10.1002/anie.200250452.

[55] A. Yamada, S. C. Chung, and K. Hinokuma. *Optimized LiFePO4 for Lithium Battery Cathodes*. J. Electrochem. Soc., 148, A224, 2001. doi: 10.1149/1.1348257.

[56] M.-J. Lee, S. Lee, P. Oh, Y. Kim, and J. Cho. *High Performance LiMn2O4 Cathode Materials Grown with Epitaxial Layered Nanostructure for Li-Ion Batteries*. Nano Lett., 14, 993–999, 2014. doi: 10.1021/nl404430e.

[57] F. Lin, I. M. Markus, D. Nordlund, T.-C. Weng, M. D. Asta, H. L. Xin, and M. M. Doeff. *Surface reconstruction and chemical evolution of stoichiometric layered cathode materials for lithium-ion batteries*. Nat Commun, 5, 3529, 2014. doi: 10.1038/ncomms4529.

[58] S. Hamed, F. Obrezkov, S. Huotari, M. Colalongo, S. Mousavihashemi, and T. Kallio. *Optimized NMC622 electrodes with a high content of the active material: A comprehensive study*. Journal of Power Sources, 608, 234549, 2024. doi: 10.1016/j.jpowsour.2024.234549.

[59] R. C. McNulty, E. Hampson, L. N. Cutler, C. P. Grey, W. M. Dose, and L. R. Johnson. *Understanding the limits of Li-NMC811 half-cells*. J. Mater. Chem. A, 11, 18302–18312, 2023. doi: 10.1039/D3TA00912B.

[60] S. K. Martha, O. Haik, E. Zinigrad, I. Exnar, T. Drezen, J. H. Miners, and D. Aurbach. *On the Thermal Stability of Olivine Cathode Materials for Lithium-Ion Batteries*. J. Electrochem. Soc., 158, A1115, 2011. doi: 10.1149/1.3622849.

[61] N. A. Kaskhedikar and J. Maier. *Lithium Storage in Carbon Nanostructures*. Advanced Materials, 21, 2664–2680, 2009. doi: 10.1002/adma.200901079.

[62] N. Takami, K. Hoshina, and H. Inagaki. *Lithium Diffusion in Li4/3Ti5/3O4 Particles during Insertion and Extraction*. J. Electrochem. Soc., 158, A725, 2011. doi: 10.1149/1.3574037.

[63] X. Zhang, D. Wang, X. Qiu, Y. Ma, D. Kong, K. Müllen, X. Li, and L. Zhi. *Stable high-capacity and high-rate silicon-based lithium battery anodes upon two-dimensional covalent encapsulation*. Nat Commun, 11, 3826, 2020. doi: 10.1038/s41467-020-17686-4.

[64] C. M. Julien, A. Mauger, K. Zaghib, and H. Groult. *Comparative Issues of Cathode Materials for Li-Ion Batteries*. Inorganics, 2, 132–154, 2014. doi: 10.3390/inorganics2010132.

[65] J. W. Fergus. *Recent developments in cathode materials for lithium ion batteries*. Journal of Power Sources, 195, 939–954, 2010. doi: https://doi.org/10.1016/j.jpowsour.2009.08.089.

[66] J.-L. Shi, D.-D. Xiao, M. Ge, X. Yu, Y. Chu, X. Huang, X.-D. Zhang, Y.-X. Yin, X.-Q. Yang, Y.-G. Guo, L. Gu, and L.-J. Wan. *High-Capacity Cathode Material with High Voltage for Li-Ion Batteries*. Advanced Materials, 30, 1705575, 2018. doi: https://doi.org/10.1002/adma.201705575.

[67] P. Kalyani and N. Kalaiselvi. *Various aspects of $LiNiO_2$ chemistry: A review*. Science and Technology of Advanced Materials, 6, 689–703, 2005. doi: 10.1016/j.stam.2005.06.001.

[68] K. Mukai, J. Sugiyama, and Y. Aoki. *Structural, magnetic, and electrochemical studies on lithium insertion materials $LiNi_{1-x}Co_xO_2$ with $0\leq x\leq 0.25$*. Journal of Solid State Chemistry France, 183, 1726–1732, 2010. doi: 10.1016/j.jssc.2010.05.019.

[69] S. Liu, L. Xiong, and C. He. *Long cycle life lithium ion battery with lithium nickel cobalt manganese oxide NCM cathode*. Journal of Power Sources, 261, 285–291, 2014. doi: https://doi.org/10.1016/j.jpowsour.2014.03.083.

[70] Z. Lun, B. Ouyang, D.-H. Kwon, Y. Ha, E. E. Foley, T.-Y. Huang, Z. Cai, H. Kim, M. Balasubramanian, Y. Sun, J. Huang, Y. Tian, H. Kim, B. D. McCloskey, W. Yang, R. J. Clément, H. Ji, and G. Ceder. *Cation-disordered rocksalt-type high-entropy cathodes for Li-ion batteries*. Nat. Mater., 20, 214–221, 2021. doi: 10.1038/s41563-020-00816-0.

[71] E. A. Olivetti, G. Ceder, G. G. Gaustad, and X. Fu. *Lithium-Ion Battery Supply Chain Considerations: Analysis of Potential Bottlenecks in Critical Metals*. Joule, 1, 229–243, 2017. doi: 10.1016/j.joule.2017.08.019.

[72] S. Moharana, G. West, M. Walker, X. S. Yan, and M. Loveridge. *Controlling Li Dendritic Growth in Graphite Anodes by Potassium Electrolyte Additives for Li-Ion Batteries*. ACS Appl. Mater. Interfaces, 14, 42078–42092, 2022. doi: 10.1021/acsami.2c11175.

[73] B. Scrosati and J. Garche. *Lithium batteries: Status, prospects and future*. Journal of Power Sources, 195, 2419–2430, 2010. doi: 10.1016/j.jpowsour.2009.11.048.

[74] K. Zaghib, M. Dontigny, A. Guerfi, P. Charest, I. Rodrigues, A. Mauger, and C. M. Julien. *Safe and fast-charging Li-ion battery with long shelf life for power applications*. Journal of Power Sources, 196, 3949–3954, 2011. doi: 10.1016/j.jpowsour.2010.11.093.

[75] J. Saint, M. Morcrette, D. Larcher, L. Laffont, S. Beattie, J.-P. Pérès, D. Talaga, M. Couzi, and J.-M. Tarascon. *Towards a Fundamental Understanding of the Improved Electrochemical Performance of Silicon–Carbon Composites*. Advanced Functional Materials, 17, 1765–1774, 2007. doi: 10.1002/adfm.200600937.

[76] T. R. Jow, K. Xu, O. Borodin, and M. Ue. *Electrolytes for Lithium and Lithium-Ion Batteries*, volume 58. Springer, 2014. doi: 10.1007/978-1-4939-0302-3.

[77] Y.-K. Liu, C.-Z. Zhao, J. Du, X.-Q. Zhang, A.-B. Chen, and Q. Zhang. *Research Progresses of Liquid Electrolytes in Lithium-Ion Batteries*. Small, 19, 2205315, 2023. doi: 10.1002/smll.202205315.

[78] H. Q. Pham, H.-Y. Lee, E.-H. Hwang, Y.-G. Kwon, and S.-W. Song. *Non-flammable organic liquid electrolyte for high-safety and high-energy density Li-ion batteries*. Journal of Power Sources, 404, 13–19, 2018. doi: 10.1016/j.jpowsour.2018.09.075.

[79] X. Yu, R. Chen, L. Gan, H. Li, and L. Chen. *Battery Safety: From Lithium-Ion to Solid-State Batteries*. Engineering, 21, 9–14, 2023. doi: 10.1016/j.eng.2022.06.022.

[80] J. Awaka, N. Kijima, H. Hayakawa, and J. Akimoto. *Synthesis and structure analysis of tetragonal Li7La3Zr2O12 with the garnet-related type structure*. Journal of Solid State Chemistry, 182, 2046–2052, 2009. doi: 10.1016/j.jssc.2009.05.020.

[81] C. A. Geiger, E. Alekseev, B. Lazic, M. Fisch, T. Armbruster, R. Langner, M. Fechtelkord, N. Kim, T. Pettke, and W. Weppner. *Crystal Chemistry and Stability of "$Li_7La_3Zr_2O_{12}$" Garnet: A Fast Lithium-Ion Conductor*. Inorg. Chem., 50, 1089–1097, 2011. doi: 10.1021/ic101914e.

[82] J. Wu, S. Liu, F. Han, X. Yao, and C. Wang. *Lithium/Sulfide All-Solid-State Bat-*

teries using Sulfide Electrolytes. Advanced Materials, 33, 2000751, 2021. doi: 10.1002/adma.202000751.

[83] X. Cheng, J. Pan, Y. Zhao, M. Liao, and H. Peng. *Gel Polymer Electrolytes for Electrochemical Energy Storage*. Advanced Energy Materials, 8, 1702184, 2018. doi: 10.1002/aenm.201702184.

[84] J. Castillo, A. Santiago, X. Judez, I. Garbayo, J. A. Coca Clemente, M. C. Morant-Miñana, A. Villaverde, J. A. González-Marcos, H. Zhang, M. Armand, and C. Li. *Safe, Flexible, and High-Performing Gel-Polymer Electrolyte for Rechargeable Lithium Metal Batteries*. Chem. Mater., 33, 8812–8821, 2021. doi: 10.1021/acs.chemmater.1c02952.

[85] M. Armand and J.-M. Tarascon. *Building better batteries*. Nature, 451, 652–657, 2008. doi: 10.1038/451652a.

[86] A. Manthiram, X. Yu, and S. Wang. *Lithium battery chemistries enabled by solid-state electrolytes*. Nat Rev Mater, 2, 1–16, 2017. doi: 10.1038/natrevmats.2016.103.

[87] H. Sun, S. Kang, and L. Cui. *Prospects of LLZO type solid electrolyte: From material design to battery application*. Chemical Engineering Journal, 454, 140375, 2023. doi: 10.1016/j.cej.2022.140375.

[88] H. Duan, H. Zheng, Y. Zhou, B. Xu, and H. Liu. *Stability of garnet-type Li ion conductors: An overview*. Solid State Ionics, 318, 45–53, 2018. doi: 10.1016/j.ssi.2017.09.018.

[89] Q. Liu, Z. Geng, C. Han, Y. Fu, S. Li, Y.-b. He, F. Kang, and B. Li. *Challenges and perspectives of garnet solid electrolytes for all solid-state lithium batteries*. Journal of Power Sources, 389, 120–134, 2018. doi: 10.1016/j.jpowsour.2018.04.019.

[90] J.-W. Yeh, S.-K. Chen, S.-J. Lin, J.-Y. Gan, T.-S. Chin, T.-T. Shun, C.-H. Tsau, and S.-Y. Chang. *Nanostructured High-Entropy Alloys with Multiple Principal Elements: Novel Alloy Design Concepts and Outcomes*. Advanced Engineering Materials, 6, 299–303, 2004. doi: 10.1002/adem.200300567.

[91] B. Cantor, I. T. H. Chang, P. Knight, and A. J. B. Vincent. *Microstructural development in equiatomic multicomponent alloys*. Materials Science and Engineering: A, 375-377, 213–218, 2004. doi: 10.1016/j.msea.2003.10.257.

[92] C. M. Rost, E. Sachet, T. Borman, A. Moballegh, E. C. Dickey, D. Hou, J. L. Jones, S. Curtarolo, and J.-P. Maria. *Entropy-stabilized oxides*. Nat Commun, 6, 8485, 2015. doi: 10.1038/ncomms9485.

[93] A. Sarkar, B. Breitung, and H. Hahn. *High entropy oxides: The role of entropy, enthalpy and synergy*. Scripta Materialia, 187, 43–48, 2020. doi: 10.1016/j.scriptamat.2020.05.019.

[94] Y. Cui, P. A. Sukkurji, K. Wang, R. Azmi, A. M. Nunn, H. Hahn, B. Breitung, Y.-Y. Ting, P. M. Kowalski, P. Kaghazchi, Q. Wang, S. Schweidler, and M. Botros. *High entropy fluorides as conversion cathodes with tailorable electrochemical performance*. J. Energy Chem., 72, 342–351, 2022. doi: 10.1016/j.jechem.2022.05.032.

[95] Y. He, S. L. Dreyer, Y.-Y. Ting, Y. Ma, Y. Hu, D. Goonetilleke, Y. Tang, T. Diemant, B. Zhou, P. M. Kowalski, M. Fichtner, H. Hahn, J. Aghassi-Hagmann, T. Brezesinski, B. Breitung, and Y. Ma. *Entropy-Mediated Stable Structural Evolution of Prussian White Cathodes for Long-Life Na-Ion Batteries*. Angew. Chem. Int. Ed., 63, e202315371, 2024. doi: 10.1002/ange.202315371.

[96] J. Lee, D.-H. Seo, M. Balasubramanian, N. Twu, X. Li, and G. Ceder. *A new class of high capacity cation-disordered oxides for rechargeable lithium batteries: Li-Ni-Ti-Mo oxides*. Energy Environ. Sci., 8, 3255–3265, 2015. doi: 10.1039/C5EE02329G.

[97] A. Sarkar, L. Velasco, D. Wang, Q. Wang, G. Talasila, L. de Biasi, C. Kübel, T. Brezesinski, S. S. Bhattacharya, H. Hahn, and B. Breitung. *High entropy oxides for reversible energy storage*. Nat Commun, 9, 3400, 2018. doi: 10.1038/s41467-018-05774-5.

[98] A. Sarkar, R. Djenadic, N. J. Usharani, K. P. Sanghvi, V. S. K. Chakravadhanula, A. S. Gandhi, H. Hahn, and S. S. Bhattacharya. *Nanocrystalline multicomponent entropy stabilised transition metal oxides*. Journal of the European Ceramic Society, 37, 747–754, 2017. doi: 10.1016/j.jeurceramsoc.2016.09.018.

[99] R. Wang, X. Li, L. Liu, J. Lee, D.-H. Seo, S.-H. Bo, A. Urban, and G. Ceder. *A disordered rock-salt Li-excess cathode material with high capacity and substantial oxygen redox activity: Li1.25Nb0.25Mn0.5O2*. Electrochemistry Communications, 60, 70–73, 2015. doi: 10.1016/j.elecom.2015.08.003.

[100] D. Bérardan, S. Franger, A. K. Meena, and N. Dragoe. *Room temperature lithium superionic conductivity in high entropy oxides*. J. Mater. Chem. A, 4, 9536–9541, 2016. doi: 10.1039/C6TA03249D.

[101] E. Castle, T. Csanádi, S. Grasso, J. Dusza, and M. Reece. *Processing and Properties of High-Entropy Ultra-High Temperature Carbides*. Sci Rep, 8, 8609, 2018. doi: 10.1038/s41598-018-26827-1.

[102] M. Qin, Q. Yan, Y. Liu, and J. Luo. *A new class of high-entropy M3B4 borides*. J Adv Ceram, 10, 166–172, 2021. doi: 10.1007/s40145-020-0438-x.

[103] C.-W. Tsai, S.-W. Lai, K.-H. Cheng, M.-H. Tsai, A. Davison, C.-H. Tsau, and J.-W. Yeh. *Strong amorphization of high-entropy AlBCrSiTi nitride film*. Thin Solid Films, 520, 2613–2618, 2012. doi: 10.1016/j.tsf.2011.11.025.

[104] T. Jin, X. Sang, R. R. Unocic, R. T. Kinch, X. Liu, J. Hu, H. Liu, and S. Dai. *Mechanochemical-Assisted Synthesis of High-Entropy Metal Nitride via a Soft Urea Strategy*. Advanced Materials, 30, 1707512, 2018. doi: 10.1002/adma.201707512.

[105] T. Wang, H. Chen, Z. Yang, J. Liang, and S. Dai. *High-Entropy Perovskite Fluorides: A New Platform for Oxygen Evolution Catalysis*. J. Am. Chem. Soc., 142, 4550–4554, 2020. doi: 10.1021/jacs.9b12377.

[106] R.-Z. Zhang, F. Gucci, H. Zhu, K. Chen, and M. J. Reece. *Data-Driven Design of Ecofriendly Thermoelectric High-Entropy Sulfides*. Inorg. Chem., 57, 13027–13033, 2018. doi: 10.1021/acs.inorgchem.8b02379.

[107] B. S. Murty, J.-W. Yeh, S. Ranganathan, and P. P. Bhattacharjee. *High-Entropy Alloys*. Elsevier, 2019.

[108] S. L. Shang, Y. Wang, D. E. Kim, C. L. Zacherl, Y. Du, and Z. K. Liu. *Structural, vibrational, and thermodynamic properties of ordered and disordered* $Ni_{1-x}Pt_x$ *alloys from first-principles calculations*. Phys. Rev. B, 83, 144204, 2011. doi: 10.1103/PhysRevB.83.144204.

[109] C. Wouters, C. Sutton, L. M. Ghiringhelli, T. Markurt, R. Schewski, A. Hassa, H. von Wenckstern, M. Grundmann, M. Scheffler, and M. Albrecht. *Investigating the ranges of (meta)stable phase formation in* $(In_xGa_{1.x})_2O_3$*: Impact of the cation coordination*. Phys. Rev. Mater., 4, 125001, 2020. doi: 10.1103/PhysRevMaterials.4.125001.

[110] J. Liu, X. Wang, A. P. Singh, H. Xu, F. Kong, and F. Yang. *The Evolution of Intermetallic Compounds in High-Entropy Alloys: From the Secondary Phase to the Main Phase*. Metals, 11, 2054, 2021. doi: 10.3390/met11122054.

[111] F. Otto, Y. Yang, H. Bei, and E. P. George. *Relative effects of enthalpy and entropy on the phase stability of equiatomic high-entropy alloys*. Acta Materialia, 61, 2628–2638, 2013. doi: 10.1016/j.actamat.2013.01.042.

[112] A. Navrotsky. *Thermodynamics of solid electrolytes and related oxide ceramics based on the fluorite structure*. J. Mater. Chem., 20, 10577–10587, 2010. doi: 10.1039/C0JM01521K.

[113] S. Finkeldei, P. Kegler, P. M. Kowalski, C. Schreinemachers, F. Brandt, A. A. Bukaemskiy, V. L. Vinograd, G. Beridze, A. Shelyug, A. Navrotsky, and D. Bosbach. *Composition*

dependent order-disorder transition in $Nd_xZr_{1-x}O_{2-0.5x}$ pyrochlores: A combined structural, calorimetric and ab initio modeling study. Acta Materialia, 125, 166–176, 2017. doi: 10.1016/j.actamat.2016.11.059.

[114] P. M. Kowalski. *Formation enthalpy of $Ln_2B_2O_7$-type (B=Ti,Sn,Hf,Zr) compounds*. Scr. Mater, 189, 7–10, 2020.

[115] A. A. Bukaemskiy, V. L. Vinograd, and P. M. Kowalski. *Ion distribution models for defect fluorite ZrO_2 - $AO_{1.5}$ (A = Ln, Y) solid solutions: I. Relationship between lattice parameter and composition*. Acta Materialia, 202, 99–111, 2021. doi: 10.1016/j.actamat.2020.10.045.

[116] J. Dąbrowa, M. Zajusz, W. Kucza, G. Cieślak, K. Berent, T. Czeppe, T. Kulik, and M. Danielewski. *Demystifying the sluggish diffusion effect in high entropy alloys*. Journal of Alloys and Compounds, 783, 193–207, 2019. doi: 10.1016/j.jallcom.2018.12.300.

[117] B. Ouyang and Y. Zeng. *The rise of high-entropy battery materials*. Nat Commun, 15, 973, 2024. doi: 10.1038/s41467-024-45309-9.

[118] Y. Zeng, B. Ouyang, J. Liu, Y.-W. Byeon, Z. Cai, L. J. Miara, Y. Wang, and G. Ceder. *High-entropy mechanism to boost ionic conductivity*. Science, 378, 1320–1324, 2022. doi: 10.1126/science.abq1346.

[119] J. Lin, G. Cherkashinin, M. Schäfer, G. Melinte, S. Indris, A. Kondrakov, J. Janek, T. Brezesinski, and F. Strauss. *A High-Entropy Multicationic Substituted Lithium Argyrodite Superionic Solid Electrolyte*. ACS Materials Lett., 4, 2187–2194, 2022. doi: 10.1021/acsmaterialslett.2c00667.

[120] H. Chen, N. Qiu, B. Wu, Z. Yang, S. Sun, and Y. Wang. *A new spinel high-entropy oxide $(Mg_{0.2}Ti_{0.2}Zn_{0.2}Cu_{0.2}Fe_{0.2})_3O_4$ with fast reaction kinetics and excellent stability as an anode material for lithium ion batteries*. RSC Adv., 10, 9736–9744, 2020. doi: 10.1039/D0RA00255K.

[121] J. Yan, D. Wang, X. Zhang, J. Li, Q. Du, X. Liu, J. Zhang, and X. Qi. *A high-entropy perovskite titanate lithium-ion battery anode*. J Mater Sci, 55, 6942–6951, 2020. doi: 10.1007/s10853-020-04482-0.

[122] S.-K. Jung, H. Gwon, H. Kim, G. Yoon, D. Shin, J. Hong, C. Jung, and J.-S. Kim. *Unlocking the hidden chemical space in cubic-phase garnet solid electrolyte for efficient quasi-all-solid-state lithium batteries*. Nat Commun, 13, 7638, 2022. doi: 10.1038/s41467-022-35287-1.

[123] Y. Li, S. Song, H. Kim, K. Nomoto, H. Kim, X. Sun, S. Hori, K. Suzuki, N. Matsui, M. Hirayama, T. Mizoguchi, T. Saito, T. Kamiyama, and R. Kanno. *A lithium superionic conductor for millimeter-thick battery electrode*. Science, 381, 50–53, 2023. doi: 10.1126/science.add7138.

[124] M. P. Stockham, B. Dong, and P. R. Slater. *High entropy lithium garnets - Testing the compositional flexibility of the lithium garnet system*. Journal of Solid State Chemistry, 308, 122944, 2022. doi: 10.1016/j.jssc.2022.122944.

[125] M. P. Stockham, A. Griffiths, B. Dong, and P. R. Slater. *Assessing the Importance of Cation Size in the Tetragonal-Cubic Phase Transition in Lithium-Garnet Electrolytes*. Chemistry - A European Journal, 28, e202103442, 2022. doi: 10.1002/chem.202103442.

[126] Z. Fu and J. Ferguson. *Processing and characterization of an $Li_7La_3Zr_{0.5}Nb_{0.5}Ta_{0.5}Hf_{0.5}O_{12}$ high-entropy Li-garnet electrolyte*. Journal of the American Ceramic Society, 105, 6175–6183, 2022. doi: 10.1111/jace.18576.

[127] Y. Chen, T. Wang, H. Chen, W. H. Kan, W. Yin, Z. Song, C. Wang, J. Ma, W. Luo, and Y. Huang. *Local structural features of medium-entropy garnet with ultra-long cycle life*. Matter, 6, 1530–1541, 2023. doi: 10.1016/j.matt.2023.03.002.

[128] Y. Feng, L. Yang, Z. Yan, D. Zuo, Z. Zhu, L. Zeng, Y. Zhu, and J. Wan. *Discovery of high entropy garnet solid-state electrolytes via ultrafast synthesis*. Energy Storage Materials, 63, 103053, 2023. doi: 10.1016/j.ensm.2023.103053.

[129] T. Zhang, D. Li, Z. Tao, and J. Chen. *Understanding electrode materials of rechargeable lithium batteries via DFT calculations*. Progress in Natural Science: Materials International, 23, 256–272, 2013. doi: https://doi.org/10.1016/j.pnsc.2013.04.005.

[130] P. M. Kowalski, T. Bornhake, O. Cheong, N. Dohrmann, A. L. Koch Liston, S. K. Potts, A. Shad, R. Tesch, and Y.-Y. Ting. *Fundamentals of energy storage from first principles simulations: Challenges and opportunities*. Frontiers in Energy Research, 10, 2023. doi: 10.3389/fenrg.2022.1096190.

[131] P. J. Hasnip, K. Refson, M. I. J. Probert, J. R. Yates, S. J. Clark, and C. J. Pickard. *Density functional theory in the solid state*. Philosophical Transactions of the Royal Society A: Mathematical, Physical and Engineering Sciences, 372, 20130270, 2014. doi: 10.1098/rsta.2013.0270.

[132] W. Kohn, A. D. Becke, and R. G. Parr. *Density Functional Theory of Electronic Structure*. The Journal of Physical Chemistry, 100, 12974–12980, 1996. doi: 10.1021/jp960669l.

[133] S. Jahn and P. M. Kowalski. *Theoretical approaches to structure and spectroscopy of earth materials*. Rev. Mineral. Geochem., 78, 691, 2014. doi: 10.2138/rmg.2014.78.17.

[134] A. Urban, I. Matts, A. Abdellahi, and G. Ceder. *Computational Design and Preparation of Cation-Disordered Oxides for High-Energy-Density Li-Ion Batteries*. Adv. Energy Mater., 6, 1600488, 2016. doi: 10.1002/aenm.201600488.

[135] M. Beyramali Kivy, M. Asle Zaeem, and S. Lekakh. *Investigating phase formations in cast AlFeCoNiCu high entropy alloys by combination of computational modeling and experiments*. Materials & Design, 127, 224–232, 2017. doi: 10.1016/j.matdes.2017.04.086.

[136] P. Brommer, A. Kiselev, D. Schopf, P. Beck, J. Roth, and H.-R. Trebin. *Classical interaction potentials for diverse materials from ab initio data: a review of potfit*. Modelling and Simulation in Materials Science and Engineering, 23, 074002, 2015. doi: 10.1088/0965-0393/23/7/074002.

[137] J. Behler. *Perspective: Machine learning potentials for atomistic simulations*. J. Chem. Phys., 145, 170901, 2016. doi: 10.1063/1.4966192.

[138] L. Wu and T. Li. *A machine learning interatomic potential for high entropy alloys*. Journal of the Mechanics and Physics of Solids, 187, 105639, 2024. doi: 10.1016/j.jmps.2024.105639.

[139] A. Zunger. *First-Principles Statistical Mechanics of Semiconductor Alloys and Intermetallic Compounds*. In *Statics and Dynamics of Alloy Phase Transformations*, pages 361–419. Springer US, 1994.

[140] A. Abdellahi, A. Urban, S. Dacek, and G. Ceder. *The Effect of Cation Disorder on the Average Li Intercalation Voltage of Transition-Metal Oxides*. Chem. Mater., 28, 3659–3665, 2016. doi: 10.1021/acs.chemmater.6b00205.

[141] A. Urban, A. Abdellahi, S. Dacek, N. Artrith, and G. Ceder. *Electronic-Structure Origin of Cation Disorder in Transition-Metal Oxides*. Phys. Rev. Lett., 119, 176402, 2017. doi: 10.1103/PhysRevLett.119.176402.

[142] J. H. Yang, T. Chen, L. Barroso-Luque, Z. Jadidi, and G. Ceder. *Approaches for handling high-dimensional cluster expansions of ionic systems*. npj Comput Mater, 8, 1–11, 2022. doi: 10.1038/s41524-022-00818-3.

[143] A. J. Cohen, P. Mori-Sánchez, and W. Yang. *Insights into Current Limitations of Density Functional Theory*. Science, 321, 792–794, 2008. doi: 10.1126/science.1158722.

[144] W. Li, C. F. J. Walther, A. Kuc, and T. Heine. *Density Functional Theory and Beyond for Band-Gap Screening: Performance for Transition-Metal Oxides and Dichalco-*

genides. Journal of Chemical Theory and Computation, 9, 2950–2958, 2013. doi: 10.1021/ct400235w.

[145] M. Cococcioni and S. de Gironcoli. *Linear response approach to the calculation of the effective interaction parameters in the LDA+U method*. Phys. Rev. B, 71, 035105, 2005. doi: 10.1103/PhysRevB.71.035105.

[146] V. I. Anisimov, J. Zaanen, and O. K. Andersen. *Band theory and Mott insulators: Hubbard U instead of Stoner I*. Phys. Rev. B, 44, 943–954, 1991. doi: 10.1103/PhysRevB.44.943.

[147] W. Olszewski, S. Baiju, P. Kaghazchi, C. Marini, B. Mortemard de Boisse, M. Okubo, A. Yamada, T. Mizokawa, N. L. Saini, and L. Simonelli. *The role of the local structural properties in the electrochemical characteristics of Na1-xFe1-yNiyO2 cathodes*. Materials Today Energy, 40, 101519, 2024. doi: 10.1016/j.mtener.2024.101519.

[148] A. Chakraborty, M. Dixit, D. Aurbach, and D. T. Major. *Predicting accurate cathode properties of layered oxide materials using the SCAN meta-GGA density functional*. npj Computational Materials, 4, 1–9, 2018.

[149] R. Tesch and P. M. Kowalski. *Hubbard U parameters for transition metals from first principles*. Phys. Rev. B, 105, 195153, 2022. doi: 10.1103/PhysRevB.105.195153.

[150] A. Jain, G. Hautier, C. J. Moore, S. Ping Ong, C. C. Fischer, T. Mueller, K. A. Persson, and G. Ceder. *A high-throughput infrastructure for density functional theory calculations*. Computational Materials Science, 50, 2295–2310, 2011. doi: 10.1016/j.commatsci.2011.02.023.

[151] Y.-Y. Ting and P. M. Kowalski. *Refined DFT+U method for computation of layered oxide cathode materials*. Electrochimica Acta, 443, 141912, 2023. doi: 10.1016/j.electacta.2023.141912.

[152] D. Kramer and G. Ceder. *Tailoring the Morphology of $LiCoO_2$: A First Principles Study*. Chemistry of Materials, 21, 3799–3809, 2009. doi: 10.1021/cm9008943.

[153] Z. Chen, H. Zou, X. Zhu, J. Zou, and J. Cao. *First-principle investigation of Jahn-Teller distortion and topological analysis of chemical bonds in $LiNiO_2$*. J. Solid State Chem., 184, 1784–1790, 2011. doi: https://doi.org/10.1016/j.jssc.2011.05.024.

[154] Y. Kim, H. Lee, and S. Kang. *First-principles and experimental investigation of the morphology of layer-structured $LiNiO_2$ and $LiCoO_2$*. J. Mater. Chem., 22, 12874–12881, 2012. doi: 10.1039/C2JM31145C.

[155] M. Ihrig, M. Finsterbusch, A. M. Laptev, C. Tu, N. T. T. Tran, C. Lin, L.-Y. Kuo, R. Ye, Y. J. Sohn, P. Kaghazchi, S.-K. Lin, D. Fattakhova-Rohlfing, and O. Guillon. *Study of $LiCoO_2$/$Li_7La_3Zr_2O_{12}$:Ta Interface Degradation in All-Solid-State Lithium Batteries*. ACS Applied Materials & Interfaces, 14, 11288–11299, 2022. doi: 10.1021/acsami.1c22246.

[156] L. Wang, T. Maxisch, and G. Ceder. *Oxidation energies of transition metal oxides within the* $\mathrm{GGA} + \mathrm{U}$ *framework*. Phys. Rev. B, 73, 195107, 2006. doi: 10.1103/PhysRevB.73.195107.

[157] G.-Y. Huang, C.-Y. Wang, and J.-T. Wang. *Detailed check of the LDA + U and GGA + U corrected method for defect calculations in wurtzite ZnO*. Computer Physics Communications, 183, 1749–1752, 2012. doi: 10.1016/j.cpc.2012.03.017.

[158] K. O. Kvashnina, P. M. Kowalski, S. M. Butorin, G. Leinders, J. Pakarinen, R. Bès, H. Li, and M. Verwerft. *Trends in the valence band electronic structures of mixed uranium oxides*. Chem. Commun., 54, 9757–9760, 2018. doi: 10.1039/C8CC05464A.

[159] F. Zhou, M. Cococcioni, C. A. Marianetti, D. Morgan, and G. Ceder. *First-principles prediction of redox potentials in transition-metal compounds with LDA+U*. Phys. Rev. B, 70, 235121, 2004. doi: 10.1103/PhysRevB.70.235121.

[160] P. M. Kowalski, Z. He, and O. Cheong. *Electrode and Electrolyte Materials From Atomistic Simulations: Properties of LixFEPO4 Electrode and Zircon-Based Ionic Conductors*.

Frontiers in Energy Research, 9, 653542, 2021. doi: 10.3389/fenrg.2021.653542.

[161] G. L. Murphy, Z. Zhang, R. Tesch, P. M. Kowalski, M. Avdeev, E. Y. Kuo, D. J. Gregg, P. Kegler, E. V. Alekseev, and B. J. Kennedy. *Tilting and Distortion in Rutile-Related Mixed Metal Ternary Uranium Oxides: A Structural, Spectroscopic, and Theoretical Investigation*. Inorganic Chemistry, 60, 2246–2260, 2021. doi: 10.1021/acs.inorgchem.0c03077.

[162] T. Vitova, I. Pidchenko, S. Biswas, G. Beridze, P. W. Dunne, D. Schild, Z. Wang, P. M. Kowalski, and R. J. Baker. *Dehydration of the Uranyl Peroxide Studtite, $[UO_2(\eta_2{-}O_2)(H_2O)_2]\cdot 2\,H_2O$, Affords a Drastic Change in the Electronic Structure: A Combined X-ray Spectroscopic and Theoretical Analysis*. Inorganic Chemistry, 57, 1735–1743, 2018. doi: 10.1021/acs.inorgchem.7b02326.

[163] M. Kick, K. Reuter, and H. Oberhofer. *Intricacies of DFT+U, Not Only in a Numeric Atom Centered Orbital Framework*. Journal of Chemical Theory and Computation, 15, 1705–1718, 2019. doi: 10.1021/acs.jctc.8b01211.

[164] N. Marzari and D. Vanderbilt. *Maximally localized generalized Wannier functions for composite energy bands*. Phys. Rev. B, 56, 12847–12865, 1997. doi: 10.1103/PhysRevB.56.12847.

[165] R. M. Martin. *Electronic Structure: Basic Theory and Practical Methods*. Cambridge University Press, 2020. doi: 10.1017/9781108555586.

[166] F. Jensen. *Introduction to Computational Chemistry*. John Wiley & Sons, 2016.

[167] E. Schrödinger. *Quantisierung als Eigenwertproblem*. Annalen der Physik, 384, 361–376, 1926. doi: 10.1002/andp.19263840404.

[168] M. Born and R. Oppenheimer. *Zur Quantentheorie der Molekeln*. Annalen der Physik, 389, 457–484, 1927. doi: 10.1002/andp.19273892002.

[169] H. Hellmann. *A New Approximation Method in the Problem of Many Electrons*. The Journal of Chemical Physics, 3, 61, 1935. doi: 10.1063/1.1749559.

[170] P. Schwerdtfeger. *The Pseudopotential Approximation in Electronic Structure Theory*. ChemPhysChem, 12, 3143–3155, 2011. doi: 10.1002/cphc.201100387.

[171] D. S. Sholl and J. A. Steckel. *Density Functional Theory: A Practical Introduction*. John Wiley & Sons, 2011.

[172] P. Hohenberg and W. Kohn. *Inhomogeneous Electron Gas*. Phys. Rev., 136, B864–B871, 1964. doi: 10.1103/PhysRev.136.B864.

[173] W. Kohn and L. J. Sham. *Self-Consistent Equations Including Exchange and Correlation Effects*. Phys. Rev., 140, A1133–A1138, 1965. doi: 10.1103/PhysRev.140.A1133.

[174] J. P. Perdew and K. Schmidt. *Jacob's ladder of density functional approximations for the exchange-correlation energy*. AIP Conference Proceedings, 577, 1–20, 2001. doi: 10.1063/1.1390175.

[175] J. P. Perdew. *Climbing the ladder of density functional approximations*. MRS Bulletin, 38, 743–750, 2013. doi: 10.1557/mrs.2013.178.

[176] J. P. Perdew, K. Burke, and M. Ernzerhof. *Generalized Gradient Approximation Made Simple*. Phys. Rev. Lett., 77, 3865–3868, 1996. doi: 10.1103/PhysRevLett.77.3865.

[177] J. P. Perdew, A. Ruzsinszky, G. I. Csonka, O. A. Vydrov, G. E. Scuseria, L. A. Constantin, X. Zhou, and K. Burke. *Restoring the Density-Gradient Expansion for Exchange in Solids and Surfaces*. Phys. Rev. Lett., 100, 136406, 2008. doi: 10.1103/PhysRevLett.100.136406.

[178] J. Sun, A. Ruzsinszky, and J. P. Perdew. *Strongly Constrained and Appropriately Normed Semilocal Density Functional*. Phys. Rev. Lett., 115, 036402, 2015. doi: 10.1103/PhysRevLett.115.036402.

[179] J. Tao, J. P. Perdew, V. N. Staroverov, and G. E. Scuseria. *Climbing the Density*

Functional Ladder: Nonempirical Meta–Generalized Gradient Approximation Designed for Molecules and Solids. Phys. Rev. Lett., 91, 146401, 2003. doi: 10.1103/PhysRevLett.91.146401.

[180] J. Heyd, G. E. Scuseria, and M. Ernzerhof. *Hybrid functionals based on a screened Coulomb potential*. The Journal of Chemical Physics, 118, 8207–8215, 2003. doi: 10.1063/1.1564060.

[181] J. Heyd, G. E. Scuseria, and M. Ernzerhof. *Erratum: "Hybrid functionals based on a screened Coulomb potential" [J. Chem. Phys. 118, 8207 (2003)]*. The Journal of Chemical Physics, 124, 219906, 2006. doi: 10.1063/1.2204597.

[182] S. Grimme. *Semiempirical hybrid density functional with perturbative second-order correlation*. The Journal of Chemical Physics, 124, 034108, 2006. doi: 10.1063/1.2148954.

[183] V. I. Anisimov and O. Gunnarsson. *Density-functional calculation of effective Coulomb interactions in metals*. Phys. Rev. B, 43, 7570–7574, 1991. doi: 10.1103/PhysRevB.43.7570.

[184] V. I. Anisimov, I. V. Solovyev, M. A. Korotin, M. T. Czyżyk, and G. A. Sawatzky. *Density-functional theory and NiO photoemission spectra*. Phys. Rev. B, 48, 16929–16934, 1993. doi: 10.1103/PhysRevB.48.16929.

[185] I. V. Solovyev, P. H. Dederichs, and V. I. Anisimov. *Corrected atomic limit in the local-density approximation and the electronic structure of d impurities in Rb*. Phys. Rev. B, 50, 16861–16871, 1994. doi: 10.1103/PhysRevB.50.16861.

[186] B. Himmetoglu, A. Floris, S. de Gironcoli, and M. Cococcioni. *Hubbard-corrected DFT energy functionals: The LDA+U description of correlated systems*. International Journal of Quantum Chemistry, 114, 14–49, 2014. doi: 10.1002/qua.24521.

[187] A. I. Liechtenstein, V. I. Anisimov, and J. Zaanen. *Density-functional theory and strong interactions: Orbital ordering in Mott-Hubbard insulators*. Phys. Rev. B, 52, R5467–R5470, 1995. doi: 10.1103/PhysRevB.52.R5467.

[188] S. L. Dudarev, G. A. Botton, S. Y. Savrasov, C. J. Humphreys, and A. P. Sutton. *Electron-energy-loss spectra and the structural stability of nickel oxide: An LSDA+U study*. Phys. Rev. B, 57, 1505–1509, 1998. doi: 10.1103/PhysRevB.57.1505.

[189] D.-H. Seo, A. Urban, and G. Ceder. *Calibrating transition-metal energy levels and oxygen bands in first-principles calculations: Accurate prediction of redox potentials and charge transfer in lithium transition-metal oxides*. Phys. Rev. B, 92, 115118, 2015. doi: 10.1103/PhysRevB.92.115118.

[190] M. Shishkin and H. Sato. *Self-consistent parametrization of DFT+U framework using linear response approach: Application to evaluation of redox potentials of battery cathodes*. Phys. Rev. B, 93, 085135, 2016. doi: 10.1103/PhysRevB.93.085135.

[191] G. Lan, J. Song, and Z. Yang. *A linear response approach to determine Hubbard U and its application to evaluate properties of $Y_2B_2O_7$, B=transition metals 3d, 4d and 5d*. Journal of Alloys and Compounds, 749, 909–925, 2018. doi: https://doi.org/10.1016/j.jallcom.2018.03.336.

[192] A. Blanca Romero, P. M. Kowalski, G. Beridze, H. Schlenz, and D. Bosbach. *Performance of DFT+U method for prediction of structural and thermodynamic parameters of monazite-type ceramics*. Journal of Computational Chemistry, 35, 1339–1346, 2014. doi: 10.1002/jcc.23618.

[193] T. Connor, O. Cheong, T. Bornhake, A. C. Shad, R. Tesch, M. Sun, Z. He, A. Bukayemsky, V. L. Vinograd, S. C. Finkeldei, and P. M. Kowalski. *Pyrochlore Compounds From Atomistic Simulations*. Frontiers in Chemistry, 9, 2021.

[194] G. Beridze and P. M. Kowalski. *Benchmarking the DFT+U Method for Thermochemical Calculations of Uranium Molecular Compounds and Solids*. The Journal of Physical

Chemistry A, 118, 11797–11810, 2014. doi: 10.1021/jp5101126.

[195] I. Timrov, N. Marzari, and M. Cococcioni. *Hubbard parameters from density-functional perturbation theory*. Phys. Rev. B, 98, 085127, 2018. doi: 10.1103/PhysRevB.98.085127.

[196] I. Timrov, N. Marzari, and M. Cococcioni. *HP - A code for the calculation of Hubbard parameters using density-functional perturbation theory*. Computer Physics Communications, 279, 108455, 2022. doi: https://doi.org/10.1016/j.cpc.2022.108455.

[197] F. Bloch. *Über die Quantenmechanik der Elektronen in Kristallgittern*. Z. Physik, 52, 555–600, 1929. doi: 10.1007/BF01339455.

[198] G. H. Wannier. *The Structure of Electronic Excitation Levels in Insulating Crystals*. Phys. Rev., 52, 191–197, 1937. doi: 10.1103/PhysRev.52.191.

[199] N. Marzari, A. A. Mostofi, J. R. Yates, I. Souza, and D. Vanderbilt. *Maximally localized Wannier functions: Theory and applications*. Rev. Mod. Phys., 84, 1419–1475, 2012. doi: 10.1103/RevModPhys.84.1419.

[200] A. Moradabadi and P. Kaghazchi. *Defect chemistry in cubic Li6.25Al0.25La3Zr2O12 solid electrolyte: A density functional theory study*. Solid State Ionics, 338, 74–79, 2019. doi: 10.1016/j.ssi.2019.04.023.

[201] T. Binninger, A. Marcolongo, M. Mottet, V. Weber, and T. Laino. *Comparison of computational methods for the electrochemical stability window of solid-state electrolyte materials*. Journal of Materials Chemistry A, 8, 1347–1359, 2020. doi: 10.1039/C9TA09401F.

[202] L.-Y. Kuo, O. Guillon, and P. Kaghazchi. *On the origin of non-monotonic variation of the lattice parameters of $LiNi_{1/3}Co_{1/3}Mn_{1/3}O_2$ with lithiation/delithiation: a first-principles study*. J. Mater. Chem. A, 8, 13832–13841, 2020. doi: 10.1039/D0TA02319A.

[203] R. Xia, K. Zhao, L.-Y. Kuo, L. Zhang, D. M. Cunha, Y. Wang, S. Huang, J. Zheng, B. Boukamp, P. Kaghazchi, C. Sun, J. E. ten Elshof, and M. Huijben. *Nickel Niobate Anodes for High Rate Lithium-Ion Batteries*. Advanced Energy Materials, 12, 2102972, 2022. doi: 10.1002/aenm.202102972.

[204] K. Okhotnikov, T. Charpentier, and S. Cadars. *Supercell program: a combinatorial structure-generation approach for the local-level modeling of atomic substitutions and partial occupancies in crystals*. J Cheminform, 8, 17, 2016. doi: 10.1186/s13321-016-0129-3.

[205] P. P. Ewald. *Die Berechnung optischer und elektrostatischer Gitterpotentiale*. Annalen der Physik, 369, 253–287, 1921. doi: 10.1002/andp.19213690304.

[206] A. Ferrari, F. Körmann, M. Asta, and J. Neugebauer. *Simulating short-range order in compositionally complex materials*. Nat Comput Sci, 3, 221–229, 2023. doi: 10.1038/s43588-023-00407-4.

[207] T. Binninger, Y.-Y. Ting, P. M. Kowalski, and M. H. Eikerling. *Optimization of ionic configurations in battery materials by quantum annealing*. Phys. Rev. B, 110, L180202, 2024. doi: 10.1103/PhysRevB.110.L180202.

[208] R. H. Swendsen and J.-S. Wang. *Replica Monte Carlo Simulation of Spin-Glasses*. Phys. Rev. Lett., 57, 2607–2609, 1986. doi: 10.1103/PhysRevLett.57.2607.

[209] M. C. Gao, C. Niu, C. Jiang, and D. L. Irving. *Applications of Special Quasi-random Structures to High-Entropy Alloys*, pages 333–368. Springer International Publishing, 2016.

[210] D. Shin, A. van de Walle, Y. Wang, and Z.-K. Liu. *First-principles study of ternary fcc solution phases from special quasirandom structures*. Phys. Rev. B, 76, 144204, 2007. doi: 10.1103/PhysRevB.76.144204.

[211] M. C. Gao, Y. Suzuki, H. Schweiger, Ö. N. Doğan, J. Hawk, and M. Widom. *Phase*

stability and elastic properties of Cr–V alloys. J. Phys.: Condens. Matter, 25, 075402, 2013. doi: 10.1088/0953-8984/25/7/075402.

[212] S.-H. Wei, L. G. Ferreira, J. E. Bernard, and A. Zunger. *Electronic properties of random alloys: Special quasirandom structures*. Phys. Rev. B, 42, 9622–9649, 1990. doi: 10.1103/PhysRevB.42.9622.

[213] Z. W. Lu, S.-H. Wei, and A. Zunger. *Electronic structure of ordered and disordered* Cu_3Au *and* Cu_3Pd. Phys. Rev. B, 45, 10314–10330, 1992. doi: 10.1103/PhysRevB.45.10314.

[214] Z. Rák, J.-P. Maria, and D. Brenner. *Evidence for Jahn-Teller compression in the (Mg, Co, Ni, Cu, Zn)O entropy-stabilized oxide: A DFT study*. Materials Letters, 217, 300–303, 2018. doi: 10.1016/j.matlet.2018.01.111.

[215] A. van de Walle, P. Tiwary, M. de Jong, D. L. Olmsted, M. Asta, A. Dick, D. Shin, Y. Wang, L. Q. Chen, and Z. K. Liu. *Efficient stochastic generation of special quasirandom structures*. Calphad, 42, 13–18, 2013. doi: 10.1016/j.calphad.2013.06.006.

[216] A. Zunger, S.-H. Wei, L. G. Ferreira, and J. E. Bernard. *Special quasirandom structures*. Phys. Rev. Lett., 65, 353–356, 1990. doi: 10.1103/PhysRevLett.65.353.

[217] R. J. Clément, D. Kitchaev, J. Lee, and C. Gerbrand. *Short-Range Order and Unusual Modes of Nickel Redox in a Fluorine-Substituted Disordered Rocksalt Oxide Lithium-Ion Cathode*. Chem. Mater., 30, 6945–6956, 2018. doi: 10.1021/acs.chemmater.8b03794.

[218] H. Ji, A. Urban, D. A. Kitchaev, D.-H. Kwon, N. Artrith, C. Ophus, W. Huang, Z. Cai, T. Shi, J. C. Kim, H. Kim, and G. Ceder. *Hidden structural and chemical order controls lithium transport in cation-disordered oxides for rechargeable batteries*. Nat Commun, 10, 592, 2019. doi: 10.1038/s41467-019-08490-w.

[219] S. Liu, E. Martínez, and J. LLorca. *Prediction of the Al-rich part of the Al-Cu phase diagram using cluster expansion and statistical mechanics*. Acta Materialia, 195, 317–326, 2020. doi: 10.1016/j.actamat.2020.05.018.

[220] P. A. Žguns, A. V. Ruban, and N. V. Skorodumova. *Phase diagram and oxygen–vacancy ordering in the* CeO_2*–*Gd_2O_3 *system: a theoretical study*. Phys. Chem. Chem. Phys., 20, 11805–11818, 2018. doi: 10.1039/C8CP01029C.

[221] R. Drautz, R. Singer, and M. Fähnle. *Cluster expansion technique: An efficient tool to search for ground-state configurations of adatoms on plane surfaces*. Phys. Rev. B, 67, 035418, 2003. doi: 10.1103/PhysRevB.67.035418.

[222] A. Seko, K. Yuge, F. Oba, A. Kuwabara, and I. Tanaka. *Prediction of ground-state structures and order-disorder phase transitions in II-III spinel oxides: A combined cluster-expansion method and first-principles study*. Phys. Rev. B, 73, 184117, 2006. doi: 10.1103/PhysRevB.73.184117.

[223] J. M. Sanchez, F. Ducastelle, and D. Gratias. *Generalized cluster description of multicomponent systems*. Physica A: Statistical Mechanics and its Applications, 128, 334–350, 1984. doi: 10.1016/0378-4371(84)90096-7.

[224] D. D. Fontaine. *Cluster Approach to Order-Disorder Transformations in Alloys*. In *Solid State Physics*, volume 47, pages 33–176. Academic Press, 1994. doi: 10.1016/S0081-1947(08)60639-6.

[225] A. van de Walle. *Multicomponent multisublattice alloys, nonconfigurational entropy and other additions to the Alloy Theoretic Automated Toolkit*. Calphad, 33, 266–278, 2009. doi: 10.1016/j.calphad.2008.12.005.

[226] K. Binder and D. W. Heermann. *Monte Carlo Simulation in Statistical Physics*, volume 80. Springer, 1988. doi: 10.1007/978-3-662-08854-8.

[227] A. F. Kohan, P. D. Tepesch, G. Ceder, and C. Wolverton. *Computation of alloy phase diagrams at low temperatures*. Computational Materials Science, 9, 389–396, 1998. doi: 10.1016/S0927-0256(97)00168-7.

[228] F. Ducastelle. *Order and phase stability in alloys*. North-Holland ; Sole distributors for the USA and Canada, Elsevier Science Pub. Co., 1991.

[229] A. van de Walle and M. Asta. *Self-driven lattice-model Monte Carlo simulations of alloy thermodynamic properties and phase diagrams*. Modelling Simul. Mater. Sci. Eng., 10, 521, 2002. doi: 10.1088/0965-0393/10/5/304.

[230] P. Giannozzi, S. Baroni, N. Bonini, M. Calandra, R. Car, C. Cavazzoni, D. Ceresoli, G. L. Chiarotti, M. Cococcioni, I. Dabo, A. D. Corso, S. d. Gironcoli, S. Fabris, G. Fratesi, R. Gebauer, U. Gerstmann, C. Gougoussis, A. Kokalj, M. Lazzeri, L. Martin-Samos, N. Marzari, F. Mauri, R. Mazzarello, S. Paolini, A. Pasquarello, L. Paulatto, C. Sbraccia, S. Scandolo, G. Sclauzero, A. P. Seitsonen, A. Smogunov, P. Umari, and R. M. Wentzcovitch. *QUANTUM ESPRESSO: a modular and open-source software project for quantum simulations of materials*. J. Phys.: Condens. Matter, 21, 395502, 2009. doi: 10.1088/0953-8984/21/39/395502.

[231] D. Vanderbilt. *Soft self-consistent pseudopotentials in a generalized eigenvalue formalism*. Phys. Rev. B, 41, 7892–7895, 1990. doi: 10.1103/PhysRevB.41.7892.

[232] G. M. Dongho Nguimdo and D. P. Joubert. *A density functional (PBE, PBEsol, HSE06) study of the structural, electronic and optical properties of the ternary compounds* $AgAlX_2$ *(X= S, Se, Te)*. The European Physical Journal B, 88, 1–10, 2015.

[233] V. I. Anisimov, F. Aryasetiawan, and A. I. Lichtenstein. *First-principles calculations of the electronic structure and spectra of strongly correlated systems: the LDA+U method*. Journal of Physics: Condensed Matter, 9, 767–808, 1997. doi: 10.1088/0953-8984/9/4/002.

[234] H. J. Monkhorst and J. D. Pack. *Special points for Brillouin-zone integrations*. Phys. Rev. B, 13, 5188–5192, 1976. doi: 10.1103/PhysRevB.13.5188.

[235] M. Wang and A. Navrotsky. *Enthalpy of formation of* $LiNiO_2$*,* $LiCoO_2$ *and their solid solution,* $LiNi_{1-x}Co_xO_2$. Solid State Ionics, 166, 167–173, 2004. doi: https://doi.org/10.1016/j.ssi.2003.11.004.

[236] V. I. Anisimov, M. A. Korotin, and E. Z. Kurmaev. *Band-structure description of Mott insulators (NiO, MnO, FeO, CoO)*. J. Phys.: Condens. Matter, 2, 3973, 1990. doi: 10.1088/0953-8984/2/17/008.

[237] R. Gillen and J. Robertson. *Accurate screened exchange band structures for the transition metal monoxides MnO, FeO, CoO and NiO*. J. Phys.: Condens. Matter, 25, 165502, 2013. doi: 10.1088/0953-8984/25/16/165502.

[238] R. Malik, V. K. Tomer, Y. K. Mishra, and L. Lin. *Functional gas sensing nanomaterials: A panoramic view*. Appl. Phys. Rev., 7, 021301, 2020. doi: 10.1063/1.5123479.

[239] Z. Zhang, S. Mondal, S. Mandal, J. M. Allred, N. A. Aghamiri, A. Fali, Z. Zhang, H. Zhou, H. Cao, F. Rodolakis, J. L. McChesney, Q. Wang, Y. Sun, Y. Abate, K. Roy, K. M. Rabe, and S. Ramanathan. *Neuromorphic learning with Mott insulator NiO*. Proceedings of the National Academy of Sciences, 118, e2017239118, 2021. doi: 10.1073/pnas.2017239118.

[240] E. J. Cheng, N. J. Taylor, J. Wolfenstine, and J. Sakamoto. *Elastic properties of lithium cobalt oxide* $LiCoO_2$. Journal of Asian Ceramic Societies, 5, 113–117, 2017. doi: https://doi.org/10.1016/j.jascer.2017.03.001.

[241] E. Lee, S. Muhammad, T. Kim, H. Kim, W. Lee, and W.-S. Yoon. *Tracking the Influence of Thermal Expansion and Oxygen Vacancies on the Thermal Stability of Ni-Rich Layered Cathode Materials*. Advanced Science, 7, 1902413, 2020. doi: https://doi.org/10.1002/advs.201902413.

[242] M. Ernzerhof and G. E. Scuseria. *Assessment of the Perdew-Burke-Ernzerhof exchange-correlation functional*. The Journal of Chemical Physics, 110, 5029–5036,

1999. doi: 10.1063/1.478401.

[243] J. Akimoto, Y. Gotoh, and Y. Oosawa. *Synthesis and Structure Refinement of $LiCoO_2$ Single Crystals*. Journal of Solid State Chemistry, 141, 298–302, 1998. doi: https://doi.org/10.1006/jssc.1998.7966.

[244] C.-C. Chang and P. N. Kumta. *Mechanochemical synthesis of $LiNiO_2$*. Materials Science and Engineering: B, 116, 341–345, 2005. doi: https://doi.org/10.1016/j.mseb.2004.05.042.

[245] Y.-Y. Ting, B. Breitung, S. Schweidler, J. Wang, M. Eikerling, P. M. Kowalski, O. Guillon, and P. Kaghazchi. *Delithiation-induced secondary phase formation in Li-rich cathode materials*. J. Mater. Chem. A, 12, 33268–33276, 2024. doi: 10.1039/D4TA06030J.

[246] J. van Elp, J. L. Wieland, H. Eskes, P. Kuiper, G. A. Sawatzky, F. M. F. de Groot, and T. S. Turner. *Electronic structure of CoO, Li-doped CoO, and $LiCoO_2$*. Phys. Rev. B, 44, 6090–6103, 1991. doi: 10.1103/PhysRevB.44.6090.

[247] S. Laubach, S. Laubach, P. C. Schmidt, D. Ensling, S. Schmid, W. Jaegermann, A. Thißen, K. Nikolowski, and H. Ehrenberg. *Changes in the crystal and electronic structure of $LiCoO_2$ and $LiNiO_2$ upon Li intercalation and de-intercalation*. Phys. Chem. Chem. Phys., 11, 3278–3289, 2009. doi: 10.1039/B901200A.

[248] A. G. Petukhov, I. I. Mazin, L. Chioncel, and A. I. Lichtenstein. *Correlated metals and the LDA+U method*. Phys. Rev. B, 67, 153106, 2003. doi: 10.1103/PhysRevB.67.153106.

[249] S. Ryee and M. J. Han. *The effect of double counting, spin density, and Hund interaction in the different DFT+U functionals*. SCIENTIFIC REPORTS, 8, 2018. doi: 10.1038/s41598-018-27731-4.

[250] T. Yoshida, K. Hongo, and R. Maezono. *First-Principles Study of Structural Transitions in $LiNiO_2$ and High-Throughput Screening for Long Life Battery*. The Journal of Physical Chemistry C, 123, 14126–14131, 2019. doi: 10.1021/acs.jpcc.8b12556.

[251] X. Zhu, N. Chen, F. Lian, Y. Song, and Y. Li. *First principle calculation of lithiation/delithiation voltage in Li-ion battery materials*. Chinese Science Bulletin, 56, 3229–3232, 2011.

[252] M. Mock, M. Bianchini, F. Fauth, K. Albe, and S. Sicolo. *Atomistic understanding of the $LiNiO_2$–NiO_2 phase diagram from experimentally guided lattice models*. J. Mater. Chem. A, 9, 14928–14940, 2021. doi: 10.1039/D1TA00563D.

[253] Y. Gu, S. Zhu, X. Wang, J. Hu, and H. Chen. *A substantial hybridization between correlated Ni-d orbital and itinerant electrons in infinite-layer nickelates*. Commun Phys, 3, 1–9, 2020. doi: 10.1038/s42005-020-0347-x.

[254] X. Li, Q. Wang, H. Guo, N. Artrith, and A. Urban. *Understanding the Onset of Surface Degradation in LiNiO2 Cathodes*. ACS Appl. Energy Mater., 5, 5730–5741, 2022. doi: 10.1021/acsaem.2c00012.

[255] T. Ohzuku, A. Ueda, and M. Nagayama. *Electrochemistry and Structural Chemistry of $LiNiO_2$ (R3m) for 4 Volt Secondary Lithium Cells*. J. Electrochem. Soc., 140, 1862, 1993. doi: 10.1149/1.2220730.

[256] G. Beridze, A. Birnie, S. Koniski, Y. Ji, and P. M. Kowalski. *DFT+U as a reliable method for efficient ab initio calculations of nuclear materials*. Progress in Nuclear Energy, 92, 142–146, 2016. doi: 10.1016/j.pnucene.2016.07.012.

[257] J. Molenda, P. Wilk, and J. Marzec. *Structural, electrical and electrochemical properties of LiNiO2*. Solid State Ionics, 146, 73–79, 2002. doi: 10.1016/S0167-2738(01)00992-4.

[258] Y. Takahashi, N. Kijima, K. Dokko, M. Nishizawa, I. Uchida, and J. Akimoto. *Structure and electron density analysis of electrochemically and chemically delithiated $LiCoO_2$ single crystals*. Journal of Solid State Chemistry, 180, 313–321, 2007. doi: 10.1016/j.jssc.2006.10.018.

[259] C. S. Johnson, J.-S. Kim, C. Lefief, N. Li, J. T. Vaughey, and M. M. Thackeray. *The significance of the Li_2MnO_3 component in 'composite' $xLi_2MnO_3 \cdot (1-x)LiMn_{0.5}Ni_{0.5}O_2$ electrodes*. Electrochemistry Communications, 6, 1085–1091, 2004. doi: 10.1016/j.elecom.2004.08.002.

[260] Y. Xie, Y. Jin, and L. Xiang. *Li-rich layered oxides: Structure, capacity and voltage fading mechanisms and solving strategies*. Particuology, 61, 1–10, 2022. doi: 10.1016/j.partic.2021.05.011.

[261] Z. Lu, D. D. MacNeil, and J. R. Dahn. *Layered Cathode Materials $Li[Ni_xLi_{1/3-2x/3}Mn_{2/3-x/3}]O_2$ for Lithium-Ion Batteries*. Electrochem. Solid-State Lett., 4, A191, 2001. doi: 10.1149/1.1407994.

[262] W. Zuo, M. Luo, X. Liu, J. Wu, H. Liu, J. Li, M. Winter, R. Fu, W. Yang, and Y. Yang. *Li-rich cathodes for rechargeable Li-based batteries: reaction mechanisms and advanced characterization techniques*. Energy Environ. Sci., 13, 4450–4497, 2020. doi: 10.1039/D0EE01694B.

[263] H.-Y. Jang, D. Eum, J. Cho, J. Lim, Y. Lee, J.-H. Song, H. Park, B. Kim, D.-H. Kim, S.-P. Cho, S. Jo, J. H. Heo, S. Lee, J. Lim, and K. Kang. *Structurally robust lithium-rich layered oxides for high-energy and long-lasting cathodes*. Nat Commun, 15, 1288, 2024. doi: 10.1038/s41467-024-45490-x.

[264] M. Sathiya, G. Rousse, K. Ramesha, C. P. Laisa, H. Vezin, M. T. Sougrati, M.-L. Doublet, D. Foix, D. Gonbeau, W. Walker, A. S. Prakash, M. Ben Hassine, L. Dupont, and J.-M. Tarascon. *Reversible anionic redox chemistry in high-capacity layered-oxide electrodes*. Nature Mater, 12, 827–835, 2013. doi: 10.1038/nmat3699.

[265] K. Luo, M. R. Roberts, R. Hao, N. Guerrini, D. M. Pickup, Y.-S. Liu, K. Edström, J. Guo, A. V. Chadwick, L. C. Duda, and P. G. Bruce. *Charge-compensation in 3d-transition-metal-oxide intercalation cathodes through the generation of localized electron holes on oxygen*. Nature Chem, 8, 684–691, 2016. doi: 10.1038/nchem.2471.

[266] G. Assat and J.-M. Tarascon. *Fundamental understanding and practical challenges of anionic redox activity in Li-ion batteries*. Nat Energy, 3, 373–386, 2018. doi: 10.1038/s41560-018-0097-0.

[267] H. Konishi, T. Hirano, D. Takamatsu, A. Gunji, X. Feng, and S. Furutsuki. *Origin of hysteresis between charge and discharge processes in lithium-rich layer-structured cathode material for lithium-ion battery*. Journal of Power Sources, 298, 144–149, 2015. doi: 10.1016/j.jpowsour.2015.08.056.

[268] S. H. Lee, J.-S. Moon, M.-S. Lee, T.-H. Yu, H. Kim, and B. M. Park. *Enhancing phase stability and kinetics of lithium-rich layered oxide for an ultra-high performing cathode in Li-ion batteries*. Journal of Power Sources, 281, 77–84, 2015. doi: 10.1016/j.jpowsour.2015.01.158.

[269] G. Assat, D. Foix, C. Delacourt, A. Iadecola, R. Dedryvère, and J.-M. Tarascon. *Fundamental interplay between anionic/cationic redox governing the kinetics and thermodynamics of lithium-rich cathodes*. Nat Commun, 8, 2219, 2017. doi: 10.1038/s41467-017-02291-9.

[270] G. Assat, S. L. Glazier, C. Delacourt, and J.-M. Tarascon. *Probing the thermal effects of voltage hysteresis in anionic redox-based lithium-rich cathodes using isothermal calorimetry*. Nat Energy, 4, 647–656, 2019. doi: 10.1038/s41560-019-0410-6.

[271] W. D. Richards, S. T. Dacek, D. A. Kitchaev, and G. Ceder. *Fluorination of Lithium-Excess Transition Metal Oxide Cathode Materials*. Adv. Energy Mater., 8, 1701533, 2018. doi: 10.1002/aenm.201701533.

[272] J. Xu, F. Lin, M. M. Doeff, and W. Tong. *A review of Ni-based layered oxides for rechargeable Li-ion batteries*. J. Mater. Chem. A, 5, 874–901, 2017. doi: 10.1039/C6TA07991A.

[273] J. Zheng, Y. Ye, T. Liu, Y. Xiao, C. Wang, F. Wang, and F. Pan. *Ni/Li Disordering in Layered Transition Metal Oxide: Electrochemical Impact, Origin, and Control*. Acc. Chem. Res., 52, 2201–2209, 2019. doi: 10.1021/acs.accounts.9b00033.

[274] E. McCalla, M. T. Sougrati, G. Rousse, E. J. Berg, A. Abakumov, N. Recham, K. Ramesha, M. Sathiya, R. Dominko, G. Van Tendeloo, P. Novák, and J.-M. Tarascon. *Understanding the Roles of Anionic Redox and Oxygen Release during Electrochemical Cycling of Lithium-Rich Layered* Li_4FeSbO_6. J. Am. Chem. Soc., 137, 4804–4814, 2015. doi: 10.1021/jacs.5b01424.

[275] W. E. Gent, K. Lim, Y. Liang, Q. Li, T. Barnes, S.-J. Ahn, K. H. Stone, M. McIntire, J. Hong, J. H. Song, Y. Li, A. Mehta, S. Ermon, T. Tyliszczak, D. Kilcoyne, D. Vine, J.-H. Park, S.-K. Doo, M. F. Toney, W. Yang, D. Prendergast, and W. C. Chueh. *Coupling between oxygen redox and cation migration explains unusual electrochemistry in lithium-rich layered oxides*. Nat Commun, 8, 2091, 2017. doi: 10.1038/s41467-017-02041-x.

[276] D. Qian, B. Xu, M. Chi, and Y. S. Meng. *Uncovering the roles of oxygen vacancies in cation migration in lithium excess layered oxides*. Phys. Chem. Chem. Phys., 16, 14665–14668, 2014. doi: 10.1039/C4CP01799D.

[277] Q. Li, D. Ning, D. Wong, K. An, Y. Tang, D. Zhou, G. Schuck, Z. Chen, N. Zhang, and X. Liu. *Improving the oxygen redox reversibility of Li-rich battery cathode materials via Coulombic repulsive interactions strategy*. Nat Commun, 13, 1123, 2022. doi: 10.1038/s41467-022-28793-9.

[278] B. Silván, E. Gonzalo, L. Djuandhi, N. Sharma, F. Fauth, and D. Saurel. *On the dynamics of transition metal migration and its impact on the performance of layered oxides for sodium-ion batteries: NaFeO2 as a case study*. J. Mater. Chem. A, 6, 15132–15146, 2018. doi: 10.1039/C8TA02473A.

[279] J. Huang, B. Ouyang, Y. Zhang, L. Yin, D.-H. Kwon, Z. Cai, Z. Lun, G. Zeng, M. Balasubramanian, and G. Ceder. *Inhibiting collective cation migration in Li-rich cathode materials as a strategy to mitigate voltage hysteresis*. Nat. Mater., 22, 353–361, 2023. doi: 10.1038/s41563-022-01467-z.

[280] M. D. Radin, J. Vinckeviciute, R. Seshadri, and A. Van der Ven. *Manganese oxidation as the origin of the anomalous capacity of Mn-containing Li-excess cathode materials*. Nat Energy, 4, 639–646, 2019. doi: 10.1038/s41560-019-0439-6.

[281] Z. Zhang, S. Zhao, B. Wang, and H. Yu. *Local Redox Reaction of High Valence Manganese in Li2MnO3-Based Lithium Battery Cathodes*. Cell Reports Physical Science, 1, 100061, 2020. doi: 10.1016/j.xcrp.2020.100061.

[282] K. Kawai, X.-M. Shi, N. Takenaka, J. Jang, B. M. d. Boisse, A. Tsuchimoto, D. Asakura, J. Kikkawa, M. Nakayama, M. Okubo, and A. Yamada. *Kinetic square scheme in oxygen-redox battery electrodes*. Energy Environ. Sci., 15, 2591–2600, 2022. doi: 10.1039/D1EE03503G.

[283] H. Zhang, H. Liu, L. F. J. Piper, M. S. Whittingham, and G. Zhou. *Oxygen Loss in Layered Oxide Cathodes for Li-Ion Batteries: Mechanisms, Effects, and Mitigation*. Chem. Rev., 122, 5641–5681, 2022. doi: 10.1021/acs.chemrev.1c00327.

[284] T. Zhao, N. Zhou, X. Zhang, Q. Xue, Y. Wang, M. Yang, L. Li, and R. Chen. *Structure Evolution from Layered to Spinel during Synthetic Control and Cycling Process of Fe-Containing Li-Rich Cathode Materials for Lithium-Ion Batteries*. ACS Omega, 2, 5601–5610, 2017. doi: 10.1021/acsomega.7b00689.

[285] W. Hua, S. Wang, M. Knapp, S. J. Leake, A. Senyshyn, C. Richter, M. Yavuz, J. R. Binder, C. P. Grey, H. Ehrenberg, S. Indris, and B. Schwarz. *Structural insights into the formation and voltage degradation of lithium- and manganese-rich layered oxides*. Nat Commun, 10, 5365, 2019. doi: 10.1038/s41467-019-13240-z.

[286] W. Liu, P. Oh, X. Liu, S. Myeong, W. Cho, and J. Cho. *Countering Voltage Decay and Capacity Fading of Lithium-Rich Cathode Material at 60 ℃ by Hybrid Surface Protection Layers*. Advanced Energy Materials, 5, 1500274, 2015. doi: 10.1002/aenm.201500274.

[287] Y.-Y. Ting, R. Ye, E. Dashjav, Q. Ma, S. Taminato, D. Mori, N. Imanishi, M. Finsterbusch, M. H. Eikerling, O. Guillon, P. Kaghazchi, and P. M. Kowalski. *Thermodynamic and structural characterization of high-entropy garnet electrolytes for all-solid-state battery*. Front. Energy Res., 12, 2024. doi: 10.3389/fenrg.2024.1393914.

[288] R. Ye, Y.-Y. Ting, E. Dashjav, Q. Ma, S. Taminato, D. Mori, N. Imanishi, P. M. Kowalski, M. H. Eikerling, P. Kaghazchi, M. Finsterbusch, and O. Guillon. *Preparation and electrochemical properties of $Li_6La_3Zr_{0.7}Ti_{0.3}Ta_{0.5}Sb_{0.5}O_{12}$ high-entropy Li-garnet solid electrolyte*. Front. Energy Res., 12, 2024. doi: 10.3389/fenrg.2024.1379576.

[289] C. Wang, K. Fu, S. P. Kammampata, D. W. McOwen, A. J. Samson, L. Zhang, G. T. Hitz, A. M. Nolan, E. D. Wachsman, Y. Mo, V. Thangadurai, and L. Hu. *Garnet-Type Solid-State Electrolytes: Materials, Interfaces, and Batteries*. Chem. Rev., 120, 4257–4300, 2020. doi: 10.1021/acs.chemrev.9b00427.

[290] K. Meier, T. Laino, and A. Curioni. *Solid-State Electrolytes: Revealing the Mechanisms of Li-Ion Conduction in Tetragonal and Cubic LLZO by First-Principles Calculations*. J. Phys. Chem. C, 118, 6668–6679, 2014. doi: 10.1021/jp5002463.

[291] N. Bernstein, M. D. Johannes, and K. Hoang. *Origin of the Structural Phase Transition in $Li_7La_3Zr_2O_{12}$*. Phys. Rev. Lett., 109, 205702, 2012. doi: 10.1103/PhysRevLett.109.205702.

[292] H.-K. Tian, B. Xu, and Y. Qi. *Computational study of lithium nucleation tendency in $Li_7La_3Zr_2O_{12}$ (LLZO) and rational design of interlayer materials to prevent lithium dendrites*. Journal of Power Sources, 392, 79–86, 2018. doi: 10.1016/j.jpowsour.2018.04.098.

[293] M. Xu, M. S. Park, J. M. Lee, T. Y. Kim, Y. S. Park, and E. Ma. *Mechanisms of Li^+ transport in garnet-type cubic $Li_{3+x}La_3M_2O_{12}$ (M = Te, Nb, Zr)*. Phys. Rev. B, 85, 052301, 2012. doi: 10.1103/PhysRevB.85.052301.

[294] J. Awaka, A. Takashima, K. Kataoka, N. Kijima, Y. Idemoto, and J. Akimoto. *Crystal Structure of Fast Lithium-ion-conducting Cubic $Li_7La_3Zr_2O_{12}$*. Chem. Lett., 40, 60–62, 2011. doi: 10.1246/cl.2011.60.

[295] H. Xie, J. A. Alonso, Y. Li, M. T. Fernández-Díaz, and J. B. Goodenough. *Lithium Distribution in Aluminum-Free Cubic $Li_7La_3Zr_2O_{12}$*. Chem. Mater., 23, 3587–3589, 2011. doi: 10.1021/cm201671k.

[296] S. V. Borisov, S. A. Magarill, and N. V. Pervukhina. *Crystallographic Analysis of Symmetry-Stability Relations in Atomic Structures*. J Struct Chem, 60, 1191–1218, 2019. doi: 10.1134/S0022476619080018.

[297] R. D. Shannon. *Revised effective ionic radii and systematic studies of interatomic distances in halides and chalcogenides*. Acta Cryst A, 32, 751–767, 1976. doi: 10.1107/S0567739476001551.

[298] M. P. Stockham, B. Dong, M. S. James, Y. Li, Y. Ding, E. Kendrick, and P. R. Slater. *Evaluation of $Ga_{0.2}Li_{6.4}Nd_3Zr_2O_{12}$ garnets: exploiting dopant instability to create a mixed conductive interface to reduce interfacial resistance for all solid state batteries*. Dalton Trans., 50, 13786–13800, 2021. doi: 10.1039/D1DT02474D.

[299] S. Ramakumar, L. Satyanarayana, S. V. Manorama, and R. Murugan. *Structure and Li^+ dynamics of Sb-doped $Li_7La_3Zr_2O_{12}$ fast lithium ion conductors*. Phys. Chem. Chem. Phys., 15, 11327–11338, 2013. doi: 10.1039/C3CP50991E.

[300] Y. Li, J.-T. Han, C.-A. Wang, H. Xie, and J. B. Goodenough. *Optimizing Li^+ conductivity in a garnet framework*. J. Mater. Chem., 22, 15357–15361, 2012. doi:

10.1039/C2JM31413D.

[301] S. Hu, Y.-F. Li, R. Yang, Z. Yang, and L. Wang. *Structure and ionic conductivity of* $Li_7La_3Zr_{2-x}Ge_xO_{12}$ *garnet-like solid electrolyte for all solid state lithium ion batteries*. Ceramics International, 44, 6614–6618, 2018. doi: 10.1016/j.ceramint.2018.01.065.

[302] C. Shao, Z. Yu, H. Liu, Z. Zheng, N. Sun, and C. Diao. *Enhanced ionic conductivity of titanium doped* $Li_7La_3Zr_2O_{12}$ *solid electrolyte*. Electrochimica Acta, 225, 345–349, 2017. doi: 10.1016/j.electacta.2016.12.140.

[303] D. Wang, G. Zhong, O. Dolotko, Y. Li, M. J. McDonald, J. Mi, R. Fu, and Y. Yang. *The synergistic effects of Al and Te on the structure and* Li^+*-mobility of garnet-type solid electrolytes*. J. Mater. Chem. A, 2, 20271–20279, 2014. doi: 10.1039/C4TA03591G.

[304] M. Abdulai, K. B. Dermenci, and S. Turan. *Lanthanide doping of* $Li_7La_{3-x}M_xZr_2O_{12}$ *(M=Sm, Dy, Er, Yb; x=0.1-1.0) and dopant size effect on the electrochemical properties*. Ceramics International, 47, 17034–17040, 2021. doi: 10.1016/j.ceramint.2021.03.010.

[305] E. Hanc, W. Zając, and J. Molenda. *Synthesis procedure and effect of Nd, Ca and Nb doping on structure and electrical conductivity of* $Li_7La_3Zr_2O_{12}$ *garnets*. Solid State Ionics, 262, 617–621, 2014. doi: 10.1016/j.ssi.2013.11.033.

[306] E. A. Il'ina, A. A. Raskovalov, and O. G. Reznitskikh. *Thermodynamic properties of solid electrolyte* $Li_7La_3Zr_2O_{12}$. The Journal of Chemical Thermodynamics, 128, 68–73, 2019. doi: 10.1016/j.jct.2018.08.009.

[307] D. Rettenwander, P. Blaha, R. Laskowski, K. Schwarz, P. Bottke, M. Wilkening, C. A. Geiger, and G. Amthauer. *DFT Study of the Role of* Al^{3+} *in the Fast Ion-Conductor* $Li_{7-3x}Al_{3+x}La_3Zr_2O_{12}$ *Garnet*. Chem. Mater., 26, 2617–2623, 2014. doi: 10.1021/cm5000999.

[308] T. Thompson, J. Wolfenstine, J. L. Allen, M. Johannes, A. Huq, I. N. David, and J. Sakamoto. *Tetragonal vs. cubic phase stability in Al - free Ta doped* $Li_7La_3Zr_2O_{12}$ *(LLZO)*. J. Mater. Chem. A, 2, 13431–13436, 2014. doi: 10.1039/C4TA02099E.

[309] D. O. Shin, K. Oh, K. M. Kim, K.-Y. Park, B. Lee, Y.-G. Lee, and K. Kang. *Synergistic multi-doping effects on the* $Li_7La_3Zr_2O_{12}$ *solid electrolyte for fast lithium ion conduction*. Sci Rep, 5, 18053, 2015. doi: 10.1038/srep18053.

[310] Y. Li, P. M. Kowalski, G. Beridze, A. R. Birnie, S. Finkeldei, and D. Bosbach. *Defect formation energies in* $A_2B_2O_7$ *pyrochlores*. Scripta Materialia, 107, 18–21, 2015. doi: 10.1016/j.scriptamat.2015.05.010.

[311] M. Matsui, K. Takahashi, K. Sakamoto, A. Hirano, Y. Takeda, O. Yamamoto, and N. Imanishi. *Phase stability of a garnet-type lithium ion conductor* $Li_7La_3Zr_2O_{12}$. Dalton Trans., 43, 1019–1024, 2013. doi: 10.1039/C3DT52024B.

[312] G. Larraz, A. Orera, and M. L. Sanjuán. *Cubic phases of garnet-type* $Li_7La_3Zr_2O_{12}$*: the role of hydration*. J. Mater. Chem. A, 1, 11419–11428, 2013. doi: 10.1039/C3TA11996C.

[313] J. L. Allen, J. Wolfenstine, E. Rangasamy, and J. Sakamoto. *Effect of substitution (Ta, Al, Ga) on the conductivity of* $Li_7La_3Zr_2O_{12}$. Journal of Power Sources, 206, 315–319, 2012. doi: 10.1016/j.jpowsour.2012.01.131.

[314] Y. V. Baklanova, A. P. Tyutyunnik, N. V. Tarakina, A. D. Fortes, L. G. Maksimova, D. V. Korona, and T. A. Denisova. *Stabilization of cubic* $Li_7La_3Hf_2O_{12}$ *by Al-doping*. Journal of Power Sources, 391, 26–33, 2018. doi: 10.1016/j.jpowsour.2018.04.066.

[315] R. Ye, C.-L. Tsai, M. Ihrig, S. Sevinc, M. Rosen, E. Dashjav, Y. J. Sohn, E. Figgemeier, and M. Finsterbusch. *Water-based fabrication of garnet-based solid electrolyte separators for solid-state lithium batteries*. Green Chem., 22, 4952–4961, 2020. doi: 10.1039/D0GC01009J.

[316] Y. He, Y.-Y. Ting, H. Hu, T. Diemant, Y. Dai, J. Lin, S. Schweidler, G. C. Marques, H. Hahn, Y. Ma, T. Brezesinski, P. M. Kowalski, B. Breitung, and J. Aghassi-Hagmann.

Printed High-Entropy Prussian Blue Analogs for Advanced Non-Volatile Memristive Devices. Adv. Mater., 37, 2410060, 2025. doi: 10.1002/adma.202410060.

[317] Q. Huang, T. P. Pollard, X. Ren, D. Kim, A. Magasinski, O. Borodin, and G. Yushin. *Fading Mechanisms and Voltage Hysteresis in FeF2-NiF2 Solid Solution Cathodes for Lithium and Lithium-Ion Batteries*. Small, 15, 1804670, 2019. doi: 10.1002/smll.201804670.

[318] S.-W. Kim, K.-W. Nam, D.-H. Seo, J. Hong, H. Kim, H. Gwon, and K. Kang. *Energy storage in composites of a redox couple host and a lithium ion host*. Nano Today, 7, 168–173, 2012. doi: 10.1016/j.nantod.2012.04.004.

[319] X. Fan, E. Hu, X. Ji, Y. Zhu, F. Han, S. Hwang, J. Liu, S. Bak, Z. Ma, T. Gao, S.-C. Liou, J. Bai, X.-Q. Yang, Y. Mo, K. Xu, D. Su, and C. Wang. *High energy-density and reversibility of iron fluoride cathode enabled via an intercalation-extrusion reaction*. Nat Commun, 9, 2324, 2018. doi: 10.1038/s41467-018-04476-2.

[320] Y. Zhao, K. Wei, H. Wu, S. Ma, J. Li, Y. Cui, Z. Dong, Y. Cui, and C. Li. *LiF Splitting Catalyzed by Dual Metal Nanodomains for an Efficient Fluoride Conversion Cathode*. ACS Nano, 13, 2490–2500, 2019. doi: 10.1021/acsnano.8b09453.

[321] D. Gordon, Q. Huang, A. Magasinski, A. Ramanujapuram, N. Bensalah, and G. Yushin. *Mixed Metal Difluorides as High Capacity Conversion-Type Cathodes: Impact of Composition on Stability and Performance*. Advanced Energy Materials, 8, 1800213, 2018. doi: 10.1002/aenm.201800213.

[322] C. Villa, S. Kim, Y. Lu, V. P. Dravid, and J. Wu. *Cu-Substituted NiF_2 as a Cathode Material for Li-Ion Batteries*. ACS Appl. Mater. Interfaces, 11, 647–654, 2019. doi: 10.1021/acsami.8b15791.

[323] E. Lökçü, Ç. Toparli, and M. Anik. *Electrochemical Performance of $(MgCoNiZn)_{1-x}Li_xO$ High-Entropy Oxides in Lithium-Ion Batteries*. ACS Appl. Mater. Interfaces, 12, 23860–23866, 2020. doi: 10.1021/acsami.0c03562.

[324] X. Zhao, Y. Tian, Z. Lun, Z. Cai, T. Chen, B. Ouyang, and G. Ceder. *Design principles for zero-strain Li-ion cathodes*. Joule, 6, 1654–1671, 2022. doi: 10.1016/j.joule.2022.05.018.

[325] L.-Y. Kuo, O. Guillon, and P. Kaghazchi. *Origin of Structural Phase Transitions in Ni-Rich $Li_xNi_{0.8}Co_{0.1}Mn_{0.1}O_2$ with Lithiation/Delithiation: A First-Principles Study*. ACS Sustainable Chem. Eng., 9, 7437–7446, 2021. doi: 10.1021/acssuschemeng.0c07675.

[326] J. Peng, W. Zhang, Q. Liu, J. Wang, S. Chou, H. Liu, and S. Dou. *Prussian Blue Analogues for Sodium-Ion Batteries: Past, Present, and Future*. Advanced Materials, 34, 2108384, 2022. doi: 10.1002/adma.202108384.

[327] J. Qian, C. Wu, Y. Cao, Z. Ma, Y. Huang, X. Ai, and H. Yang. *Prussian Blue Cathode Materials for Sodium-Ion Batteries and Other Ion Batteries*. Advanced Energy Materials, 8, 1702619, 2018. doi: 10.1002/aenm.201702619.

[328] Q. Liu, Z. Hu, M. Chen, C. Zou, H. Jin, S. Wang, S.-L. Chou, Y. Liu, and S.-X. Dou. *The Cathode Choice for Commercialization of Sodium-Ion Batteries: Layered Transition Metal Oxides versus Prussian Blue Analogs*. Advanced Functional Materials, 30, 1909530, 2020. doi: 10.1002/adfm.201909530.

[329] W. Li, C. Han, W. Wang, Q. Xia, S. Chou, Q. Gu, B. Johannessen, H. Liu, and S. Dou. *Stress Distortion Restraint to Boost the Sodium Ion Storage Performance of a Novel Binary Hexacyanoferrate*. Advanced Energy Materials, 10, 1903006, 2020. doi: 10.1002/aenm.201903006.

[330] L. Wang, J. Song, R. Qiao, L. A. Wray, M. A. Hossain, Y.-D. Chuang, W. Yang, Y. Lu, D. Evans, J.-J. Lee, S. Vail, X. Zhao, M. Nishijima, S. Kakimoto, and J. B. Goodenough. *Rhombohedral prussian white as cathode for rechargeable sodium-ion batteries*. J Am Chem Soc, 137, 2548–2554, 2015. doi: 10.1021/ja510347s.

[331] Y. Shang, X. Li, J. Song, S. Huang, Z. Yang, Z. J. Xu, and H. Y. Yang. *Unconventional Mn Vacancies in Mn–Fe Prussian Blue Analogs: Suppressing Jahn-Teller Distortion for Ultrastable Sodium Storage*. Chem, 6, 1804–1818, 2020. doi: 10.1016/j.chempr.2020.05.004.

[332] V. Renman, D. O. Ojwang, C. Pay Gómez, T. Gustafsson, K. Edström, G. Svensson, and M. Valvo. *Manganese Hexacyanomanganate as a Positive Electrode for Nonaqueous Li-, Na-, and K-Ion Batteries*. J. Phys. Chem. C, 123, 22040–22049, 2019. doi: 10.1021/acs.jpcc.9b06338.

[333] K. Hurlbutt, S. Wheeler, I. Capone, and M. Pasta. *Prussian Blue Analogs as Battery Materials*. Joule, 2, 1950–1960, 2018. doi: 10.1016/j.joule.2018.07.017.

[334] X. Huang, C. Yang, and Y. You. *Polycrystalline Prussian White Aggregates as a High-Rate and Long-Life Cathode for High-Temperature Sodium-Ion Batteries*. ACS Appl. Energy Mater., 5, 8123–8131, 2022. doi: 10.1021/acsaem.2c00646.

[335] L. Jiang, Y. Lu, C. Zhao, L. Liu, J. Zhang, Q. Zhang, X. Shen, J. Zhao, X. Yu, H. Li, X. Huang, L. Chen, and Y.-S. Hu. *Building aqueous K-ion batteries for energy storage*. Nat Energy, 4, 495–503, 2019. doi: 10.1038/s41560-019-0388-0.

[336] D. Yang, J. Xu, X.-Z. Liao, Y.-S. He, H. Liu, and Z.-F. Ma. *Structure optimization of Prussian blue analogue cathode materials for advanced sodium ion batteries*. Chem. Commun., 50, 13377–13380, 2014. doi: 10.1039/C4CC05830E.

[337] J. Zhang, J. Wan, M. Ou, S. Liu, B. Huang, J. Xu, S. Sun, Y. Xu, Y. Lin, C. Fang, and J. Han. *Enhanced all-climate sodium-ion batteries performance in a low-defect and Na-enriched Prussian blue analogue cathode by nickel substitution*. energymater, 3, N/A–N/A, 2023. doi: 10.20517/energymater.2022.71.

[338] Y. You, X.-L. Wu, Y.-X. Yin, and Y.-G. Guo. *High-quality Prussian blue crystals as superior cathode materials for room-temperature sodium-ion batteries*. Energy Environ. Sci., 7, 1643–1647, 2014. doi: 10.1039/C3EE44004D.

[339] J. Song, L. Wang, Y. Lu, J. Liu, B. Guo, P. Xiao, J.-J. Lee, X.-Q. Yang, G. Henkelman, and J. B. Goodenough. *Removal of Interstitial H2O in Hexacyanometallates for a Superior Cathode of a Sodium-Ion Battery*. J. Am. Chem. Soc., 137, 2658–2664, 2015. doi: 10.1021/ja512383b.

[340] Y. Xu, J. Wan, L. Huang, M. Ou, C. Fan, P. Wei, J. Peng, Y. Liu, Y. Qiu, X. Sun, C. Fang, Q. Li, J. Han, Y. Huang, J. A. Alonso, and Y. Zhao. *Structure Distortion Induced Monoclinic Nickel Hexacyanoferrate as High-Performance Cathode for Na-Ion Batteries*. Advanced Energy Materials, 9, 1803158, 2019. doi: 10.1002/aenm.201803158.

[341] Y. Tang, W. Li, P. Feng, M. Zhou, K. Wang, Y. Wang, K. Zaghib, and K. Jiang. *High-Performance Manganese Hexacyanoferrate with Cubic Structure as Superior Cathode Material for Sodium-Ion Batteries*. Advanced Functional Materials, 30, 1908754, 2020. doi: 10.1002/adfm.201908754.

[342] L. Deng, J. Qu, X. Niu, J. Liu, J. Zhang, Y. Hong, M. Feng, J. Wang, M. Hu, L. Zeng, Q. Zhang, L. Guo, and Y. Zhu. *Defect-free potassium manganese hexacyanoferrate cathode material for high-performance potassium-ion batteries*. Nat Commun, 12, 2167, 2021. doi: 10.1038/s41467-021-22499-0.

[343] Y. You, H.-R. Yao, S. Xin, Y.-X. Yin, T.-T. Zuo, C.-P. Yang, Y.-G. Guo, Y. Cui, L.-J. Wan, and J. B. Goodenough. *Subzero-Temperature Cathode for a Sodium-Ion Battery*. Advanced Materials, 28, 7243–7248, 2016. doi: 10.1002/adma.201600846.

[344] W.-J. Li, S.-L. Chou, J.-Z. Wang, J.-L. Wang, Q.-F. Gu, H.-K. Liu, and S.-X. Dou. *Multifunctional conducing polymer coated* $Na_{1+x}MnFeCN_6$ *cathode for sodium-ion batteries with superior performance via a facile and one-step chemistry approach*. Nano Energy, 13, 200–207, 2015. doi: 10.1016/j.nanoen.2015.02.019.

[345] G. Kresse and J. Furthmüller. *Efficiency of ab-initio total energy calculations for metals*

and semiconductors using a plane-wave basis set. Computational Materials Science, 6, 15–50, 1996. doi: 10.1016/0927-0256(96)00008-0.

[346] P. E. Blöchl. *Projector augmented-wave method*. Phys. Rev. B, 50, 17953–17979, 1994. doi: 10.1103/PhysRevB.50.17953.

[347] A. van de Walle, M. Asta, and G. Ceder. *The alloy theoretic automated toolkit: A user guide*. Calphad, 26, 539–553, 2002. doi: 10.1016/S0364-5916(02)80006-2.

[348] Y.-T. Liu, X.-B. Li, H. Zheng, N.-K. Chen, X.-P. Wang, X.-L. Zhang, H.-B. Sun, and S. Zhang. *High-Throughput Screening for Phase-Change Memory Materials*. Advanced Functional Materials, 31, 2009803, 2021. doi: 10.1002/adfm.202009803.

[349] S.-T. Han, Y. Zhou, and V. a. L. Roy. *Towards the Development of Flexible Non-Volatile Memories*. Advanced Materials, 25, 5425–5449, 2013. doi: 10.1002/adma.201301361.

[350] M.-K. Song, J.-H. Kang, X. Zhang, W. Ji, A. Ascoli, I. Messaris, A. S. Demirkol, B. Dong, S. Aggarwal, W. Wan, S.-M. Hong, S. G. Cardwell, I. Boybat, J.-s. Seo, J.-S. Lee, M. Lanza, H. Yeon, M. Onen, J. Li, B. Yildiz, J. A. del Alamo, S. Kim, S. Choi, G. Milano, C. Ricciardi, L. Alff, Y. Chai, Z. Wang, H. Bhaskaran, M. C. Hersam, D. Strukov, H.-S. P. Wong, I. Valov, B. Gao, H. Wu, R. Tetzlaff, A. Sebastian, W. Lu, L. Chua, J. J. Yang, and J. Kim. *Recent Advances and Future Prospects for Memristive Materials, Devices, and Systems*. ACS Nano, 17, 11994–12039, 2023. doi: 10.1021/acsnano.3c03505.

[351] K. Zhu, S. Pazos, F. Aguirre, Y. Shen, Y. Yuan, W. Zheng, O. Alharbi, M. A. Villena, B. Fang, X. Li, A. Milozzi, M. Farronato, M. Muñoz-Rojo, T. Wang, R. Li, H. Fariborzi, J. B. Roldan, G. Benstetter, X. Zhang, H. N. Alshareef, T. Grasser, H. Wu, D. Ielmini, and M. Lanza. *Hybrid 2D–CMOS microchips for memristive applications*. Nature, 618, 57–62, 2023. doi: 10.1038/s41586-023-05973-1.

[352] G. Zhang, J. Qin, Y. Zhang, G. Gong, Z.-Y. Xiong, X. Ma, Z. Lv, Y. Zhou, and S.-T. Han. *Functional Materials for Memristor-Based Reservoir Computing: Dynamics and Applications*. Advanced Functional Materials, 33, 2302929, 2023. doi: 10.1002/adfm.202302929.

[353] J. C. Gonzalez-Rosillo, M. Balaish, Z. D. Hood, N. Nadkarni, D. Fraggedakis, K. J. Kim, K. M. Mullin, R. Pfenninger, M. Z. Bazant, and J. L. M. Rupp. *Lithium-Battery Anode Gains Additional Functionality for Neuromorphic Computing through Metal–Insulator Phase Separation*. Advanced Materials, 32, 1907465, 2020. doi: 10.1002/adma.201907465.

[354] C. Zhang, M. Chen, Y. Pan, Y. Li, K. Wang, J. Yuan, Y. Sun, and Q. Zhang. *Carbon Nanodots Memristor: An Emerging Candidate toward Artificial Biosynapse and Human Sensory Perception System*. Advanced Science, 10, 2207229, 2023. doi: 10.1002/advs.202207229.

[355] Y. Huang, Y. Gu, S. Mohan, A. Dolocan, N. D. Ignacio, S. Kutagulla, K. Matthews, A. Londoño-Calderon, Y.-F. Chang, Y.-C. Chen, J. H. Warner, M. T. Pettes, J. C. Lee, and D. Akinwande. *Reliability Improvement and Effective Switching Layer Model of Thin-Film MoS2 Memristors*. Advanced Functional Materials, 34, 2214250, 2024. doi: 10.1002/adfm.202214250.

[356] Y. van de Burgt, E. Lubberman, E. J. Fuller, S. T. Keene, G. C. Faria, S. Agarwal, M. J. Marinella, A. Alec Talin, and A. Salleo. *A non-volatile organic electrochemical device as a low-voltage artificial synapse for neuromorphic computing*. Nature Mater, 16, 414–418, 2017. doi: 10.1038/nmat4856.

[357] A. Sebastian, M. Le Gallo, R. Khaddam-Aljameh, and E. Eleftheriou. *Memory devices and applications for in-memory computing*. Nat. Nanotechnol., 15, 529–544, 2020. doi: 10.1038/s41565-020-0655-z.

[358] Y. Lin, F. Meng, T. Zeng, Q. Zhang, Z. Wang, Y. Cheng, X. Zhao, L. Gu, H. Xu, and Y. Liu.

Direct Observation of Oxygen Ion Dynamics in a WO3-x based Second-Order Memristor with Dendritic Integration Functions. Advanced Functional Materials, 33, 2302787, 2023. doi: 10.1002/adfm.202302787.

[359] R. Marquardt, F. Zahari, J. Carstensen, G. Popkirov, O. Gronenberg, G. Kolhatkar, H. Kohlstedt, and M. Ziegler. *Impedance Spectroscopy on Hafnium Oxide-Based Memristive Devices*. Advanced Electronic Materials, 9, 2201227, 2023. doi: 10.1002/aelm.202201227.

[360] E. Carlos, R. Branquinho, R. Martins, A. Kiazadeh, and E. Fortunato. *Recent Progress in Solution-Based Metal Oxide Resistive Switching Devices*. Advanced Materials, 33, 2004328, 2021. doi: 10.1002/adma.202004328.

[361] Y. Abbas, S. M. Ansari, I. Taha, H. Abunahla, M. U. Khan, M. Rezeq, H. M. Aldosari, and B. Mohammad. *Stopping Voltage-Dependent PCM and RRAM-Based Neuromorphic Characteristics of Germanium Telluride*. Advanced Functional Materials, 34, 2214615, 2024. doi: 10.1002/adfm.202214615.

[362] M. D. Tran, H. Kim, J. S. Kim, M. H. Doan, T. K. Chau, Q. A. Vu, J.-H. Kim, and Y. H. Lee. *Two-Terminal Multibit Optical Memory via van der Waals Heterostructure*. Advanced Materials, 31, 1807075, 2019. doi: 10.1002/adma.201807075.

[363] S. Batool, M. Idrees, S.-R. Zhang, S.-T. Han, and Y. Zhou. *Novel charm of 2D materials engineering in memristor: when electronics encounter layered morphology*. Nanoscale Horiz., 7, 480–507, 2022. doi: 10.1039/D2NH00031H.

[364] S. P. Rath, D. Thompson, S. Goswami, and S. Goswami. *Many-Body Molecular Interactions in a Memristor*. Advanced Materials, 35, 2204551, 2023. doi: 10.1002/adma.202204551.

[365] E. J. Yoo, M. Lyu, J.-H. Yun, C. J. Kang, Y. J. Choi, and L. Wang. *Resistive Switching Behavior in Organic–Inorganic Hybrid $CH_3NH_3PbI_3Cl$ Perovskite for Resistive Random Access Memory Devices*. Advanced Materials, 27, 6170–6175, 2015. doi: 10.1002/adma.201502889.

[366] J. H. Heo, D. H. Shin, S. H. Moon, M. H. Lee, D. H. Kim, S. H. Oh, W. Jo, and S. H. Im. *Memory effect behavior with respect to the crystal grain size in the organic-inorganic hybrid perovskite nonvolatile resistive random access memory*. Sci Rep, 7, 16586, 2017. doi: 10.1038/s41598-017-16805-4.

[367] Y. Lin, X. Zhang, X. Shan, T. Zeng, X. Zhao, Z. Wang, Z. Kang, H. Xu, and Y. Liu. *Photo-tunable organic resistive random access memory based on PVP/N-doped carbon dot nanocomposites for encrypted image storage*. J. Mater. Chem. C, 8, 14789–14795, 2020. doi: 10.1039/D0TC03907A.

[368] C. Li, L. Han, H. Jiang, M.-H. Jang, P. Lin, Q. Wu, M. Barnell, J. J. Yang, H. L. Xin, and Q. Xia. *Three-dimensional crossbar arrays of self-rectifying Si/SiO_2/Si memristors*. Nat Commun, 8, 15666, 2017. doi: 10.1038/ncomms15666.

[369] H. Yeon, P. Lin, C. Choi, S. H. Tan, Y. Park, D. Lee, J. Lee, F. Xu, B. Gao, H. Wu, H. Qian, Y. Nie, S. Kim, and J. Kim. *Alloying conducting channels for reliable neuromorphic computing*. Nat. Nanotechnol., 15, 574–579, 2020. doi: 10.1038/s41565-020-0694-5.

[370] C. Chen, Y. C. Yang, F. Zeng, and F. Pan. *Bipolar resistive switching in Cu/AlN/Pt nonvolatile memory device*. Applied Physics Letters, 97, 083502, 2010. doi: 10.1063/1.3483158.

[371] H. D. Kim, H. M. An, S. M. Hong, and T. G. Kim. *Forming-free SiN-based resistive switching memory prepared by RF sputtering*. Physica Status Solidi (A) Applications and Materials Science, 210, 1822–1827, 2013. doi: 10.1002/pssa.201329021.

[372] X. Zhao, Z. Wang, Y. Xie, H. Xu, J. Zhu, X. Zhang, W. Liu, G. Yang, J. Ma, and Y. Liu. *Photocatalytic Reduction of Graphene Oxide–TiO_2 Nanocomposites for Improving Resistive-*

Switching Memory Behaviors. Small, 14, 1801325, 2018. doi: 10.1002/smll.201801325.

[373] A. Sood, A. D. Poletayev, D. A. Cogswell, P. M. Csernica, J. T. Mefford, D. Fraggedakis, M. F. Toney, A. M. Lindenberg, M. Z. Bazant, and W. C. Chueh. *Electrochemical ion insertion from the atomic to the device scale*. Nat Rev Mater, 6, 847–867, 2021. doi: 10.1038/s41578-021-00314-y.

[374] H. Yi, R. Qin, S. Ding, Y. Wang, S. Li, Q. Zhao, and F. Pan. *Structure and Properties of Prussian Blue Analogues in Energy Storage and Conversion Applications*. Advanced Functional Materials, 31, 2006970, 2021. doi: 10.1002/adfm.202006970.

[375] Y. Ma, Y. Hu, Y. Pramudya, T. Diemant, Q. Wang, D. Goonetilleke, Y. Tang, B. Zhou, H. Hahn, W. Wenzel, M. Fichtner, Y. Ma, B. Breitung, and T. Brezesinski. *Resolving the Role of Configurational Entropy in Improving Cycling Performance of Multicomponent Hexacyanoferrate Cathodes for Sodium-Ion Batteries*. Advanced Functional Materials, 32, 2202372, 2022. doi: 10.1002/adfm.202202372.

[376] Y. Ma, Y. Ma, S. L. Dreyer, Q. Wang, K. Wang, D. Goonetilleke, A. Omar, D. Mikhailova, H. Hahn, B. Breitung, and T. Brezesinski. *High-Entropy Metal–Organic Frameworks for Highly Reversible Sodium Storage*. Advanced Materials, 33, 2101342, 2021. doi: 10.1002/adma.202101342.

[377] T. Shibata and Y. Moritomo. *Ultrafast cation intercalation in nanoporous nickel hexacyanoferrate*. Chem. Commun., 50, 12941–12943, 2014. doi: 10.1039/C4CC04564E.

[378] M. Takachi, Y. Fukuzumi, and Y. Moritomo. *Na+ diffusion kinetics in nanoporous metal-hexacyanoferrates*. Dalton Trans., 45, 458–461, 2015. doi: 10.1039/C5DT03276H.

[379] D. A. Robinson, M. E. Foster, C. H. Bennett, A. Bhandarkar, E. R. Webster, A. Celebi, N. Celebi, E. J. Fuller, V. Stavila, C. D. Spataru, D. S. Ashby, M. J. Marinella, R. Krishnakumar, M. D. Allendorf, and A. A. Talin. *Tunable Intervalence Charge Transfer in Ruthenium Prussian Blue Analog Enables Stable and Efficient Biocompatible Artificial Synapses*. Advanced Materials, 35, 2207595, 2023. doi: 10.1002/adma.202207595.

[380] K. Yan, J. Li, L. Pan, and Y. Shi. *Inkjet printing for flexible and wearable electronics*. APL Materials, 8, 120705, 2020. doi: 10.1063/5.0031669.

[381] H. Hu, A. Scholz, Y. Liu, Y. Tang, G. C. Marques, and J. Aghassi-Hagmann. *A Fully Inkjet-Printed Unipolar Metal Oxide Memristor for Nonvolatile Memory in Printed Electronics*. IEEE Transactions on Electron Devices, 70, 3051–3056, 2023. doi: 10.1109/TED.2023.3269405.

[382] H. Zhang, X. Ju, Y. Zhou, C. Gu, J. Pan, and D. S. Ang. *Realization of Self-Compliance Resistive Switching Memory via Tailoring Interfacial Oxygen*. ACS Appl. Mater. Interfaces, 11, 41490–41496, 2019. doi: 10.1021/acsami.9b11772.

[383] G. Ding, Y. Wang, G. Zhang, K. Zhou, K. Zeng, Z. Li, Y. Zhou, C. Zhang, X. Chen, and S.-T. Han. *2D Metal–Organic Framework Nanosheets with Time-Dependent and Multilevel Memristive Switching*. Advanced Functional Materials, 29, 1806637, 2019. doi: 10.1002/adfm.201806637.

[384] N. Casa Branca, J. Deuermeier, J. Martins, E. Carlos, M. Pereira, R. Martins, E. Fortunato, and A. Kiazadeh. *2D Resistive Switching Based on Amorphous Zinc–Tin Oxide Schottky Diodes*. Advanced Electronic Materials, 6, 1900958, 2020. doi: 10.1002/aelm.201900958.

[385] M. Ahn, Y. Park, S. H. Lee, S. Chae, J. Lee, J. T. Heron, E. Kioupakis, W. D. Lu, and J. D. Phillips. *Memristors Based on (Zr, Hf, Nb, Ta, Mo, W) High-Entropy Oxides*. Advanced Electronic Materials, 7, 2001258, 2021. doi: 10.1002/aelm.202001258.

[386] J. C. Wojdeł, I. de P. R. Moreira, S. T. Bromley, and F. Illas. *On the prediction of the crystal and electronic structure of mixed-valence materials by periodic density functional calculations: The case of Prussian Blue*. The Journal of Chemical Physics, 128, 044713,

2008. doi: 10.1063/1.2824966.

[387] S. Watanabe, Y. Sawada, M. Nakaya, M. Yoshino, T. Nagasaki, T. Kameyama, T. Torimoto, Y. Inaba, H. Takahashi, K. Takeshita, and J. Onoe. *Intra- and inter-atomic optical transitions of Fe, Co, and Ni ferrocyanides studied using first-principles many-electron calculations*. Journal of Applied Physics, 119, 235102, 2016. doi: 10.1063/1.4954070.

[388] E. Targholi, S. M. Mousavi-Khoshdel, M. Rahmanifara, and M. Yahya. *Cu- and Fe-hexacyanoferrate as cathode materials for Potassium ion battery: A First-principles study*. Chemical Physics Letters, 687, 244–249, 2017. doi: 10.1016/j.cplett.2017.09.029.

[389] Z. Wang, X. Zhang, S. Zhou, K. Edström, M. Strømme, and L. Nyholm. *Lightweight, Thin, and Flexible Silver Nanopaper Electrodes for High-Capacity Dendrite-Free Sodium Metal Anodes*. Advanced Functional Materials, 28, 1804038, 2018. doi: 10.1002/adfm.201804038.

[390] N. Zhu, X. Mao, G. Wang, M. Zhu, H. Wang, G. Xu, M. Wu, H. K. Liu, S.-X. Dou, and C. Wu. *Stable sodium metal anodes with a high utilization enabled by an interfacial layer composed of yolk–shell nanoparticles*. J. Mater. Chem. A, 9, 13200–13208, 2021. doi: 10.1039/D1TA01800K.

[391] H. Wang, Y. Wu, S. Liu, Y. Jiang, D. Shen, T. Kang, Z. Tong, D. Wu, X. Li, and C.-S. Lee. *3D Ag@C Cloth for Stable Anode Free Sodium Metal Batteries*. Small Methods, 5, 2001050, 2021. doi: 10.1002/smtd.202001050.

[392] V. S. Nguyen, V. H. Mai, P. Auban Senzier, C. Pasquier, K. Wang, M. J. Rozenberg, N. Brun, K. March, F. Jomard, J. Giapintzakis, C. N. Mihailescu, E. Kyriakides, P. Nukala, T. Maroutian, G. Agnus, P. Lecoeur, S. Matzen, P. Aubert, S. Franger, R. Salot, P.-A. Albouy, D. Alamarguy, B. Dkhil, P. Chrétien, and O. Schneegans. *Direct Evidence of Lithium Ion Migration in Resistive Switching of Lithium Cobalt Oxide Nanobatteries*. Small, 14, 1801038, 2018. doi: 10.1002/smll.201801038.

[393] K. Kushida and K. Kuriyama. *Mott-type hopping conduction in the ordered and disordered phases of $LiCoO_2$*. Solid State Communications, 129, 525–528, 2004. doi: 10.1016/j.ssc.2003.11.028.

[394] A. Milewska, K. Świerczek, J. Tobola, F. Boudoire, Y. Hu, D. K. Bora, B. S. Mun, A. Braun, and J. Molenda. *The nature of the nonmetal–metal transition in Li_xCoO_2 oxide*. Solid State Ionics, 263, 110–118, 2014. doi: 10.1016/j.ssi.2014.05.011.

[395] E. Flores, N. Mozhzhukhina, U. Aschauer, and E. J. Berg. *Operando Monitoring the Insulator–Metal Transition of $LiCoO_2$*. ACS Appl. Mater. Interfaces, 13, 22540–22548, 2021. doi: 10.1021/acsami.1c04383.

[396] P. Hauke, H. G. Katzgraber, W. Lechner, H. Nishimori, and W. D. Oliver. *Perspectives of quantum annealing: methods and implementations*. Rep. Prog. Phys., 83, 054401, 2020. doi: 10.1088/1361-6633/ab85b8.

[397] M. Jünger, E. Lobe, P. Mutzel, G. Reinelt, F. Rendl, G. Rinaldi, and T. Stollenwerk. *Quantum Annealing versus Digital Computing: An Experimental Comparison*. ACM J. Exp. Algorithmics, 26, 1.9:1–1.9:30, 2021. doi: 10.1145/3459606.

[398] B. C. B. Symons, D. Galvin, E. Sahin, V. Alexandrov, and S. Mensa. *A practitioner's guide to quantum algorithms for optimisation problems*. J. Phys. A: Math. Theor., 56, 453001, 2023. doi: 10.1088/1751-8121/ad00f0.

[399] A. Van der Ven, M. K. Aydinol, G. Ceder, G. Kresse, and J. Hafner. *First-principles investigation of phase stability in Li_xCoO_2*. Phys. Rev. B, 58, 2975–2987, 1998. doi: 10.1103/PhysRevB.58.2975.

[400] C. Wolverton and A. Zunger. *First-Principles Prediction of Vacancy Order-Disorder and Intercalation Battery Voltages in Li_xCoO_2*. Phys. Rev. Lett., 81, 606–609, 1998. doi: 10.1103/PhysRevLett.81.606.

[401] J. N. Reimers and J. R. Dahn. *Electrochemical and In Situ X-Ray Diffraction Studies of Lithium Intercalation in Li_xCoO_2*. J. Electrochem. Soc., 139, 2091, 1992. doi: 10.1149/1.2221184.

[402] J. Brugger, C. Seidel, M. Streif, F. A. Wudarski, C. Dittel, and A. Buchleitner. *Output statistics of quantum annealers with disorder*. Phys. Rev. A, 105, 042605, 2022. doi: 10.1103/PhysRevA.105.042605.

[403] T. Zhao, H. Mahandra, R. Marthi, X. Ji, W. Zhao, S. Chae, M. Traversy, W. Li, F. Yu, L. Li, Y. Choi, A. Ghahreman, Z. Zhao, C. Zhang, Y. Kang, Y. Lei, and Y. Song. *An overview on the life cycle of lithium iron phosphate: synthesis, modification, application, and recycling*. Chemical Engineering Journal, 485, 149923, 2024. doi: 10.1016/j.cej.2024.149923.

[404] N. Huittinen, Y. Arinicheva, P. M. Kowalski, V. L. Vinograd, S. Neumeier, and D. Bosbach. *Probing structural homogeneity of $La_{1-x}Gd_xPO_4$ monazite-type solid solutions by combined spectroscopic and computational studies*. Journal of Nuclear Materials, 486, 148–157, 2017. doi: 10.1016/j.jnucmat.2017.01.024.

[405] N. Clavier, R. Podor, and N. Dacheux. *Crystal chemistry of the monazite structure*. Journal of the European Ceramic Society, 31, 941–976, 2011. doi: 10.1016/j.jeurceramsoc.2010.12.019.

[406] P. M. Kowalski, Y. Ji, Y. Li, Y. Arinicheva, G. Beridze, S. Neumeier, A. Bukaemskiy, and D. Bosbach. *Simulation of ceramic materials relevant for nuclear waste management: Case of $La_{1-x}Eu_xPO_4$ solid solution*. Nuclear Instruments and Methods in Physics Research Section B: Beam Interactions with Materials and Atoms, 393, 68–72, 2017. doi: 10.1016/j.nimb.2016.09.029.

[407] H. Schlenz, J. Dellen, P. Kegler, C. Gatzen, C. Schreinemachers, A. Shelyug, M. Klinkenberg, A. Navrotsky, and D. Bosbach. *Structural and thermodynamic mixing properties of $La_{1-x}Nd_xPO_4$ monazite-type solid solutions*. Journal of Solid State Chemistry, 270, 470–478, 2019. doi: https://doi.org/10.1016/j.jssc.2018.11.040.

[408] Y. Li, P. M. Kowalski, A. Blanca-Romero, V. Vinograd, and D. Bosbach. *Ab initio calculation of excess properties of $La_{1-x}(Ln,An)_xPO_4$ solid solutions*. Journal of Solid State Chemistry, 220, 137–141, 2014. doi: 10.1016/j.jssc.2014.08.005.

List of publications

Journal articles

- Cui, Y., Sukkurji, P. A., Wang, K., Azmi, R., Nunn, A. M., Hahn, H., Breitung, B., **Ting, Y.-Y.**, Kowalski, P. M., Kaghazchi, P., Wang, Q., Schweidler, S., Botros, M., *High entropy fluorides as conversion cathodes with tailorable electrochemical performance*, J. Energy Chem. 72, 342–351, 2022, doi: 10.1016/j.jechem.2022.05.032.
- **Ting, Y.-Y.**, Kowalski, P. M., *Refined DFT+U method for computation of layered oxide cathode materials*, Electrochim. Acta 443, 141912, 2023, doi: 10.1016/j.electacta.2023.141912.
- Kowalski, P. M., Bornhake, T., Cheong, O., Dohrmann, N., Koch Liston, A. L., Potts, S. K., Shad, A., Tesch, R., **Ting, Y.-Y.**, *Fundamentals of energy storage from first principles simulations: Challenges and opportunities*, Front. Energy Res. 10, 1096190, 2023, doi: 10.3389/fenrg.2022.1096190.
- He, Y., Dreyer, S. L., **Ting, Y.-Y.**, Ma, Y., Hu, Y., Goonetilleke, D., Tang, Y., Diemant, T., Zhou, B., Kowalski, P. M., Fichtner, M., Hahn, H., Aghassi-Hagmann, J., Brezesinski, T., Breitung, B., Ma, Y., *Entropy-Mediated Stable Structural Evolution of Prussian White Cathodes for Long-Life Na-Ion Batteries*, Angew. Chem. Int. Ed. 63, e202315371, 2024, doi: 10.1002/anie.202315371.
- Binninger, T., **Ting, Y.-Y.**, Kowalski, P. M., Eikerling, M. H., *Optimization of ionic configurations in battery materials by quantum annealing*, Phys. Rev. B 110, L180202, 2024, doi: 10.1103/PhysRevB.110.L180202.
- **Ting, Y.-Y.**, Breitung, B., Schweidler, S., Wang, J., Eikerling, M., Kowalski, P. M., Guillon, O., Kaghazchi, P., *Delithiation-induced secondary phase formation in Li-rich cathode materials*, J. Mater. Chem. A 12, 33268-33276, 2024, doi: 10.1039/D4TA06030J.
- **Ting, Y.-Y.**, Ye, R., Dashjav, E., Ma, Q., Taminato, S., Mori, D., Imanishi, N., Finsterbusch, M., Eikerling, M. H., Guillon, O., Kaghazchi, P., Kowalski, P. M., *Thermodynamic and structural characterization of high-entropy garnet electrolytes for all-solid-state battery*, Front. Energy Res. 12, 1393914, 2024, doi: 10.3389/fenrg.2024.1393914.
- Ye, R., **Ting, Y.-Y.**, Dashjav, E., Ma, Q., Taminato, S., Mori, D., Imanishi, N., Kowalski, P. M., Eikerling, M. H., Kaghazchi, P., Finsterbusch, M., Guillon, O., *Preparation and elec-*

trochemical properties of $Li_6La_3Zr_{0.7}Ti_{0.3}Ta_{0.5}Sb_{0.5}O_{12}$ high-entropy Li-garnet solid electrolyte, Front. Energy Res. 12, 1379576, 2024, doi: 10.3389/fenrg.2024.1379576.

- He, Y., **Ting, Y.-Y.**, Hu, H., Diemant, T., Dai, Y., Lin, J., Schweidler, S., Marques, G. C., Hahn, H., Ma, Y., Brezesinski, T., Kowalski, P. M., Breitung, B., Aghassi-Hagmann, J., *Printed High-Entropy Prussian Blue Analogs for Advanced Non-Volatile Memristive Devices*, Adv. Mater. 37, 2410060, 2025, doi: 10.1002/adma.202410060.
- Binninger, T., **Ting, Y.-Y.**, Köster, K., Bruch, N., Kaghazchi, P., Kowalski, P. M., Eikerling, M. H., *Simulating charging characteristics of lithium iron phosphate by electro-ionic optimization on a quantum annealer*, submitted.

Conference talks

- **Ting, Y.-Y.**, Kowalski, P. M., *Reliable Computational Methodology for High-Entropy, Mixed Transition Metal Oxide Electrode Materials*, 2022 Annual meeting of Materials Research Society-Taiwan (MRST), November 2022 (Taiwan, Maoli).
- **Ting, Y.-Y.**, Kowalski, P. M., *Accurate First-Principle Study of High-Entropy Materials for Lithium-Ion Batteries*, 243rd Electrochemical Society (ECS) meeting, June 2023 (USA, Boston).
- **Ting, Y.-Y.**, *Computational Design of High-Entropy Materials for Next-Generation Batteries*, 75th Annual Meeting of the International Society of Electrochemistry (ISE), August, 2024 (Canada, Montreal).
- Kowalski, P. M., **Ting, Y.-Y.**, Price, C., Tipp, F., Eikerling, M.,*Decoding Electrochemical Interfaces with Computational Approaches: The Case of NiOOH Catalyst*, PRiME 2024 Electrochemical Society (ECS) meeting, October 2024 (Hawaii, Honolulu).

Conference posters

- **Ting, Y.-Y.**, Kaghazchi, P., Kowalski, P. M., *Computation of High Entropy, Mixed Transition Metal Oxide Cathode Materials*, 31^{st} Topical Meeting of the International Society of Electrochemistry (ISE), May 2022 (Germany, Aachen).
- **Ting, Y.-Y.**, Kaghazchi, P., Kowalski, P. M., *Reliable Computational Methodology for High-Entropy, Mixed Transition Metal Oxide Electrode Materials*, 11^{th} Neumann Institute for Computing (NIC) Symposium, September 2022 (Germany, Jülich).
- **Ting, Y.-Y.**, Kowalski, P. M., *Advancements in Atomistic Simulations of High-Entropy Materials for Lithium-ion Batteries*, European Materials Research Society (EMRS) Fall meeting, September 2023 (Poland, Warsaw).

- Price, C., Kowalski, P. M., Binninger, T., **Ting, Y.-Y.**, *Atomistic Modeling of Energy Materials on Emerging Computational Infrastructures*, CECAM Workshop, February 2024 (Germany, Berlin).
- Parisi, F., **Ting, Y.-Y.**, Price, C., Kowalski, P. M.,*Computational Materials Modelling of Energy Materials: Out of the Box Approach*, European Materials Research Society (EMRS) Fall meeting, September 2024 (Poland, Warsaw).

Awards

- Poster Award, 31st ISE Topical Meeting, May 2022 (Germany, Aachen).
- Student Talk Award, MRST Annual Meeting, November 2022 (Taiwan, Maoli).
- Student Talk Award, 243rd ECS Meeting, June 2023 (USA, Boston).

Band / Volume 663
Advances in Understanding Nitrate Aerosol Formation and the Implications for Atmospheric Radiative Balance
A. Milousis (2025), 195 pp
ISBN: 978-3-95806-823-0

Band / Volume 664
Optimization of NaSICON-type lithium-ion conductors for solid-state batteries
A. Loutati (2025), viii, 104 pp
ISBN: 978-3-95806-824-7

Band / Volume 665
Innovative Plasma Sprayed Thermal Barrier Coatings for Enhanced Flexibility in Gas Turbine Operation
J. Igel (2025), V, 153, XXXVI pp
ISBN: 978-3-95806-827-8

Band / Volume 666
Techno- ökonomisches Potenzial dezentraler und autarker Energiesysteme
S. K. A. Risch (2025), xxiii, 210 pp
ISBN: 978-3-95806-829-2

Band / Volume 667
Reactive Field Assisted Sintering of Novel Rare Earth Garnets for Plasma Etching Applications
C. Stern (2025), VII, 101, XXVIII pp
ISBN: 978-3-95806-833-9

Band / Volume 668
Effects of mucilage and extracellular polymeric substances on soil gas diffusion
A. Haupenthal (2025), v, 99 pp
ISBN: 978-3-95806-834-6

Band / Volume 669
Quantifying Recombination Losses and Charge Extraction in Halide Perovskite Solar Cells
L. Krückemeier (2025), vi, 286 pp
ISBN: 978-3-95806-835-3

Band / Volume 670
Investigation of Dynamic Material Changes During the Preparation of ZnPd Nanoparticles Supported on ZnO and their Catalytic Application in Methanol Steam Reforming on the Atomic Level
A. Meise (2025), xviii, 175 pp
ISBN: 978-3-95806-838-4

Schriften des Forschungszentrums Jülich
Reihe Energie & Umwelt / Energy & Environment

Band / Volume 671
Improving Energy Efficiency of Public Buildings by Influencing Occupant Behaviour using Dashboards and Gamification
E. Ubachukwu (2025), xxi, 191 pp
ISBN: 978-3-95806-840-7

Band / Volume 672
Exploring Plant Responses to Changing Environments: Integrating Phenotyping and Modeling Across Scales
F. M. Bauer (2025), xxix, 188 pp
ISBN: 978-3-95806-845-2

Band / Volume 673
A constitutive theory to represent non-idealities in contacting of SOC interconnect contacts
R. M. Pinto (2025), xii, 139 pp
ISBN: 978-3-95806-846-9

Band / Volume 674
Strontium titanate based materials for use as oxygen transport membranes in membrane reactors
Y. Tang (2025), XIV, 132 pp
ISBN: 978-3-95806-849-0

Band / Volume 675
Scaling Methods for the Production of Tungsten Fiber-Reinforced Composites via Chemical Vapor Deposition
A. Lau (2025), untersch. Pag.
ISBN: 978-3-95806-851-3

Band / Volume 676
Nanoscale analysis of high-temperature oxidation mechanisms of Cr_2AlC MAX phase and W-Cr-Y self-passivating tungsten alloy
A.J. S. Reuban (2025), ix, 142 pp
ISBN: 978-3-95806-855-1

Band / Volume 677
First principles simulations of high-entropy materials for energy storage
Y. Ting (2025), xviii, 169 pp
ISBN: 978-3-95806-858-2

Weitere ***Schriften des Verlags im Forschungszentrum Jülich*** unter
http://wwwzb1.fz-juelich.de/verlagextern1/index.asp

Energie & Umwelt / Energy & Environment
Band / Volume 677
ISBN 978-3-95806-858-2

Mitglied der Helmholtz-Gemeinschaft

JÜLICH
Forschungszentrum